Discovery of Emission above 100 GeV from The Crab Pulsar With VERITAS

Andrew McCann

Doctor of Philosophy

Department of Physics

McGill University

Montreal, Quebec

2011-07-15

A thesis submitted to McGill University in partial fulfillment of the requirements of the degree of Doctor of Philosophy.

DEDICATION

To the wonderful women in my life: my mother, Lily, my wife, Loes, and my three sisters; Sinéad, Ailish and Áine.

ACKNOWLEDGEMENTS

I am so very grateful for the support, guidance and friendship I have received from many people over the period of my doctoral studies.

First I wish to thank my supervisor Prof. David Hanna who has given unwavering support over the last five and a half years. For stimulating, encouraging and guiding me, and for always being there to discuss and argue with me, I am sincerely grateful. Thanks must also go to Prof. Ken Ragan for his many keen insights and stimulating conversations.

I must also thank the staff of the Physics Department for all their hard work concerning red tape and the day-to-day administrative burden. I offer special thanks to Paul Mercure and Juan Gallego for their tireless work maintaining the computing resources and for their many technical and computing insights.

Next, I must thank the graduate students and post-docs at the Department of Physics, both past and present. To Michael, Audrey, Luis, John, Gustavo, Cibran, Roxanne, Gernot, Peter, Mary, Gordana, Sean, Jonathan, Simon and David, thank you all for your friendship and for working with me and teaching and supporting me.

Huge thanks are also due to the members of the VERITAS collaboration, who have shared with me an extremely stimulating and exciting research project. Particular thanks are due to M. Schroedter and N. Otte, with whom I have worked very closely over the last year. Particular thanks are also due to G. Maier for his help using *EventDisplay* and to M. Lyutikov for help with theoretical interpretations. Special thanks must also go to the collaboration members based at the VERITAS site who took such good care of me during my time in Arizona: to T. C. Weekes, K. Gibbs, J. Perkins and D. Perkins, G. Gardner, J. Musser and G. Jones, thank you.

Most especially I would like to thank my family for their never-ending love and support. To Mam, Dad, Sinéad, Ailish, Áine, and Conor, I say thank you. Huge thanks must also go to Éadaoin, Dermot, Kate, Victor, Dave, Stephen and Edwige in Ireland and to Karen, Döerte, Raúl, Erica, Louigi, Rosie, Cees, Hanna, Pétur, Dora, Noémi, Michael and Ian here in Canada and around the world for the chats, the laughs and the distractions you have provided over the last few years.

Finally, I wish to thank my loving and caring wife Loes, who has taken such wonderful care of me over the last five years. I would not have made it without you.

ABSTRACT

Pulsars are highly magnetised rotating neutron stars that emit regular, periodic pulses of radiation across a wide range of the electromagnetic spectrum. Originally only observed in radio waves, pulsars are now regularly seen to emit x-ray and gamma-ray radiation. Although they were discovered over forty years ago and the number of known pulsars now exceeds 2000, the processes that generate the observed emission from pulsars are still poorly understood.

This work describes the detection of emission from the Crab Pulsar above 100 gigaelectronvolts (GeV), which is the highest radiation energy ever detected from a pulsar. Such an observation was not expected and presents a challenge to the most favoured pulsar emission models. This observation was made using the Very Energetic Radiation Imaging Telescope Array System (VERITAS), an array of four 12-meter-diameter atmospheric Cherenkov telescopes located in southern Arizona.

The detected pulsed excess has a statistical significance above 7 standard deviations and yields a derived pulsar flux that is less than 1% of the Crab Nebula flux between 140 and 880 GeV. This measurement is used to rule out an exponentially-shaped cut-off in the emission of the Crab Pulsar above $\sim$6 GeV, which was previously the preferred spectral shape. Furthermore, this measurement is used to set a limit on the minimum altitude of the gamma-ray emission site to greater than 10 times the neutron star radius, representing the most constraining limit ever set. Finally, it is shown that the emission seen by VERITAS challenges the role played by curvature radiation in current models of pulsar emission.

RÉSUMÉ

Les pulsars sont des étoiles à neutrons fortement magnétisées tournant sur ellesmmes, qui émettent réguliérement des impulsions de rayonnement périodiques à travers le spectre électromagnétique. Initialement observée seulement dans le spectre des ondes radio, les pulsars ont maintenant été détectés dans la gamme des rayons X et gamma. Bien qu'ils aient été découverts il y a plus de quarante ans et que le nombre de pulsars connus dépassent 2000, les processus générant les émissions observées provenant des pulsars sont encore mal compris.

Ce travail décrit la détection d'émission du Pulsar du Crabe au-delà de 100 gigaélectron-volt (GeV), ce qui est la radiation la plus énergétique jamais détectée provenant d'un pulsar. Une telle observation n'était pas attendue et présente un défi aux modéles d'émission de pulsar acceptés. Cette observation a été faite en utilisant un réseau de 4 télescopes atmosphriques Cherenkov de 12 métres de diamétre situé dans le sud de l'Arizona, appelé VERITAS (Very Energetic Radiation Imaging Telescope Array System).

L'excédent de l'impulsion détecté a une signification statistique de plus de 7 écart-types et donne un flux calculé de moins de 1% du flux de la Nébuleuse du Crabe entre 140 et 880 GeV. Cette mesure est utilisée pour exclure une coupure en forme dexponentielle dans l'émission du Pulsar du Crabe au-dessus de 6 GeV, qui était auparavant la meilleure forme expliquant le spectre. De plus, cette mesure est utilisée pour fixer une limite sur l'altitude minimale du site d'émission des rayons gamma de 10 fois le rayon de l'étoile à neutron, représentant la limite la plus contraignante jamais établie. Finalement, ce travail montre aussi que l'émission observée par VERITAS questionne le rôle du rayonnement de courbure des modéles courants d'émissions de pulsar.

STATEMENT OF ORIGINAL CONTRIBUTIONS

Over the course of his doctoral studies, the author of this thesis has contributed in many ways to the building, running and maintaining of the VERITAS telescopes as well as to the scientific output of the VERITAS collaboration.

Over five years, the author spent more than two hundred days at the VERITAS site undertaking observing, maintenance and upgrade work. Principal among this was the installation of the LED flasher system which replaced a nitrogen laser as the primary PMT calibration light source in October 2009 (see Section 3.5.6 of the thesis and [45]).

Approximately a year of his time was dedicated to the development of a new mirror alignment system for the VERITAS telescopes (see Section 3.6.2 of this thesis and [79]). The author took complete responsibility for this project, from the initial design to a fully functioning and user-friendly end product. This included the development of all real-time control software and off-line data analysis pipelines and the implementation of several full alignments of the VERITAS telescopes. This development reduced the size of the optical PSF of the telescopes by more than 30%. This improvement has led to a reduction in the VERITAS pointing error and also to reduction in the energy threshold, which is particularly important for the research presented in here. For his development of this alignment system, the author was awarded the 2010 Reginald Fessenden Prize in Innovation from the McGill Faculty of Science.

The author also designed and developed several software utilities which are in broad use throughout the VERITAS collaboration, including an on-line web application for daily monitoring and rating of the data acquired by the VERITAS telescopes as well as a software tool used to measure their optical point-spread-functions.

The author gave presentations about his research at two student workshops and at the CASCA meeting in 2010, for which he received the award for best student presentation. He presented his research as a poster at the International Cosmic Ray Conference in 2009, gave three intra-department talks and a seminar at the DESY Institute in Zeuthen, Berlin.

Of the material presented in this thesis, Chapter 5 contains the most important results, which represent the author's own work. It presents an independent analysis of the VERITAS Crab Pulsar data set, including the first-ever measurements of emission from the Crab Pulsar above 100 GeV. Included in the chapter is also the author's analysis of public data from NASA's *Fermi* satellite. The material presented in this chapter forms a foundational analysis for a paper on the subject published in the journal *Science* [110].

TABLE OF CONTENTS

LIST OF TABLES

LIST OF FIGURES

Figure page

CHAPTER 1
Introduction

1.1 VERITAS and Very-High-Energy Gamma-ray Astronomy

Astronomy, the study and observation of celestial objects, is one of the oldest fields of science. For centuries, the naked eye was the primary tool for observation, and for this reason, optical astronomy is the oldest, and perhaps most dominant, branch of astronomy. Advances in instrumentation and technique have always been the primary forces driving new astronomical discoveries. Advances in physics in the 20th century led to the emergence of astronomy across the whole electromagnetic spectrum; from radio waves to gamma rays.

Gamma-ray astronomy was born out of the investigation into the origin of *cosmic rays*. Cosmic rays are charged particles (protons, atomic nuclei and electrons) which bombard the Earth and originate in outer space. Their extraterrestrial origin was discovered in 1912 by Victor Hess, who noticed that an electroscope, a device which measures charge, registered increasing charge with increasing altitude. Until then, this mysterious ionising radiation was believed to originate within the Earth and this discovery prompted the award of the Nobel prize in physics to Hess in 1936. Cosmic rays are believed to be created in extreme astrophysical environments. The exact location of their production sites is still unknown. The fact that cosmic rays are charged means that their path from the source to the Earth is influenced by magnetic fields which permeate space. As a result, the arrival directions of cosmic

rays at the Earth are isotropic, concealing their true origin. High energy photons are also produced in the extreme environments responsible for the production of cosmic rays and they are not deflected by magnetic fields and thus are considered excellent tracers of cosmic ray production.

Although the search for the origin of cosmic rays was the starting point for gamma-ray astronomy, the field has developed far beyond this single goal, into a branch of main-stream astronomy. Gamma rays provide a unique probe of *non-thermal* radiation processes which occur in only the most extreme and energetic astrophysical environments, such as those created by supernova remnants and super-massive black holes. In these environments, particles are accelerated to relativistic energies, and emit radiation by various mechanisms which differ fundamentally from the more familiar thermal processes. The energy budget of some astrophysical objects is often dominated by gamma-ray radiation, so gamma-ray observations are necessary to gain an understanding of the physical processes involved.

Gamma ray is the collective name for photons with an energy exceeding $\sim$100 keV. This huge range is divided in to several sub-ranges, one of which is *very-high-energy* gamma rays, which covers the range from 100 GeV to 100 TeV (see Table 1.1 for the classification of the various ranges). Observations made in the very-high-energy (VHE) gamma-ray regime with the VERITAS telescope are the main subject of this work.

VERITAS, which stands for; **V**ery **E**nergetic **R**adiation **I**maging **T**elescope **A**rray **S**ystem, is the name of an array of four VHE gamma-ray telescopes operating at the Fred Lawrence Whipple Observatory, in Amado, Arizona, USA. VERITAS

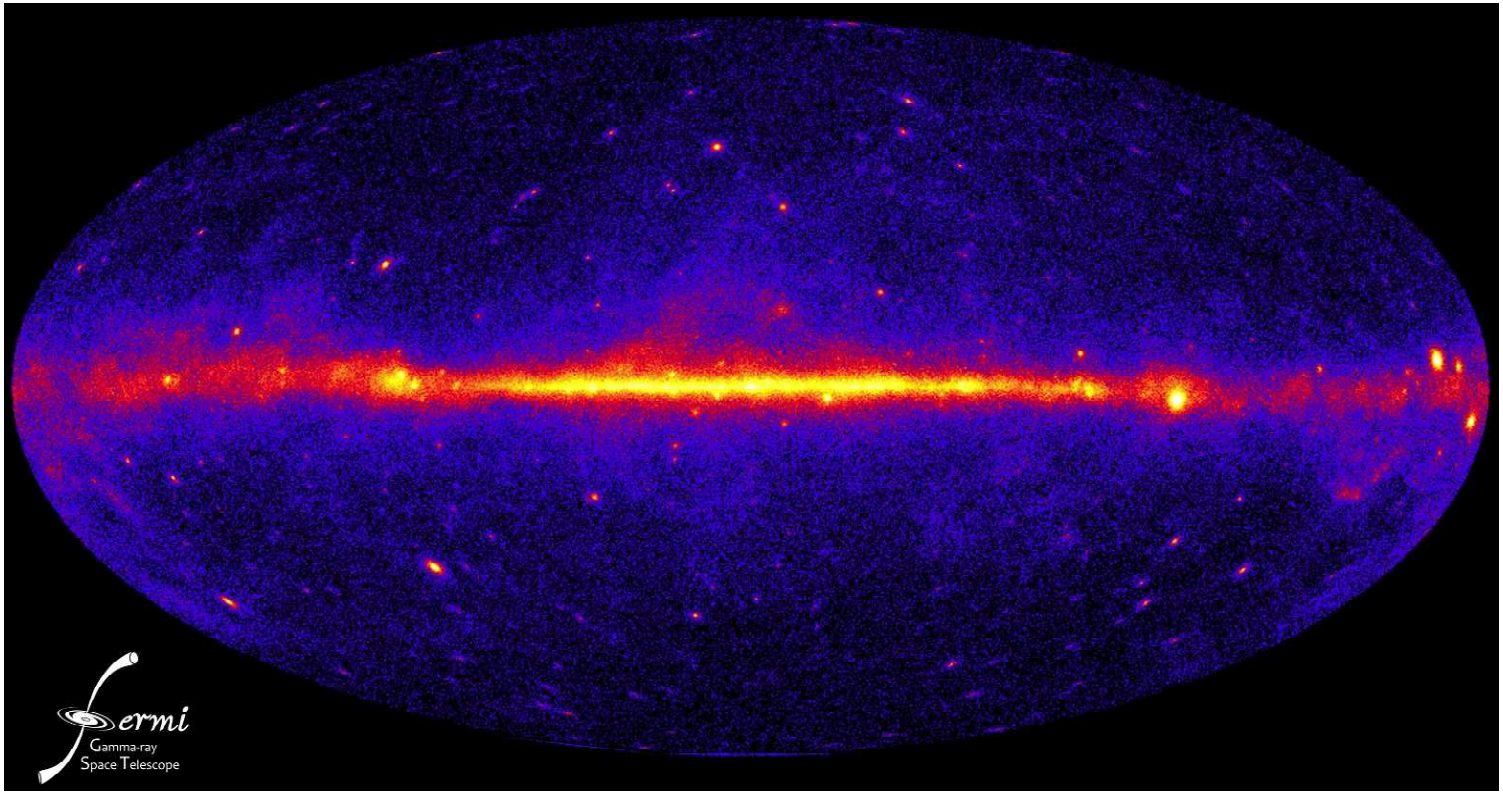

Figure 1–1: The non-thermal universe above 30 MeV as seen from one year of data from the *Fermi* satellite. The emission from the galactic plane is the most visible feature. Several bright galactic sources are visible, including the Crab Pulsar, which is the right-most bright spot along the plane. Image taken from http://www.nasa.gov/mission_pages/GLAST/news/first_year.html

Energy range	Designation	Detection technique
100 keV to 10 MeV	Low energy (LE)	Satellite-based Compton scattering
10 MeV to 30 MeV	Medium energy (ME)	Satellite-based Compton scattering
30 MeV to 100 GeV	High energy (HE)	Satellite-based Pair production
100 GeV to 100 TeV	Very high energy (VHE)	Ground-based Imaging Cherenkov
100 TeV to 100 PeV	Ultra high energy (UHE)	Ground-based Particle Detector
100 PeV and above	Extremely high energy (EHE)	Ground-based Air Fluorescence

Table 1–1: Classification of the sub-divisions within the broad gamma-ray energy regime. The third column specifies the most common detection mechanisms for photons within each energy range. This table is based on classifications in [112] and [57].

Figure 1–2: Image of the VERITAS Telescope Array in September 2009. The VERITAS array consists of four VHE gamma-ray telescopes and is located at the Fred Lawrence Whipple Observatory, in Amado, Arizona, USA.

was designed and built, and is operated, by an international collaboration of scientists and academic institutions called The VERITAS Collaboration (see Appendix B). The array, which consists of four telescopes built sequentially, began operations as a single telescope in February, 2005 and was completed in March, 2007. VERITAS is one of four major ground-based gamma-ray telescopes in operation today (see Table 1–2). A Photograph of VERITAS is shown in Figure 1–2.

VERITAS is an *imaging atmospheric Cherenkov* Telescope. Atmospheric Cherenkov emission occurs when an energetic particle, such as a gamma ray, interacts with the atmosphere. This interaction leads to the formation of a cascade of energetic relativistic particles which disturb the atoms in the atmosphere causing them to emit a flash of photons. This radiation is called Cherenkov emission. This flash of photons, when observed from the ground, lasts only a few nanoseconds and illuminates a large area ($\sim 10^5\, m^2$) and can be recorded by sensitive photon detectors, such as photo-multiplier tubes (see Figure 1–3). The VERITAS telescopes are equipped

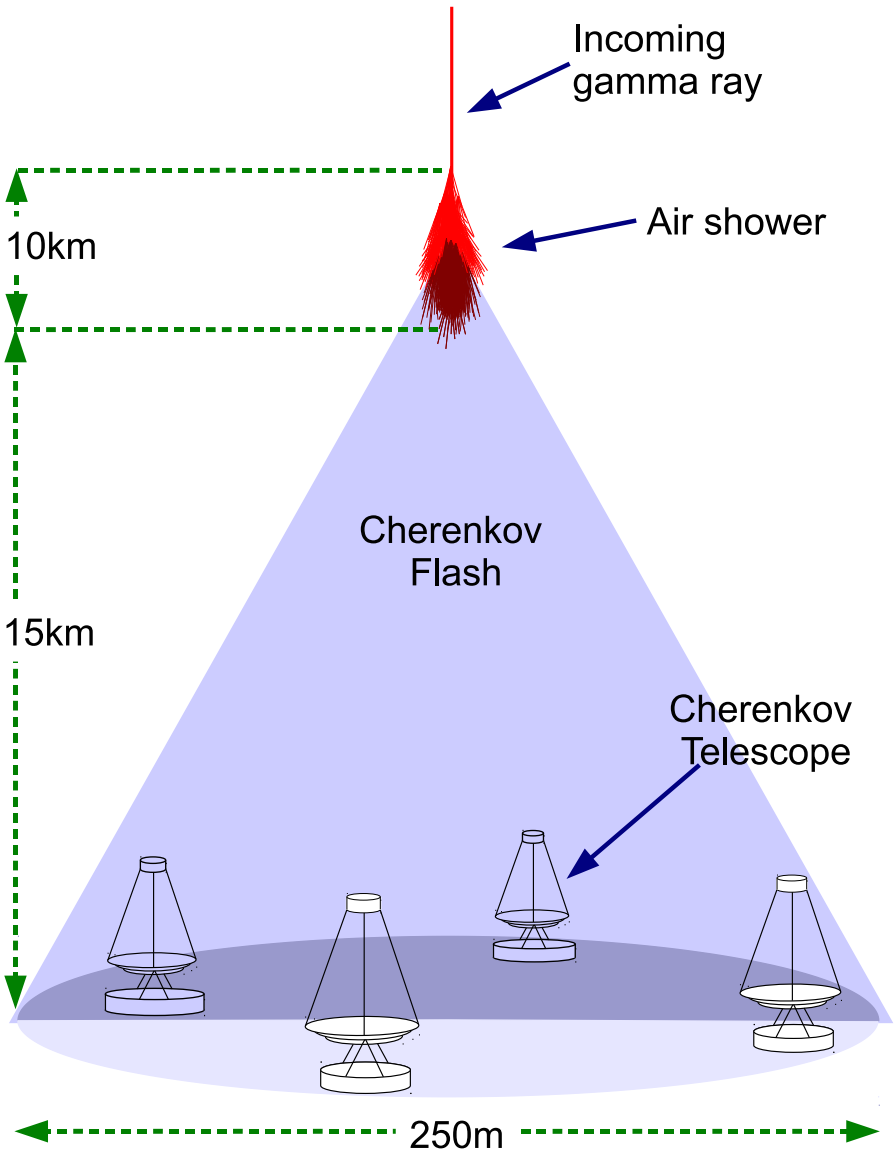

Figure 1–3: Cartoon of atmospheric Cherenkov emission and detection. An incoming gamma ray causes a cascading air shower. The particles in the shower cause the emission of Cherenkov radiation which is emitted in a flash which illuminates an area on the ground of $\sim 10^5\, m^2$. Telescopes with large reflectors focus the flash on to sensitive cameras and form an image of the shower.

Group	Site	Number of Telescopes	Reflector diameter	First Light
Whipple	Arizona, USA	1	10 m	1984
MAGIC II	La Palma, Canary Islands, Spain	2	17 m	2003
HESS	Khomas Highland, Namibia	4	12 m	2003
VERITAS	Arizona, USA	4	12 m	2005

Table 1–2: A list of the major imaging atmospheric Cherenkov Telescopes in operation today. The Whipple $10m$ telescope pioneered the imaging technique and laid the foundational bases for the subsequent new generation of Cherenkov Telescopes.

with twelve-meter-diameter reflectors, which can form an image of the atmospheric cascade via the Cherenkov radiation it generated. By imaging the shower, and using sophisticated data processing, telescopes such as VERITAS can measure the arrival direction and energy of the gamma ray which initiated the cascade. A detailed description of VERITAS and the imaging atmospheric Cherenkov technique is presented in Chapter 3.

1.2 Gamma-ray Pulsars

This work is concerned with gamma-ray pulsars, specifically the Crab Pulsar; a well-known powerful young pulsar which is bright across the entire electromagnetic spectrum and inhabits the Crab Nebula. Pulsars are highly magnetised spinning neutron stars which are formed from the cores of massive stars which have exploded, having first collapsed under their own gravitational pressure. The defining characteristic of pulsars is the emission of periodic pulses of radiation which occur at the pulsar's signature rotational frequency, most commonly in the radio band. Pulsars have a typical mass of 1.4 solar masses and have rotational periods which range from a few milliseconds to several seconds and were first detected in 1967 [51].

The first observations of gamma-ray emission from pulsars was made in the mid 1970s by the NASA SAS-2 satellite [39] and European COS-B satellite [96]. They discovered gamma-ray emission above 100 MeV from the Crab pulsar, the Vela pulsar, and the previously unknown Geminga pulsar. The number of known gamma-ray pulsars rose to seven following the launch of the EGRET instrument on board NASAs Compton Gamma Ray Observatory (CGRO) in 1991 and there it stayed for over a decade. Since launch of the NASA *Fermi* satellite in 2008, the number of known gamma-ray pulsars has rapidly increased, with 39 new gamma-ray pulsars being discovered during the first six months of operations alone [4]. At the time of writing the *Fermi* satellite has detected 101 pulsars[1] . These discoveries have revolutionised the field of pulsar astrophysics, where inquiry into the nature of pulsed gamma-ray emission has yielded a variety of open questions. The two principal questions are:

- What are the radiation mechanisms responsible for the observed gamma-ray emission?
- Where, within the local environment around the pulsar, does the gamma-ray emission originate?

In this work, these questions are addressed in the light of VHE observations of the Crab Pulsar.

[1] https://confluence.slac.stanford.edu/display/GLAMCOG/Public+List+of+LAT-Detected+Gamma-Ray+Pulsars

1.2.1 Emission Models

It is generally accepted that pulsars are surrounded by a dense plasma which co-rotates with the pulsar. Within this plasma, vacuum gaps are believed to form, and within these gaps, electric fields exist which can accelerate particles to relativistic velocities. These particles can subsequently generate the observed gamma rays via a variety of non-thermal emission mechanisms. Three popular model classes exist which argue in favour of three different gap locations;

- The Polar Cap models argue that particle acceleration and emission occurs in a gap above the magnetic pole of the neutron star.
- The Outer Gap models argue in favour of an emission zone away from the stellar surface, in regions where the plasma co-rotation velocity approaches the speed of light.
- The Slot Gap models argue that an asymptotically narrowing gap extends outwards from the magnetic pole, flaring outwards along the poloidal magnetic field lines.

No proposed model satisfactorily describes all of the observational data, and for this reason, broad debate continues regarding their underlying assumptions and postulates. Unlike the sites of emission, consensus is building on the most likely radiation mechanism. *Curvature radiation*, which occurs when charged particles are accelerated in the presence of an extremely large magnetic field ($\sim 10^{12}\ G$), can accommodate the bulk of the observed gamma-ray emission properties. Particularly, all of the pulsars observed by the *Fermi* satellite, exhibit a common spectral feature; a cut-off in the emission above a few GeV. Such a feature is expected if curvature radiation is

the principal component of the emission due to a balance which exists between the acceleration gains and radiation losses from particles which emit curvature radiation. If curvature radiation is the dominant emission mechanism, no gamma-ray emission is expected in the VERITAS energy regime.

Pulsars, and the theoretical framework of gamma-ray emission, are discussed in detail in Chapter 2.

1.3 Thesis Overview

This work describes observations of the Crab Pulsar with the VERITAS gamma-ray telescope. These measurements, along with measurements derived from data recorded by the *Fermi* satellite, are described within the context of the current theories of emission from pulsars.

Chapter 2 provides a description of the physical properties of pulsars, including a review of stellar evolution and pulsar formation. This chapter also details the major non-thermal emission mechanisms which can occur within the energetic environments created by pulsars. A broad review of the three principal emission models (briefly discussed earlier) is also provided, alongside a description of the recent findings of the *Fermi* satellite. This chapter concludes with a review of the Crab Nebula and Pulsar.

Chapter 3 presents a thorough account of the imaging atmospheric Cherenkov technique. The mechanisms behind the creation of Cherenkov photons are detailed in conjunction with a description of the properties of atmospheric particle cascades. Here, particular attention is given to the discernible differences which exist between cascades initiated by gamma rays and those created by cosmic rays and how these

differences may be exploited by ground-based detectors. This chapter also describes in detail the function and technical specifications of the principal hardware components of the VERITAS telescopes, concluding with a review of the calibration of their primary subsystems.

Chapter 4 provides an extensive description of the analytical formalisms and processing stages employed in the unpacking of VERITAS data. Detailed in particular are the prescriptions used to differentiate between gamma-ray initiated and background events and the methods used to determine the energy and arrival direction of these events. Chapter 4 also details the particular treatment of the recorded event arrival time which is necessary when searching for signals imprinted by putative periodic sources. This chapter concludes with a review of statistical tests which may be used to identify periodic signals within a time series data sample.

Chapter 5 presents the results of an analysis of a VERITAS data set obtained on the location of the Crab Pulsar. These data contain a total exposure duration of 103 hours and were recorded between September 2007 and February 2011. This chapter reports on the analysis of the strong steady (un-pulsed) VHE emission from the Crab Nebula alongside a search for emission from the Crab Pulsar. Also presented is an analysis of the publicly available data from the *Fermi* satellite. Where possible, measurements extracted from the *Fermi* data are contrasted and compared with similar measurements obtained from the VERITAS data.

Chapter 6 presents the conclusions which can be drawn from the results described in Chapter 5.

CHAPTER 2
Pulsars and Radiative Emission Mechanisms

2.1 Introduction

Pulsars are rapidly rotating highly magnetised neutron stars born after the explosion of a massive star. They are most commonly identified by the observation of periodic pulses of radiation, particularly radio waves.

The first detection of a pulsar was made in 1967 by Hewish and Bell working with the Cambridge 4.5 acre radio antenna array [51, 50]. Shortly after [100], the Crab Pulsar, PSR J0534+220, was detected in the Crab Nebula. Today the number of known pulsars exceeds 2,000 [64] and continues to grow. Pulsars are divided into two categories which are based on the power source that is responsible for the observed emission. The shedding of rotational energy powers the emission from *rotation-powered pulsars* while the accretion of matter from a companion star provides the energy of *accretion-powered pulsars*. The latter are mainly visible through thermal emission, typically soft x-rays, and are therefore less likely to emit high-energy radiation. Rotation powered pulsars are, however, known to emit non-thermal radiation, from radio waves to high-energy gamma-rays [19].

The following chapter will describe how pulsars form and will detail the bulk properties of rotation-powered pulsars. Further, the current theories of radiative emission from pulsars are described with an emphases on gamma-ray emission. These

theories are then reviewed in the context of the observations of the *Fermi* satellite. The chapter concludes with a review of the Crab Nebula and Pulsar.

2.2 Pulsar formation

The evolution of a star, after it leaves the main sequence, is based mainly on its mass and whether it is part of a binary system. Low-mass stars, where $M < 8M_{\odot}$, begin burning helium and carbon in their core when the supply of hydrogen in the core is finally exhausted. At this point, the radiation pressure increases with the fusion of these heavier elements, and the outer layers of the star are eventually blown off. The remaining carbon core eventually collapses under gravity until electron degeneracy pressure balances the collapse. The core cools and the star becomes a white dwarf.

High-mass stars, where $M > 8M_{\odot}$, follow a different evolutionary path. Here, when helium and carbon are burning in the core, the radiation pressure is not strong enough to blow off the surrounding mass, which continues to apply gravitation pressure and further heat up the core. Fusion continues past the exhaustion of the remaining helium, burning all the remaining light elements, until the formation of iron. Iron has the highest binding energy per nucleon of all the elements, thus the fusion reaction in the core is halted, since the amount of required input energy is greater than the output energy. The gravitational pressure applied to the core by the outer layers is sufficiently large that it overcomes the electron degeneracy pressure and the core once again begins to collapse. Accompanying this collapse is another increase in temperature in the core allowing photo-disintegration of the iron into

helium;

$$^{56}Fe + \gamma \longrightarrow 13\,^{4}He + 4\,n$$

The helium then disintegrates into two neutrons and two protons which subsequently combine with ambient electrons forming more neutrons. Eventually the collapsing core will consist entirely of neutrons at which point the neutron degeneracy pressure stops the collapse. The collapsing outer layers, unable to compress the core further, rebound off the core causing a shock wave which reverberates outwards. The star explodes. The outer layers are ejected in a massive blast into space, while the core becomes a *neutron star*. The ejected matter from the explosion forms a *supernova remnant*. This is an example of a type II supernova, a category of supernovae whose progenitor was a massive young star. Type I supernovae occur in binary systems when a white dwarf accretes matter from its binary companion, until the point when the gravitational pressure of the total mass of the star is greater than the radiative pressure produced by the white dwarf's core. Within these two categories are subgroups which describe more precisely the evolution of the supernova. In cases where the newly formed pulsar and companion star remain gravitationally bound, the system may evolve, with the neutron star accreting matter from its companion star. This accretion process can transfer angular momentum to the pulsar causing it to spin faster. This process is believed to be responsible for the creation of a distinct population of pulsars, called *millisecond* pulsars; pulsars with rotational periods less than 10 milliseconds.

Parameter	Typical	Crab	Unit
Magnetic Field	1×10^{12}	4×10^{12}	G
Rotation Rate	2	29	Hz
Radius	10	10	km
Mass	1.4	1.4	$M_{\odot}$
Moment of Inertia	1×10^{45}	1×10^{45}	$g\,cm^2$
Electric Field	6×10^{12}	6×10^{10}	$V\,cm^{-1}$

Table 2–1: Typical values of the principal physical parameters which describe pulsars. Adapted from [112].

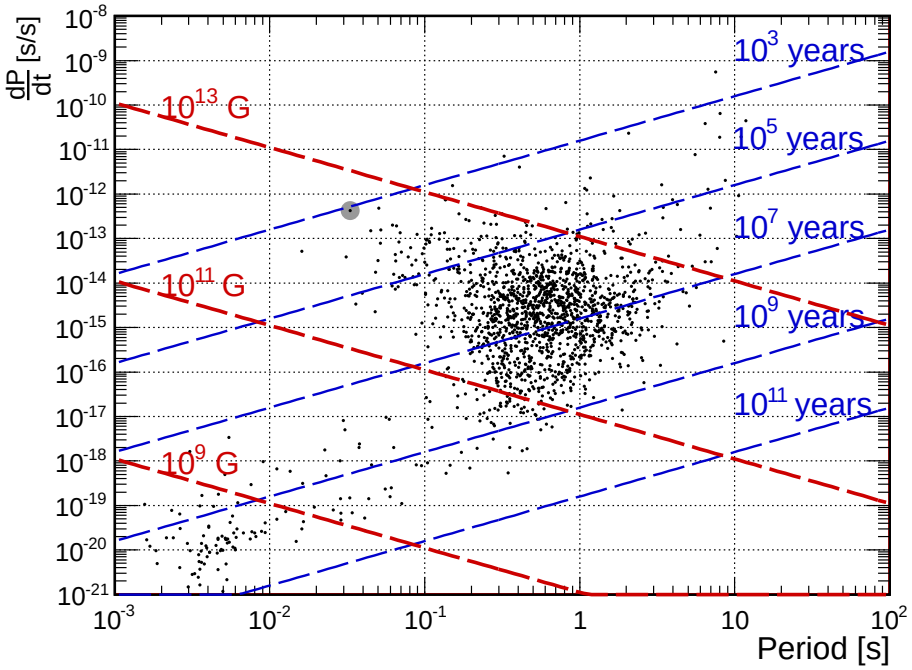

Figure 2–1: Distribution of pulsar period and period derivatives from the ATNF on-line pulsar catalogue (http://www.atnf.csiro.au/research/pulsar/psrcat) [77]. The grey marker highlights the location of the Crab pulsar. The blue dashed lines represent the characteristic spin down age contours and the red dashed lines represent the derived surface field strength contours. The population of pulsars in the lower left corner, with periods $< 10^{-2}s$ are millisecond pulsars.

2.3 Pulsar Properties

Following a supernova, neutron stars are born with a mass of $1.4M_{\odot}$ and a radius of $\sim$10 km. The bulk properties of rotation-powered pulsars can be determined from the observed period, P, and period derivative, $\dot{P}$, by considering the behaviour of a spherical rotating magnetic dipole. The energy of a rigid rotator is

$$E = \frac{1}{2}I\omega^2 \quad , \quad \omega = 2\pi/P \quad , \quad I = \frac{2}{5}MR^2$$

where I is the moment of inertia of the object (sphere), M is its mass, R is its radius and ω is its angular rotation frequency. The rate of energy loss of a pulsar, called the *spin-down luminosity*, is formulated as

$$-\frac{dE}{dt} = 4\pi^2 \frac{I}{P^3}\dot{P}$$

The energy loss of a rotating dipole is

$$-\frac{dE}{dt} = \frac{\mu_0 |\ddot{\vec{p}}_m|^2}{6\pi c^2}$$

where $\vec{p}_m$ is the magnetic moment of the dipole. Combining the two equations above, and applying the typical values of the mass, radius and magnetic permeability of a neutron star yields

$$B_s \simeq 3 \times 10^{19} \sqrt{\frac{P\dot{P}}{s}} \quad [G]$$

as the magnetic field strength at the surface of a pulsar, where s is seconds. If we assume that B_s is constant then,

$$P\dot{P} = \left(\frac{B_s}{3 \times 10^{19}}\right)^2 = constant$$

Thus

$$\begin{aligned} P\dot{P} &= P\frac{dP}{dt} \\ \Rightarrow P\dot{P}dt &= PdP \\ \Rightarrow \int_0^{\tau}(P\dot{P})dt &= \int_{P_0}^{P} PdP \\ \Rightarrow P\dot{P}\tau &= (1/2)(P^2 - P_0^2) \end{aligned}$$

If we assume the original period, P_0, is much smaller than the current period, P, then

$$\tau = \frac{P}{2\dot{P}}$$

where τ is the *characteristic spin-down age*. This is typically used as an approximation for the age of the pulsar. From such equations as these, the value of general physical parameters can be derived. Some such values are shown in Table 2.3.

2.4 High Energy Photon Emission and Absorption

While the presented picture of a pulsar allows simple approximations to be made about pulsar "energetics", there is no general agreement on the mechanisms by which pulsars radiate. Rotation-powered pulsars emit two types of radiation; coherent and incoherent. Coherent emission occurs when a bunch of accelerated particles all radiate together. The observed radio emission from pulsars is believed to be coherently emitted, since the observed radio luminosity is too high to come from single-particle emission. Incoherent emission, when each generated photon comes from a single accelerated particle, is responsible for the observed optical, x-ray and gamma-ray emission from pulsars. The following sections will detail some photon

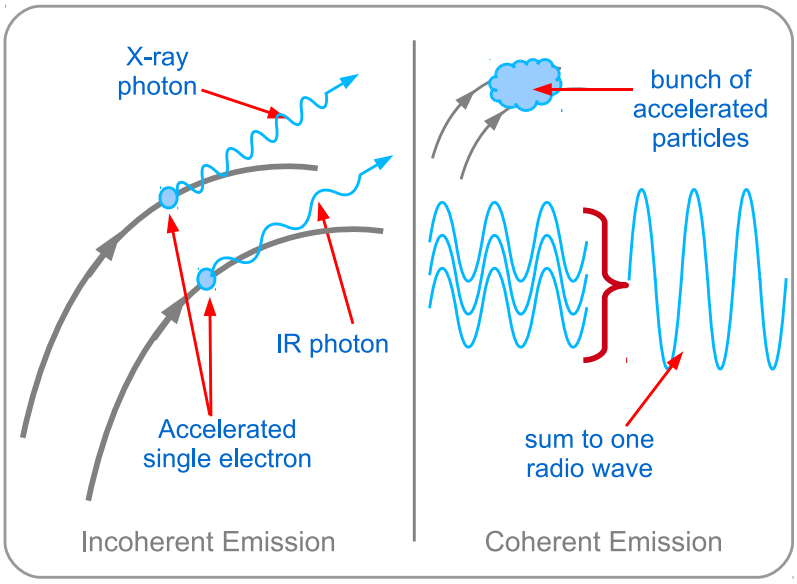

Figure 2–2: Illustration of the two types of radiated emission from pulsars; coherent and incoherent emission. Coherent emission occurs when a bunch of accelerated particle all radiate together. The observed radio emission from pulsars is coherently emitted. Incoherent emission, when each generated photon comes from a single accelerated particle, is responsible for the observed optical, x-ray and gamma-ray emission from pulsars.

emission and absorption processes which are important when considering pulsars, such as synchrotron emission, curvature radiation, inverse-Compton scattering and pair production.

2.4.1 Cyclotron Radiation

Cyclotron radiation is created when a non-relativistic charged particle moves in a magnetic field. When the particle enters the field, it is acted on by the Lorentz force

$$\vec{F} = q(\vec{v} \times \vec{B})$$

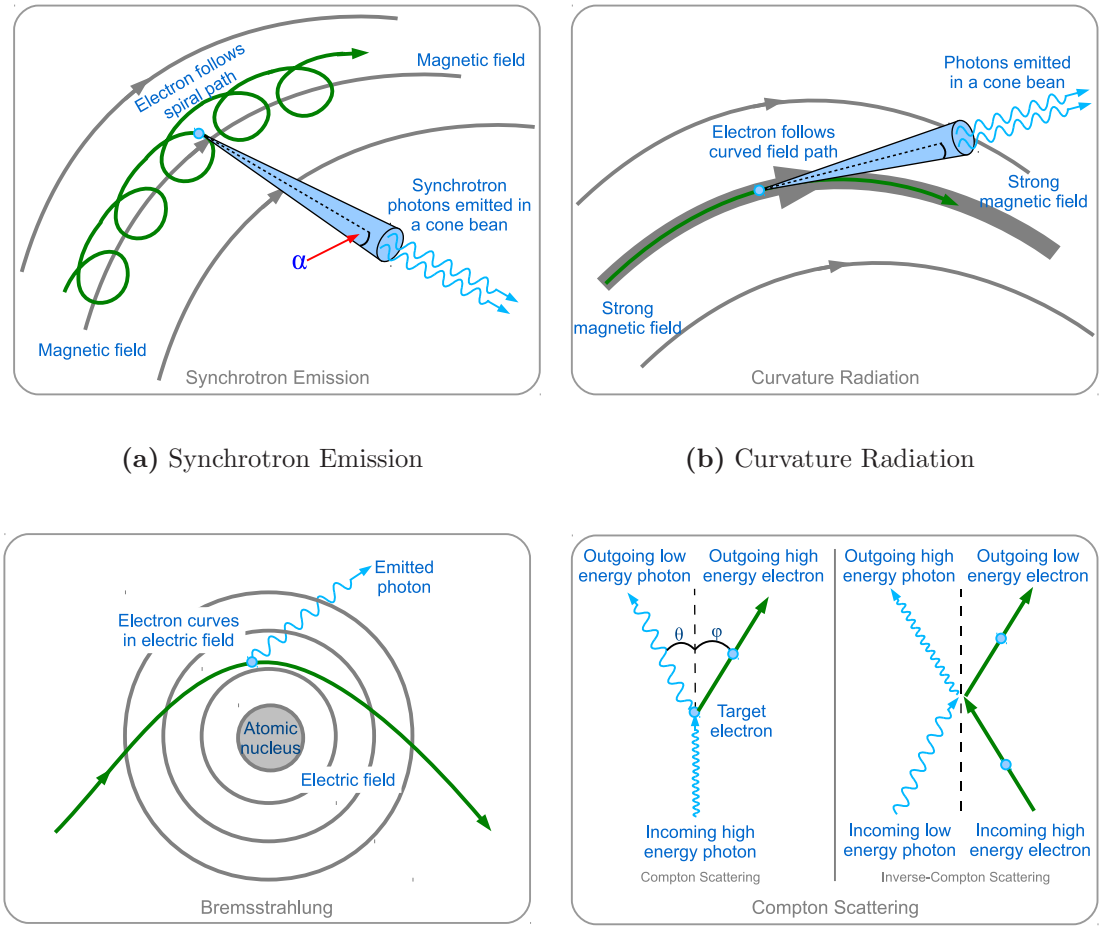

(a) Synchrotron Emission

(b) Curvature Radiation

(c) Bremsstrahlung

(d) Compton Scattering

Figure 2–3: Cartoon representations of four important high-energy emission processes.

which acts perpendicularly to the field direction and the direction of the moving particle. This perpendicular force causes the centripetal acceleration of the particle and as a result the particle spirals around the magnetic field lines. This spiralling charge then radiates electromagnetic energy. The angular frequency of the particle as it spirals (cyclotron frequency) is determined by equating the centripetal force to the Lorentz force, thus

$$\begin{aligned} \frac{mv^2}{r} &= qvB \\ \Rightarrow \frac{v}{r} &\equiv \omega_c = \frac{qB}{m} \end{aligned}$$

where m, v, q are the particle's mass, velocity and charge respectively, and B is the magnetic field strength. The particle radiates like a dipole with the frequency $\omega_c/2\pi$ or its harmonics. The radiation is highly circularly or linearly polarised if viewed along or perpendicular to the spiral axis, respectively.

2.4.2 Synchrotron Radiation

When a charged particle moves relativistically within a magnetic field it emits synchrotron radiation. Unlike cyclotron emission, where the radiation frequency equals the gyration frequency, synchrotron photons are emitted with a continuum of frequencies. This continuum falls off exponentially when the photons are emitted above the critical frequency,

$$\omega_c = \frac{3c}{2\rho_c}\gamma^3 \tag{2.1}$$

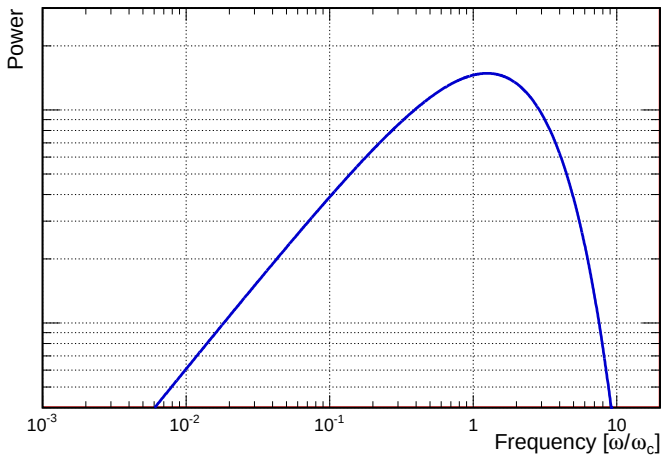

Figure 2–4: Characteristic shape of the emitted power spectrum from synchrotron emission. The frequency is in units of the critical frequency (see Equation 2.1). Emission falls exponentially above the critical frequency, ω_c. Power is shown on a log scale with arbitrary units.

where γ is the Lorentz factor and ρ_c is the radius of curvature of the path of the charged particle [72]. This results in a very characteristic spectral shape (see Figure 2–4) where the peak energy is dependent on the strength of the magnetic field and the energy of the particle.

Given the relativistic nature of this process, the roughly isotropic emission directions in the particle's rest frame are collapsed in the observers frame to a forwardly beamed emission cone (see Figure 2–3(a)). The opening angle of the cone, α, is determined by the particle mass and energy via,

$$\alpha \approx \frac{mc^2}{E}$$

thus the higher the energy of the particle, the more collimated the beam. As with cyclotron emission, the photons are also highly polarised. The high degree of polarisation and characteristic continuum spectrum shape makes synchrotron radiation easily determinable in astrophysical observations.

2.4.3 Curvature Radiation

In cases where the magnetic field is extremely strong, $\sim 10^{12}G$, a relativistic charged particle trapped in the field will radiate curvature radiation. Due to the high magnetic field strength, the particle gyration around the field line is quickly damped by synchrotron losses. The particle then propagates along the magnetic field lines and this motion along the curved path of the magnetic field lines itself causes the particle to radiate (see Figure 2–3(b)). Curvature-radiated photons are relativistically beamed in the forward direction and the radiation can reach gamma-ray energies. It is considered one of the principal gamma-ray production mechanisms of pulsars, due to the strength of their polar magnetic fields.

Electrons which radiate curvature photons can reach a maximum Lorentz factor of

$$\gamma_{max} = \frac{E_e^{max}}{m_e c^2} \simeq \left(\frac{3\rho_c^2 E_\parallel}{2e} \right)^{1/4} \tag{2.2}$$

where $E_\parallel$ is the electric field strength parallel to the magnetic field and ρ_c is the radius of curvature of the magnetic field. At this energy, the electrons have reached the *radiation-reaction limit*, which occurs when the rate of radiative loss to curvature photons is equal to the accelerated energy gain rate. The emitted curvature photon

spectrum will thus have a break at the photon energy

$$E_{\gamma}^{break} = \rho_c^{1/2}\,(hc)\left(\frac{3}{2}\right)^{7/4}\left(\frac{E_{\|}}{e}\right)^{3/4} = \gamma_{max}\,(hc)\left(\frac{3}{4}\right)^{3/4}\left(\frac{E_{\|}}{e}\right)^{1/2} \tag{2.3}$$

with emission falling exponentially above the break energy. This equation shows that the maximum emitted gamma-ray energy is a function of the maximum accelerated electron energy. Inside a pulsar, this equation can be written in the form

$$E_{\gamma}^{max} \simeq \left(\frac{8c}{r|\vec{\omega}|}\right)\left(\frac{\rho_c}{r}\right)^{1/2}(\varepsilon_{\|}B_{12})^{3/4}(P_{0.1})^{-7/4} \quad [GeV] \tag{2.4}$$

where r is the height of the emission region, $\vec{\omega}$ is the pulsar's rotational vector, B_{12} is the surface polar magnetic field strength in units of $10^{12}G$ and $P_{0.1}$ is the period of the pulsar in units of $0.1s$ [23]. Introduced in the above equation is $\varepsilon_{\|} \leq 1$ which is an efficiency factor of the accelerating electric field, $E_{\|}$, such that

$$E_{\|} = \varepsilon_{\|}\frac{r|\vec{\omega}|B}{c}$$

Equation 2.4 relates the maximum energy of the curvature photons which can be created within an acceleration region with the distance above the star's surface and the strength of the magnetic field.

Photon/B-Field Pair Creation

It is important to note that high energy photons often subsequently undergo pair production in interactions with the strong magnetic field, which appears as photons in their frame of reference. The cross-section for this interaction is proportional to $B_{\perp}$, the component of the magnetic field perpendicular to the photon's direction,

with pair-production beginning once the following criterion is met:

$$\frac{4}{3}\frac{mc^2}{E_\gamma}\frac{B_{crit}}{B_\perp} < 1 \tag{2.5}$$

where E_γ is the photon energy and B_{crit} is the *critical* magnetic field strength

$$B_{crit} = \frac{m^2c^3}{e\hbar} = 4.41 \times 10^{13} G$$

[109]. Such a configuration allows for creation of electromagnetic cascades, where emitted curvature photons pair produce and the resulting pair then subsequently emits more curvature photons. This cascade mechanism has the effect of limiting the maximum energy of the photons which can escape the acceleration region of a pulsar to

$$E_\gamma^{max} \simeq 0.4\sqrt{\frac{P}{sec}\frac{r}{R_0}} \times \max\left[1\ ,\ \frac{B_{crit}}{10B_0}\left(\frac{r}{R_0}\right)^3\right] \quad [GeV] \tag{2.6}$$

where P is the pulsar spin period, r is the distance of the emission zone from the star surface, R_0 is the radius of the neutron star and B_0 is the magnetic field strength at the pole [22]. This equation allows a bound to be set on the distance between the stellar surface and the site of emission of observed gamma-ray photons.

2.4.4 Compton Scattering

The scattering of an unbound electron is known as Compton scattering and the geometry and kinematics of the interaction are easily understood using the laws of conservation of energy and momentum. Inverse-Compton (IC) scattering occurs when a high-energy electron collides with a low-energy photon. During the collision the electron transfers some of its energy to the photon, resulting in a photon of

energy,

$$E_\gamma^{scat} = \frac{E_\gamma}{\frac{E_\gamma}{m_e c^2}(1-\cos\theta)+1} \tag{2.7}$$

where E_γ is the original photon energy, E_γ^{scat} is the new photon energy and θ is the deflection angle, with the interaction viewed in the electron rest frame. Considering the case

$$\frac{E_\gamma}{m_e c^2} \ll 1$$

it is clear from Equation 2.7 that the photon energy does not change by a large amount. This is referred to as the Thomson regime and the cross section for the interaction is

$$\sigma_T = \frac{8\pi}{3} r_0^2 \simeq 6.65 \times 10^{-25} cm^2 \tag{2.8}$$

where r_0 is the classical radius of the electron.

In the limit where

$$\frac{E_\gamma}{m_e c^2} > 1$$

there is a quantum mechanical suppression of the interaction cross-section, since the de Broglie wavelength of the electron is now much larger than the photon wavelength. This is referred to as the Klein-Nishina (KN) regime and the interaction cross-section is given by

$$\sigma_{KN} = \frac{3\sigma_T}{8\kappa_0}\left[\left(1-\frac{2}{\kappa_0}-\frac{2}{\kappa_0^2}\right)\ln(1+2\kappa_0)+\frac{1}{2}+\frac{4}{\kappa_0}-\frac{1}{2(1+2\kappa_0)^2}\right] \tag{2.9}$$

where κ_0 is the energy of the photon times the energy of the electron prior to the collision (see Figure 2–5) [14].

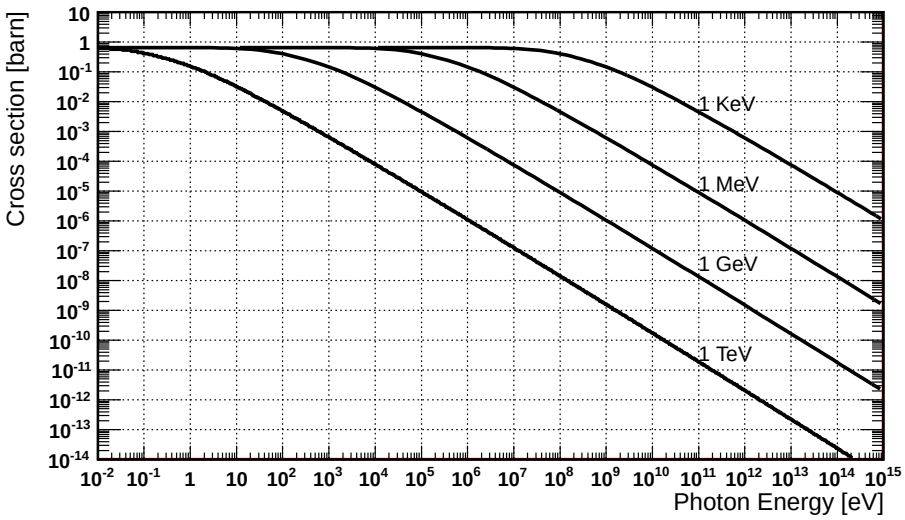

Figure 2–5: Plot of the inverse-Compton scattering cross-section for different electron energies against the target photon energy. The location of the turn over in each curve marks the onset of the KN suppression. These curves follow directly from Equation 2.9.

To determine the energy of the photon after scattering, the preferred frame for calculation is the electron rest frame. The conversion of energy from one frame to another is given by

$$E' = \gamma E \tag{2.10}$$

where γ is the Lorentz boost factor. Before the collision in the electron rest frame the energy of the photon is

$$E'_\gamma = \gamma E_\gamma$$

In the rest frame of the electron after the collision the photon energy will be

$$E'^{scat}_\gamma \simeq E'_\gamma = \gamma E_\gamma$$

Here we consider the interaction to occur in the Thomson regime where the photon energy does not change but the momentum direction of the photon does change. Transferring this photon back to the observer frame, its energy is

$$E_{\gamma}^{scat} = \gamma E'^{scat}_{\gamma} \simeq \gamma(\gamma E_{\gamma}) = \gamma^2 E_{\gamma}$$

The resultant scattered photon energy is increased by a factor of γ^2. In the KN-regime, the scattered photon energy is boosted only by a single factor of γ. In this regime, the cross section is much lower, but when collisions do occur, the photon absorbs almost the entire energy of the electron.

When a population of accelerated electrons with a distribution

$$I_e(E) \propto E^{-\Gamma_e}$$

up-scatters a distribution of soft photons, the resulting scattered photon energy distribution is

$$I_{\gamma}(E) \propto E^{-(\Gamma_e+1)/2}$$

This process of up-scattering the energy of photons is very important in astrophysics. It is the principal mechanism behind the Sunyaev-Zel'dovich effect, where distant galaxy clusters are visible through the IC-scattering of the cosmic microwave background. IC-scattering is also one of the principal processes in high energy gamma-ray production as the emitted gamma rays can reach energies similar to the energy of the scattering electron population. Another important IC-scattering process is

synchrotron-self-Compton (SSC) scattering, which occurs when synchrotron photons are scattered to higher energies by the same population of electrons that emitted them. Such a phenomenon is commonly seen in blazars[1] where the spectral energy distribution is described by two "humps". The lower energy hump is caused by synchrotron emission while the higher energy hump is caused by IC-scattering of the synchrotron photons. In high activity states both the synchrotron and IC distributions grow simultaneously, reinforcing the SSC connection (see Figure 2–6).

2.4.5 Pion Production and Decay

A very common interaction in high energy astrophysical systems is that of high-energy cosmic ray protons colliding with stationary atomic or molecular gas. If the kinetic energy of the incident proton is greater than 290 MeV, these collisions produce excited states in the nucleons leading to the emission of π-mesons. The most common interaction has the form:

$$p + p \longrightarrow N + N + n_1(\pi^+ + \pi^-) + n_2(\pi^0)$$

where N is a proton or neutron and n_1 and n_2 are integers. The charged pions decay into muons and neutrinos while the neutral pions decay into two gamma rays. In the rest frame of the neutral pion, each gamma ray carries away half the energy of the pion's rest mass, $\sim$70 MeV, and are emitted in opposite directions. Boosted into

[1] Blazars are galaxies whose emission spectrum is dominated by radiation from a jet which is orientated towards the observer and is formed by a super-massive black hole ($M_{BH} > 10^6\, M_\odot$) at the galaxy's centre.

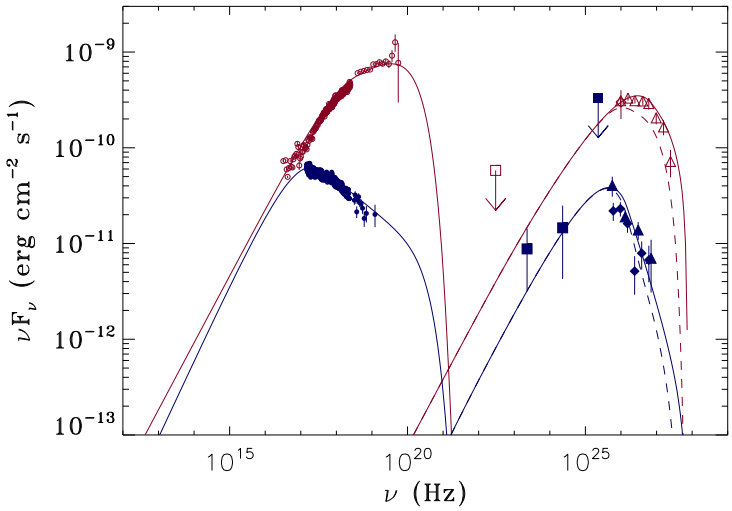

Figure 2–6: Spectral energy distribution of the blazar Markarian 501 in low and high activity states. The spectral energy distribution is described by two "humps". The lower energy hump is caused by synchrotron emission while the higher energy hump is caused by synchrotron-self-Compton scattering. In the high-activity state (red markers) both the synchrotron and IC distributions grow together, reinforcing the SSC connection. Figure taken from [7].

the lab frame, the photons are predominately emitted in the same direction as the pion and their energy is increased by the Lorentz factor.

If the incident protons' energy distribution is a power law with a spectral index Γ_p, the resultant gamma rays will have a power-law distribution with the spectral index $\Gamma_\gamma = 4/3(\Gamma_p - 1/2)$ and a peak at an energy of $\sim$70 MeV. Thus, such a gamma-ray spectral distribution can be a detection mechanism for cosmic-ray production sites. This hadronic emission process is immensely important in the production of gamma rays, but it is not considered a principal mechanism in pulsar emission.

2.4.6 Bremsstrahlung

Bremsstrahlung, a German work meaning "braking radiation", is the name given to the radiation emitted when a charged particle is decelerated in the Coulomb field of an atomic nucleus (see Figure 2–3(c)). In the case of relativistic electrons, the emitted photon energy can match that of the accelerated electron. Thus, in the case of a power-distribution of electron energies, the bremsstrahlung-emitted photons will have the same spectral index [112].

Bremsstrahlung does not play a significant role in gamma-ray emission processes or in pulsar physics. Its role in the detection of gamma rays from the ground, however, is immensely important and will be discussed in Chapter 3.

2.4.7 Photon-Photon Pair Production

An important gamma-ray attenuation process is photon-photon pair creation, of the form

$$\gamma + \gamma \rightarrow e^+ + e^-$$

which can occur when the center-of-mass energy of the system exceeds $\sim 2\times 511\ keV$. The cross section for this process peaks when

$$E_\gamma h\nu(1-\cos\theta) \simeq 2(m_e c^2)^2 = 0.522(MeV)^2 \tag{2.11}$$

where E_γ is the energy of the high energy photon which scatters off a soft photon with energy $h\nu$ (this relation is plotted in Figure 2–7). Photons in the energy range 0.1-1 TeV are most likely to scatter off photons with wavelengths 230-2300 nm, thus high energy gamma rays are most attenuated by UV/optical and IR photon fields. This absorption is important with dealing with dense photon fields or when photons travel huge distances. The absorption on the extragalactic background light (EBL) of TeV gamma-rays from distant blazars is of particular importance. Absorption by photon-photon pair creation also plays an important role in gamma-ray emission from pulsars where the observed flux and spectral shape of high-energy photons depends on the density of local soft photon fields.

2.5 Radiative Emission From Pulsars

The existence of a vacuum surrounding a pulsar was challenged by Goldreich and Julian (GJ) in 1968 [41] who showed that an electric field exists at the surface of the star which is strong enough to pull particles off the surface and form a surrounding layer of plasma. GJ formed a picture of star a surrounded by a dense plasma which co-rotated with the pulsar. Within a bounding cylindrical zone, called the light-cylinder, the plasma is locked to the closed dipolar magnetic field. Outside the light-cylinder, the magnetic field does not return to the star and plasma streams out and away from the star along these open field lines. This picture, of a rotating

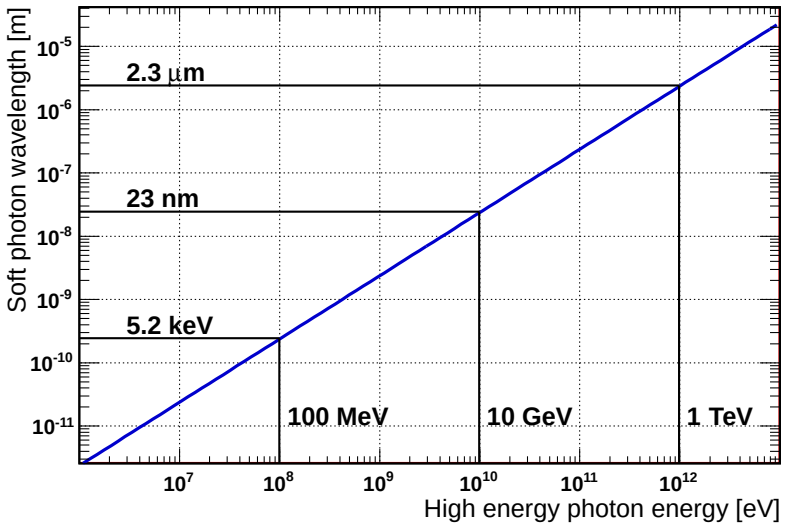

Figure 2–7: The wavelength of soft photons as a function of the energy of high energy photons at the point when their pair-production cross section peaks for head-on collisions. This relation follows directly from Equation 2.11.

neutron star surrounded by a magnetospheric plasma, is the foundational basis upon which the bulk of theories of pulsar emission are based. In the following sections some of these theories will be detailed, with an emphasis on theories of high-energy emission.

2.5.1 Can A Pulsar Exist In a Vacuum?

The interior of a neutron star can be considered to be an excellent conductor and to possess an extremely large magnetic field. Here the charges inside the star will rearrange themselves to eliminate the magnetic force acting on them. This implies the Lorentz force condition, thus

$$\vec{E}^{in} + \frac{\vec{v}}{c} \times \vec{B}^{in} = 0 \tag{2.12}$$

where $\vec{v} = \vec{w} \times \vec{r}$, $\vec{E}^{in}$ is the interior electric field, $\vec{B}^{in}$ is the interior magnetic field and $\vec{\omega}$ is the star's rotational vector. The arrangement of the surface charges will result in an electric field inside and outside of the star. From the above equation it is clear that inside the star

$$\vec{E}^{in} \cdot \vec{B}^{in} = 0$$

Assuming the star is in a vacuum allows one to solve the Laplace equation for the electric potential

$$\nabla^2 \phi = 0$$

Using the calculated potential, the electric field outside the star is determined by

$$\vec{E}^{out} = \nabla \phi$$

and it can be shown that

$$\vec{E}^{out} \cdot \vec{B}^{out} = -\left(\frac{\omega R}{c}\right)\left(\frac{R}{r}\right)^7 B_0 \cos^2\theta \tag{2.13}$$

where R is the radius of the star, B_0 is the magnetic field strength at the surface and θ is the polar angle. This expression shows that outside the star, $\vec{E}^{out} \cdot \vec{B}^{out} \neq 0$. The value of $\vec{E}^{in} \cdot \vec{B}^{in}$ must change continuously from zero to its exterior value. This means that, at the surface, the electric field must have a component along the direction of the magnetic field. The force on surface particles by this component of the electric field is greater than the gravitational force holding the particles to the star's surface. As a result, particles are pulled off the surface to form a layer of plasma around the star. The resulting space-charge density around this star, is

given by

$$\rho_0 = \frac{\vec{\bigtriangledown} \cdot \vec{E}}{4\pi} = -\frac{\vec{\omega} \cdot \vec{B}}{2\pi c} \frac{1}{1 - (|\vec{\omega}|r/c)^2 \sin^2\theta} \tag{2.14}$$

This is called the Goldreich-Julian density. In this plasma region around the star, the magnetic field lines are essentially equipotentials. As a result the plasma slides along these equipotentials and forms a co-rotating magnetosphere. The sphere exists out to a radius of $R_{LC} = c/|\vec{\omega}|$. Beyond this distance the particles would be moving faster than the speed of light. R_{LC} is the radius of the light cylinder which is bounded by the planes above and below $z = \pm R_{LC}$. Magnetic field lines which cross the light-cylinder are open, since if they were to re-connect to the star they would carry information faster than the speed of light. Particles can stream out from the magnetosphere along these open field lines. This flow is such that the star's net charge is conserved. The magnetosphere is separated into three charge regions by the null surfaces $\vec{\omega} \cdot \vec{B} = 0$. Charges of one sign collect around the poles with charges of the opposite sign collecting around the equator as specified by Equation 2.14.

GJ further divided the regions beyond the light cylinder into two zones; the wind zone and boundary zone. The boundary zone exists out to a distance D beyond the star, where D is the radius out to which the expanding supernova shell has swept up the surrounding interstellar material. The wind zone occupies the region from the light cylinder out to a distance $\sim D/10$. Inside the wind zone the open magnetic field lines form a large toroidal component which extend out to the boundary zone where they finally close (see Figure 2–8).

In summary, the Goldreich and Julian description of a pulsar contains following essential points:

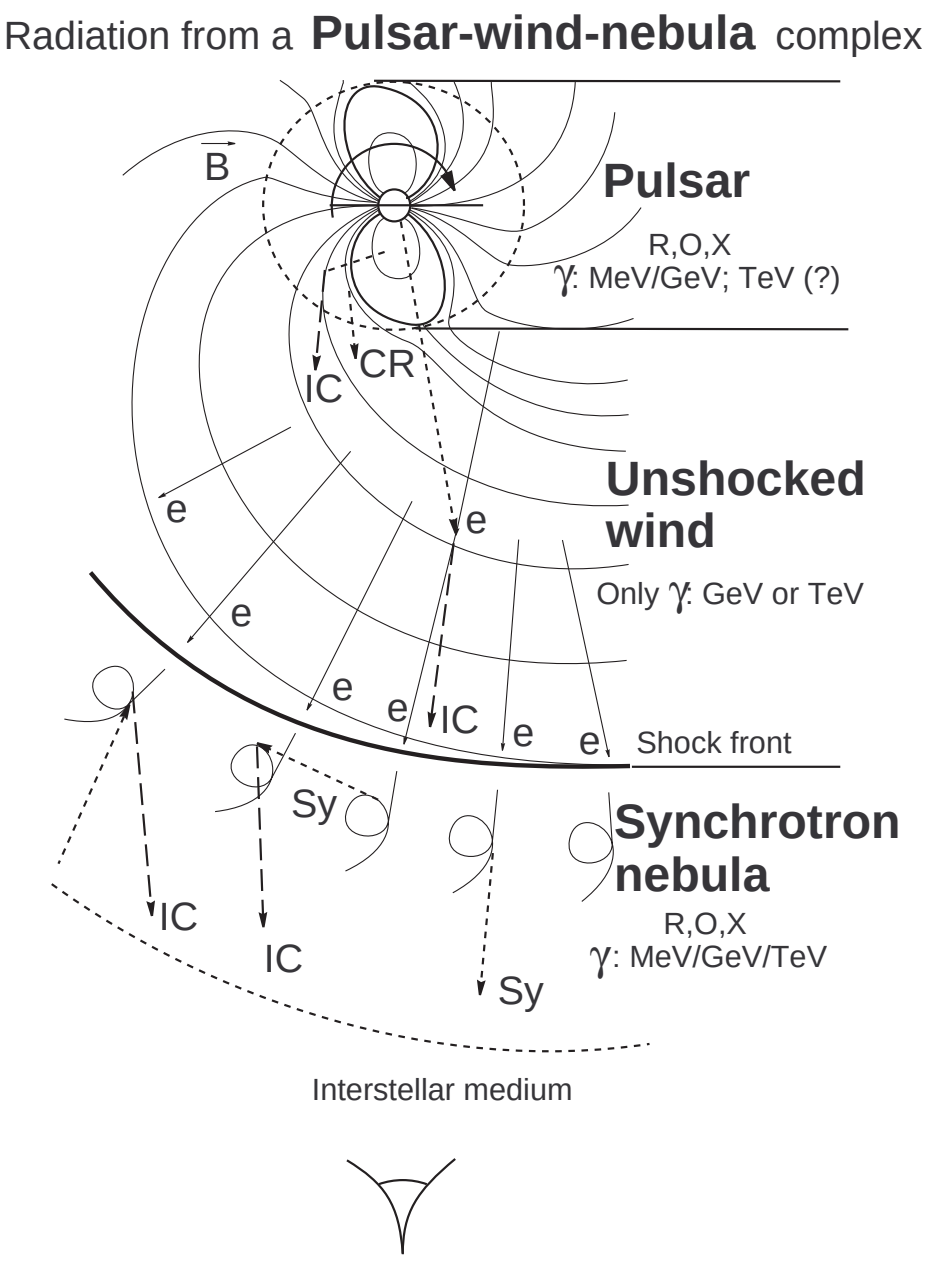

Figure 2–8: Schematic representation of a pulsar wind nebula. The dotted circular region shows the light cylinder, inside which the magnetic field lines are closed. The region beyond, the wind zone, contains open toroidal and radial field lines and is filled with plasma which originated from inside the light cylinder. Beyond the wind zone, the observed radiation is caused by the supernova shock wave as it propagates outward into the interstellar medium. Figure taken from [17].

- A pulsar consists of a magnetic dipole
- Pulsars are surrounded by a co-rotating magnetosphere with the Goldreich-Julian space charge density.
- Plasma escapes from the sphere along magnetic field lines that exit the light cylinder.
- Net charge is conserved.

This is the basis upon which the majority of pulsar emission models build.

2.5.2 Magnetospheric Gaps

Within the idealised GJ magnetospheric plasma there is no accelerating field since the charges within the plasma will arrange themselves to short out any such field. Since particle acceleration is necessary for radiative emission it is generally considered that there are locations within the magnetosphere where vacuum gaps exist, or at least where the density of plasma is lower than the GJ density. Within these regions, the accelerating field can energise particles which emit radiation via the processes discussed previously; synchrotron radiation, curvature radiation and IC-scattering. Historically, three gap locations have been presented in the literature which are;

- Above the neutron star surface at the location of the magnetic poles. This is called *The Polar Cap* (PC).
- Regions in the outer magnetosphere between the null surface and the boundary of the light cylinder. This is called *The Outer Gap* (OG).
- The region between the last closed and first opened magnetic field line as the field lines diverge over the polar region. This is called *The Slot Gap* (SG).

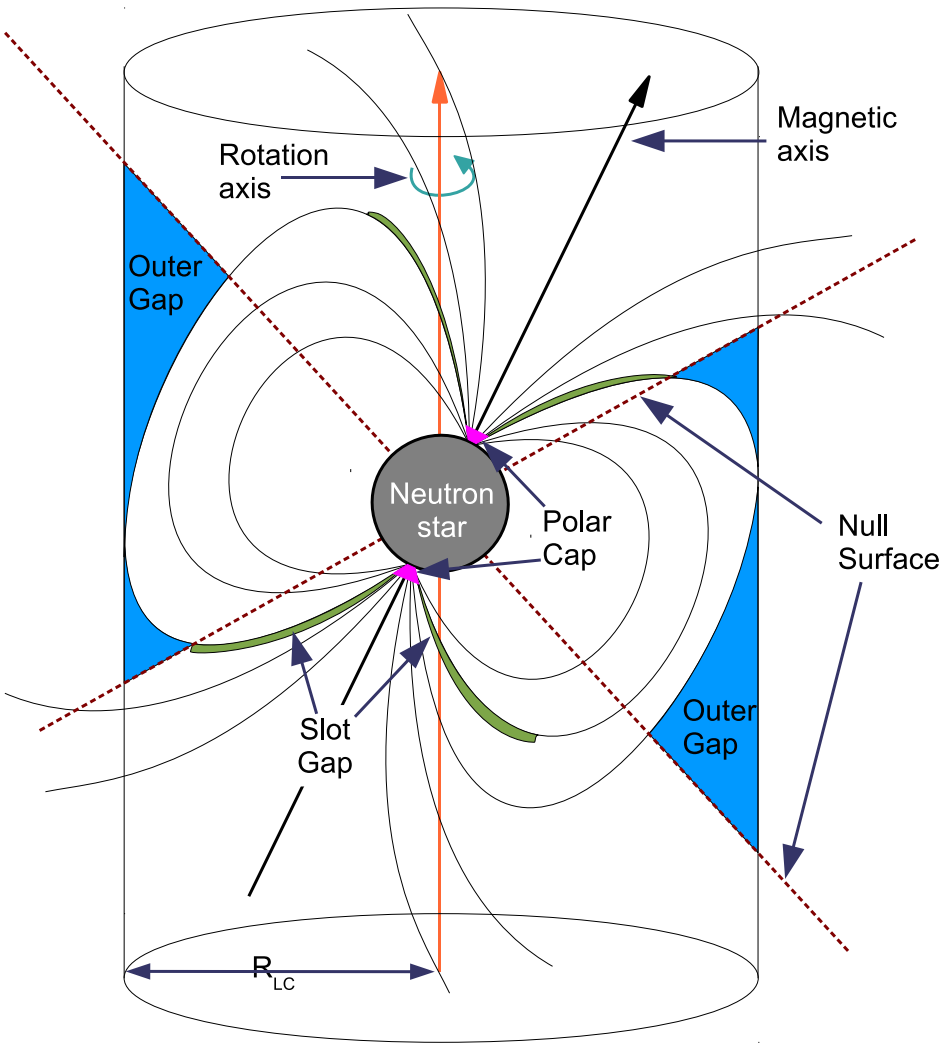

Figure 2–9: Schematic diagram of the emission zones within a pulsar magnetosphere. The last closed magnetic field line defines the boundary of the light cylinder of radius R_{LC}. Field lines which pass through the light cylinder do not reconnect to the star and charges within the magnetosphere flow out along them. The charge density inside the light cylinder is given by Equation 2.14. The magnetosphere is separated into three charge regions by the null surfaces $\vec{\omega} \cdot \vec{B} = 0$. Charges of one sign collect around the poles with charges of the opposite sign collecting around the equator.

The location of each of these regions is depicted in Figure 2–9.

A self-consistent and robust picture of the emission from pulsars has never been presented. Understanding the behaviour and evolution of the magnetosphere is very complicated and only a small fraction of a pulsar's energy budget ($\ll 10\%$) is released in the form of magnetospheric emission [74, 99]. The following models present geometrical and acceleration scenarios which broadly match the observed emission.

2.5.3 Polar Cap Models

The original PC model was presented by Sturrock [104] who proposed that as the open field lines which emanate from the poles lag into their toroidal shape they generate a current which flows from the polar caps. Each polar cap is divided into two zones; the proton polar zone (PPZ) and the electron polar zone (EPZ), depending on which particles provide the flow of current from the poles. Emission occurs in the following way. As an electron leaves the EPZ it tracks the curved path of the magnetic field lines and radiates curvature radiation. The emitted gamma rays will interact with the strong B field and pair-produce. The newly produced positrons will, however, be attracted to the electron-emitting region on the star's surface and the return current of positrons will damp the emission of electrons from the EPZ. This configuration sets up a spasmodic oscillating current where charges are drawn off the EPZ in large sheets. It is argued that the charges in these currents sheets then radiate coherent synchrotron radiation as they move along the magnetic field lines which emanate from the polar caps, resulting in the observed radio emission. These sheets of charge create "electromagnetic shadows" inter-spaced between them, which balance the accelerating field. As a result, charged particles, created by the

pair production process, "coast behind" each sheet. The particles then, in the case of Crab-like pulsars, emit incoherent synchrotron radiation producing the observed optical and x-ray spectrum components. Gamma rays are argued to originate from curvature radiation responsible for the polar cap cascade.

The Sturrock model also proposed a reason for the observed sub and interpulses in pulsar light curves, suggesting that this was due to the observer's line of sight across the various polar zones (see Figure 2–10). For the Sturrock model to agree with the contemporaneous Crab data, it was required that radiation was observed from the PPZs of both poles, while observing radiation from neither of the EPZs. This requirement stretched the model too far for it to be considered a totally successful one. However, Sturrock introduced many of the ideas which were commonly used in future models, particularly the role of curvature radiation and pair production and the idea that the line of sight across the emission zone determined the shape of the pulse profile.

The Ruderman and Sutherland model [95] introduced the idea of a plasma depletion region (gap) at the polar cap. They argued that the strong magnetic field of the pulsar would cause the particles on the surface (mainly iron) to form a lattice of tight molecular chains with their axes parallel to the magnetic field direction. This strong surface binding prevents ions from being drawn off the star, in contradiction to the Sturrock picture. Charged particles are, however, still drawn out of the magnetosphere along the open polar field lines. This causes the formation of a depleted charge region at the star's surface, forming a magnetospheric gap. An electric field

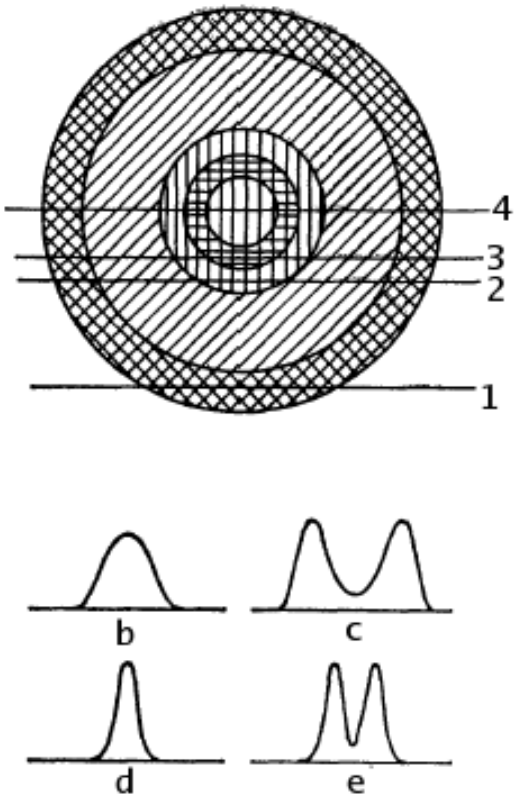

Figure 2–10: Polar Cap emission zones and associated pulse profiles. Horizontal and/or vertical hatching represents current of one sign while diagonal hatching is of the opposite sign. Double hatched regions carry more current than single hatched regions. Pulses b and c occur if the outer region is the EPZ and the line of sight is along 1 and 2. Pulses d and e occur if the inner region is the EPZ and the line of sight is along 3 and 4. Taken from [104].

can now form across the gap, the strength of which will increase as the region depletes more and the gap grows in size. When the voltage drop across the gap reaches $\sim 10^{12}\,V$, further gap growth is halted by the production of electron-positron pairs by thermal or stray photon interactions with the strong electric and magnetic fields. The resultant pairs are accelerated in the field and radiate curvature photons which subsequently generate more pairs causing a cascade (see Figure 2–11). The resulting cascade completely fills the gap with particles and quenches the accelerating field. At this point, the cycle begins again, as a charge-depleted region once again begins to form as magnetospheric charges flow outward.

As before, curvature photons which escape the polar region are responsible for the observed gamma-ray emission while accelerated particles which escape generate lower energy photons through synchrotron emission.

Most advances in the study of emission from the polar cap, beyond the early theories presented above, have come from the increased power and availability of computers and the heightened sophistication of numerical simulations [34]. The previously introduced concepts of gap formation, pair cascades and field quenching are considered with more rigorous attention to geometrical and general relativistic effects. Additional emission and cascade-inducing mechanisms, such as IC-scattering [103], were also included in the models. Beyond these refinements, however, the basic scenario of polar cap emission is unchanged.

2.5.4 The Slot Gap

In the PC model, the gap develops directly above the surface of the star and the maximal height of the gap is determined by the mean-free path of a photon

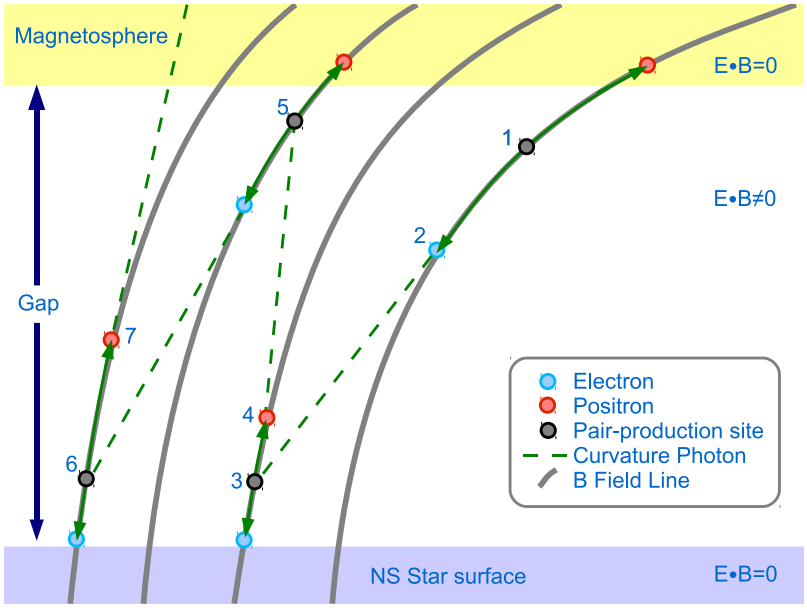

Figure 2–11: Schematic of electron-positron pair cascades in the polar magnetospheric gap. An electron-positron pair is formed at point 1. The positron escapes along the magnetic field line and the electron is drawn to the surface while emitting curvature radiation. A photon emitted at point 2 will cause pair production at point 3. From there the electron is drawn to the surface while the positron is drawn out of the gap, emitting curvature radiation at point 4 which will cause pair production at point 5, and so on.

in the high E and B field region. The observed gamma-ray emission from pulsars presents a challenge for models with an acceleration zone near the star's surface, since gamma-ray photons are easily absorbed in the high B field at the pole. The Slot Gap model [20, 46, 47] postulates the existence of an asymptotically narrowing gap which extends outwards from the magnetic pole, flaring outwards along the poloidal magnetic field lines (see Figure 2–12). This narrow gap can extend all the way out to the light cylinder, such that high-energy radiation can escape.

The formation of the SG starts with a similar premise as the standard PC except that the field across the gap is considered to weaken at the edge of the polar cap

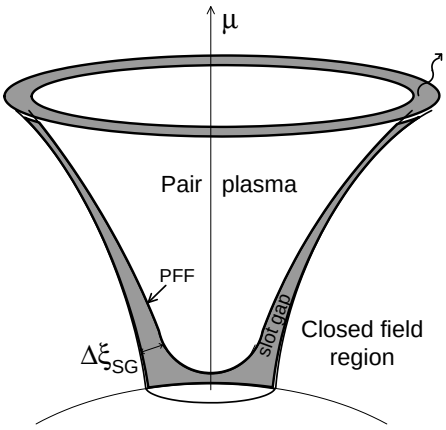

Figure 2–12: Schematic diagram of the Slot Gap. Due to the weaker electric field at the boundary of the polar cap, pair production is less efficient and thus the pair formation plasma forms at higher altitudes, close to the boundary. An outward fanning "hollow cone" emission profile is produced around the magnetic poles enabling various light curve shapes depending on the angle between the rotation and magnetic axes and observer's line of sight across the emission region. Figure taken from [46]

region, close to the last closed field line. This is under the assumption that the boundary of the PC region is perfectly conducting. Since the electric field near the boundary is weaker, larger distances are required for the electrons to accelerate to the Lorentz factor necessary to radiate photons energetic enough to pair produce. The pair formation front (PFF) thus occurs at higher and higher altitudes as the boundary is approached and curves upward. This causes a gap which is asymptotically parallel to the last open field line. Within the pair plasma, the accelerating fields are screened and the SG is considered to be enclosed by two conducting boundaries, one on each side. There is a negligible amount of pair production in the SG, and in this way, the

SG can form and exist in a steady state, unlike the PC which continually oscillates. The accelerating field is maintained at the outer rim of the polar cap at altitudes comparable to the radius of the light cylinder. In pulsars like the Crab, the potential drop across the gap can reach $10^{13}\,V$ [56].

An outward fanning "hollow cone" emission profile is produced around the magnetic poles enabling various light curve shapes depending on the angle between the rotation and magnetic axes and observer's line of sight across the emission region. Light travel-time and relativistic effects throughout the emission region create caustics where emission photons "pile up" at certain phases. These caustics can explain the double-peaked emission commonly seen in gamma-ray pulsars [38] .

Similar to the PC models, curvature, synchrotron and IC radiation from both primary accelerated electrons and pairs can produce a broad incoherent emission spectrum from infra-red to GeV energies [47].

2.5.5 Outer Gap model

The original OG emission model was presented by Cheng, Ho and Ruderman (CHR) in the mid 1980s [29, 30], although the existence of gaps in the outer magnetosphere had previously been postulated [61, 81]. These models considered a pulsar to be an inclined rotator with $\vec{\omega} \cdot \vec{B} < 0$, meaning that positive charges collected around the polar areas of the magnetosphere while negative charges surrounded the equatorial regions, consistent with the GJ charge density (Equation 2.14).

Implicit in the GJ model is the existence of two null surfaces in the magnetosphere defined by $\vec{\omega} \cdot \vec{B} = 0$ (see Figure 2–9). CHR postulated that electrons which flow out through the light cylinder from the region between the null surfaces and the

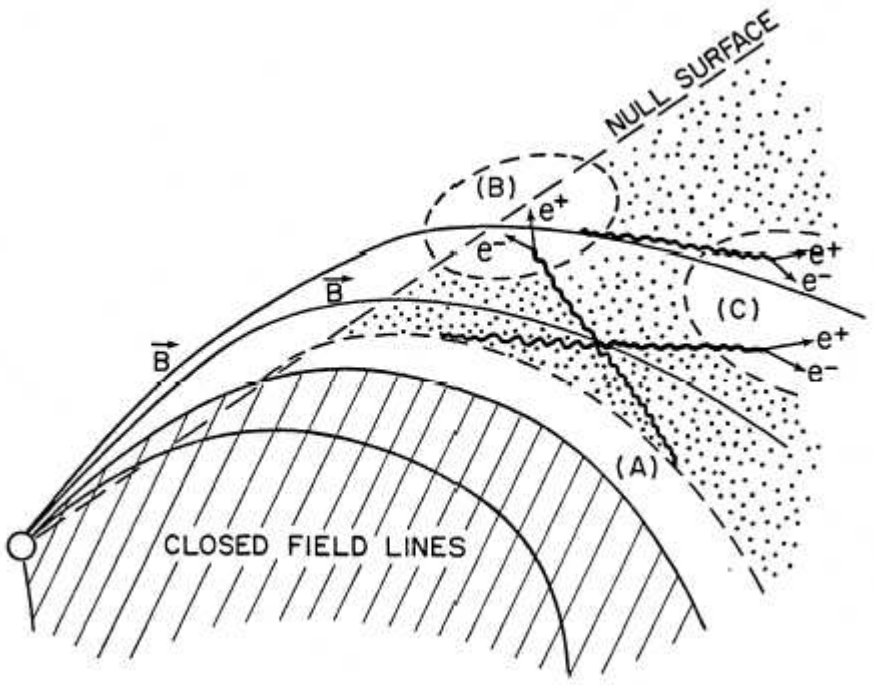

Figure 2–13: Three possible outer gaps (A), (B) and (C). (A) occurs beside the last closed field line, (B) occurs along the null surface and (C) occurs arbitrarily within the outer magnetosphere. Depicted is the possible pair production initiated by gamma rays produced in nearby gaps. From [29].

last closed magnetic field line will leave behind a negative-charge depleted region. These gaps form in the magnetosphere in the region between the last closed magnetic field line and a light cylinder along the null surface, see Figure 2–13.

It has been shown [80, 81] that unabated growth of such gaps can lead to a completely depleted magnetosphere which will produce no emission; a so called "dead pulsar". Such a process will take $\geq 10^7$ years. CHR showed, however, that fast spinning young pulsars (Crab, Vela etc) have strong enough magnetic fields to cause pair production within the gaps which limit their growth and produce stable gaps.

Electrons accelerated in the outer gaps radiate gamma rays via curvature radiation, synchrotron radiation and soft photon IC-scattering. Pair production cascades, necessary to stabilise the gap growth, are initiated by gamma ray and soft photon (x-ray/optical/IR) collisions. Photons from inward acclerating pairs collide head on with thermal x-ray and optical photons produced on the hot neutron star surface. Once initiated, these cascades can continue through gamma-ray interactions with the magnetic field. The potential drop formed in the outer gap in pulsars like the Crab can reach $10^{15}V$ [56].

Inverse-Compton scattering of soft photons can play a role in OG emission [105] which may lead to observable TeV emission in the case of strong young pulsars, such as the Crab [55]. The level and energy of IC emission depends on the density and wavelength of the target photon fields in and around the magnetosphere. Due to the Klein-Nishina suppression, photons with energies $\sim$0.01 eV (IR) are most effectively IC-scattered into the TeV regime.

This geometrical picture of vacuum gaps in the outer magnetosphere close to the light cylinder proves broadly compatible with observational pulsar data. In these gaps, radiation is emitted in a fan, spreading out in directions tangential to the last closed field line. Here, both positrons and electrons emit observable radiation, which they radiate in oppositely directed beams. Similar to the arguments for the PC and SG, a variety of emission profiles are achieved due to the presumed gap locations and geometries and by light crossing time and relativistic aberration effects.

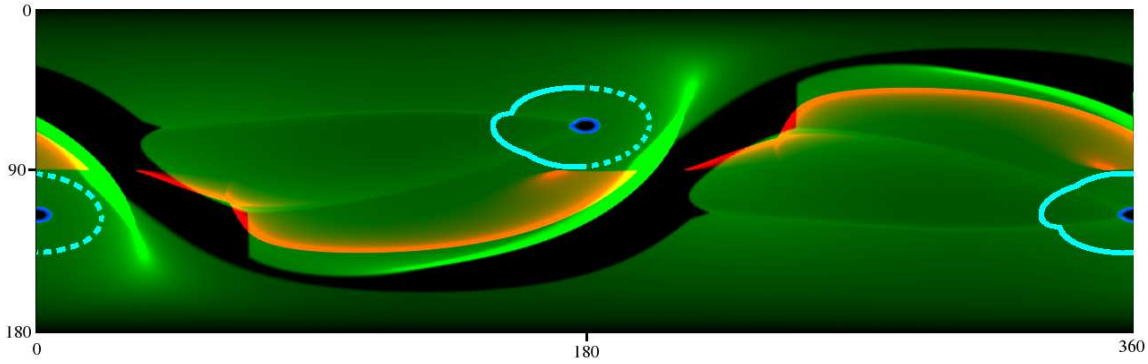

Figure 2–14: Figure of the simulated emission intensity from a pulsar where the angle between the spin and magnetic axes is 65°. The x axis is the emission phase while the y axis is the line of sight angle of an observer. The green shades represent the emission from the SG, the red shades represent emission from the OG and the blue shades represent emission from the PC. The cyan lines show the location of the high-altitude radio emission. Figure taken from [111].

2.5.6 Emission models and *Fermi* Pulsars

To favour one model over another using gamma-ray observations one can match the possible light curves and energy spectra for each model to the measured data from the *Fermi* satellite. The 46 brightest gamma-ray pulsars are measured and presented in the first *Fermi*-LAT pulsar catalogue [4].

Light Curve

The shape, position and number of gamma-ray emission peaks is suggested by each of the various pulsar emission models (see Figure 2–14). Gamma-ray pulsars typically have a pulse profile with two dominant sharp peaks or occasionally one broad peak (see Figure 2–15). Two peaked profiles are easily accommodated by the "hollow cone" emission structure of the SG and the outward fanning emission of the OG. Single, wide peaks are also easily accommodated, resulting from viewing the emission zone in a tangential slice. The PC model is challenged by these profiles

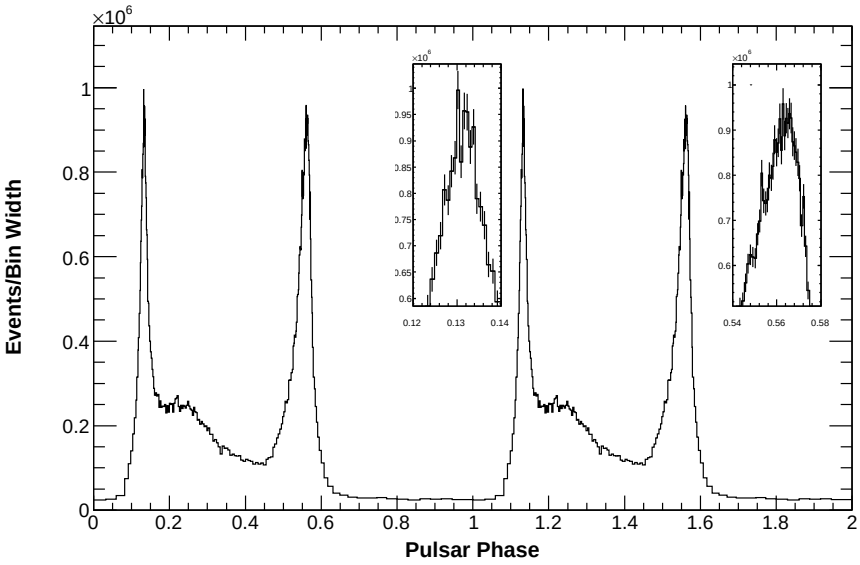

(a) Vela >20 MeV

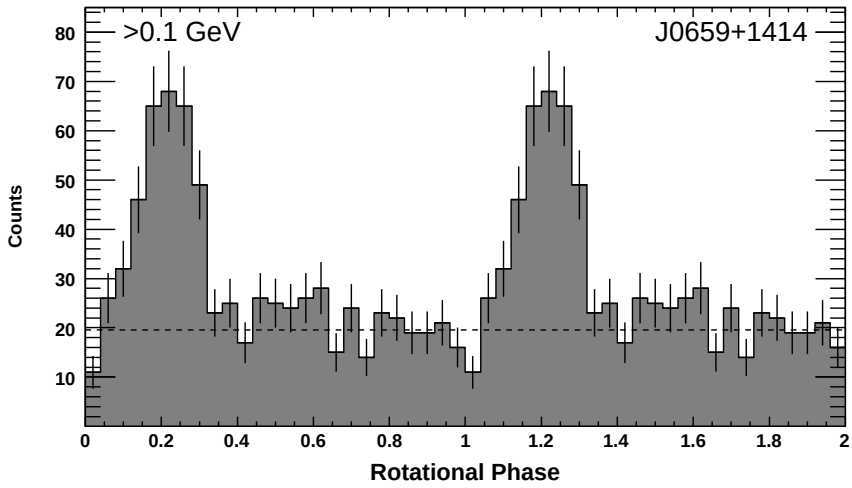

(b) PSR J0659+1414 >100 MeV

Figure 2–15: Example *Fermi* pulsar light curves. The Vela Pulsar has a period of 0.089 seconds and is the brightest non-transient source in the *Fermi* energy range. PSR J0659+1414 is a known x-ray and radio pulsar and was firmly detected by *Fermi* . It has a period of 0.385 seconds. Figures taken from [1] and [116].

since wide peak separation is only possible when the magnetic inclination angle is small (similar in size to the radio beam opening angle). Pulsars which can be seen in gamma-rays but not in radio, so called "radio-quiet" pulsars, such as Geminga, are also a challenge to the PC model.

Radio lag, which is the phase difference between the radio emission beam and the nearest gamma-ray pulse is another indicator of the emission geometry. Radio lags of 0.0 to 0.5 are not uncommon, with the largest fraction of *Fermi* pulsars lagging between 0.2 and 0.3, slightly favouring the OG scenario [4]. In general, however, the SG and OG models can broadly reproduce the observed emission profiles. In the case of specific pulsars, measurements of the magnetic inclinations and observation angle can limit the free parameters available in the models to better match the theory with the observational data. Magnetic inclination angle measurements are occasionally possible through radio polarisation measurements [84] and observer viewing angles can be obtained from x-ray observations of pulsar wind nebula geometries.

Spectral Cut-Off

All of the pulsars in the first *Fermi*-LAT pulsar catalogue exhibit a cut-off in their energy spectrum between $\sim$1 and 10 GeV (see Figure 2–16). The uniformity of this emission cut-off suggests a common gamma-ray emission scenario for all pulsars, regardless of whether they are normal radio pulsars, millisecond pulsars or radio-quiet pulsars. A cut-off, such as this, is expected if curvature radiation is the dominant emission mechanism. In the case where electrons emit at the radiation-reaction limit (Equation 2.4), where the acceleration gains are matched by curvature emission losses, the shape of the cut-off is expected to be exponential. An observation of

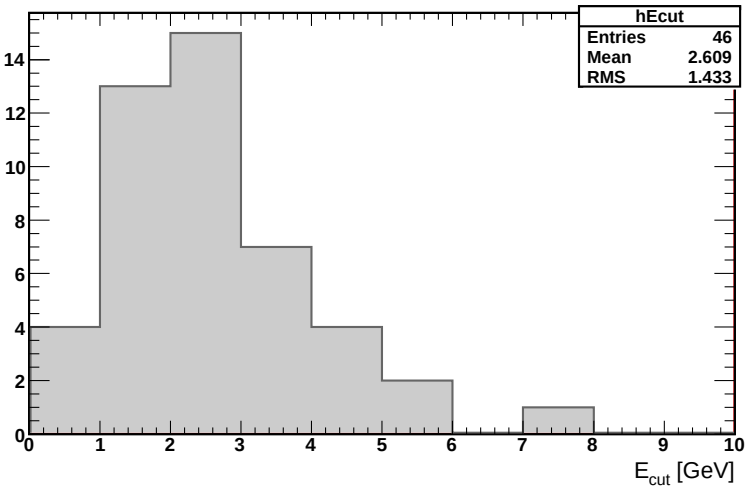

Figure 2–16: Distribution in the measured cut-off energy of the *Fermi* pulsars. Data taken from [4]

a super-exponential cut-off would indicate that the emission takes place in a region where single photon/B-field pair creation can take place. The observed *Fermi* pulsars with B-fields $> 10^{12}\,G$ and cut-off energies $\sim$2 GeV impose a minimum distance of 2-3 stellar radii from the star's surface for the location of the emission region. This is determined from the maximal escape energy for photons which can undergo single photon/B-field pair creation (Equation 2.6). Such constraints disfavour the PC models, implicating outer magnetosphere emission (SG,OG) where the bulk of the emission occurs at tens to hundreds of stellar radii.

2.5.7 Emission Summary

The nature of the emission from pulsars is still largely a puzzle. Discussed here are the current theories of high energy emission, which depend on the magnetosphere departing from the Goldreich-Julian density; either due to particle out-flow

or surface charge retention. Within these regions, particle acceleration occurs, leading to the observed gamma-ray radiation. Gamma-ray emission is believed to be largely caused by curvature radiation which, in the several GeV regime, occurs at the radiation-reaction limit, leading to the exponential cut-offs seen by *Fermi*. IC-scattering components may exist, perhaps leading to TeV emission. The location and shape of the magnetospheric gaps are sensitive to the geometry of the magnetic field and the efficiency of pair cascades and field screening. The slot-gap and outer-gap locations can largely reproduce the emission seen by *Fermi*, however, models for individual pulsars involve fine tuning of their many free parameters. The polar cap models are, so far, disfavoured as sites of gamma-ray emission, however, the polar cap is still considered the most likely site of the observed radio emission. Although not discussed here, the mechanisms responsible for the emission of coherent radio emission are similarly not well understood. Better understanding of the nature of emission is possible through the accumulation of more data. Uniquely, emission detected above the few GeV cut-off will necessitate the inclusion of a gamma-ray emission component other than curvature radiation and will allow a firmer limit to be placed on the minimum altitude of the acceleration region.

2.6 Introduction to the Crab Pulsar

The Crab Pulsar, PSR J0534+220, is a powerful young pulsar and one of the brightest at gamma-ray energies [40, 3]. It is well studied throughout the electromagnetic spectrum and is the brightest known optical pulsar. It is the remnant of historic supernova that was observed in 1054 A.D. and is located at a distance 6500

Parameter	Value	Unit
Name	PSR J0534+2200	
RA	05:34:31.973	hms
Dec	+22:00:52.06	dms
Mass	1.4	$M_{\odot}$
Radius	1×10^{4}	m
P	0.03308471603	s
$\dot{P}$	4.227654×10^{-13}	s/s
B_{surf}	3.78×10^{12}	G
B_{LC}	9.8×10^{5}	G
$\dot{E}$	4.6×10^{38}	$ergs/s$
Spin down age	1240	yr
R_{LC}	1.58×10^{6}	m

Table 2–2: Crab Pulsar information from http://www.atnf.csiro.au/people/pulsar/psrcat [77]

light years from Earth in the Taurus constellation. The measured parameters of the Crab Pulsar are listed in Table 2–2.

The pulsar light curve is characterised by two peaks occurring at same the phase positions throughout the entire electromagnetic spectrum (see Figure 2–17). The pulse at phase 0.0 is called the main pulse and often labelled P1. The second pulse, which occurs at phase ∼0.4, is called the *inter-pulse* and often labelled P2. The relative intensity of P1 and P2 differ, at different wavelengths, with P1 being dominant from radio to soft x-ray energies. From hard x-ray to soft gamma-ray energies (30 MeV) P2 then becomes dominant, only to diminish again above 100 MeV. Above 100 MeV P1's dominance gradually reduces until 25 GeV where the intensity of P1 and P2 become equal [19]. Trends such as this are not uncommon in gamma-ray pulsars, including the Vela and Geminga pulsars [1, 5]. These pulsars

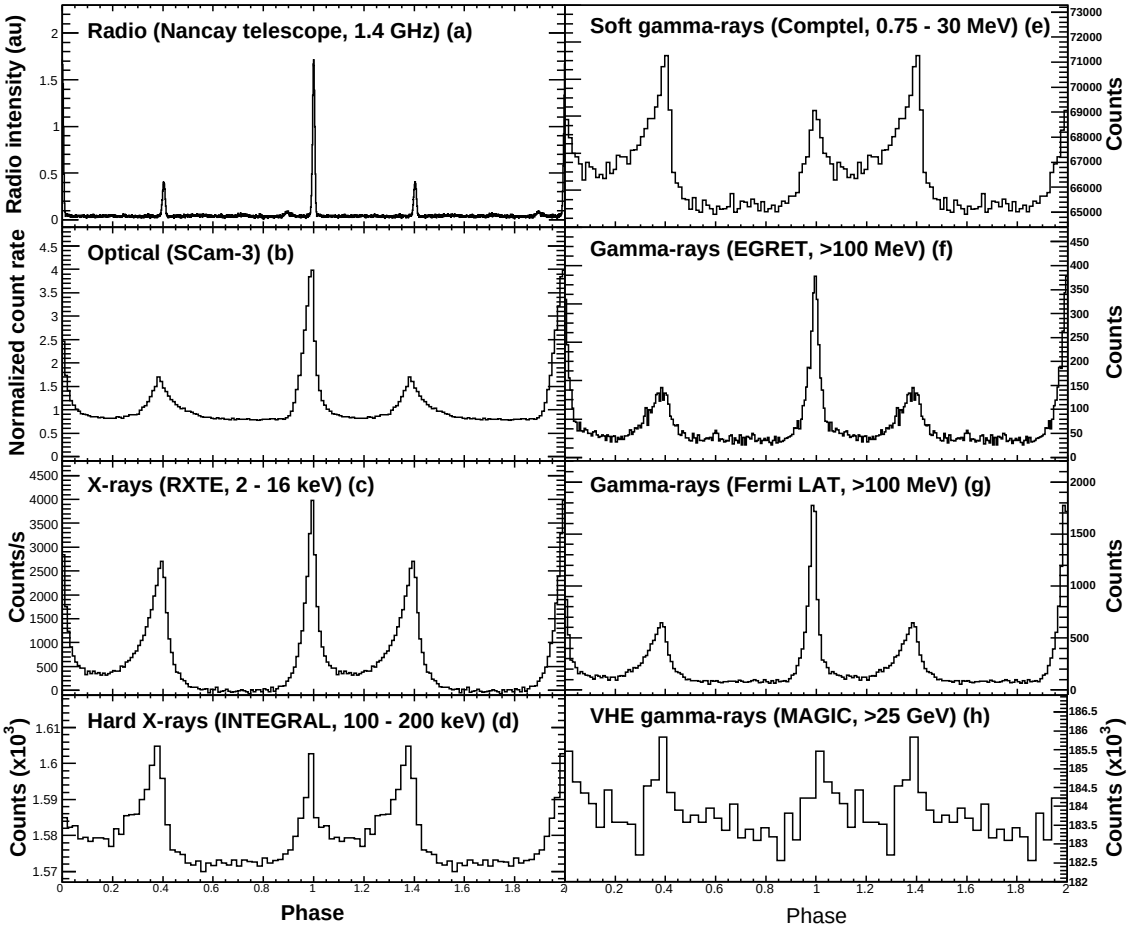

Figure 2–17: Figure of the Crab Pulsar light curve from radio to gamma-ray energies. Figure taken from [3] using data from [87, 82, 68, 19].

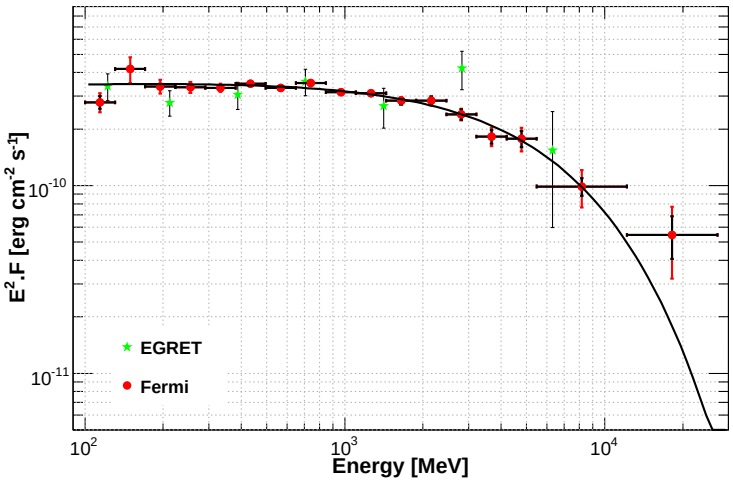

Figure 2–18: Figure of the phase averaged gamma-ray energy spectrum of the Crab Pulsar with a power-law plus exponential cut-off fit. The data are well modelled by a power-law with a spectral index of -1.97 and an exponential cut-off at occurring at 5.8 GeV. Figure taken from [3].

also display "bridge emission", which is a raised level of emission between the two main peaks.

The gamma-ray energy spectrum of the Crab follows the broad trend of all the *Fermi* gamma-ray pulsars. Above 100 MeV the phase-averaged spectrum is well modelled by a power-law with a spectral index of -1.97 and an exponential cut-off occurring at 5.8 GeV (see Figure 2–18). The MAGIC measured flux above 25 GeV, in conjunction with the measured EGRET spectrum below 10 GeV, places the cut-off energy at $\sim$20 GeV [19]. These measurements are broadly compatible within their stated uncertainties. The shape of the spectrum above the break energy is consistent with an exponential. This favours a curvature radiation scenario in the radiation-reaction limit. The MAGIC spectral point at 25 GeV point places a lower

bound on the distance between the emission site and the stellar surface of 6.2 stellar radii.

2.6.1 The Crab Nebula

The Crab Nebula (shown in Figure 2–19) is the pulsar wind nebula associated with the Crab Pulsar. It is similarly well studied across the entire electromagnetic spectrum. The observed emission from radio to gamma-ray energies is attributed to synchrotron emission from relativistic electrons which inhabit the wind zone around the pulsar. The nebula is the brightest steady TeV source known and has become the standard candle for ground based gamma-ray astronomy[2] . The TeV gamma-ray emission is caused by IC-scattering of soft photons (mainly IR) by 2-30 TeV electrons [53] (see Figure 2–20). The spectral shape in the VHE regime is well described by a power-law with an index of -2.48.

The search for, and subsequent detection of, TeV gamma rays from the Crab Nebula formed the historical foundation of ground-based gamma-ray astronomy. In the following chapter, the observational technique employed for TeV gamma-ray astronomy is described in detail.

[2] Recent nebular variability seen by AGILE [106] and *Fermi* [2] has not been seen at TeV energies [86, 78]

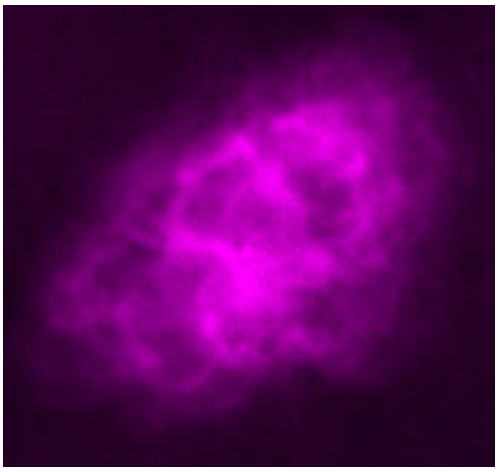

(a) Radio

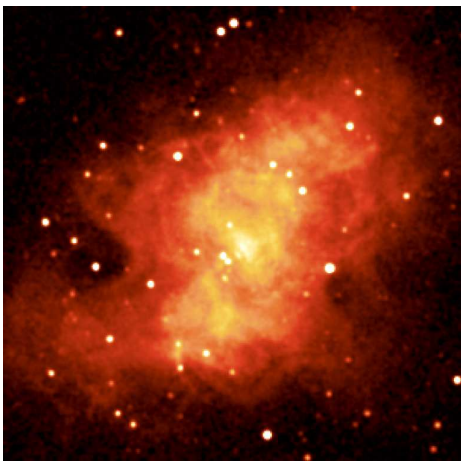

(b) Infra-red

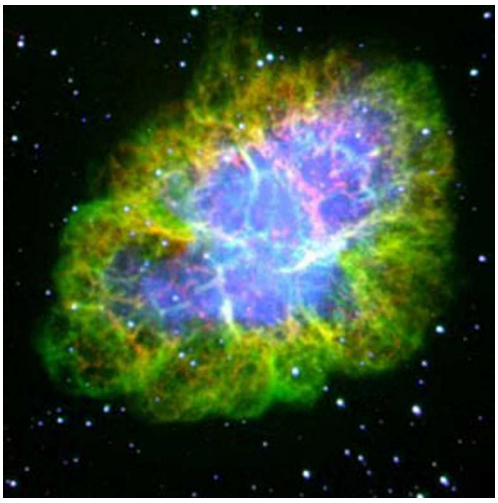

(c) Optical

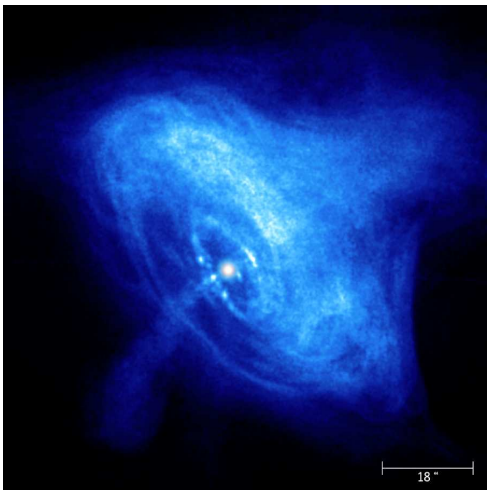

(d) X-ray

Figure 2–19: Synchrotron emission from the Crab Nebula and Pulsar in different wavelengths. Images are not to scale. Radio data are from the VLA. Infrared data are from 2MASS, UMass and IPAC. Optical data is from the HST and x-ray data are from the Chandra telescope. The x-ray image reveals the orientation of the pulsar and filaments and knots in the expanding wind. Images obtained from http://chandra.harvard.edu/photo/1999/0052/

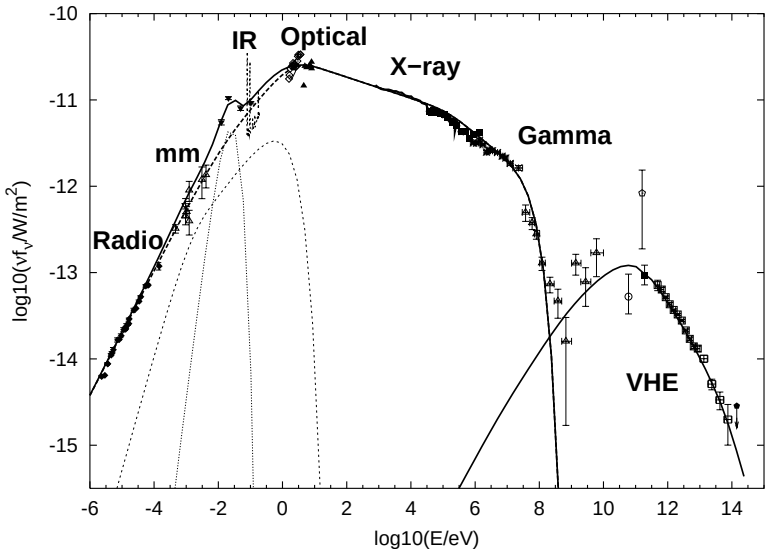

Figure 2–20: Broadband spectral energy distribution of the Crab Nebula from radio to multi-TeV energies. The SED is well described by synchrotron emission from radio to GeV energies with inverse-Compton scattering taking over in the TeV regime. Figure taken from [60].

CHAPTER 3
The VERITAS Detector and The Imaging Atmospheric Cherenkov Technique

3.1 Introduction

VERITAS, which has been introduced in the first chapter, is an astrophysical gamma-ray telescope located at the Fred Lawrence Whipple Observatory in Arizona, USA. In the following chapter the VERITAS array, its various components, their function and their performance will be described in detail. This chapter will also explain, in detail, the physical processes behind atmospheric air showers and Cherenkov photon production.

3.2 Cherenkov Radiation

Cherenkov radiation is electromagnetic radiation emitted by the atoms in a dielectric medium when traversed by a charged particle moving faster than the local speed of light. Named after Pavel A. Cherenkov, who first observed the process in 1934, this radiation is, in some ways, analogous to the sonic boom created when an object moves faster than the speed of sound in an acoustic medium.

In a dielectric material, light travels at a speed c/n, where n is the refractive index of the medium. In such a material, the electric field of a charged particle extends outwards in all directions as a spherical front moving at this speed. A second charged particle, which is encountered by this expanding front will feel the

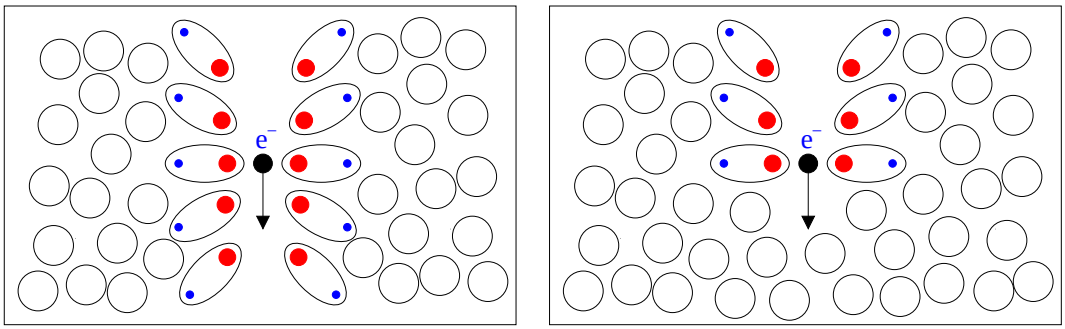

(a) $v < c/n$ **(b)** $v > c/n$

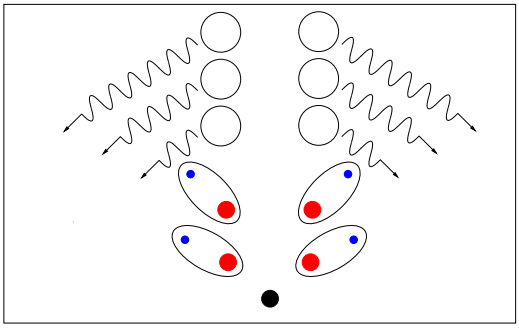

(c) $v > c/n$

Figure 3–1: Production of Cherenkov Radiation. In panel (a) the charge is moving slower than the local speed of light, thus the polarising disturbance caused by the charge is symmetric. When this system relaxes, there is no net field and thus no emission. In panel (b) the charge is moving faster than the local speed of light and the polarising disturbance is not symmetric. Panel (c) shows the emission caused by the disturbance in panel (b).

electromagnetic force of the the first particle, while a particle not yet encountered by the front will experience no force.

When a single charged particle is moving within a dielectric medium at speed v, where $v < c/n$, atoms in the vicinity of the charge become slightly polarised by its electric field. As the charge passes, the atoms depolarise. This disturbance causes the atom to radiate, however the symmetry of the polarisation yields a zero net electric field and hence, no detectable radiation.

In the case, however, when the charged particle is moving with a speed greater than c/n, the electric field of the charge does not exist in the forward direction, since it moves outward more slowly than the particle's forward velocity. This means that the polarisation of atoms in the vicinity of the charge is not symmetrically induced. Thus, when the charge passes, the depolarisation of the atoms occurs coherently, resulting in radiative emission called Cherenkov radiation (see Figure 3–1).

The emitted Cherenkov photons interfere constructively along a conical surface whose axis is the directional vector of the relativistic charge (see Figure 3–2). The opening angle of the cone is defined by:

$$\cos(\theta) = \frac{{}^{c}\!/_{n}\, t}{v\, t} = \frac{1}{\beta\, n} \tag{3.1}$$

where v is the speed of the particle and $\beta(\equiv v/c)$ is the ratio of the particle velocity to the velocity of light in a vacuum. From Equation 3.1, some important properties of atmospheric Cherenkov emission can be determined:

- For a given refractive index, n, there exists a threshold particle velocity: $\beta_t = 1/n$, below which no Cherenkov emission occurs. The corresponding particle

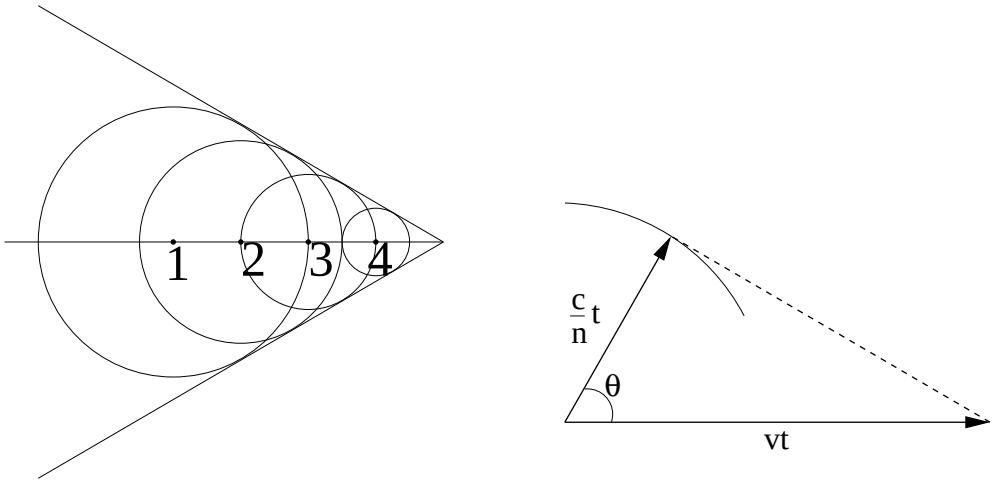

(a) Wavelet Constructive Interference **(b)** Geometry of Cherenkov Cone

Figure 3–2: Diagram of a Cherenkov Cone. Panel (a) shows emitted Cherenkov radiation wavelets and their constructive superposition along the Cherenkov cone. Panel (b) shows the derivation of the Cherenkov cone opening angle.

threshold energy is: $E_t = m_0c^2/\sqrt{1-\beta_t^2}$, where m_0 is the rest mass of the particle.

- The maximum emission angle for an ultra-relativistic particle occurs for: $\theta_{max} = \cos^{-1}(1/n)$.
- Due to the frequency dependence of the refractive index n, the condition $\beta_t = 1/n$ can only be satisfied in the Earth's atmosphere for photons with UV, or longer, wavelengths. Consequently, there is no Cherenkov emission at x-ray or gamma-ray energies.

The density of the Earth's atmosphere is not constant, and as a result, neither is its refractive index. If the refractive index, n, of the atmosphere is defined as

$$n = 1 + \eta$$

where $\eta(<< 1)$ is proportional to atmospheric density, then it can be shown [62] that the maximum emission angle is:

$$\theta_{max} = \sqrt{2\,\eta}$$

Similarly it can be shown that the threshold energy for Cherenkov emission is:

$$E_{min} = m_0 c^2 \left(\sqrt{2\,\eta} - 1\right)$$

Since the atmospheric density decreases as a function of altitude, is clear to see from these equations that the Cherenkov angle decreases with decreasing altitude while the threshold energy increases. At sea level the maximum emission angle is 1.3^o while the threshold energy is 21 MeV, 4.4 GeV and 39 GeV for electrons, muons and protons respectively. These figures show that the majority of Cherenkov emission in the atmosphere is produced by relativistic electrons. In the case of a relativistic electron moving a distance l through the atmosphere, the number of Cherenkov photons created is

$$N = 2\pi\alpha l \left(\frac{1}{\lambda_2} - \frac{1}{\lambda_1}\right)\left(1 - \frac{1}{\beta^2 n^2}\right)$$

where α is the fine structure constant and λ_1 and λ_2 define the wavelength range over which emission occurs. The inverse relationship of photon wavelength to photon intensity means that the majority of photons emitted are high frequency photons.

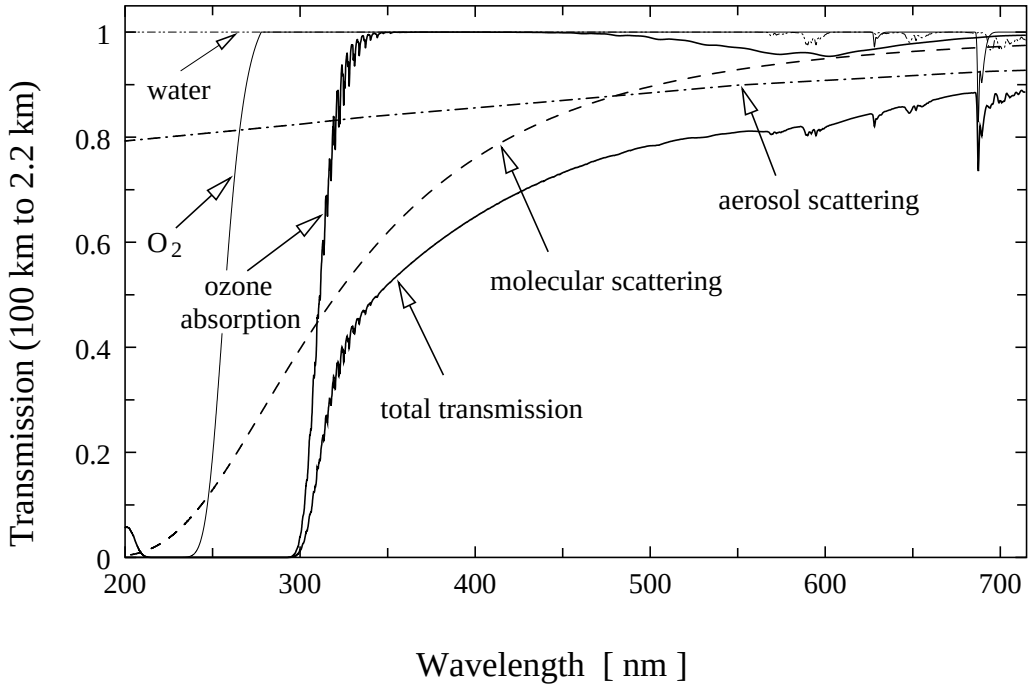

Figure 3–3: Plot of the transmission of the Earth's atmosphere in the UV/optical range generated by MODTRAN [25] . Ozone absorption sharply attenuates UV emission below $300nm$. Figure taken from [26].

In the case of the Earth's atmosphere, this means the peak of photon emission is in the UV part of the electromagnetic spectrum. Attenuation processes in the atmosphere such as Rayleigh scatting, Mie scattering and ozone absorption have the effect of reducing the number of far ultra-violet photons so that the spectrum of photons which reach the ground peaks at $\sim 330nm$ and is cut off below $\sim 300nm$ (see Figure 3–3).

3.3 Extensive Air Showers

When a cosmic ray enters the Earth's atmosphere it causes a particle cascade which, depending on the primary energy, can be composed of many thousands of secondary particles. These secondary particles form an extensive air shower. Ground-based gamma-ray astronomy is founded on the ability to detect these showers and differentiate between showers caused by different initiating particles. In the GeV-TeV energy regime, gamma-ray-induced cascades are best detected via the Cherenkov light generated by the constituent particles. Below $\sim$10 GeV the Cherenkov light yield is too low to be detected on the ground, so space-based and balloon-based detection methods must be used. Above $\sim$50 TeV, the cascade particles themselves reach the ground in enough numbers to be directly detected (see Table 3–1). In these cases direct detection methods, such as water-Cherenkov tanks, are preferred since they are relatively inexpensive and can be used to instrument large areas on the ground. Such detectors are used in the *Auger* and HAWC observatories [89, 42].

The vast majority of extensive air showers are initiated by charged cosmic rays (mainly protons and helium nuclei). Hadronically-induced cascades are mediated through both hadronic and electromagnetic processes. Gamma-ray and cosmic-electron-induced showers, however, are predominantly electromagnetic in nature. The differences in how these showers evolve provide the key to discrimination between gamma rays and background events.

Energy		H_{max} km	N_{max}	N_{sl}	ρ_{sl} $photons/m^2$
10	GeV	12.8	1.6×10^1	4.0×10^{-4}	2.7×10^{-1}
100	GeV	10.3	1.3×10^2	4.0×10^{-2}	4.6×10^0
1	TeV	8.4	1.1×10^3	3.0×10^0	7.4×10^1
10	TeV	6.8	1.0×10^4	1.3×10^2	1.1×10^3
100	TeV	5.5	9.3×10^4	4.5×10^3	1.6×10^4
1	PeV	4.4	8.6×10^5	1.1×10^5	1.9×10^5

Table 3–1: Gamma-ray shower parameters as a function of energy. H_{max} is the height of the shower where it contains its maximum number of particles, N_{max}. N_{sl} is the number of particles surviving at sea level and ρ_{sl} is the Cherenkov photon density at sea level. Table adapted from [112].

3.3.1 Electromagnetic Cascades

The dominant interaction process for VHE gamma rays in the Earth's atmosphere is electron-positron pair production in the Coulomb field of atmospheric nuclei. The radiation length[1] for this type of reaction is 37.7 $g\,cm^{-2}$ and, given that the total atmospheric depth is $\sim$1000 $g\,cm^{-2}$, gamma-ray induced showers begin to form high in the atmosphere. The resultant pair subsequently radiate gamma rays via bremsstrahlung in the Coulomb field of the atmospheric nuclei. The cross-sections for both pair production and electron bremsstrahlung are very similar and in both cases the radiation or pair is emitted predominantly in the direction of motion of the progenitor particle. The forward tendency of the bremsstrahlung emission is aided by the processes of relativistic beaming. The resulting particle cascade is therefore

[1] A radiation length for a particular particle in a given medium is the characteristic amount of matter which, when traversed, reduces the energy of the particle to $1/e(\simeq 0.367)$ of its original energy [117].

very longitudinally extended ($\sim$10 km long) and, laterally, very narrow ($\sim$30 m), with the major axis pointing in the direction of the incident gamma ray. A small amount of lateral broadening of the shower does occur and is due to Coulomb scattering of shower electrons off loosely bound atomic electrons. The cascade initially develops exponentially and, depending on the energy of the initiating primary, can contain thousands of particles. The growth of the shower is eventually halted when the photon energy is less than that required for pair production. The remaining shower energy is then dissipated via the ionisation of atmospheric atoms. A very small muon component can occur in the shower due to photon-photon collisions and photo-nuclear production of pions via the following mechanisms;

$$\begin{aligned}
\gamma + \gamma &\longrightarrow \mu^+ + \mu^- \\
\gamma + p^+ &\longrightarrow n + \pi^+ \\
&\qquad\qquad \pi^+ \longrightarrow \mu^+ + \nu_\mu \\
\gamma + n &\longrightarrow p^+ + \pi^- \\
&\qquad\qquad \pi^- \longrightarrow \mu^- + \bar{\nu_\mu}
\end{aligned} \tag{3.2}$$

However, the probability that a photon will undergo these hadronic reactions is $\sim 10^{-4}$ times that of the pair production probability. Thus, the cascade resulting from the interaction of a cosmic gamma ray with the atmosphere will be almost entirely composed of electrons and positrons which will emit Cherenkov light due to their relativistic velocities. The duration of the subsequent Cherenkov emission is $\sim$10 ns (see Equation 3.4) with the photons landing over an area of $\sim 10^5\, m^2$ in size (see Figure 3–7).

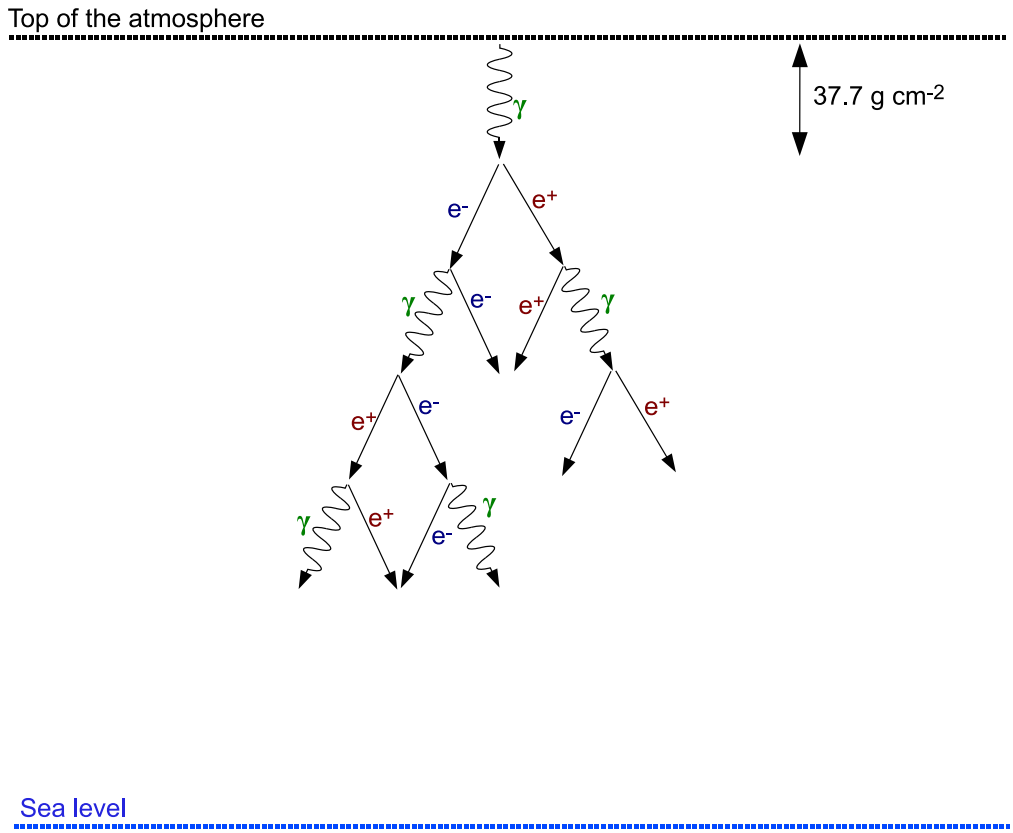

Figure 3–4: Structure of an electromagnetic shower produced by the interaction of a high-energy gamma ray with the Earth's atmosphere. The gamma ray will pair-produce in the electric field of atmospheric nuclei. The pairs subsequently radiate more gamma rays via bremsstrahlung causing a cascade.

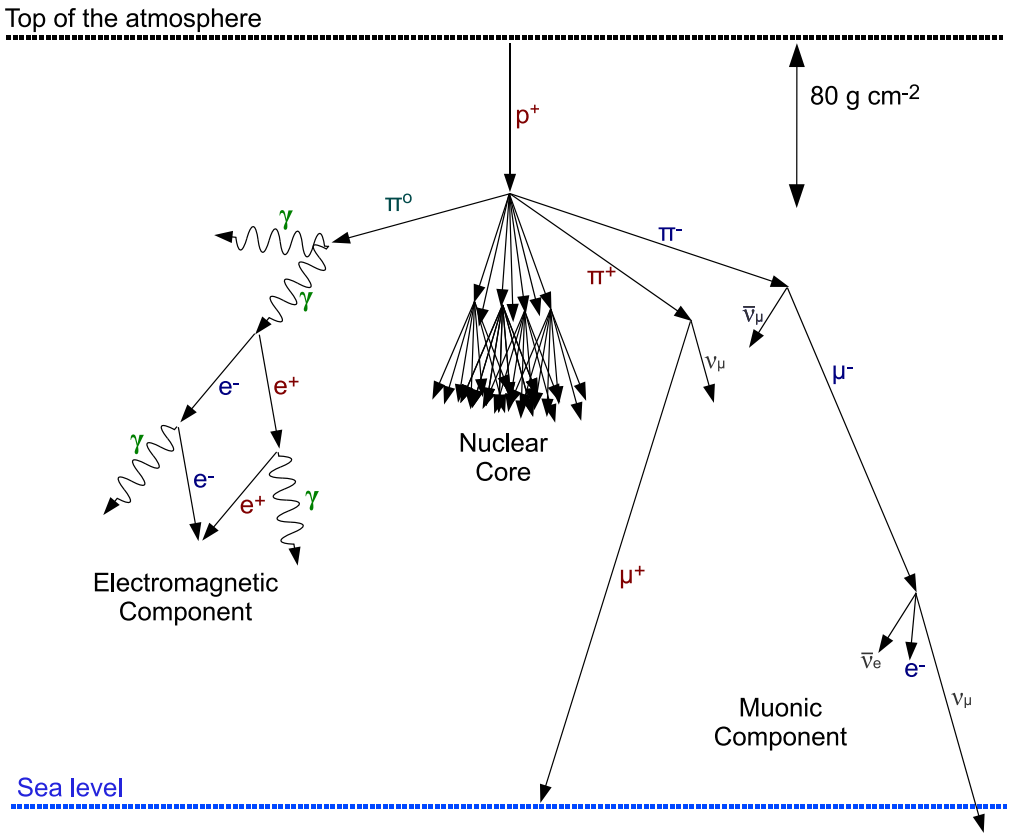

Figure 3–5: Structure of the particle shower produced by the interaction of a cosmic-ray proton with the Earth's atmosphere. The cascade forms through hadronic and electromagnetic processes. The production of pions is the dominant reaction, with the decay of neutral pions initiating electromagnetic showers. The charged pions decay to muons which often survive to sea level. The lateral extent of the diagram is not physical, but to aid in the description of the different shower components.

3.3.2 Hadronic Cascades

When a cosmic ray enters Earth's atmosphere it also initiates a particle cascade. The initial reaction of the proton is to collide with the nucleus of an atmospheric atom. The radiation length of this reaction is $\sim 80\ g\,cm^{-2}$. In the collision, the production of π mesons is the dominant reaction. These pions subsequently collide with more atmospheric atoms forming a cascade. The decay of neutral pions seeds electromagnetic showers while the charged pions decay into muons and neutrinos. The interaction channels are as follows

$$\begin{aligned} p^+ + p^+ &\longrightarrow \pi + \chi \\ \pi^0 &\longrightarrow \gamma + \gamma \\ \pi^+ &\longrightarrow \mu^+ + \nu_\mu \\ \pi^- &\longrightarrow \mu^- + \bar{\nu}_\mu \end{aligned} \tag{3.3}$$

As hadron-initiated showers have both electromagnetic and hadronic components there is a much larger variance from shower to shower than the purely electromagnetic case. The pions created in the collisions between the cosmic hadrons and the atmospheric nuclei are often created with large transverse momentum kicks, thus the resulting showers are laterally broader than the purely electromagnetic showers. The component of muons within hadronic showers is another differentiating aspect with respect to the electromagnetic case, where muon production is very rare. All of these features play a role in the separation of gamma-ray events from cosmic-ray background events.

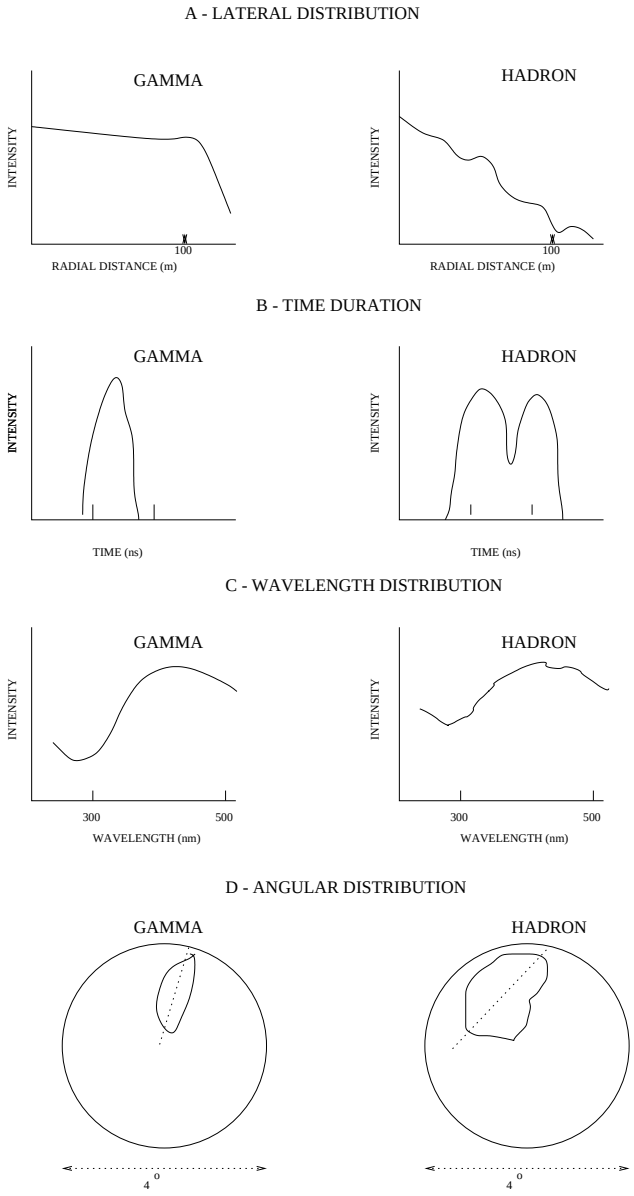

Figure 3–6: Cartoon of the differences in the Cherenkov emission from gamma-ray and cosmic ray induced showers. Figure taken from [113].

3.3.3 Differences between hadronic and electromagnetic showers

The flux of charged cosmic rays entering the Earth's atmosphere is approximately four orders of magnitude above the gamma-ray flux. Rejection of the cosmic-ray background is, therefore, of paramount importance for the successful implementation of a gamma-ray telescope. Few detectable differences exist between electromagnetic and hadronic showers in the VHE energy regime. The immense difficulty in exploiting the differences which do exist is the primary reason why the initial concept of gamma-ray astronomy [83] took thirty years to realise [114]. The differences in the shower development are revealed in the Cherenkov light distributions in the following ways:

(A) **The uniformity of the Cherenkov photon density on the ground.** Hadronic cascades can have large transverse momentum and their Cherenkov light yield has a significant contribution from muons which impact the ground at various places throughout the broader light pool. The Cherenkov photon density on the ground is higher in the immediate vicinity of these impact points. This irregular photon density does not occur in electromagnetic cascades, which have no muons and have a very flat photon density across the light-pool, centred on the impact point of the shower on the ground (see Figure 3–7).

(B) **The time of arrival profile of the Cherenkov photon front on the ground.** In electromagnetic showers, all Cherenkov photons are emitted from a single shower, which can be described as long narrow column. Since the shower particles are moving faster than the local speed of light, photons from the later stages of the shower arrive at the ground first, with the photons emitted early

in the shower arriving last. The spread in arrival time goes as

$$\delta T \approx \frac{L}{c}(n_{air} - 1) \tag{3.4}$$

where L is vertical extent of the shower. For $L = 10\ km$, $\delta T \approx 10\ ns$. The emitted photon front from hadronic showers, have less regular time profiles on the ground due to the deeply penetrating muons which arrive before the Cherenkov photons from the main shower. Thus the overall time spread can be $>20\ ns$.

(C) **The colour profile of the Cherenkov photon distribution.** Since hadronic showers start deeper in the atmosphere and spawn deeply penetrating muons, the emitted Cherenkov photons traverse less of the atmosphere before they reach the ground than the Cherenkov photons from electromagnetic showers. This means that the hadronically induced Cherenkov photon distribution has a higher component of UV photons than its electromagnetic counterpart.

(D) **The angular arrival profile of the photon front on the ground.** The angular arrival profile of the Cherenkov photons is determined by the angular extent of the air showers on the sky. Since hadronic showers are laterally broader and more irregularly shaped than electromagnetic showers, the resulting distributions of Cherenkov photon arrival directions encode these difference.

Figure 3–6 shows how each of the above differences manifest themselves diagrammatically.

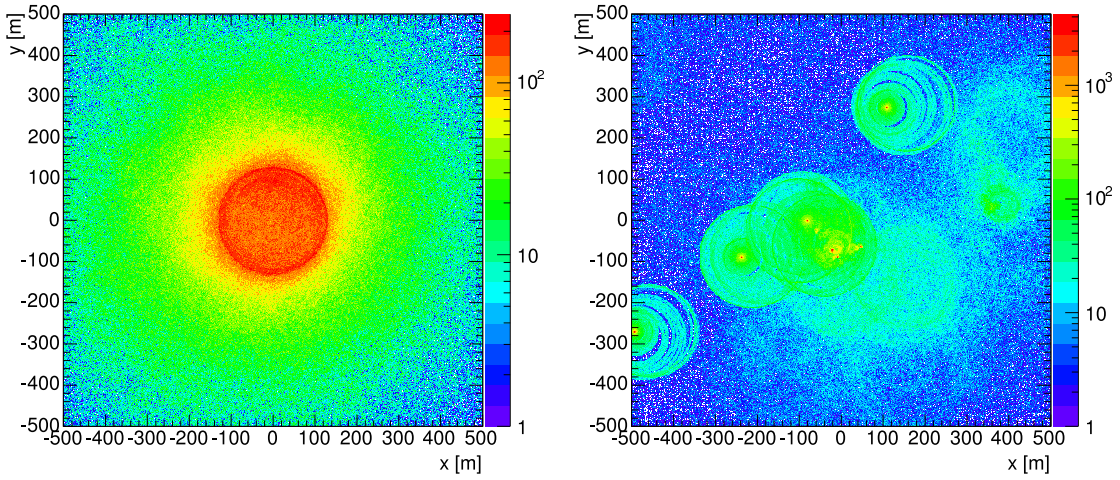

(a) 300 *GeV* Gamma ray

(b) 500 *GeV* Proton

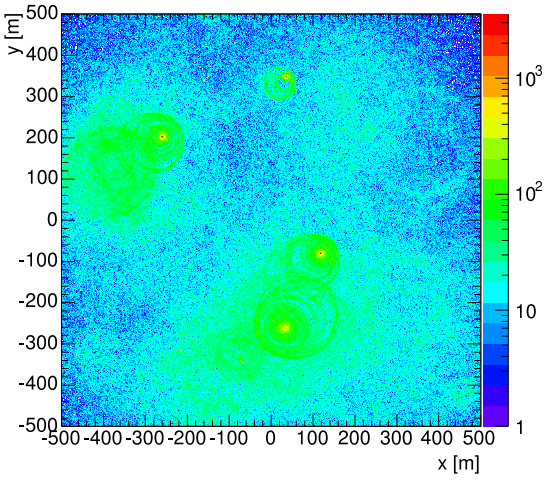

(c) 500 *GeV* Iron Nucleus

Figure 3–7: Plots of the Cherenkov photon density on the ground plane from air showers simulated with the *CORSIKA* software package [49]. Panel (a) shows the relatively uniform photon yield from a single gamma-ray initiated shower with the bulk of the photons falling in a circular region with a radius of $\sim$120 m. Panels (b) and (c) show photon densities from cosmic-ray showers. Evident is the non-uniform spread of the photons. Plots provided by Dr. Gernot Maier.

3.4 Atmospheric Cherenkov Detectors

Atmospheric Cherenkov gamma-ray detectors are designed to exploit the variance between hadronic and electromagnetically induced showers listed above. So far, and with good reason, most detectors focus on the the timing and angular differences and they are grouped into two categories; imaging detectors and wave-front sampling detectors.

Wave-front sampling detectors, such as CELESTE and STACEE [98, 28], worked by distributing detector components over a large area ($\sim$30,000m^2) on the ground. This was done to have wide and uniform and sampling of the Cherenkov photon front. Each detector was used to record the time and intensity of the Cherenkov photon front as it hit the ground. The orientation of the fronts time profile was used to determine the arrival direction of the shower. The uniformity and consistency of the time profile was used to discriminate between the different initiation primaries and the intensity of the detected Cherenkov light was used to determine their energy.

Imaging detectors, such as VERITAS, MAGIC, HESS, CANGAROO-III and the Whipple Telescope [59, 21, 54, 67, 63], employ large focusing optical reflectors instrumented with highly sensitive multi-channel cameras. Such detectors can form an image of the extensive air shower from the emitted Cherenkov light. The orientation of the image is used to determine the arrival direction of the shower, while its angular dimensions (width, length, etc) are used to discriminate between the different initiating particles. Again, the intensity of the detected Cherenkov light is used to determine the primary particle energy. Imaging detectors have, in general, proved to be more sensitive than wave-front sampling detectors. Major future atmospheric

Cherenkov projects, such as The Cherenkov Telescope Array (CTA) [31], will consist entirely of imaging detectors.

In sections 4.4 to 4.7 of Chapter 4, a more complete description of the imaging method is given. In particular, the mechanism for parametrising the recorded images and the use of this parametrisation to separate gamma-ray events from the cosmic-ray background will be explained.

3.5 The VERITAS Array

The VERITAS array consists of four telescopes located at the Fred Lawrence Whipple Observatory (FLWO) in southern Arizona, USA, at an altitude of $\sim$1300 m. The array began operations as a single telescope in February 2005 and was completed in March 2007. Due to planning difficulties with the original two planned sites for the VERITAS array, Madera Canyon and Kitt Peak, both in southern Arizona, the lay-out of the VERITAS array after construction at the FLWO was not optimal. In particular, two telescopes were separated by a distance of $\sim$38 m and thus were both triggered at a high rate by muons. Between June and September 2009 the first VERITAS telescope, T1, was relocated to a position $\sim$180 m east of its original location (see Figure 3–8), resulting in an array configuration with an average baseline between telescopes of 114 m.

The primary components of each telescope are: a 12-meter-diameter reflector, a 499-pixel camera, a telescope triggering system and a data acquisition system. The four telescopes are controlled from a central building which houses an array-level triggering system. The remainder of this chapter describes in detail the functions of each of these systems.

(a) VERITAS array prior to September 2009

(b) VERITAS array after September 2009

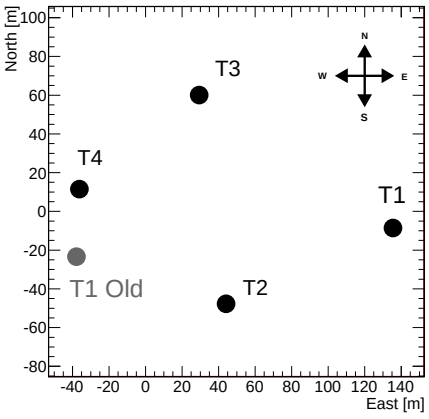

(c) VERITAS Telescope Ground Locations

Figure 3–8: Photos of the VERITAS array before and after the relocation of T1 in the summer of 2009 and a map of the telescope ground positions.

Figure 3–9: Photograph of a VERITAS optical-support-structure during the telescope construction phase.

3.5.1 Mechanical Structure

Each VERITAS telescope consists of a commercial altitude-over-azimuth positioner, a steel custom-made optical-support-structure (OSS), quadropod camera support arms and counterweights. A mechanical bypass support is attached to the uppermost quadropod arm and transfers its load directly to the counterweights.

The motion of the telescope is controlled by servo motors which drive the telescopes with typical slew speeds of one degree per second. Raw positional encoder values are written to a database at a rate of 4 Hz, along with the corrected azimuth and elevation. Further corrections to the telescope pointing are provided by optical pointing monitors (discussed in section 3.5.7).

3.5.2 The Reflectors

The VERITAS array employs four twelve-meter-diameter f-1.0 reflectors of the Davies-Cotton type [35]. This type of reflector consists of a spherical optical support

structure (OSS), with radius of curvature of r, upon which many spherical mirror facets with a radius of curvature of $2r$ are mounted.

Davies-Cotton reflectors offer many benefits over parabolic reflectors; all mirrors are identical and therefore the reflectors are relatively inexpensive, alignment of the mirrors is simple (see section 3.6.2) and on-axis and off-axis aberrations are smaller than those inherent in parabolic reflectors. The single main disadvantage of Davies-Cotton reflectors is that they are asynchronous, with the VERITAS reflectors introducing a spread of $\sim$4 ns to the incoming Cherenkov shower front [66].

The VERITAS reflectors have 345 identical hexagonal mirror facets mounted on each OSS. Each facet has a surface area of 0.322 m^2 and is made of slumped, polished glass, which is aluminized and anodised at an on-site optical coating laboratory. To prevent degradation due to exposure to wind-blown sand from the Arizona desert, facets are periodically re-coated and replaced to maintain their peak reflectivity above $\sim$90% [94]. The reflectivity of a sample of VERITAS facets is plotted in Figure 3.5.2.

The facets are attached to the OSS by a triangular three-point suspension mount. At each vertex, a mounting gimbal and adjustment nut are threaded onto a stainless-steel rod. Any mis-alignment of the facet can be corrected by turning two of these adjustment nuts. Figure 3–11 shows photographs of the VERITAS reflector, mirrors and mirror mounts.

3.5.3 The Camera

The VERITAS camera (see Figure 3–12(a)) is a pixelated photo-detector comprising 499 photo-multiplier-tubes (PMTs). Each PMT has a diameter of 28.6 mm and 10 gain stages. The model, *Photonis* XP2970/02, is optimised to be sensitive to

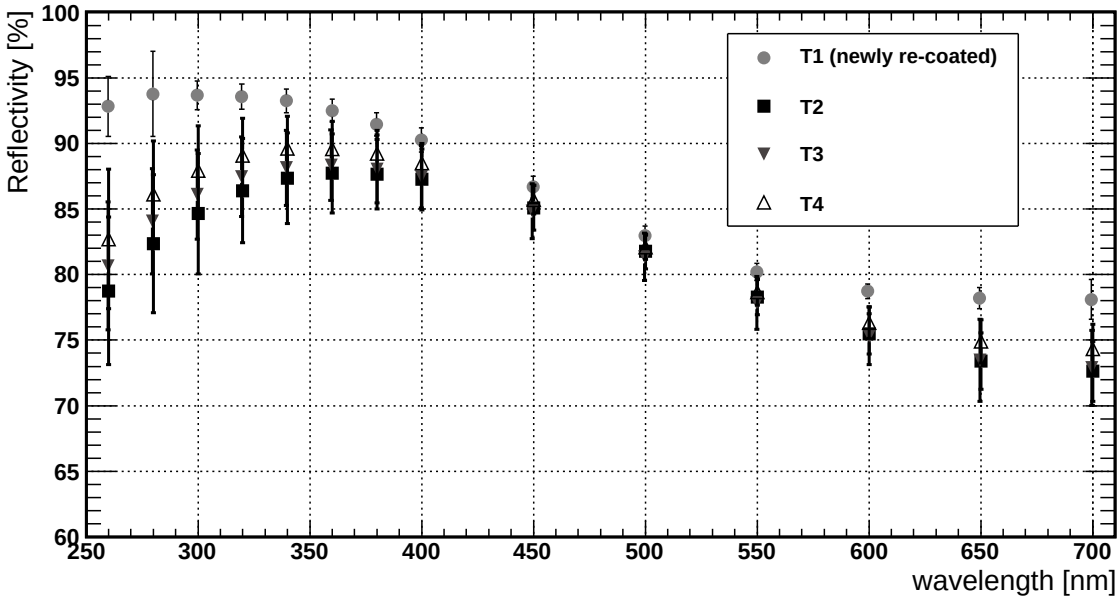

Figure 3–10: Reflectivity measurements made of reference mirrors from the VERITAS telescopes in February, 2008. Points mark the mean reflectivity of each population, while the error bars represent the standard deviation. The mirrors of Telescope 1 were newly re-coated when these measurement were made.

(a) Triangular three-point suspension mirror mount.

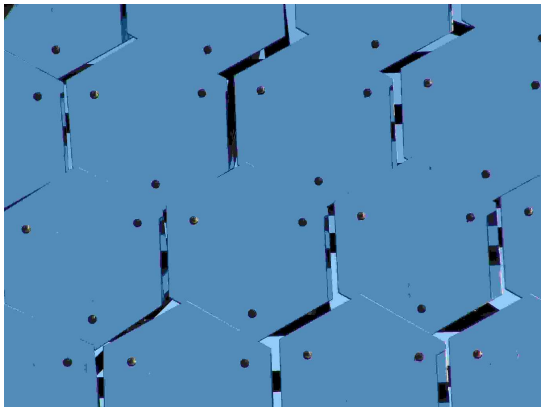

(b) A close-up view of the hexagonal VERITAS mirror facets (from [59]).

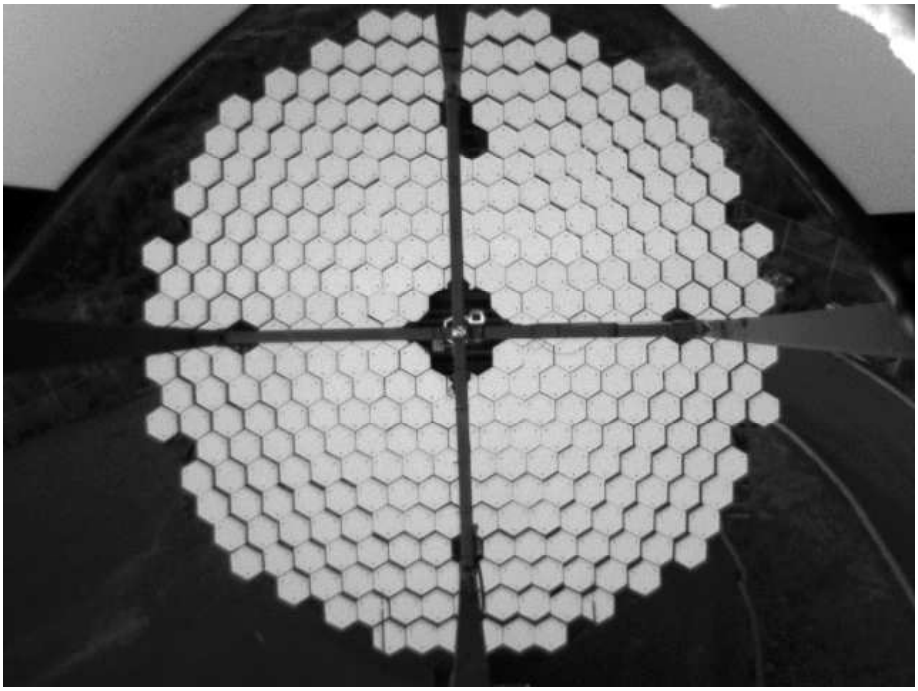

(c) An image of one of the VERITAS reflectors as seen from the focal plane.

Figure 3–11: Photos of the VERITAS reflector.

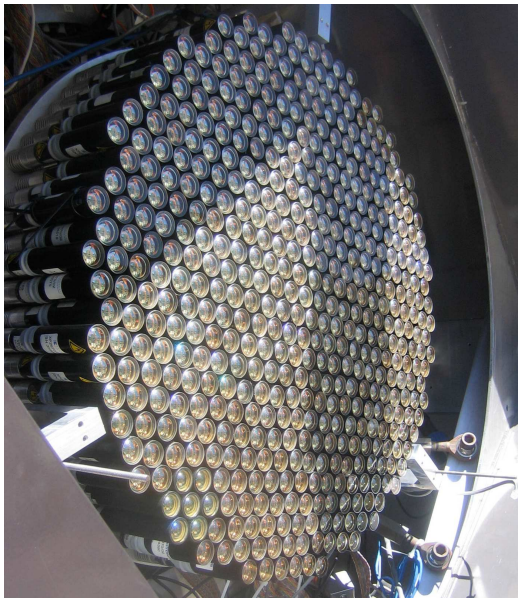

(a) Image of the VERITAS PMT camera.

(b) Image of some the VERITAS light concentrators.

Figure 3–12: Photographs of the VERITAS camera and light concentrators.

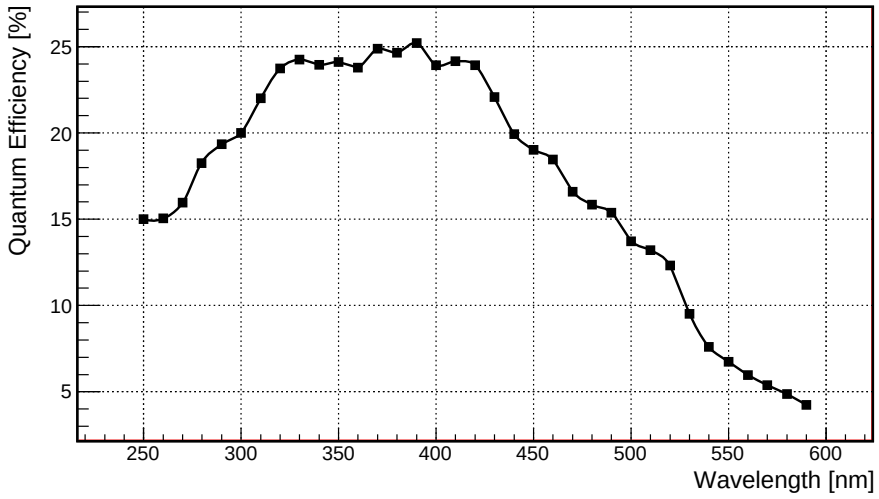

Figure 3–13: Plot of the measured quantum efficiency of the VERITAS PMTs. Measurements are made by illuminating the PMTs by a calibrated light source and recording the PMT response. Plot provided by Dr Nepomuk Otte.

the UV/blue part of the electromagnetic spectrum with a quantum efficiency >20% at 300 nm (see Figure 3–13).

Positioned in front of each camera is a light cone plate consisting of 499 modified Winston cones; segmented parabolic reflective baffles, which act as light concentrators(see Figure 3–12(b)). These have the effect of restricting the incoming photons which can hit the photo-sensitive surface of the PMTs to those which come from the direction of the reflector. This prevents stray, off-axis, light from contaminating the signals in the PMTs while also reducing camera dead-space caused by the PMTs' thick casing and gaps in their packing structure. The optical plate scale of the VERITAS telescopes is $0.0477^{\circ}/cm$, resulting in a 0.148° angular field of view for each PMT and a total field of view 3.5° per camera.

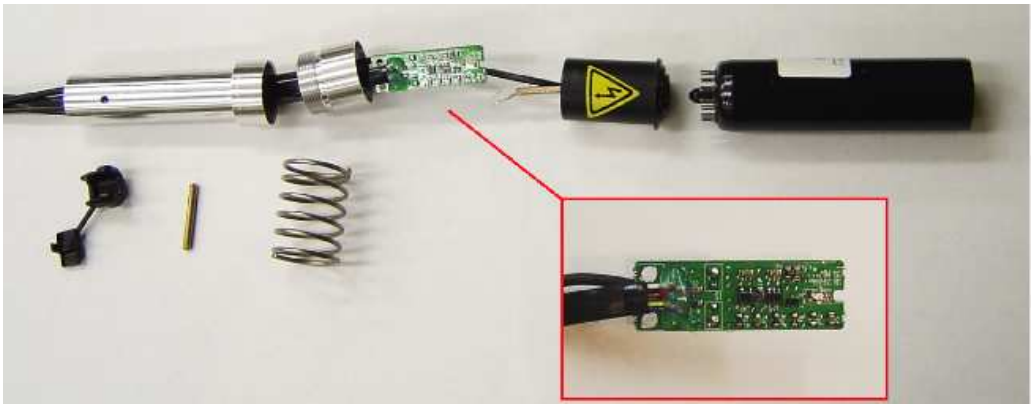

Figure 3–14: Image of a VERITAS pixel before assembly. Moving left to right the principal components are; a cylindrical aluminium casing, a pre-amplifier circuit (also shown in inset), the PMT base connector (voltage divider) and the photomultiplier tube.

The high voltage required to operate the PMTs is provided by a multichannel modular commercial power supply manufactured by *CAEN* (model SY1527). The VERITAS PMTs are typically run at a voltage of 700-800 V, which yields a gain of $\sim 2 \times 10^5$. A custom-built high-bandwidth (300 MHz) two-stage pre-amplifier is installed in the base of each PMT. This, along with the PMT itself, a HV/signal PMT base connector, a cylindrical aluminium casing and a spring to provide connective compression, forms a single VERITAS pixel (see Figure 3–14). The pre-amplification circuit is primarily designed to provide an extra gain of 6.6 to the PMT signals. The circuit also enables the monitoring of the PMT anode currents and allows for the injection of externally generated test pulses into the coaxial cable (RG-59) which carries the PMT signal to the readout electronics. These test pulses are used to test the trigger and readout electronics, in situ, during day-light hours, when the PMTs cannot be turned on. The PMT currents, which must be closely monitored to prevent unnecessary ageing and damage, are read by an array of 8-bit FADC channels which

are grouped in 16 FPGA-controlled circuit boards containing 32 channels each. The current values are recorded with $0.5\mu A$ resolution via custom readout and display software. Average PMT currents between 4 and 7 μA are typical during astronomical observations.

3.5.4 The VERITAS Trigger System

The VERITAS trigger system is designed to preferentially record the $\sim$10 ns flashes of Cherenkov light resulting from gamma-ray induced particle cascades in the atmosphere. These brief events occur against the background of: star-light, moon-light, distant lightning, terrestrial light (cars, street lights, etc..), local muon-generated Cherenkov flashes and PMT noise and after-pulsing. To achieve this the VERITAS trigger system is stratified into three different levels. Briefly:

- The Level-one trigger (L1) is a pixel-wise trigger, which fires when the signal in an individual PMT crosses a certain threshold. The output signal from the L1 trigger is sent to the Level-two trigger.
- The Level-two trigger (L2) is a telescope-wise pattern trigger. It fires when contiguous PMTs fire their L1 trigger within a narrow time window. The output signal from the L2 trigger is sent to the Level-three trigger.
- The Level-three trigger (L3) is an array-wise multiplicity trigger. It fires when the required number of L2 signals is received within the required time window. If the L3 trigger criteria are met, the VERITAS readout and data acquisition processes record the event information in each telescope.

Level One

The VERITAS Level-1 trigger (described in [43]) is a pixel-wise trigger which is designed to trigger on the fast rising ($\sim$4 ns) current pulses generated by the PMTs in response to a Cherenkov flash. In order to use the narrowest possible coincidence window at the L2 stage, it is desirable that the L1 trigger pulse formation is not strongly dependent on the amplitude of the PMT pulse. It is also desirable that the L1 trigger rate is not strongly driven by the changing night-sky conditions, when a bright star sits in the field of view of a pixel, for example. This requires the L1 trigger to modify its response when triggered at a high rate. To meet these conditions, a specialised circuit was designed which employs a threshold discriminator (TD), a zero-crossing discriminator (ZCD) and a rate feed-back (RFB) mechanism. A block diagram of this circuit is shown in Figure 3–15. Each component works in the following way:

- The TD operates with a simple programmable threshold, typically set to 50 mV. This means that the TD will fire if the PMT input pulse rises above 50 mV. While the 50 mV threshold insures that a large fraction of small pulses from night-sky background (NSB) photons or electronic noise do not fire the trigger, it has undesirable characteristics. Since the TD employs a simple threshold, it will fire earlier for large pulses than it will for small ones, as a large pulse will reach the threshold level before a small one, even if they were injected at the same time. To overcome the jitter associated with a simple threshold discriminator, the TD is used in conjunction with a ZCD.

- The main feature of a ZCD is that it will fire at the same point on an input pulse, independent of its amplitude. The ZCD is fed by two branches of the input PMT pulse. The first is scaled in amplitude by some fractional value, f, while the second is delayed by some time ($\sim$2.5 ns) and inverted. The two pulses are then summed together (these pulse modifications are plotted in Figure 3–16). The trigger criterion is then reached when this resultant pulse crosses zero. The L1 trigger condition is met if the ZCD condition is reached while the input pulse is still above threshold in the TD. This combination of a TD with a ZCD, called a constant-fraction discriminator (CFD), allows for the discrimination of pulses based on their amplitude, while keeping the trigger time jitter to a minimum. This combination has a second desirable feature, which causes the rejection of pulses from single NSB photons which fire the TD. Single photon pulses are intrinsically narrower than the pulses due to a Cherenkov event. Therefore these pulses fall below the threshold of the TD, before the ZCD fires (see Figure 3–16).
- The RFB circuit adds a small DC offset to the inverted pulse entering the ZCD, the size of which is determined by a frequency-to-voltage converter. This converter, calculates the frequency at which the CFD is triggering, over one second, and adjusts the offset voltage by 52 mV/MHz. This has the effect of regulating the effective threshold of the CFD, based on the amount of CFD triggers. This mechanism prevents the L1 trigger rates from being strongly driven by changes in the background light and noise.

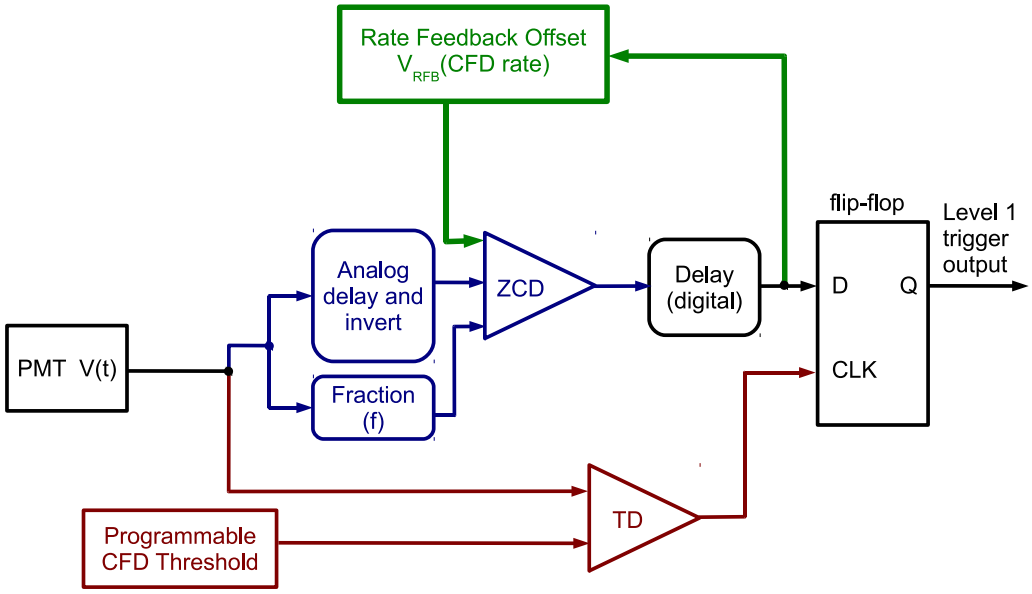

Figure 3–15: Block diagram of the VERITAS Level 1 trigger. The PMT pulse is split and sent into a zero-crossing-discriminator and a threshold discriminator. The output from these two trigger decisions is processed by the flip-flop gate. This has the effect of insuring that the trigger decision is not strongly dependent the input pulse amplitude. The rate-feed-back circuit biases the input to the ZCD effectively adjusting the trigger threshold based on the trigger rate. Diagram is based on Figure 1 from [43]

The L1 trigger units on VERITAS emit $\sim$10 ns emitter-coupled logic (ECL) pulses to the L2 trigger. Each L1 channel employs a programmable output pulse delay, up to 6 ns in duration, which can account for differences in the lengths of the signal cables from the PMTs. The typical operational L1 trigger rates under dark skies, range from $\sim$3 kHz to $\sim$3 MHz with the median rate per camera between 35 and 55 kHz.

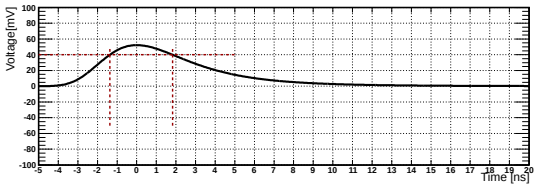

(a) Example pulse entering the L1 trigger

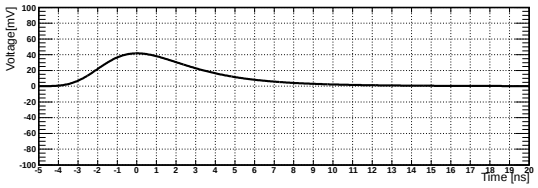

(b) Example pulse, scaled by f, in the CFD.

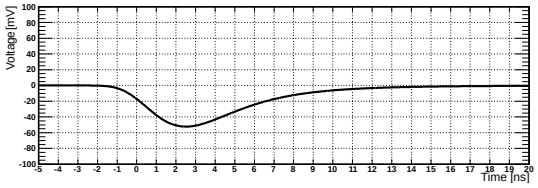

(c) Example pulse, delayed and inverted, in the CFD.

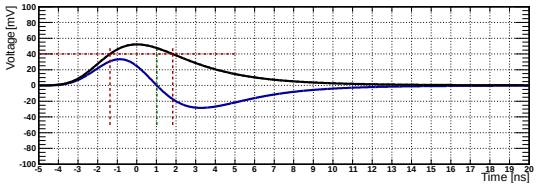

(d) Resultant pulse in the ZCD; Delayed and inverted pulse added to the scaled pulse.

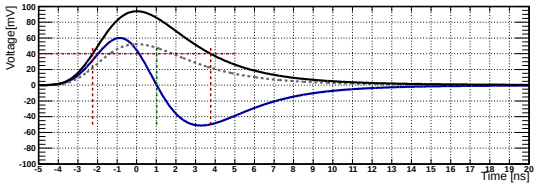

(e) Result when a large pulse enters the system (dashed line represent the pulses in panel d).

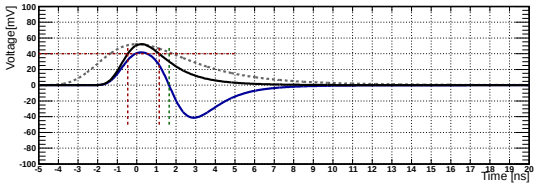

(f) Result when a very narrow pulse enters the system (dashed line represent the pulses in panel d).

Figure 3–16: Plot of the pulse scaling, inversion and addition technique used in the VERITAS constant fraction discriminators. The pulses in panels (a),(b) and (c) are combined in panel (d). In panel (d) the horizontal line represents the threshold discriminator and the vertical line represented the zero-crossing discriminator. Panels (e) and (f) show the same process as panel (d) but with a large amplitude and narrow pulse respectively.

Level Two

The VERITAS L2 trigger condition is met when L1 pulses from contiguous pixels, above some programmable number (typically 3), arrive within a $\sim$6 ns window. The main function of this topological trigger is to reduce the number of triggers from random NSB events, which are unlikely to cluster in regions of the camera over short time windows, without losing sensitivity to the gamma-ray induced events. A block diagram of this trigger is shown in Figure 3–17. The L2 trigger is implemented by grouping the L1 channels from the camera into 19 overlapping patches of $\sim$59 channels (see Figure 3–18). Every L1 channel inhabits 3-5 of these 19 patches. Each patch is wired to a custom-built electronic module which was designed and built by Hytec Electronics Ltd and is powered and programmed by a commercial CAMAC controller crate [27]. The modules act as a comparator, which compares the pattern of triggers in the module to a pre-programmed bank of chosen patterns stored in the modules RAM. The trigger decision of each module is then fed to an OR logical circuit. Thus, a positive trigger decision in any one module results in a positive trigger from the OR device. This constitutes the L2 trigger. The comparator modules are typically loaded with all the patterns possible from three neighbouring pixels, but can in principal be loaded with any patterns. The L2 decision logic takes $\sim$60 ns to generate a trigger and the typical operational L2 trigger rates under dark skies range from $\sim$500 Hz to $\sim$5 kHz. Each telescope independently generates five identical copies of its L2 trigger pulse. Four are fed directly into a spare channels in the PMT readout electronics, which are distributed across four local data acquisition crates.

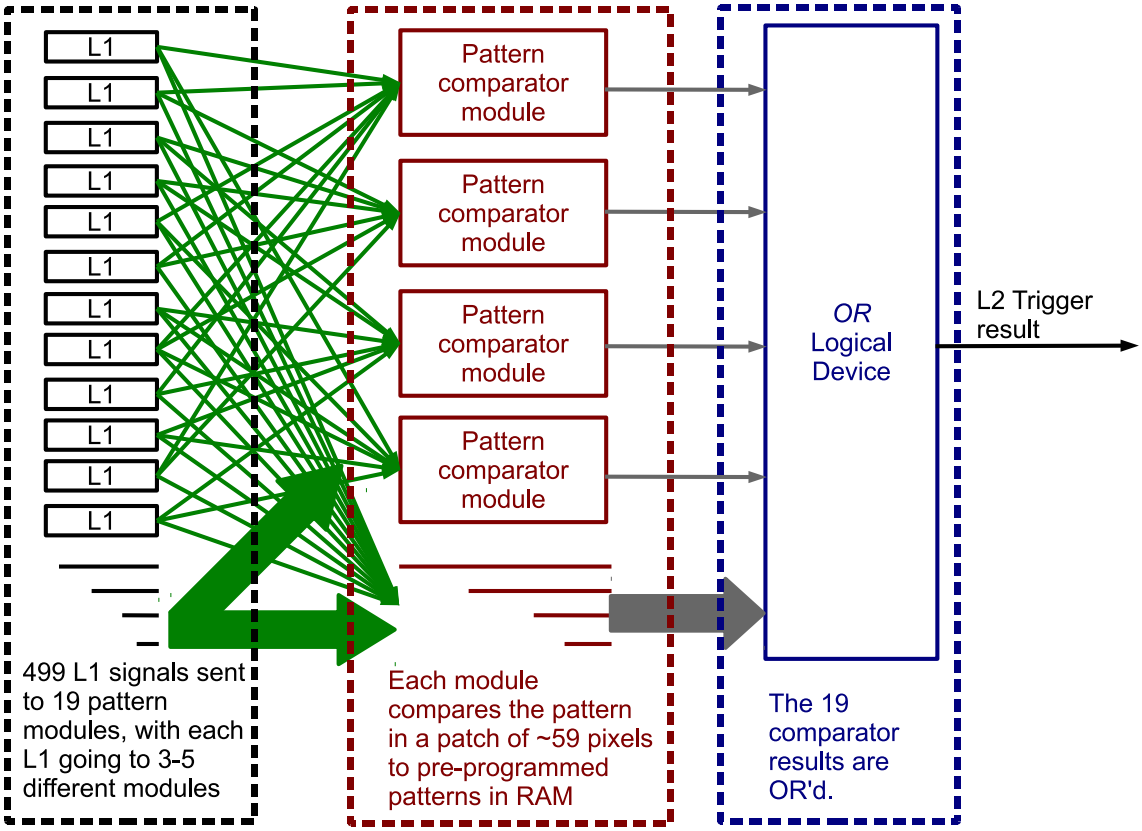

Figure 3–17: Block diagram of the L2 trigger system. The L2 trigger is implemented by grouping the L1 channels from the camera into 19 comparator modules. Each module compares the pattern of triggers to a pre-programmed bank of chosen patterns stored in its RAM. The trigger decision of each module is fed to an *OR* logical circuit. A positive trigger decision in any one module results in a positive trigger from the *OR* device.

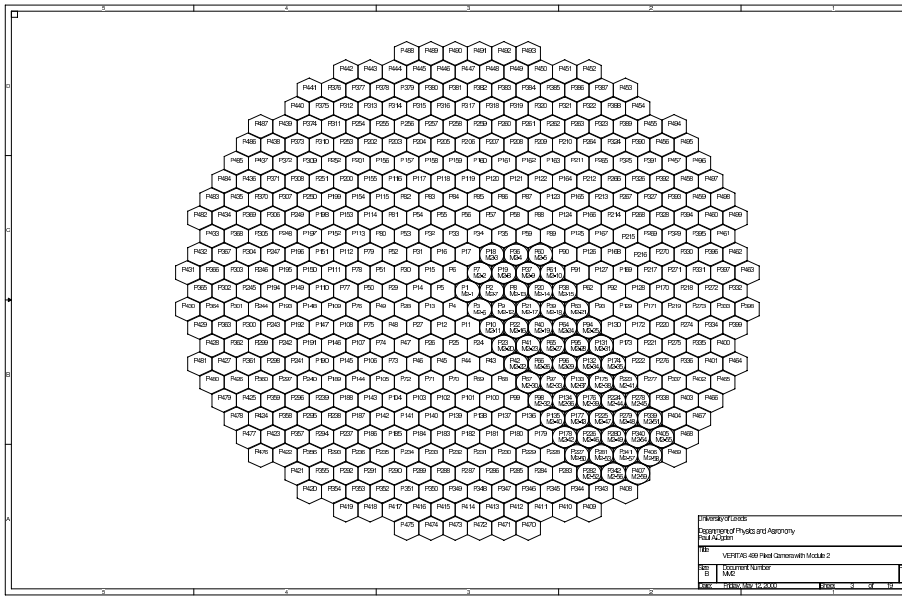

(a) L2 trigger patch 2.

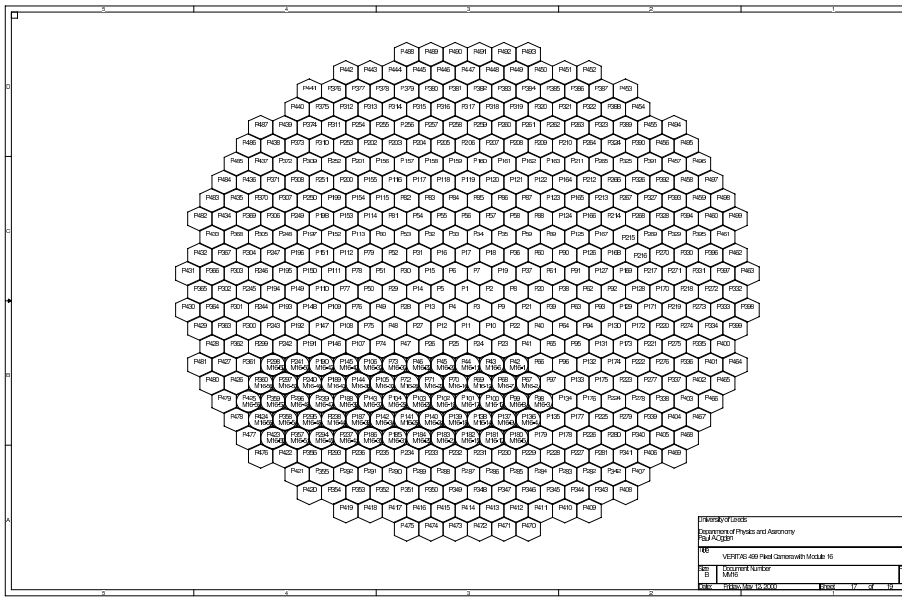

(b) L2 trigger patch 16.

Figure 3–18: Maps of two of the nineteen overlapping patches in the VERITAS L2 trigger.

These pulses are used later to synchronise the data readout in the four crates. The fifth L2 pulse is sent to the L3 trigger system.

Level Three

The VERITAS Level 3 trigger (described in [115]) is an array-wise trigger which is designed to fire on multiple L2 signals whose arrival times are consistent with triggering on the same gamma-ray event. The L3 trigger is also designed to initiate event read-out. This requires the signalling of the individual telescope data acquisition systems to read their buffered PMT signals and to parse those data with array-wide indices and information, such as time-stamps and event numbers, so that data from multiple telescopes can be asynchronously combined. To do this, the L3 system uses several different components, including: Digital Asynchronous Transceiver modules (DATs), programmable pulse delay modules (PDMs), time-to-digital converters (TDCs), GPS clocks, and a custom-designed FPGA computer called, the Sub-Array Trigger (SAT) board. A block diagram of this system is shown in Figure 3–19. Each component's function is explained below:

- The DATs consist of multi-channel opto-electric converters and optical transceivers. These *VME* based devices enable transmission of the L2 trigger signals to the L3 system and transmission of the L3 readout signal and event information to the individual telescope data acquisition systems. These signals are transmitted over optical fibre, providing fast and electrically decoupled communication between the telescopes and the control room, where the L3 trigger and array-event building computer, called the Harvester, are located.

- The PDMs, also *VME* based devices, have 32 independent programmable delay channels each and are capable of applying a delay from 100 ns to 16 μs in 2 ns steps. The L3 system employs the PDMs to delay the incoming L2 signals, before sending them to the L3 coincidence logic and to delay the outgoing "readout" L3 signal to the telescopes. These delays are used to compensate for the different distances over which the L2 and L3 signals will travel over the optical fibres to the different telescopes. Typical operational values for these delays are listed in Table 3–2. A further delay is applied to the incoming L2 signals to compensate for differing arrival times that the planar front of Cherenkov photons, emitted from a gamma-ray induced shower, will reach the telescopes on the ground, based on the pointing direction of the telescopes. The value of this delay is calculated via information from the telescope tracking system and is updated to the PDM every 5 seconds. This delay has the effect of rejecting L2 events which arise from any light flash which does not originate from the direction the telescopes are pointing (such as distant lightening).
- The SAT board is a *VME*-based FPGA, upon which the coincidence test is performed. The delay-corrected L2 signals are converted to an arrival time via on-board TDCs, which have a timing resolution of 1.25 ns. These times are then buffered and processed by a configurable coincidence algorithm running on the board. The configurability of this algorithm provides L3 with the ability to run multiple sub-arrays in parallel. In typical operations, the coincidence criteria is satisfied when two or more delay-corrected L2 signals coincide within 50 ns. When this condition is met the L3 trigger signal and supplementary

Telescope	Incoming delay $[ns]$	Outgoing delay $[ns]$	Round trip time $[ns]$
T1	1121	1317	2438
T2	1110	1138	2248
T3	729	1018	1747
T4	607	829	1436

Table 3–2: Example L3 trigger PDM delay configuration (2010/2011 observing season). These delays are applied to incoming and outgoing trigger signals to account for the different signal cable lengths between the L3 trigger and the telescopes.

information, such as an event-number, are sent via the PDMs and DATs to the individual telescopes. Other information, such as the L3 GPS time-stamp, is sent to a first-in-first-out (FIFO) buffer which is asynchronously sent to the array-event building processed, running on the Harvester. When an L3 trigger signal is received by the data-acquisition electronics at a given telescope, a trigger veto signal or "busy" signal is sent back to the L3 trigger. This signal prevents further readout signals from being sent from L3 until the current data-acquisition event is finished.

The typical operational L3 trigger rate is 200-300 Hz. The trigger rates of the L2 and L3 systems are plotted against the L1 threshold in Figure 3–20. Such a plot is called a *bias curve*. Two features are clear in this plot; the slow increase in the L2 and L3 rate as the L1 threshold is lowered to $\sim$45 mV and the huge increase in the rates as the L1 threshold is lowered below $\sim$45 mV. The slow rate increase is due to triggering on dimmer and dimmer cosmic-ray-induced Cherenkov flashes. The fast rise illustrates a regime where the L2 and L3 rates are dominated by random NSB noise. From such a plot, an optimal L1 threshold can be chosen, such that it is just

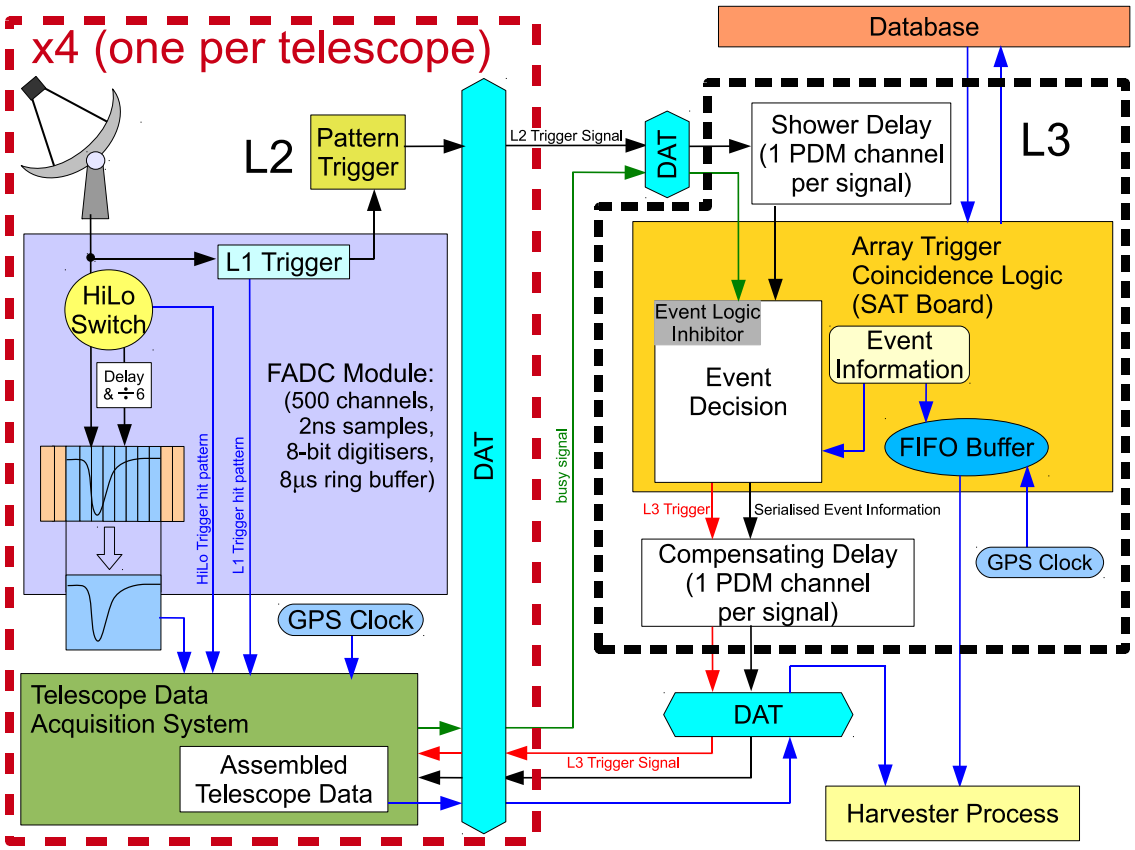

Figure 3–19: Block diagram of the L3 trigger and readout system. L2 triggers generated in each telescope are sent, via the DAT transceivers, to the L3 trigger. After appropriate delays, the coincidence logic scans for two L2 triggers within a narrow time window. If one is found, an L3 trigger signal is sent to the telescopes. This signal, initiates a readout of the buffered PMT information which is stored in the FADCs. This information is then asynchronously sent to L3 where it is compiled by the Harvester process into complete array-event data. This figure is based on Figure 1 from [115].

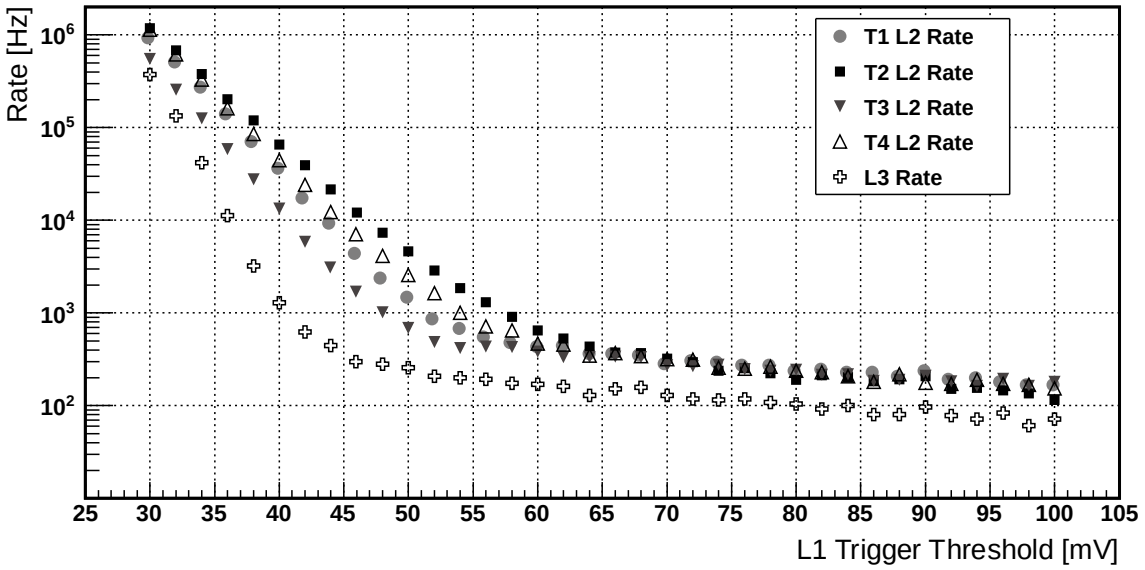

Figure 3–20: Plot of the L2 and L3 trigger rates and a function of the L1 trigger thresholds. Such a plot is called a *bias curve*. Two features are clear in this plot; the slow increase in the L2 and L3 rate as the L1 threshold is lowered to $\sim 45mV$ and the huge increase in the rates as the L1 threshold is lowered below $\sim 45mV$. The slow rate increase is due to triggering on dimmer and dimmer cosmic-ray induced Cherenkov flashes. The fast rise illustrates a regime where the L2 and L3 rates are dominated by random NSB noise. From such a plot, an optimal L1 threshold can be chosen, such that it is just above the NSB inflection point. These data were recorded on 2010-12-13 (run 53840).

above the NSB inflection point. From such a plot, the L1 threshold of 50 mV was chosen for standard dark time operations. When observing in partial moonlight, the operational L1 threshold is 70 mV.

3.5.5 The VERITAS FADCs and Data Readout

The VERITAS PMT signals are continuously digitised and buffered by a custom-built 500 mega-sample per second (MS/s) flash analogue-to-digital converter (FADC) system [92]. The 500-channel readout system for each telescope is distributed across 50 10-channel boards which reside in, and receive power from, 4 *VME* crates. Each

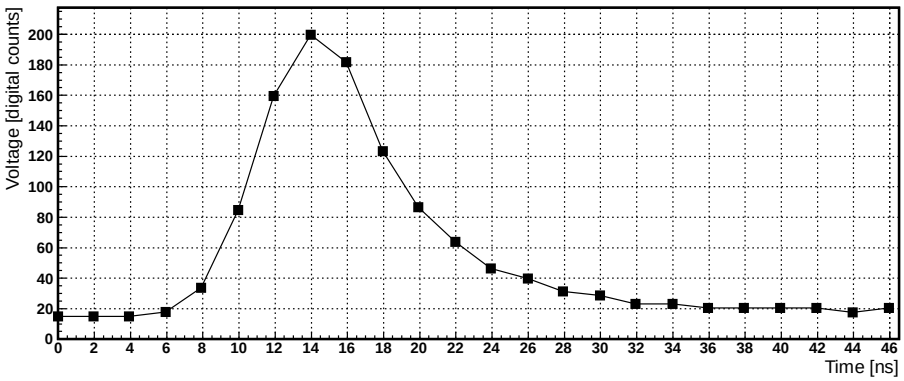

(a) FADC trace of a Cherenkov event

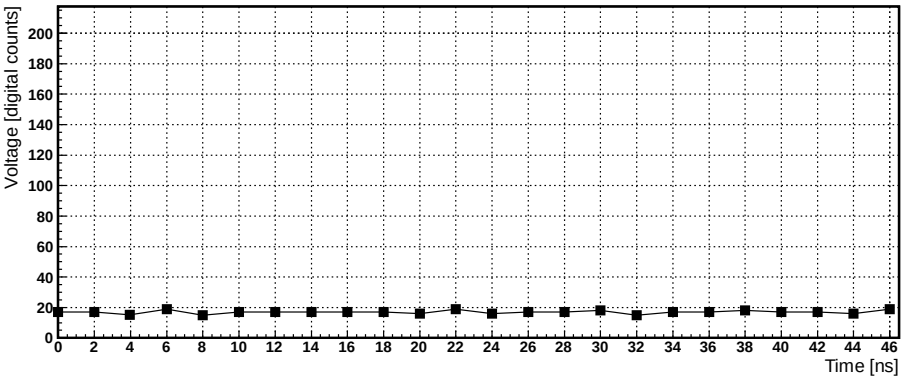

(b) FADC trace of a pedestal event

Figure 3–21: Sample PMT traces recorded by the VERITAS FADCs.

crate houses a computer board, from which the readout boards are programmed and controlled. The PMT pulses are digitised with 8-bit resolution and stored in a circular RAM buffer 8 μs deep. This system negates the need for long, dispersive, delay cables to store the PMT signals while a trigger decision is being made.

When a readout (L3) trigger is received, the buffering process halts, the busy signal is emitted, and a segment of each channel's buffer is read out. This segment is called the readout window and its depth within the buffer is precisely determined such that it contains the PMT traces of the event which generated the local L2 trigger. This depth is referred to as the "lookback" time and it is equal to:

$$\begin{aligned} T_{lookback} = \; & T_{L2\ Trigger} + T_{L3\ Trigger} + T_{Incoming\ PDM\ delay} \\ & + T_{Outgoing\ PDM\ delay} + 2\,T_{L2\ signal\ propagation} \end{aligned} \tag{3.5}$$

where; $T_{L2\ Trigger}$ and $T_{L3\ Trigger}$ are the times taken to fire the L2 and L3 trigger, respectively, $T_{Incoming\ PDM\ delay}$ and $T_{Outgoing\ PDM\ delay}$ are the PDM delays (described earlier and listed in Table 3–2) and $T_{L2\ signal\ propagation}$ is the time taken for the L2 and L3 signals to propagate between the DATs. The size of the readout window is configurable, but for typical operations is 20 FADC samples, or 40ns long.

At the input point to the FADC a DC bias voltage is applied to the PMT signal. This voltage is called the *pedestal* and it provides a non-zero voltage point, about which the PMT signal can fluctuate. Without the pedestal, the AC-coupled PMT signal would fluctuate about zero, meaning negative fluctuations could not be recorded. The pedestal voltage level is such, that in the absence of a signal in the PMT, the FADCs will record a value between ∼15 and ∼19 digital counts (d.c.). Examples of a pedestal trace and a signal trace, as recorded by the FADCs, are

shown in Figure 3–21. Measurements of the pedestal level and its fluctuations are necessary, as they measure the background within which the Cherenkov signals are recorded. Thus, in the absence of a normal L3 trigger, the L3 system sends a *pedestal trigger* to all the telescopes at a rate of $\sim$1 Hz. On these occasions the FADCs will record events with little or no signal in the trace and thus measure the pedestal. These pedestal events are used heavily in the VERITAS data analysis chain where the variance of the pedestal, about its mean value, is a measure of the night-sky background and electronic noise in the camera.

In order to increase the dynamic range of the FADCs, each channel employs a "low-gain" delay line and threshold switch. At the input point to the FADC, the PMT signal is split into three copies. One is delayed and reduced in gain by a factor of $\sim$6. The second is sent to a threshold discriminator (called the *HiLo* discriminator), which assesses if the PMT pulse is within the dynamic range of the 8-bit FADC. The third copy is sent directly into the digitiser. If the amplitude of the raw input pulse is beyond the range of the FADC, the delayed low-gain line is then fed into the digitiser, behind the unscaled copy. A flag is then set which modifies the lookback time of the FADC so that the low-gain pulse is within the read-out window, rather than the high-gain version, which will have saturated the digitiser. This system, results in a dynamic range which is $\sim$6 times larger (see Figure 3–22). At read-out time, the following information is recorded by the telescope data acquisition system;

- The 500 buffered traces which were located in the read-out window.
- The L1 trigger pattern, which is recorded by the FADCs, from the L1 modules which are housed within the FADC VME boards.

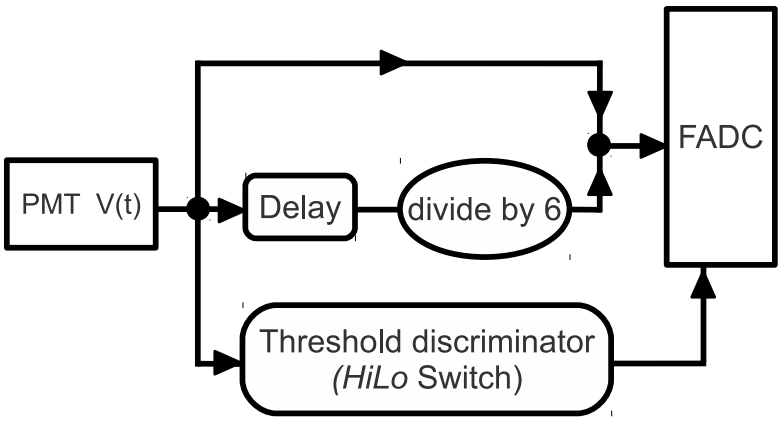

Figure 3–22: Diagram of the FADC *HiLo* switch mechanism. At the input point to the FADC, the PMT signal is split into three copies; One is delayed and reduced in gain by a factor of ∼6, the second is sent to a threshold discriminator, the third copy is sent directly into the digitiser. If the discriminator fires, the raw input pulse amplitude will saturate the 8-bit digitiser, so the FADC ignores it and instead records the delayed, scaled, pulse. This system results in a dynamic range which is ∼6 times larger.

- The HiLo discriminator pattern, recorded by the FADCs at the input to the ring buffer.
- The event information sent from L3, which accompanies the L3 trigger signal on a separate DAT channel.
- The local GPS time stamp.

Once the FADC modules have been read out by the local data acquisition computer housed next to the FADC crates, the busy signal is halted and the FADCs resume buffering the PMT signals and waiting for another L3 signal.

The data acquisition computer is continuously running a process called the *event builder*, which accumulates all the data listed above. This process asynchronously, flushes the assembled telescope data, to the Harvester at a typical rate during normal operations of $\sim 25\ Hz$. At the end of an observation run the data from all telescopes,

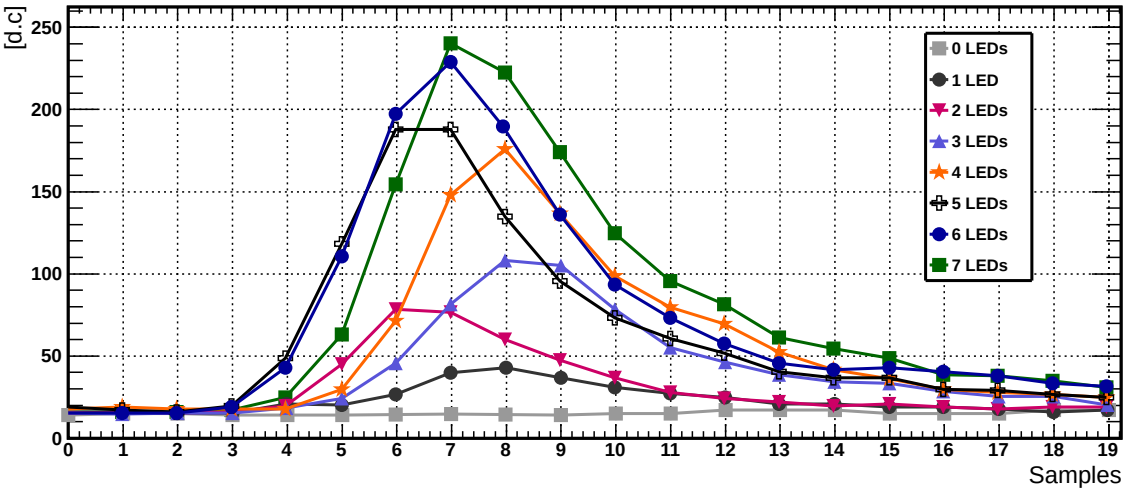

Figure 3–23: Example FADC traces from eight consecutive LED flasher events. The LEDs inside the flasher are driven by a custom-built circuit designed to continuously loop over an eight-step cycle which flashes: zero LEDs, one LED, two LEDs and so on. This ramp of intensity scans over a wide range of the PMT and FADC response, including in some cases, the FADC low gain signal path.

and the L3 trigger, are parsed and compressed together by the Harvester into a single file. This file is in a custom data format, called *compressed VERITAS bank format*, with the file extension .cvbf. A typical 20 minute four-telescope observation run with a steady L3 rate of $\sim$240 Hz yields a final data file size of $\sim$4.5 GB.

3.5.6 LED flasher

The relative gain, absolute gain, and timing characteristics of the VERITAS PMTs are measured and monitored by a light-emitting-diode (LED) flasher system [45] which is deployed on each telescope. Each flasher unit is attached to the quadropod cross-beam supports, $\sim 6m$ in front of, and facing, each camera. The units are powered by a $6V$ supply tapped from a power distribution board located inside the camera housing. Each flasher is fired by a centralised NIM-level trigger located next

to the L3 trigger hardware. The function of the flashers is to uniformly illuminate the VERITAS cameras with short ($\sim 10ns$) ultraviolet light pulses.

Each flasher unit contains seven *Nichia* NSPU510CS UV LEDs, with a peak wavelength of $375nm$. The LEDs are driven by a custom-built circuit designed to continuously loop over an eight step cycle which flashes: zero LEDs, one LED, two LEDs and so on (see Figure 3–23). This ramp of intensity scans over a wide range of the PMT and FADC response, including the FADC low gain signal path. The LEDs, driver circuit and associated trigger logic are housed inside a modified *Maglite* flash-light casing, which is hardy and durable and well suited to prolonged outdoor deployment. A $50mm$ opal diffuser (Edmund Optics NT46-106) replaces the lens of the flash-light, which spreads, uniformly, the light from the LEDs placed a few millimetres behind. This system has several features which make it more favourable than the nitrogen laser system [44] which it replaced in September 2010; including its cheap cost ($\sim$100\$), its high pulsation rates ($>1kHz$), its modularisation and its negation of the need for a fragile optical-fibre pulse distribution network.

3.5.7 Other Peripheral Devices

Several other devices are used as part of normal VERITAS operations. They include:

- Three commercial (Heitronics) far infra-red cameras. Two of the three are mounted directly on the VERITAS telescopes, and observe the sky directly in the telescope's field of few. The third is equipped with a wide angle lens ($\sim$20degrees) and observes the sky overhead. These cameras are sensitive to atmospheric temperature changes and can easily detect the presence of thin

overhead clouds. The data recorded by these cameras are continuously logged and stored in a database and are used in the assessment of VERITAS data quality.

- Eight commercial (Prosilica) CCD cameras, with two equipping each VERITAS telescope. These cameras act as pointing monitors and record an image of the sky in the field of view of the telescopes every two seconds. The star fields recorded in these images are analysed to provide corrections to the recorded telescope pointing directions. These cameras are also used to measure and monitor the optical point-spread-function (PSF) of the VERITAS reflectors.
- A commercial (Campbell Scientific) weather monitoring station. This encompasses ambient temperature and humidity sensors, a rain-gauge and a wind speed and direction sensor. The data recorded by these sensors are continuously logged and stored in a database and are used to determine data quality and safe operational weather conditions. VERITAS does not operate under rain, high humidity (>70%) or high winds (>20km/h).

3.6 VERITAS Calibration

Various parts of the VERITAS hardware (in particular the VERITAS PMTs and the optical reflector) are routinely monitored and calibrated, to ensure stable and consistent operations.

3.6.1 Gain Measurements

The health of the VERITAS PMTs is monitored by short nightly flasher runs and periodic (∼monthly) absolute-gain measurements. The effects of ageing, such as gain drift and photo-cathode degradation, must be measured and adjustments made

to the PMT high voltage to compensate. Relative gain measures the response of a collection of PMTs resulting from their simultaneous illumination by some light source. This quantity is a product of electron conversion efficiency of the photocathode (the quantum efficiency), the electron capture efficiency of the first dynode and the gain multiplication of the chain of subsequent dynodes, called the absolute gain. The absolute gain measures the signal which results from a single photoelectron hitting the first dynode. This gain is a function of the HV value, supplied to the PMTs. Since the QE and electron capture efficiency are difficult to manipulate, variances in these quantities, across a population of PMTs, can be evened out by using a particular HV value for each channel.

Relative Gain Measurements

The processes of equalising the response of a population of PMTs to a flash from some light source is called *flat fielding* and it is performed periodically on the VERITAS cameras. Flat fielding ensures that the PMTs have a narrow spread in relative gain.

The diffuser, which is housed in each VERITAS flasher unit, was chosen to deliver uniformly distributed light across every PMT in a given camera. Therefore, the output pulse from each PMT should be the same for every flash. A $\sim$3 minute flasher run, which illuminates the PMTs with $\sim$6700 8-step flasher intensity ramps, provides enough statistics to perform flat fielding. To do so the signal from every PMT for every flash is aggregated using the mean of a collection of medians to produce a flasher intensity monitor. This combination of the signals from many PMTs ensures this monitor value is unaffected by dead or pathological PMTs or by

the photo-statistical fluctuations in any individual channel. Since the LED flasher is driven in a stepwise ramp, the monitor values inhabit eight, non-overlapping, Gaussian distributions; one for each LED intensity level. Each distribution has a mean and variance, which we label $\mu_{monitor}$ and $\sigma^2_{monitor}$ respectively. Similarly, the values of the signal from each individual PMT, can be grouped into eight non-overlapping Gaussian distributions with the means and variances labelled $\mu_{channel}$ and $\sigma^2_{channel}$ respectively. For each channel we can plot the $\mu_{channel}$ against the $\mu_{monitor}$, the slope of which measures the relative gain for that channel. For a camera which is flat fielded, the value of the slope for every channel is the same, since the signal values from every PMT should be the same when illuminated by the same flash. In the case when the monitor value is determined by some averaging of the signal across the PMT population, the slopes should all have a value of one. Figure 3–24(a) plots the channel signal means against the monitor signal mean for two example channels in the VERITAS telescope 1 camera. The slopes are both equal to $\sim$1. The relative gain distribution for the four VERITAS cameras is plotted in Figure 3–25(a). The RMS is $\sim$3.5%.

Absolute Gain Measurements: photo-statistics

The absolute gain, which is the gain due to the dynode multiplication stages of a PMT, is measured in two independent ways at VERITAS. The first is called the *method of photo-statistics* which works in the following way. After many constant intensity flasher pulses, the mean number of photo-electrons which hit the first dynode of a given PMT is labelled N_{pe}. This value exhibits Poissonian (approximately

Gaussian) fluctuations with a variance of σ_{pe}^2 with

$$\sigma_{pe} \approx \sqrt{N_{pe}}.$$

For a constant flasher monitor value we can say that

$$\mu_{channel} = G_{channel} N_{pe}$$

where $G_{channel}$ is the unknown absolute gain of the PMT. We can also say

$$\sigma_{channel}^2 = G_{channel}^2 \sigma_{pe}^2 + \sigma_0^2$$

where the added σ_0^2 component accounts for noise in the pixel (electronic, NSB etc). Rearrangement of the last three expressions yields

$$\sigma_{channel}^2 = G_{channel} \mu_{channel} + \sigma_0^2 \tag{3.6}$$

This tells us that the value of slope of the plot $\sigma_{channel}^2$ against $\mu_{channel}$ is the absolute gain and the intercept is a measure of the noise, which is independent of the flasher light level. Figure 3–24(b) plots the channel signal variance against the signal mean for two example channels in the VERITAS telescope 1 camera. The absolute gain distribution for the four VERITAS cameras is plotted in Figure 3–25(b).

The expression for the gain in equation 3.6 assumes that the variance in the PMT signal is solely due to fluctuations in N_{pe} and channel noise. A modification is necessary to account for additional fluctuations inherent in multiplication stages of the PMTs itself. The variance caused by these fluctuations can be measured by looking at the signal distribution from a PMT resulting from the multiplication

of a single photo-electron (PE). If the number of photo-electrons to hit the first dynode is always one, then $N_{pe} = 1$ and $\sigma^2_{pe} = 0$, thus any remaining variance in the signal distribution is due to fluctuations in multiplication stages themselves. If the variance in the signal distribution, for a given PMT, in response to bombardment by only single PEs, is $\alpha^2_{channel}$, then the slope from equation 3.6 must be modified to be

$$G_{channel} = \frac{\sigma^2_{channel}}{\mu_{channel}} \left(\frac{1}{1 + \alpha^2_{channel}} \right) \tag{3.7}$$

This correctional factor (in parenthesises) is called the Polya correction [90]. The data plotted in Figure 3–25(b) include this correction. Calculation of α^2, is done in parallel with the second method of absolute gain measurement performed at VERITAS, called *the single photo-electron (PE) method*.

Absolute Gain Measurements: Single PEs

The single PE method involves the analysis of the single PE distribution of every PMT. This is the distribution of the values of the charge resulting from the illumination of a PMT by very faint flashes. The intensity of these flashes is such that the photo-cathode of the PMT will rarely liberate a photo-electron. In practise, these measurements are made by placing a plate with small holes in front of the camera. These holes attenuate flashes from the flasher unit and reduce the NSB contamination in the pixel. A single PE distribution is plotted in Figure 3–26. The majority of values in this distribution result from the case when zero PEs were produced. There are then smaller and smaller contributions to the distribution resulting from one, two, three, etc. PEs being emitted. A fit function for this distribution can be determined given the following observations:

- The probability of liberating a photo-electron is given by Poisson statistics, where λ is the mean number of photo-electrons liberated after every dim flash.
- The distribution of charge values resulting from successive single PEs hitting the first dynode will have mean and variance, labelled δ and α^2 respectively. The value of δ is the absolute gain of the PMT.
- The distribution of charge values resulting from no PEs hitting the first dynode will have mean and variance, labelled η and σ^2 respectively. η and σ^2 measure the mean pedestal and pedestal variance values respectively.

Given the above considerations, the single PE distribution can be fit by the following function:

$$F(q) = N \sum_{j=0}^{k} P(j, \lambda) G(\eta + j\delta, \sigma^2 + j^2\alpha^2, q) \tag{3.8}$$

where N is number of flashes, P is the Poissonian function and G is the Gaussian function. Equation 3.8 consists of k Gaussians, whose means and widths increase and whose normalisations change depending on the Poissonian probability to liberate j photo-electrons, when the mean expected number is λ. The j-th Gaussian is said to fit the distribution resulting from j photo-electrons hitting the 1st dynode. In Figure 3–26 the red Gaussion fits the zero-th peak (the pedestal-like events) while the green Gaussion fits the single PE peak.

From these fits to the single PE distributions, the absolute gain is determined. The $\alpha^2_{channel}$ is also determined, to facilitate the use of the photo-statistics method. The value of λ , also determined, is useful as it tracks the quantum efficiency of the PMTs. The main draw back of the single PE method is that it takes many flashes

to build up a statistically viable distribution. Since calibration time is limited, such gain measurement are made monthly at VERITAS.

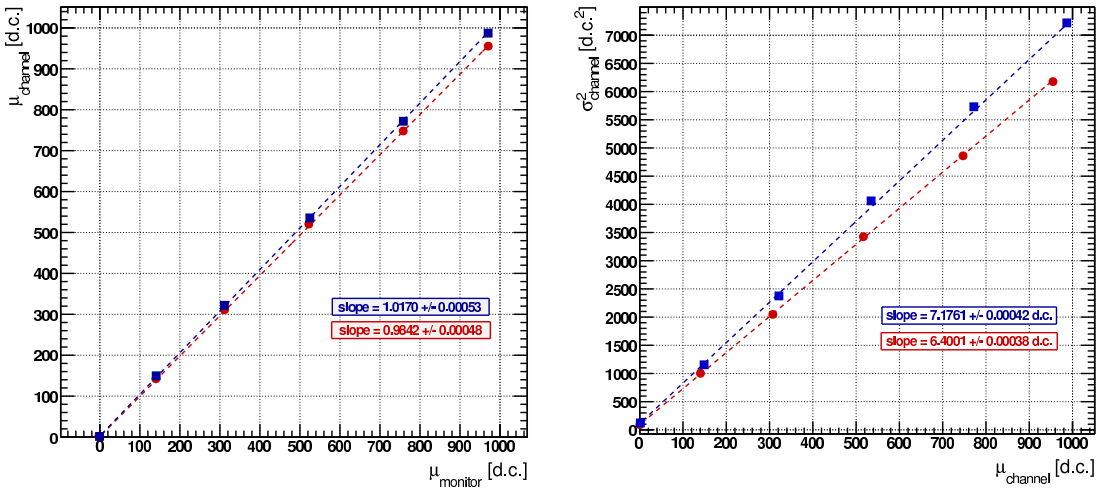

(a) Relative Gain calculation for two channels.

(b) Absolute Gain calculation for two channels.

Figure 3–24: Example plots of $\mu_{channel}$ against $\mu_{monitor}$ and $\sigma^2_{channel}$ against $\mu_{channel}$ for two VERITAS channels. The slopes of the data points in panel (a) represent the relative gain of the channels while the slopes of the data points in panel (b) represent their absolute gain. Each plot contains six data points instead of eight since, in this case, the brightest two LED flashes pushed the FADCs into their low-gain multiplication path.

3.6.2 Optical Alignment

The quality of the alignment of the VERITAS reflector is also regularly monitored; done in parallel with the monthly calibration of the VERITAS pointing monitors. The main cause of alignment degradation is the replacement of mirror facets, following re-coating. Alignment degradation is assessed by optical PSF measurements, and is corrected by the manual adjustment of poorly aligned facets. The

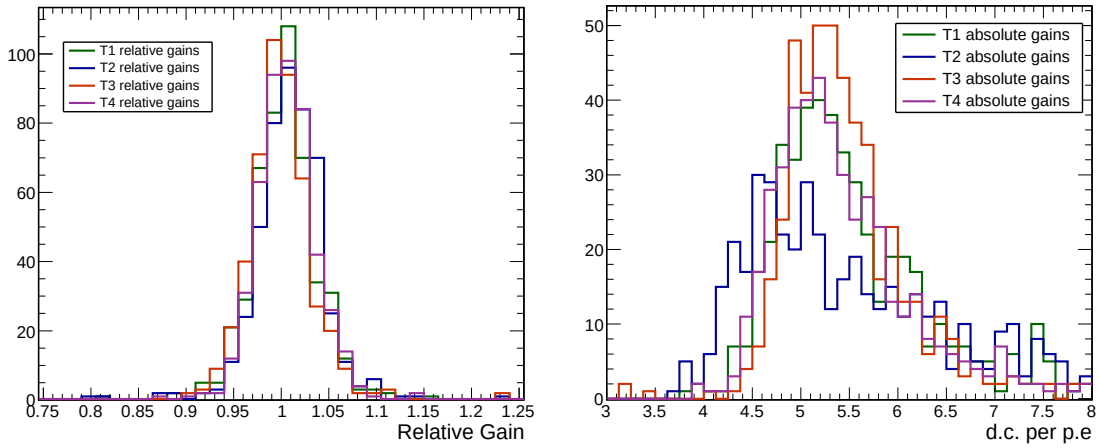

(a) Relative Gain **(b)** Absolute Gain

Figure 3–25: The distribution of the relative and absolute gains determined with the photo-statistics method. The relative gain distributions have an RMS spread of ∼3.5%. These distributions are complied from the slopes of plots like those shown in Figure 3–24.

required facet adjustments are calculated using the *raster scan* method described in [79].

The raster method employs a CCD camera which is positioned at the focal point of the reflector. This camera then acquires a series of images of the facets while the telescope is made to scan a grid of points around a bright star. Facets which are correctly aligned will appear most brightly illuminated in the CCD images when the telescope is directly pointed at the star. Poorly aligned facets will appear most brightly illuminated when the angle between the telescope and the star is twice the misalignment angle of the facet (see Figure 3–27 for a graphical representation of this argument).

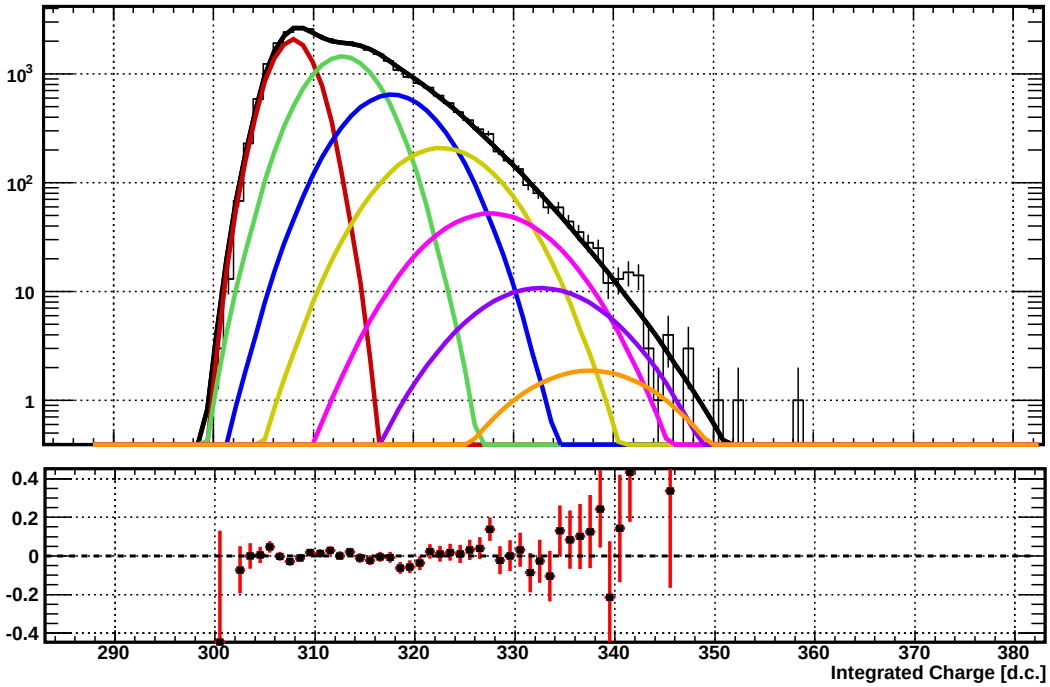

Figure 3–26: Single photo-electron distribution. The upper panel shows the single PE distribution along with the fitted function and its components described in equation 3.8. Each of the coloured Gaussian curves fits the charge distribution formed from a different number of photo-electrons. The lower panel shows the fit residuals.

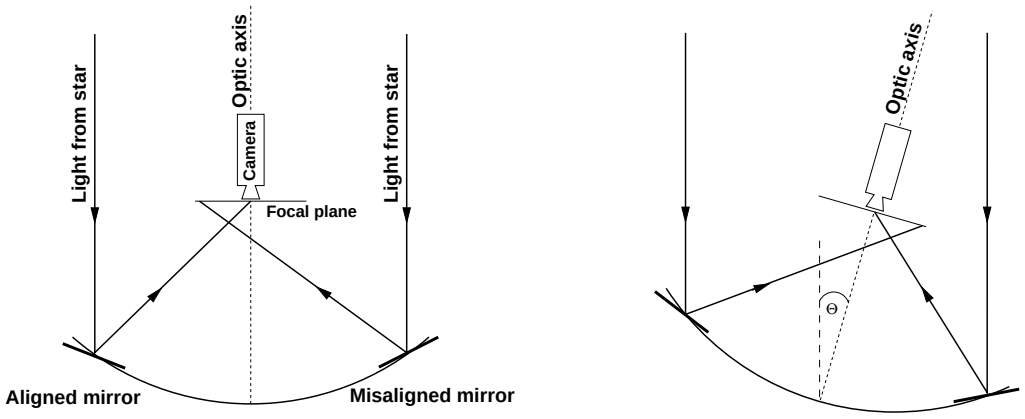

(a) On axis

(b) Off axis

Figure 3–27: An illustration of the raster scan method. In panel (a) the well-aligned facet will appear bright in the CCD-camera image while the mis-aligned facet will be dark. In panel (b) the mis-aligned facet will appear brightest when the angle between the star and the telescope pointing direction, θ, is twice the misalignment angle of the facet (plot taken from [79]).

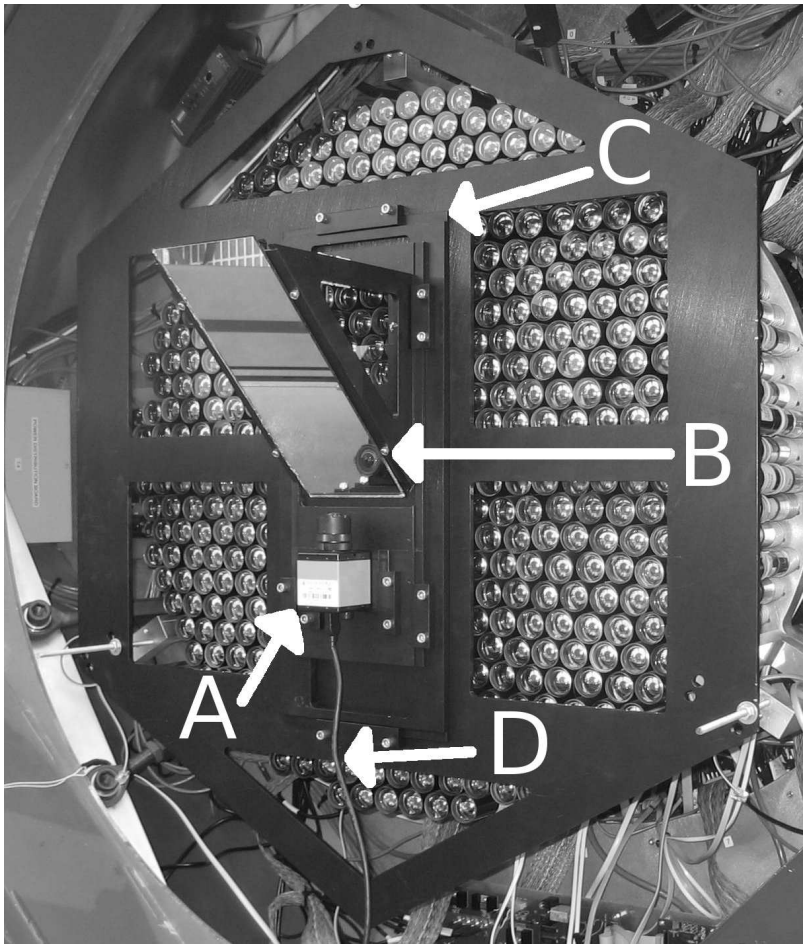

Figure 3–28: A photograph of the raster scan alignment measurement apparatus mounted on one of the VERITAS PMT cameras. Arrow A indicates a digital CCD camera; B, a 45° mirror; C, an x-y positional stage and D a cable connecting to the data acquisition notebook computer (not shown). Image taken from [79].

The apparatus which is used at VERITAS to record the CCD image of the reflector is shown in Figure 3–28. The principal components are a positional stage, upon which is mounted a CCD camera and a plane mirror. This mirror is oriented at a 45° angle to the telescope's optical axis. allowing the CCD camera to be positioned in the focal plan of the reflector, without adjusting the position of the VERITAS PMT camera.

Facet alignment measurements are made by tracking a bright star as it transits at a elevation of ∼70°. This is done so that the misalignment measurements are made while the telescope is pointing in its main operational elevation range and therefore accounts for the gravitational sagging of the OSS. As the telescope tracks, it is made to raster around a grid of angular offsets from the stars' position, with the CCD camera recording an image of the dish at each offset.

Offline, the images are analysed and for each facet a plot of intensity against telescope angular offset is compiled. From each plot, the angular offset of the maximal intensity point is chosen. For each facet, the deviation of its angular offset from the average is calculated and is deemed its mis-alignment angle. Using the deviation from the mean, rather than the actual angular offset for the maximal intensity point, insures that small errors in the positioning of the alignment apparatus are not folded into the alignment corrections.

The adjustments calculated from this analysis are applied to the facet mounts manually. The orientation of the triangular facet mounts are determined by a threaded rod and adjustable nut attached to each vertex. The pitch of the rods

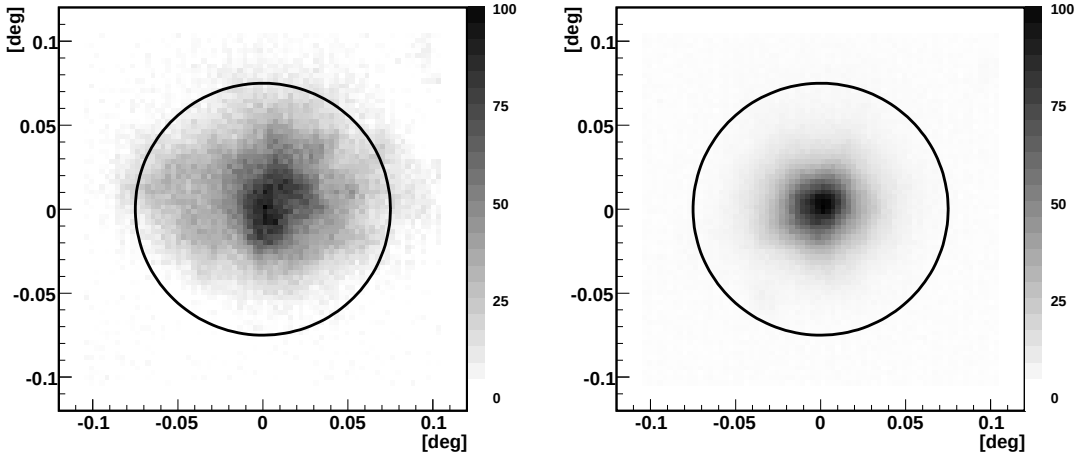

(a) PSF image before

(b) PSF image after

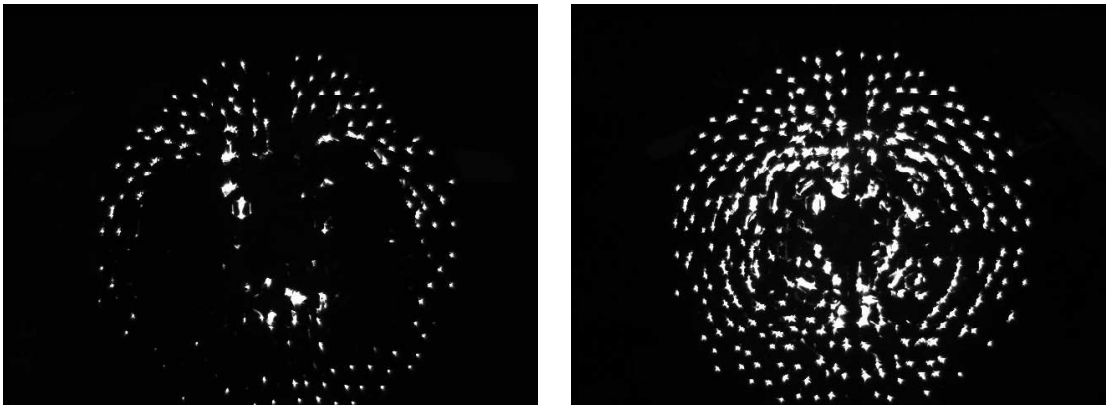

(c) Reflector image before

(d) Reflector image after

Figure 3–29: Panels (a) and (b) show the PSF of one of the VERITAS telescopes measured at ∼70° elevation, before and after the implementation of the raster scan method. The intensity values (grey-scale) are plotted in arbitrary units. The black circle indicates the size of a PMT in a VERITAS camera. PSF images are made by mounting a white screen on the telescope's focal plane and photographing, with a digital camera, the image of a bright star being tracked by the telescope. Panels (c) and (d) show images of the reflector with the telescope pointing close to a star at ∼70° elevation, before and after development of the raster scan alignment method (plot taken from [79]).

and the mirror-mount geometry is such that one full turn on a nut changes the mirror orientation by $\sim 0.1^{\circ}$. Bulk mirror replacement ($\sim$100 facets on one telescope) is performed at VERITAS every few months. Following this the alignment procedure detailed above is performed.

Prior to the development of this method the *bias alignment* method [108] was used. It proved to be less accurate, slower, and more difficult to implement than the raster method. The introduction of the raster method reduced the size of the VERITAS PSF by 30% from the values obtained with the old system. Figure 3–29 displays images of the PSF, for a telescope, before and after the introduction of the raster method. In this figure, before and after images of the reflector, acquired while the telescope was tracking a bright star, are also shown. Qualitative improvement is evident.

The current size of the PSF against star elevation, for one of the VERITAS telescopes, is plotted in Figure 3–30. Mirror alignment is typically done at VERITAS if the 95% containment radius of the PSF is above 0.075° in the operational elevation range.

The following chapter describes the analysis framework and software processing stages employed in unpacking data recorded by the VERITAS hardware.

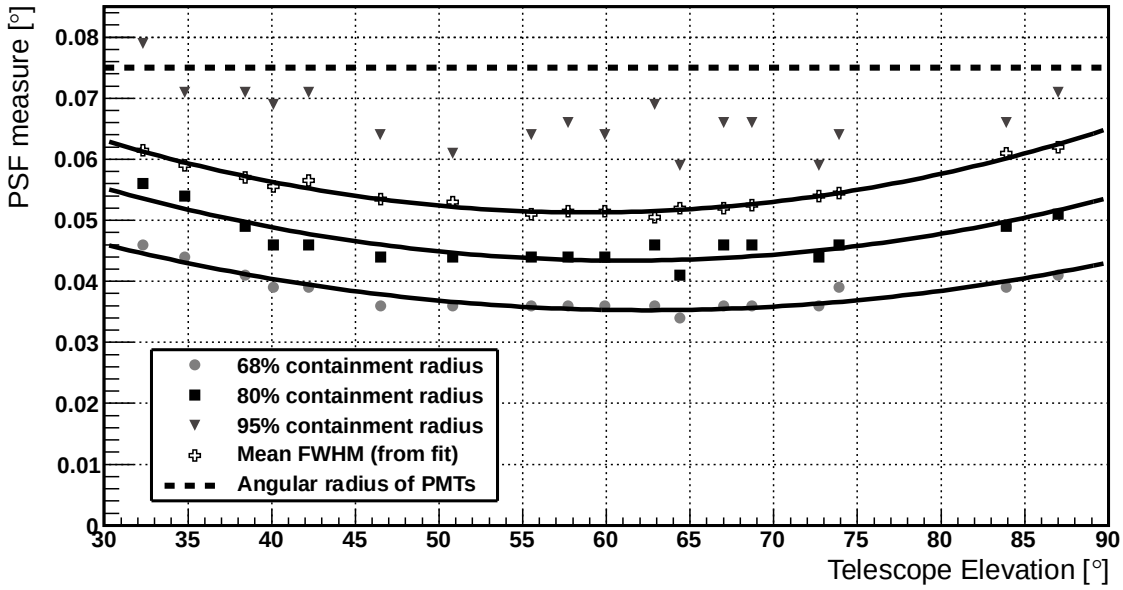

Figure 3–30: Optical point-spread-function sizes plotted versus star elevation. Due to flexing by the OSS, the PSF changes as a function of the telescope elevation. Mirror alignment is performed to ensure that the PSF is a minimum in the principal observation elevation ranges. The PSF is contained within a single pixel throughout.

CHAPTER 4
VERITAS Data Analysis Procedures and Periodicity Testing.

4.1 Introduction

As explained in the previous chapter, the VERITAS data consist of the digitised pulses from the PMTs, along with other quantities such as the GPS clock timestamps and various trigger information. These data are pushed through an analysis pipeline which, among other things, calculates the strength and significance of a gamma-ray signal in the data. The *EventDisplay* software package was used for the analysis of all the VERITAS data presented in this thesis. This is a *C++*-based analysis suite which is built around *ROOT* [91] data structures and routines and was largely written by Dr. Gernot Maier (formerly a McGill R.A. now based at DESY, Zeuthen). The processing of the VERITAS data, briefly, proceeds as follows:

- The pedestal value is calculated for every pixel and then subtracted from the digitised PMT trace values.
- The image in a given camera is *cleaned*. This means that pixels whose pedestal-subtracted sums are above some threshold are retained for further analysis while the remaining pixels have their values set to zero.
- The centroid, major and minor axis, and second moments of the cleaned images in each camera are calculated. These, and other calculated values, are used to parametrise the image.

- The determined parameter values from multiple telescopes are combined and the arrival direction and impact location of the event is reconstructed by intersecting the major axes of the images on the sky or ground planes.
- The calculated parameters of the event are compared to a library of parameters which was compiled from a large set of simulated gamma-ray events. From this comparison, expected parameter values are estimated for a gamma-ray event having the same brightness and impact distance as the measured event.
- Cosmic-ray events are rejected by comparing the measured parameters to the expected parameters for a gamma-ray event determined from the simulation set.
- The arrival directions of the remaining, gamma-ray-like, events are plotted. The number of events which arrive within a region around a gamma-ray source candidate is compared to the number found in regions of the same size which are presumed to have no gamma-ray source (background region). The statistical probability that the number of counts in the source region is consistent with Poisson fluctuations about the number counted in the other regions is then calculated. This *null hypothesis* test is used to determine the statistical probability that a gamma-ray source has been detected.

The following chapter details how each of the above steps is performed in EventDisplay. The chapter concludes with several sections which detail how event time is handled in the context of searching for the periodic emission from pulsars.

4.2 Trace Summation

The first and most fundamental step in the analysis of VERITAS data is the determining of the charge recorded by the PMT pixels. Prior to the analysis of the data events, the pedestal events are analysed, since they measure the charge which a pixel returns in the absence of a Cherenkov event.

First the run is divided into time slices which are typically 3 minutes long. Every pedestal event within this time slice is selected and for every channel a histogram is compiled of the sum, over a certain summation window width, of the pedestal event traces. Such a histogram is plotted in Figure 4–1. From these histograms the mean pedestal value and standard deviation for every channel is calculated. Similar histograms are compiled for every time slice since the noise conditions during a typical observation run may not be constant.

Once the pedestal values have been calculated, the regular triggered events are analysed. EventDisplay sums the FADC traces in two stages. In the first stage, a wide summation window is used (typically 18 samples), to calculate the charge in every pixel in the camera. Along with the charge the *Tzero* point is calculated. This is the point where the trace rises to half its maximum value (see Figure 4–2). A plane is then fit to the *Tzero* time across the event in the camera to measure the time gradient of the event, since the light from the lower part of the extensive air shower reaches the telescope before the light from the upper part. In a second stage, a smaller summation window (typically 7 or 12 samples) is positioned upon every trace in the camera, based on the gradient determined in the first stage. This two-step process, called the *double pass* method, allows the use of smaller summation windows, which

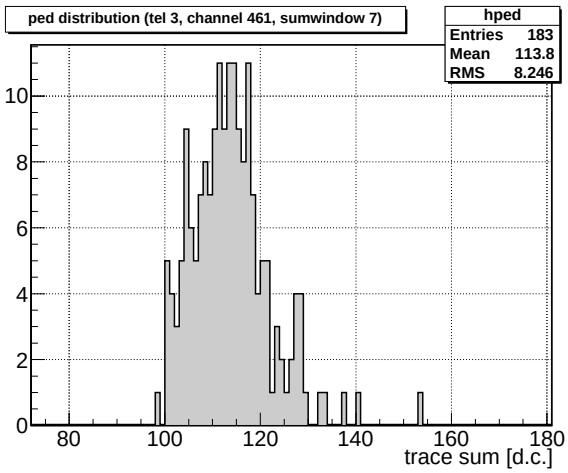

Figure 4–1: Example of the summed pedestal distribution (channel 461, telescope 3, run number 53582). From this histogram it can be seen that summing channel 461 with a summation window 7 samples wide, in the absence of a pulse, results in an average charge of 113.8 digital counts.

provide a good signal-to-noise ratio, while minimising the loss of signal from traces which form early or late in the readout window due to geometric effects. The pedestal mean values are then subtracted from the charge values, resulting in the *pedestal-subtracted charge*. This is the basic pixel signal value which is used throughout the analysis. Charge values resulting from this processing are plotted in Figure 4–3.

4.3 Image cleaning

Image Cleaning is the term used to describe the removal of pixels which are deemed to be unrelated to the Cherenkov image in the camera from further analysis. The signal in these pixels is due to electronic noise or night-sky background photons (see Figure 4–3(d) where it is clear that there are $\sim$50 pixels remaining after pedestal subtraction which are probably not related to the large contiguous signal region in the lower right of the camera). There are several different methods used to identify pixels

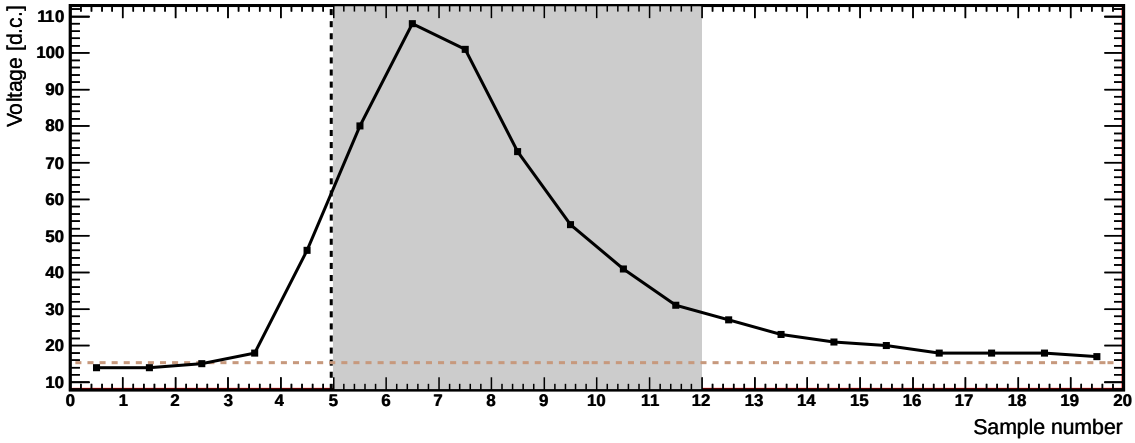

Figure 4–2: Example FADC traces calculated by EventDisplay. The horizontal dashed line represents the level of the pedestal. The vertical dashed line represents the *Tzero* point from where the summation window (grey shading) of seven sample width begins.

which are not associated with the Cherenkov image in the camera. The simplest is *fixed-threshold* cleaning, which removes pixels which have signals below some chosen threshold. This method is simple and has the advantage that the analysis image threshold is constant throughout the data sample. A major disadvantage is that one is forced to use a high threshold so that upward noise fluctuations do not contaminate the images. Another cleaning method bases the pixel signal threshold on the *pedvar*; the standard deviation of pedestal about the mean pedestal for the chosen summation window as determined from pedestal event histograms. In the analysis reported here the cleaning threshold was set to 5 times the pedvar measured for the corresponding time slice and channel. Further, a lower threshold of 2.5 times the pedvar was set to all pixels which had an adjacent pixel meeting the higher threshold requirement. Such a cleaning method is robust against changing noise in the camera, at the expense of having an analysis cleaning threshold which is not constant throughout the data

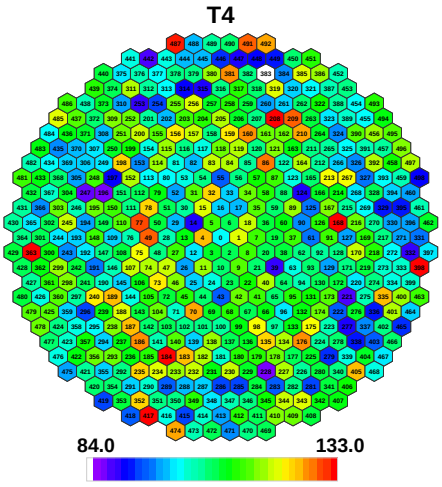

(a) Pedestal Means

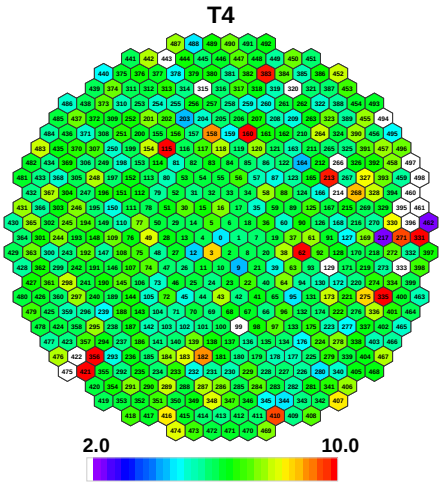

(b) Pedestal Variance

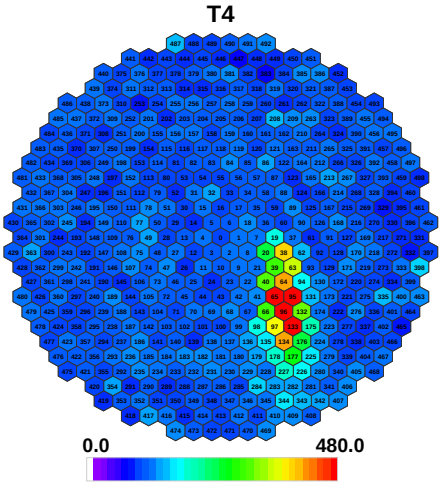

(c) Raw Image

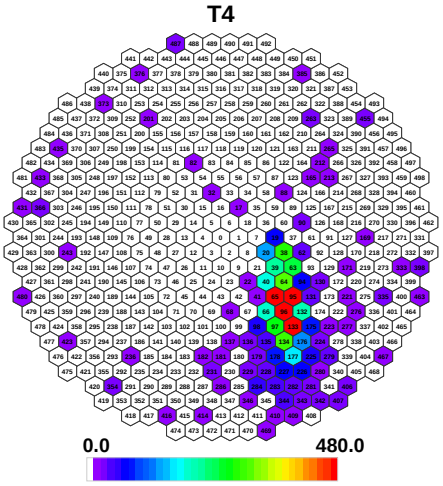

(d) Raw Image after Pedestal Subtraction

Figure 4–3: Panels (a) and (b) plot the mean pedestal value and the standard deviation respectively, for a seven sample summation window and a certain time slice plotted on a camera map. Panel (c) shows the raw sum of the pixel traces for a gamma-ray event, while panel (d) shows the same event after subtraction of the mean pedestal values plotted in panel (a). The colour scale in the above plots is in digital counts.

sample. Some example images post pedestal-subtraction and cleaning are shown in Figure 4–4 (Figure 4–4(d) corresponds to the un-cleaned image plotted in Figure 4–3(d)).

One important impact of cleaning is that it can remove useful information. A major discriminant used to separate gamma-ray images from cosmic-ray images is the uniformity of the image. Images from gamma-ray showers are typically uniform contiguous ellipsoids, while comic-ray showers are less uniform and may contain separate small clumpy structures which look like camera noise. Cleaning tends to remove some of this non-uniform structure, making cosmic-ray images look more like gamma-ray images. Other information, such as the time profile of the structure can be used to help identify if parts of the noise correlate in time with the main image in the camera, or if it is truly uncorrelated camera noise which should be cleaned away (see [97]). The *double pass* summation method described earlier does, in-part, address this issue.

4.4 Image parametrisation

As explained earlier, the shape and uniformity of the images from Cherenkov events is the key discriminant between gamma-ray and cosmic-ray events. The original categorisation and parametrisation of the images resulting from gamma-ray-initiated air showers was performed by Hillas in 1985 [52]. This work, which parametrised the events by calculating the second moments of the image about its major and minor axis, became the basis upon which ground-based gamma-ray astronomy is founded and led to the first ever detection of an astrophysical TeV gamma-ray

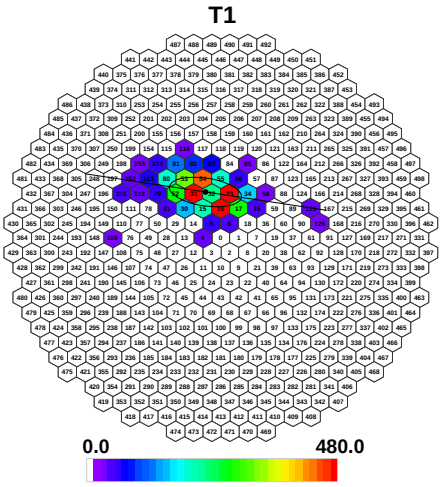

(a) Cleaned Image in T1

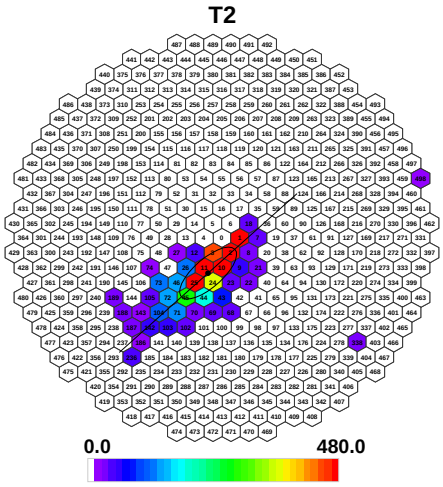

(b) Cleaned Image in T2

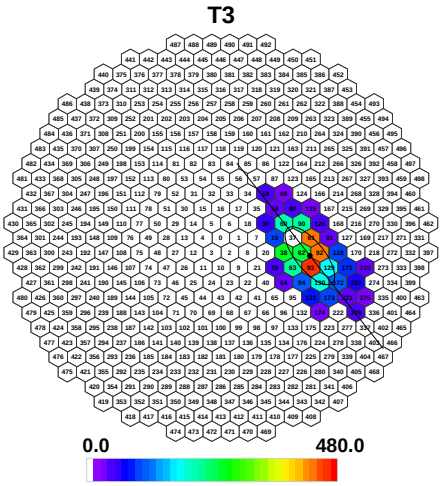

(c) Cleaned Image in T3

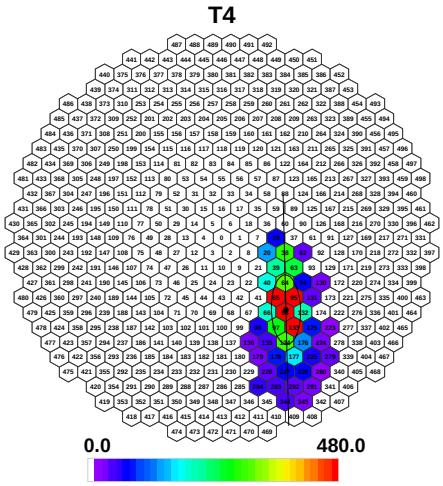

(d) Cleaned Image in T4

Figure 4–4: The images from a four telescope Cherenkov event after pedestal subtraction and image cleaning. The image in panel (d) corresponds to the un-clean image plotted in Figure 4–3(d). Plotted on each image is the centroid and major axis determined from a fitted ellipse.

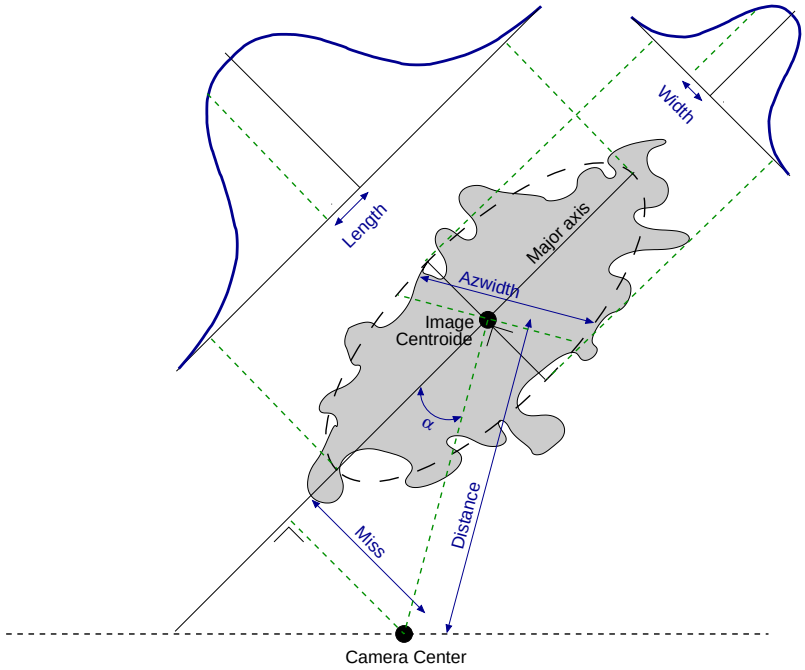

Figure 4–5: Geometrical definition of the original Hillas parameters.

source from the ground [114]. Hillas based his parametrisation on Monte-Carlo simulations of air-shower development and atmospheric Cherenkov production. Images were then formed by ray-tracing the simulated Cherenkov photons through an optical model of the Whipple $10m$ reflector and 37-pixel camera. Hillas originally proposed six parameters, though subsequently many other parameters and composite parameterisations were proposed and are now widely used (see Figure 4–5 , Table 4–1 and Appendix A). Hillas parametrisation provides the ability to measure the gross geometric properties of air showers which, in turn, allows for the separation of gamma-ray events from cosmic-ray events based on an understanding of how the differences between the showers from these events manifest themselves in the distributions of Hillas parameters. Once such difference is evident in Figure 4–6 which shows how

Size	The total pedestal-subtracted charge, in digital counts, in all pixels which form part of the image; a measure of the brightness of the shower.
Frac2*	The fraction of total size in the image which is contained in the two brightest tubes; a measure of the concentration of the image brightness.
Length*	The RMS spread of light along the major axis of the image; a measure of the shape of the image.
Width*	The RMS spread of light along the minor axis of the image; a measure of the shape of the image.
Azwidth*	The RMS spread of light along the perpendicular to the line connecting the image centroid to the centre of the field of view; a measure of the shape and orientation of the image.
Miss*	The perpendicular distance between the major axis of the image and the centre of the field of view; a measure of the orientation of the image.
Distance*	The distance between the image centroid and the centre of the field of view; a measure of the impact parameter of the particle cascade.
Alpha	The angle between the major axis of the image and a line joining the image centroid to the centre of the field of view; a measure of the orientation of the image.
Length/Size	A Measure of the compactness of the image in relation to its total light content; used to eliminate background due to local muons.
Loss	The fraction of the total size in an image which is contained within the outermost pixels in the camera; a measure of image containment.
NTubes	The total number of pixels in the image; used to estimate the quality of the image.

Table 4–1: The original six Hillas Parameters (denoted *) along with some additional parameters which are now commonly used.

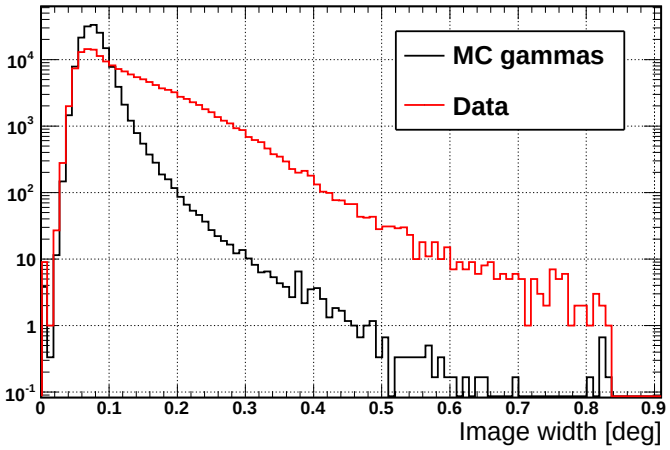

Figure 4–6: The distribution of the Hillas parameter *width* for Monte-Carlo simulated gamma rays and real data, which is dominated by cosmic-ray events. It is clear that gamma rays have a small *width* while cosmic rays have, on average, a larger *width* value. Differences like these are key to the separation of gamma rays from the cosmic-ray background.

the Hillas parameter *width* is distributed for both gamma-ray and cosmic-ray events. As well as providing a mechanism for separating the gamma-ray signal from the cosmic-ray background, Hillas parametrisation aids the reconstruction of the arrival direction and energy of the incident gamma rays. The major axis orientation of the image is an indicator of the gamma-ray's arrival direction and the *size* of the image is an indicator of its energy.

At this point it is convenient to introduce the concept of image *quality* cuts. These are basic criteria required of the image in a telescope which must be met before the telescope data are used in event reconstruction. The quality cuts applied in the analysis presented in this work are; $size > 150$ *d.c.*, $NTubes > 3$ and $Loss < 0.2$. These are markedly less stringent cuts than typically applied in VERITAS

analysis, where the lowest *size* cut value is normally 400 *d.c.*. These cut values were chosen to allow a lower analysis energy threshold.

4.5 Event reconstruction

Event reconstruction is the process of calculating the properties of the incident gamma-ray photons from the measurements made of the extensive air shower by the telescopes. Principally we wish to measure the arrival direction of the photon, the energy of the photon and the core location of the photon (the position on the ground that the photon would have struck if not absorbed by the atmosphere).

The arrival direction and core location are determined from the major axis of the shower image recorded in the camera. Recall that the shower resulting from the gamma ray incident on the atmosphere is long and narrow and that shower major axis is collinear with the incident gamma-ray direction vector. This geometry means that on the image plane, the arrival angle of the shower lies somewhere on the major axis of the shower image (see Figure 4–7). As such, there is a degeneracy in the measurement, since the angle of origin of the gamma ray can lie anywhere on the line[1] . When observations are made stereoscopically (viewing the shower with two or more telescopes) this degeneracy is broken. The arrival angle of the shower can be pinpointed by projecting the multiple images on the same plane and calculating the intersection point of their major axes (see Figure 4–9). The core location of the

[1] In principal, the angular distance between the shower direction and the image centroid, along the major axis, is constrained by the size of the Cherenkov angle. The *disp* method (algorithm 3 in [58]) enables a partial break of this degeneracy based on the eccentricity of the image.

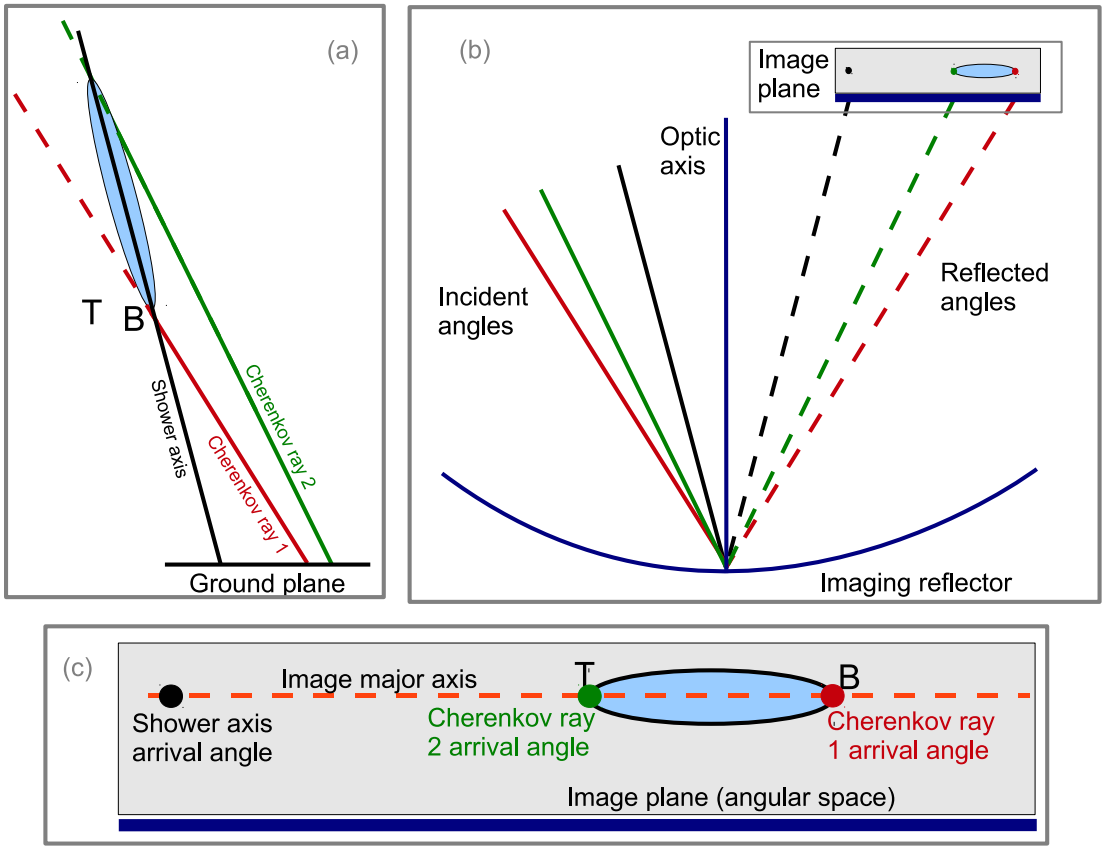

Figure 4–7: Illustration of how the imaging Cherenkov method works. Panel (a) shows the geometry of the shower in the atmosphere. Measured on the ground are the Cherenkov photons. Panel (b) shows how the image of the shower is formed on the focal plane of the telescope. Panel (c) shows a zoomed view of the focal plane image. Geometrically, the shower axis angle is known to lie on the major axis of the image. Figure 4–9 illustrates how, with multiple image of the same shower, the gamma-ray arrival direction can be measured more precisely.

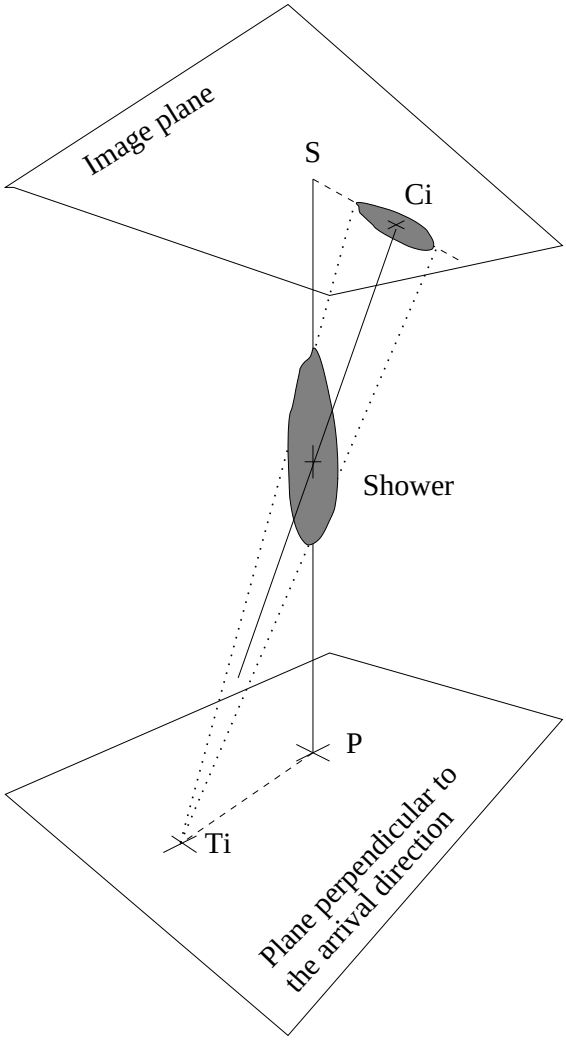

Figure 4–8: Schematic of the projection of the shower onto the image plane. S labels the source location, P labels the core location on the ground, Ti labels the location of the i-th telescope and Ci, labels the centroid of the image seen by Ti on the image plane. The correspondence between the image and ground planes is evident. If the point S and P are calculated, the height of *shower maximum* can determined by a simple trigonometric relation (see Equation 4.1). Figure taken from [69].

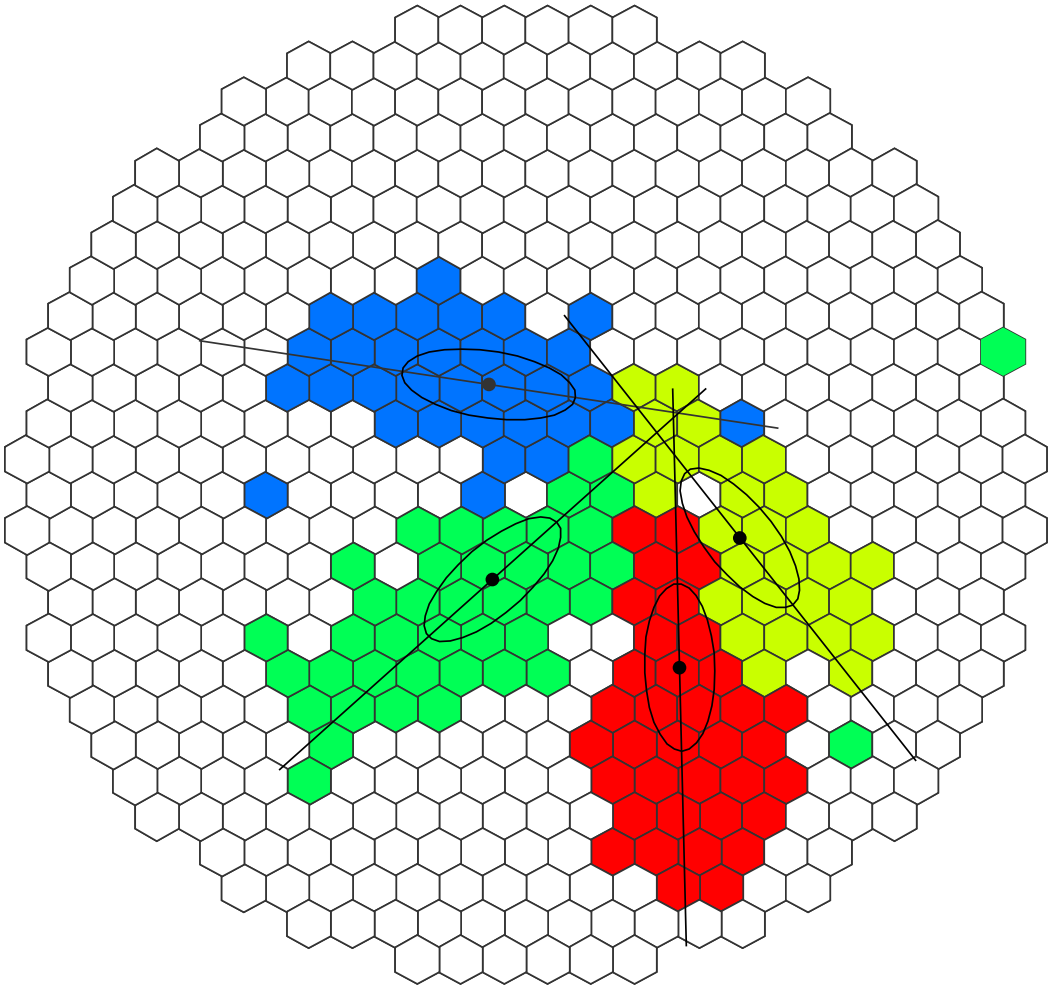

Figure 4–9: Schematic representation of arrival direction reconstruction. Plotted on a single camera map are the locations in the image plane of the images from four telescopes. The point of intersection of the four major axes is the reconstructed arrival direction of the gamma ray.

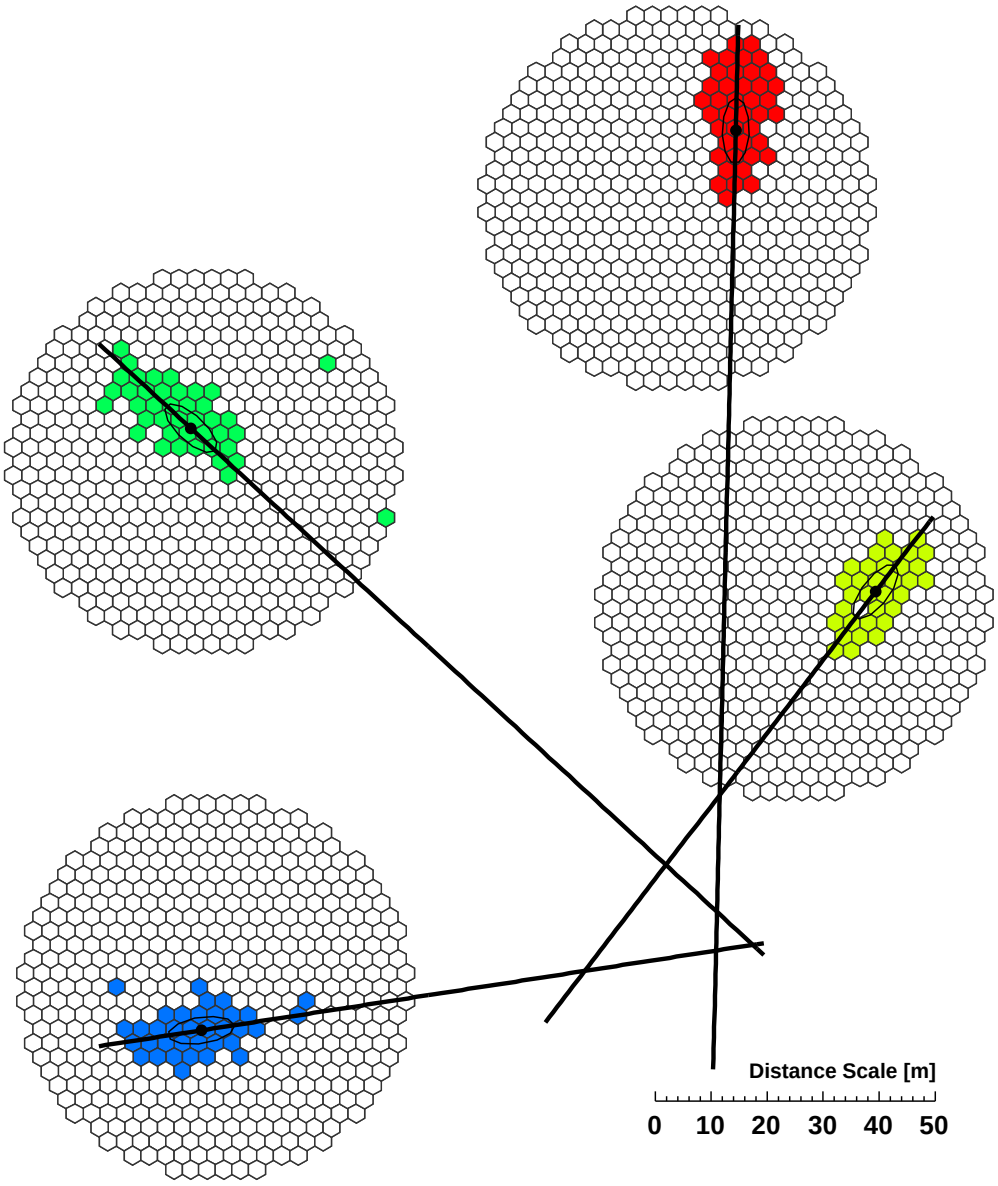

Figure 4–10: Schematic representation of shower core location reconstruction. When plotting the images from the four telescopes on the ground plane, the point of intersection of the four major axes is the reconstructed shower core location. This is the point where the gamma ray would have stuck the Earth if it had not been absorbed in the atmosphere.

shower is calculated in much the same way; by projecting the shower image recorded by each telescope on to the ground plane. The intersection point of the image major axes on this plane indicates the core location (see Figure 4–10). The symmetry between the reconstruction of the shower direction and the shower core location is illustrated in Figure 4–8.

In general, stereoscopic reconstruction of the shower direction and core location reduces to determining the aggregate intersection point between pairs of lines (this is clear in Figure 4–10). Further, when finding the average intersection point, it is sensible to weight the image axis lines by some image quality estimator, such as the image *size* or its eccentricity, since large and eccentric images will have well defined major axis directions. The gamma-ray analysis presented here determines the aggregate intersection point by weighting the intersection point from each pair of lines by the *sine* of the angle between them. This weights lines which intersect at oblique angles above lines which intersect acutely, since two lines which intersect acutely have a larger error in their intersection point. This method was commonly used by the HEGRA Cherenkov telescope array [58].

Following the calculation of the shower core and arrival direction the height of *shower maximum* can be estimated. Shower maximum refers to the point in the development of the air shower which contains the maximum number of Cherenkov emitting particles. This is the brightest point in the shower. The height of *shower maximum* is given by the following equation:

$$H_i = r_i / Tan(\theta_i) \tag{4.1}$$

where r_i is the distance between telescope i and the reconstructed shower core position and θ_i is the angular distance between the image centroid in camera i and the reconstructed arrival direction. This formula is easily derived from the geometrical correspondence between the sky and ground planes plotted in Figure 4–8. The height of shower maximum can be used as a background discriminant since cosmic-ray showers and single muons penetrate deeper into the atmosphere than showers created by gamma rays.

4.6 Energy Estimation

Energy reconstruction is based on the fact that the Cherenkov light yield from an air shower is a good proxy for the energy of the initiating primary. An understanding of how the Cherenkov light yield changes as a function of distance from the shower core and as a function of the arrival angle of the shower enables the conversion of the observed *size* in a camera to an energy estimate of the shower. An understanding such as this may be derived from detailed Monte-Carlo simulations of atmospheric air showers.

Energy estimation in EventDisplay is determined using look-up tables (LUTs) which were filled using Monte-Carlo-simulated gamma-ray showers. Gamma-ray initiated showers are simulated using *CORSIKA* [49]; a powerful and modularised software program which performs detailed simulations of extensive air showers initiated by high energy cosmic-ray particles. The showers are scattered randomly and uniformly over a 750 m-radius region on the ground from random azimuthal directions and from discrete zenith angles; 0°, 20° 30° etc. The simulated gamma rays are

thrown with a power-law energy distribution with a spectral index of -2. The resultant Cherenkov photons are then traced from generation to their impact point on the ground applying an atmospheric transmission efficiency based on the U.S. 1976 standard atmosphere [85] and local radiosonde measurements [32]. The resulting data file contains the arrival direction, impact position and wavelength of each Cherenkov photon along with a tag specifying the type of primary particle which emitted the photon; electron, muon, proton etc.

Following the shower simulation, the resultant optical photons are propagated through a detector model of the VERITAS detector called *GrISUDet*[2] [76]. This model, which simulates the VERITAS optics, electronics and trigger, accounts for;

- the wavelength dependent reflectivity of the VERITAS mirrors
- the optical alignment of the reflector
- the shadowing of the reflector by the quadropod arms and camera housing
- the collection efficiency of the light cones
- the quantum efficiency of the VERITAS photomultiplier tubes
- the efficiency and response of the VERITAS trigger and FADC digitisers

The resulting simulated data are then analysed by the EventDisplay program, with processing proceeding exactly as described for real data. With these simulated data, it is possible to generate LUTs which specify the energy one expects from a gamma-ray shower given the measured *size*, core location and observation zenith angle. Data from a LUT are shown in Figure 4–11 where the median expected shower energy for

[2] see http://www.physics.utah.edu/gammaray/GrISU/

a range of *size* and core location bins, observed at a zenith angle of 20°, is plotted. Further, given that the Level 1 trigger threshold and the image cleaning thresholds depend on the amount of noise in the camera, the above simulation process is repeated for several sky brightnesses ranging from dark extra-galactic sky brightness to moderate moonlight sky brightness. The resulting look-up table set, which is interpolated across each indexing axis, represents a function, F_E, of the form

$$\langle E_i \rangle = F_E(S_i, r_i, Ze_i, Nz_i) \tag{4.2}$$

where $\langle E_i \rangle$ is the energy estimate for the event in the i-th telescope which has a measured *size* S_i, a core distance of r_i, a zenith angle of Ze_i and a pedvar of Nz_i.

Along with building tables which contain the median expected shower energy in each indexing bin, tables containing the standard deviation of the energy distribution in each bin are also built (such a table is plotted in Figure 4–11). This standard deviation value is used to weight the estimated energy value in each telescope when calculating the average energy of the event across the array, E. The following formula is applied

$$E = \frac{\sum_{i=1}^{N} \langle E_i \rangle \langle \sigma_{Ei} \rangle^{-2}}{\sum_{i=1}^{N} \langle \sigma_{Ei} \rangle^{-2}} \tag{4.3}$$

where $\langle \sigma_{Ei} \rangle$ is the standard deviation of the energy distribution used to determine the energy estimate $\langle E_i \rangle$. $\langle \sigma_{Ei} \rangle$ is drawn from a look-up table in the same way as $\langle E_i \rangle$. The averaging in Equation 4.3 favourably weights the energy estimates which come from narrow distributions in the LUT [16].

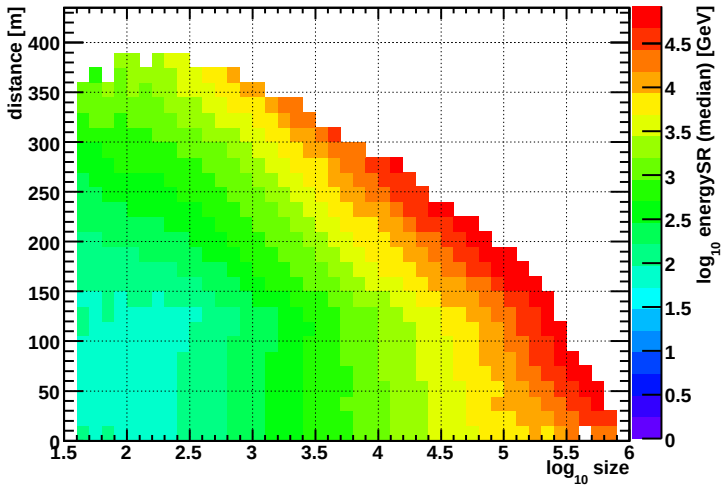

(a) Median expected energy

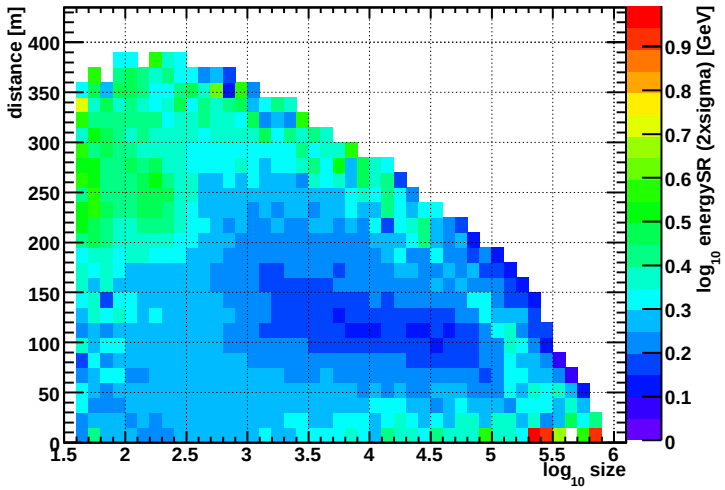

(b) Standard deviation of energy

Figure 4–11: A typical slice in the energy estimate look-up table set. Plotted in panel (a) are the median energies expected for distributions of showers having the values of *size* and core distance plotted on the axes. This slice shows showers which were thrown at a zenith angle of 20° and viewed with a camera *pedvar* level of 5 d.c. Panel (b) shows the corresponding table of standard deviations of the distributions.

4.6.1 Energy Reconstruction Performance

The performance of the energy reconstruction is determined by running the reconstruction algorithm over a second set of simulated shower data. One can then compare the simulated shower energy to the reconstructed energy. This comparison is shown in Figure 4–12, which plots the fractional difference between the reconstructed energy and simulated energy versus energy for two different zenith angles. From this plot the energy resolution can be determined to be ∼60% at 100 GeV, falling to ∼40% for energies above 1 TeV. In this plot, a reconstruction bias is also evident. At 100 GeV, the average reconstructed energy is ∼60% higher than the simulated energy, with the bias dropping to less than 10% for energies above 1 TeV.

This bias is an artifact of the telescope trigger threshold, which reduces the contribution from lower energy showers. When filling the energy LUT, a given *size* bin in the LUT is filled with events which have a higher than average energy, but fluctuate low in their photon yield. It is also filled with events which have a lower than average energy, but fluctuate high in their photon yield. As the telescope trigger threshold is approached, the contribution from upward fluctuating low energy events is diminished, meaning that the bin in LUT has higher than normal median energy. This introduces a bias when reading from the LUT.

It should be noted that the typical quoted energy resolution of VERITAS is 15% with an energy bias <10% for energies above 160 GeV [76]. The difference between the quoted nominal energy reconstruction performance and the case stated here is due entirely to the choice of reconstruction quality cuts used in this analysis. As stated earlier, the quality cuts used here are far less stringent than the nominal

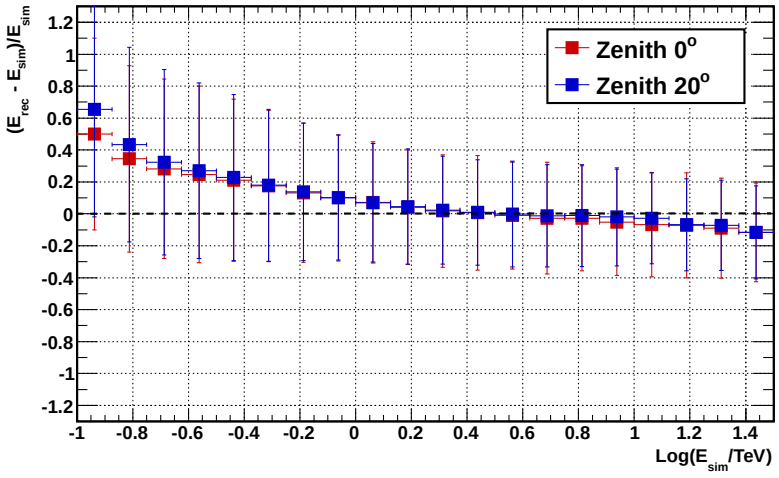

Figure 4–12: A plot of the quality of the energy reconstruction. This is a profile plot of the fractional difference between the reconstructed energy and simulated energy versus energy for two different zenith angles. The error bars represent the RMS of the distribution in each bin which, in turn, is a measure of the energy resolution in each energy range. There is a clear reconstruction bias which ranges from 60% at 100 GeV to less than 10% above 1 TeV. This bias is an artifact of the telescope trigger threshold, which reduces the contribution from lower energy showers when filling the energy LUT.

values used. This choice of quality cuts, while degrading the performance of the reconstruction in general, allows for a greater acceptance of events which are close to the detector energy threshold (see Figure 4–17).

4.7 Gamma-Hadron Separation

At this point in the analysis, all events have been parametrised. The arrival direction and core location have been calculated and an energy estimate has been made for each event. Beyond this point, the main task remaining is the separation of the gamma-ray events from the cosmic-ray background events.

The principal method of separating the gamma-ray events from the huge background of cosmic-ray initiated events starts by calculating the *expected width*, $\langle w \rangle$

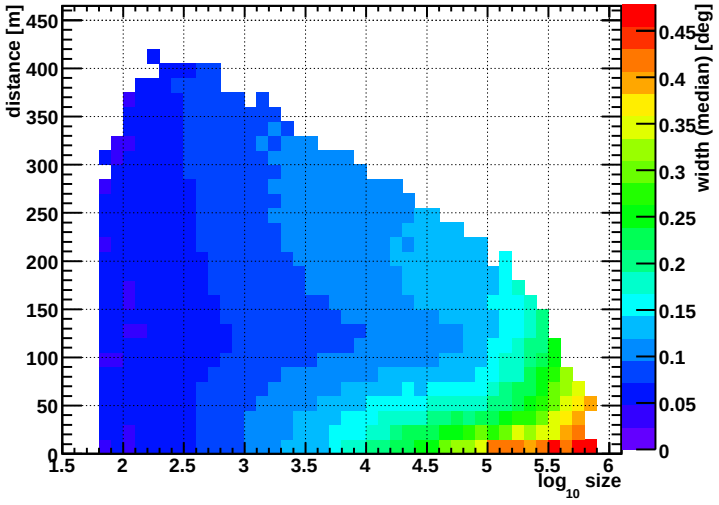

Figure 4–13: A typical slice in the *expected width* look-up table set. Plotted are the median *width* values expected for distributions of showers having the values of *size* and core distance plotted on the axes. This slice shows showers which were thrown at a zenith angle of 20° and viewed with a camera *pedvar* level of 5 d.c.

and *expected length*, $\langle l \rangle$ for each event [65, 33]. The *expected* parameter values are calculated in the same way as the estimated energy was determined in the previous section. For each parameter, a set of LUTs which are indexed by *size*, core distance, zenith angle and *pedvar*, are complied by analysing Monte-Carlo simulated gamma-ray shower data which were passed through the detector model. This results in the equations

$$\begin{aligned} \langle w_i \rangle &= F_w(S_i, r_i, Ze_i, Nz_i) \\ \langle l_i \rangle &= F_l(S_i, r_i, Ze_i, Nz_i) \end{aligned} \tag{4.4}$$

where i, once again, is the telescope's index, and the functions F_w and F_l represent the reading and interpolation of the *expected width* and *expected length* LUTs respectively. The LUT for *expected width* is plotted in Figure 4–13. With these LUTs one can compare, say, the measured *length* in a given camera to the *expected length*.

Since the LUT was filled with data from simulated gamma-ray showers, the *expected length* value and measured *length* value should be similar for gamma-ray events and less similar for cosmic-ray events. This degree of similarity between *expected* and measured values is a powerful discriminant.

Scaled parameters are the measured parameter values divided by the expected value dawn from the LUTs. *Scaled* parameters categorise how similar the measured event is to a distribution of simulated gamma-ray events in the same zenith angle, core distance and noise range. In a similar way as the estimated energy values from each participating telescopes were averaged together to form the array energy estimate the scaled parameters from each telescope are combined to from *mean scaled* parameters. Thus the *mean scaled width* (MSW) and *mean scaled length* (MSL) are defined as follows:

$$\begin{aligned} \text{MSL} &= \frac{1}{N}\sum_{i=1}^{N}\frac{length_i}{\langle l_i\rangle} \\ \text{MSW} &= \frac{1}{N}\sum_{i=1}^{N}\frac{width_i}{\langle w_i\rangle} \end{aligned} \tag{4.5}$$

where N is the number of telescopes with an image passing quality cuts. MSL and MSW are the standard parameters used to discriminate between gamma-ray showers and cosmic ray showers within the field of ground based gamma-ray astronomy. From their definition, it is clear that *mean scaled* parameter distributions peak at the value 1.0 for gamma-ray like events. Figure 4–14 shows the distribution of MSL and MSW for simulated gamma-ray events and real VERITAS data (which are dominated by cosmic rays). Typical cuts on *mean scaled* parameters, coupled with a θ^2 cut (explained in Section 4.8.2), allow the rejection of ∼99% of cosmic-ray events while retaining ∼85% of all gamma-ray events [16].

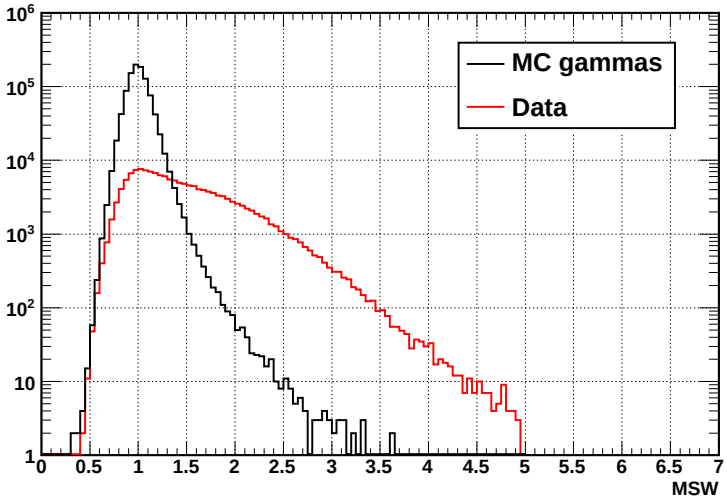

(a) Mean scaled width

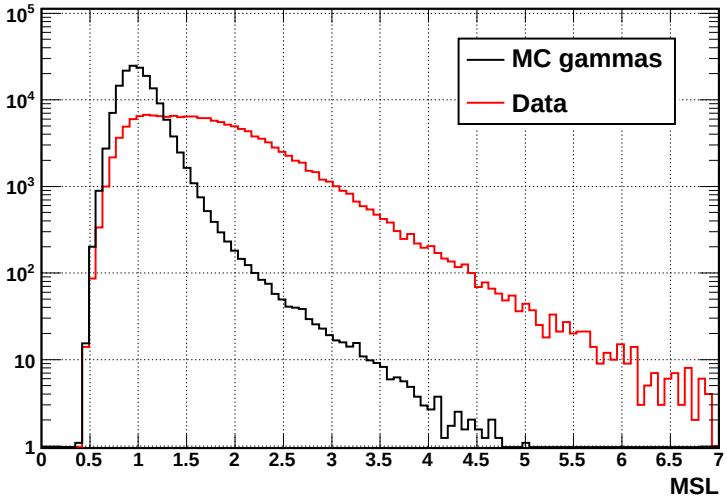

(b) Mean scaled length

Figure 4–14: The distributions of the MSW and MSL parameters for Monte-Carlo simulated gamma rays and real data, which is dominated by cosmic-ray events. It is clear that the scaled parameters provide a powerful discriminant between gamma-ray and cosmic-ray events.

4.8 Signal and Background estimation

At this point in the analysis, the events have been fully reconstructed and the background suppressing parameters, MSW and MSL, have been defined. Before proceeding further, the candidate source and appropriate background regions must be selected from the field of view of the observation.

4.8.1 *Wobble* observation mode

Astronomical observations are typically performed at VERITAS in a mode known as *wobble*-mode (see Figure 4–15). In this mode, the source under observation is not positioned at the centre of the field of view of the telescope, but at a position slightly offset from the centre. The offset size and direction are known as the *wobble* offset and *wobble* direction. This observation strategy allows for the definition of *reflected regions*, which are sections of the field of view which are offset from the centre by the same distance as the source. These regions, which have the same acceptance as the source location, are used to estimate the number of cosmic rays which are present in the source region. In this way, signal and background measurements can be made in the same observing run. Further, the direction of the *wobble* offset is changed in each observation run which means the source will occupy the same region which was used for background estimation in a previous run, thereby removing any possible bias in the acceptance which may be present across the field of view. During observations at VERITAS, the *wobble* offset is typically 0.5° and the *wobble* direction is varied uniformly between North, South, East and West.

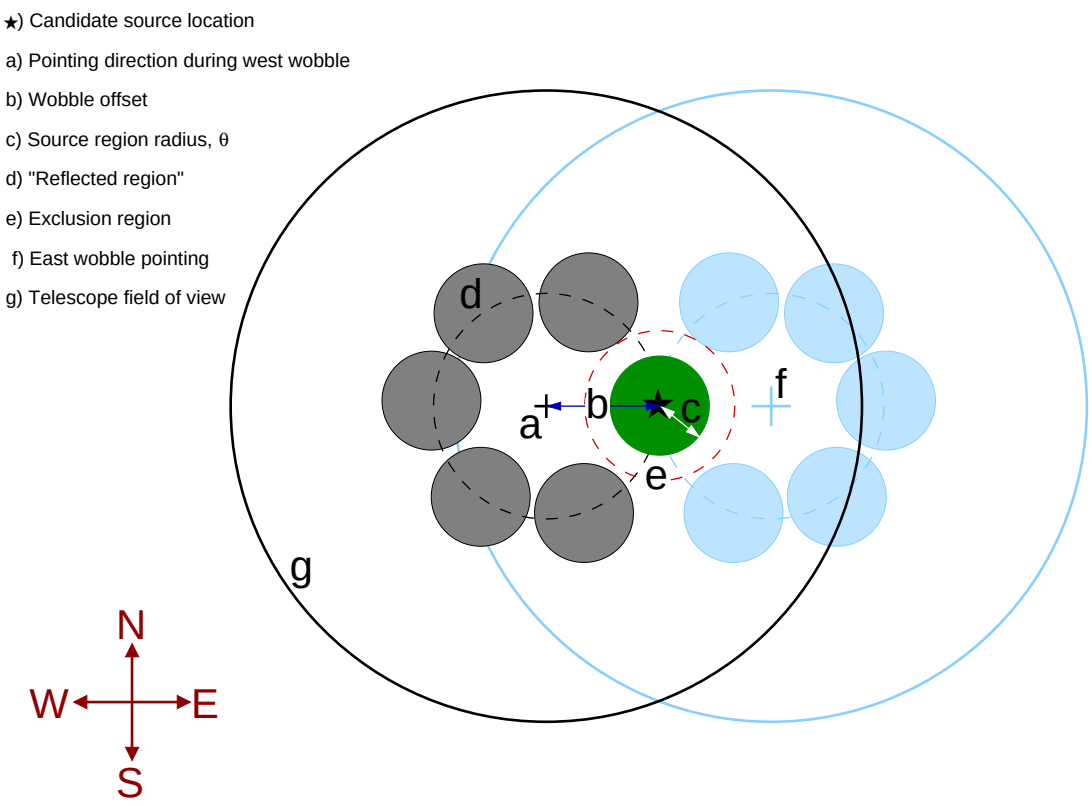

Figure 4–15: Schematic of *wobble*-mode observations. Here the telescope is pointed in a direction which is offset by some fixed angle, called the *wobble* offset, from the candidate gamma-ray source. A circular source region is defined around the source by the radius θ. Identically sized regions, which are similarly offset from the pointing direction, called *reflected regions*, are then defined to measure the background level of cosmic rays expected in the signal region. The direction of the *wobble* offset is changed during each run, to prevent possible biases which may be present across the field of view. The typical *wobble* offset used during VERITAS observations is 0.5° in the North, South, East and West directions.

4.8.2 The θ^2 parameter

In final stages of VERITAS data analysis, the size of the signal region is determined. The parameter θ, which is the angle between the reconstructed event direction and the direction of the candidate source, is defined for this purpose. The maximum allowed squared value of this angle, called the θ^2-cut value, is used for definition of the signal region, commonly called the θ^2-circle or θ^2-region. An event whose θ^2 value is below the θ^2-cut value, is counted as a signal event. Background events are selected if their θ^2 values, computed with respect to the centre of their nearest reflected region, is below the chosen cut value.

A small *exclusion* region is defined around the signal region. This determines the minimal allowed distance between the signal and reflected regions and is used to prevent poorly-reconstructed signal events from populating the background regions.

The size of the θ^2-region is chosen for a particular analysis based on the type of source which is observed and the distance to the source. When analysing extragalactic sources, which will appear point-like in VERITAS data, a tighter θ^2-cut would be chosen compared to the value used to analyse a nearby supernova remnant, which is generally extended beyond the PSF of the instrument. Also, the choice of the θ^2-cut value affects the number of possible reflected regions and thus the level of certainty on the background estimate. The parameter α is defined as the ratio of the area of the signal region to the combined area of the background regions. This parameter is used to scale the number of background counts when calculating the excess number of signal events and its significance.

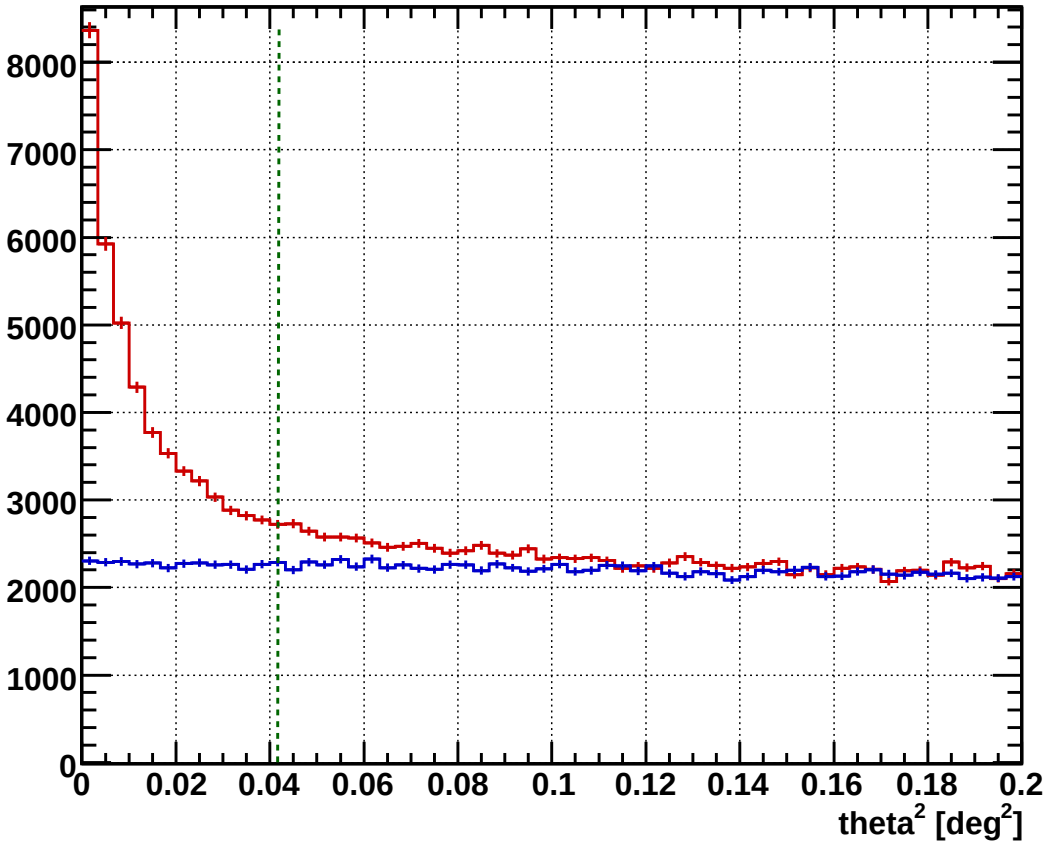

Figure 4–16: The θ^2 distribution for the signal region [red] and background regions [blue] from 16 hours of observations of the Crab Nebula by VERITAS in 2009. The green dashed line denotes the θ^2-cut value which was used in the Crab Pulsar analysis. In the presence of a gamma-ray signal, the source θ^2 distribution is expected to peak at the value zero and taper off with increasing θ^2, indicating that most of the events arrived from the center of the signal region, where the candidate gamma-ray source was located. The background θ^2 distribution should be flat, indicating that events arrived with no preferred direction, from within the background region. The signal excess evident in this plot has a significance of 85 standard deviations.

After the application of cuts on the image *quality* and background suppressing parameters (*size*, MSL, MWL etc) the strength of a gamma-ray signal can be assessed. This is done by plotting the distribution of the θ^2 values within the signal and background regions and scaling the θ^2 distribution from the background regions by the α value. Such a θ^2 plot is shown in Figure 4–16. In the presence of a gamma-ray signal, the source θ^2 distribution is expected to peak at the value zero and taper off with increasing θ^2, indicating that most of the events arrived from the center of the signal region, where the candidate gamma-ray source was located. The background θ^2 distribution should be flat, indicating that events arrived with no preferred direction, from within the background regions.

4.8.3 Significance Calculation

Finally, having chosen the θ^2 cut value the following numbers are calculated:

- N_{On}: The total number of event counts in the signal θ^2 region after the application of all image quality and background suppressing cuts.
- N_{Off}: The total number of event counts in the reflected θ^2 regions after the application of all image quality and background suppressing cuts.
- α: The ratio of the size of the signal θ^2 region to the combined size of all the reflected θ^2 regions.

Using the above determined values the measured excess counts, N_{excess} is determined as

$$N_{excess} = N_{on} - \alpha N_{off}$$

The uncertainty on N_{excess}, ΔN_{excess}, can be determined, using the propagation of uncertainty formula, as

$$\Delta N_{excess} = \sqrt{\Delta N_{on}^2 + \alpha^2 \Delta N_{off}^2}$$

where ΔN_{on} and ΔN_{off} are the errors on signal and background counts respectively. If we assume that these count values exhibit only Poisson fluctuations, then ΔN_{on} and ΔN_{off} are determined by the square root of the count values and thus the above equation becomes

$$\Delta N_{excess} = \sqrt{N_{on} + \alpha^2 N_{off}}$$

The significance of the excess count value is thus

$$\sigma = \frac{N_{excess}}{\Delta N_{excess}} = \frac{N_{on} - \alpha N_{off}}{\sqrt{N_{on} + \alpha^2 N_{off}}} \tag{4.6}$$

It has been shown by Li and Ma [71], that the above formula does not properly account for the uncertainty in the number of background counts. The authors proposed the following log-likelihood test of the null hypothesis, that all counts come from the background distribution. This equation takes the form

$$\sigma = \sqrt{2}\left\{ N_{on} \ln\left[\frac{1+\alpha}{\alpha}\left(\frac{N_{on}}{N_{on}+N_{off}}\right)\right] + N_{off} \ln\left[(1+\alpha)\left(\frac{N_{off}}{N_{on}+N_{off}}\right)\right]\right\}^{\frac{1}{2}} \tag{4.7}$$

This expression is the standard equation used to calculate the significance of measured excesses in the field of ground based gamma-ray astronomy.

4.9 Spectral Reconstruction

If a significant excess of events is found in the signal region it is then possible to examine how the measured energy is distributed throughout this excess. This, in combination with understanding of the telescope's energy response, enable a measurement of the spectral energy distribution of the observed gamma-ray source.

4.9.1 Determination of the Effective Area

The *effective area* of the telescope is a measure of its efficiency for detecting and measuring gamma rays. It is a strong function of all the key observational and analysis parameters such as; zenith angle, *pedvar*, *size* cut, MSL/W cuts etc. It is a convolution of the telescope's hardware trigger response with the analysis reconstruction and gamma-ray selection efficiency.

The effective area is determined using the same Monte-Carlo and detector model framework described in previous sections. As stated earlier, the simulated showers are scattered randomly and uniformly over a region on the ground with a radius of $750m$. The simulated input energy spectrum follows a power law with a spectral index of -2 over the energy range 30 GeV to 250 TeV. Of the 50 million simulated showers which are thrown, typically about 2-3% will trigger the simulated detector and, depending on the specific analysis, 0.5-2% will pass cuts. If the number of events thrown at a given energy is $N(E)$ and the number which finally pass analysis cuts is $S(E)$ then the effective area is defined as

$$A_{eff}(E) = \frac{S(E)}{N(E)} A_{thrown} \tag{4.8}$$

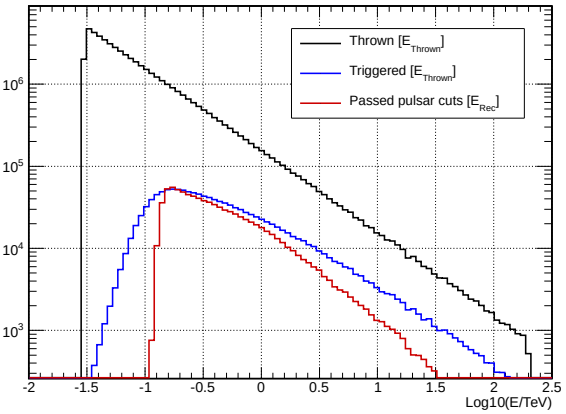

(a) Simulated Event Energy Spectrum

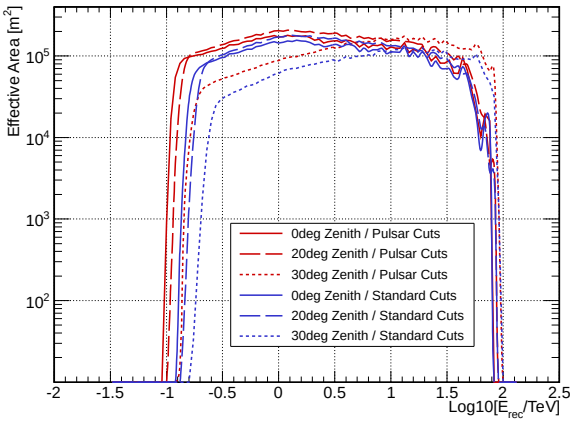

(b) Analysis Level Effective Area

Figure 4–17: The simulated gamma-ray event spectrum at the thrown, triggered and analysis levels and the resultant computed effective area. The upper panel shows the energy spectrum of simulated showers thrown at a zenith angle of 20° which were fed into the GrISUDet detector model and the resulting distribution of energy for the events which trigger the simulated detector. Also plotted in the upper panel is the distribution of energy for the events which passed the analysis-level quality and background suppression cuts. The appearance of an over-abundance of low energy events in this distribution is due to the reconstruction bias discussed in Section 4.6.1. The lower panel, which plots the effective area as a function of energy, was determined by dividing the distribution of energy of events which passed analysis cuts by the distribution of thrown energies and multiplying by the area over which the simulated showers were thrown, as described by Equation 4.8.

Where A_{thrown} is area on the ground over which the simulated showers were thrown; $750^2\pi\, m^2$ or 1.76 million m^2. Equation 4.8 determines the effective area by scaling the thrown area to the selection efficiency at each energy. Figure 4–17 shows the effective area and associated thrown and selected event distributions for a typical observation zenith angle and pedvar level.

4.9.2 Flux Measurement

Using effective areas which match the zenith angle and noise ranges of an observation data sample, which were computed with the same reconstruction and analysis cuts, a differential energy spectrum can be calculated for the source. The differential energy spectrum is the number of detected excess events detected per unit area per unit times per energy interval, or

$$\frac{dF(E)}{dE} = \frac{N_{excess}(E)}{A_{eff}(E)T_{obs}dE} \tag{4.9}$$

where T_{obs} is the dead-time corrected observation time of the data sample and dE is the width of the distribution binning. When combining several observations together, which will in general have different noise and zenith angle ranges, a weighted average rate is computed. The excess in each observation is weighted by the time and area over which the excess was accumulated, such that

$$\frac{dF(E)}{dE} = \frac{\sum_{i=0}^{n} N^i_{excess}(E)}{\sum_{i=0}^{n} A^i_{eff}(E)T^i_{obs}dE} \tag{4.10}$$

where i indexes the n observation runs.

One further complication is that the effective area is, in fact, dependent on the shape of the differential energy spectrum we are trying to measure. Recall, that the effective area was measured from simulated data which has a power law spectrum with an index of -2. The bias in the energy reconstruction will change the shape of the effective area, depending on the shape of the simulated spectrum. This interdependence is solved by iterating over the above equation. At each step the measured energy spectrum is used to correctly weight the effective area in the next iteration until the input and output spectral indices converge [11, 15]. This assumes the spectral shape can be adequately described by a power law, which is typically a valid assumption. Convergence usually occurs after 1 or 2 iterations.

4.10 Introduction to Periodic Analysis

Described in this chapter, so far, are the steps involved in a typical VERITAS data analysis; significantly detecting an excess from the direction of a candidate gamma-ray source and measuring its gamma-ray flux as a function of energy. Beyond this, and depending on the statistical strength of the detection, it is possible search for other features present in the data. In data from galactic observations, source angular extensions and morphologies are commonly investigated [12, 6]. Flux variability, which, for example can occur in blazars from month to minute time scales [10, 7], is also routinely probed. Some galactic sources are known, from measurements at other wavelengths, to yield emission which is periodic in nature. Searches for the signature of this periodic emission can be performed on the gamma-ray data from these objects [13, 9]. The remaining sections of this chapter discuss the methodology

for searching for periodic emission from known pulsars. In this process, each photon arrival time at the observatory is tagged with the corresponding pulsar phase value.

4.11 Barycentering

Barycentering is the process of converting the arrival time of a photon measured at the observatory to the arrival time of a photon created at the same instant, but detected at the solar system barycenter (SSB); the centre of mass of the solar system. This is done to remove the rotational and orbital motion of the Earth around the sun from any periodic signal which may be inherent in the source.

4.11.1 Barycentric Dynamical Time

The barycentering conversion starts with the calculation of Barycentric Dynamical Time (TDB); the independent time variable in the equations of motion of the bodies in the solar system with respect to the SSB [107]. TDB is the most convenient time system to use when describing the solar system orbital motion and is defined as follows:

$$\text{TDB} = \text{UTC} + \text{LS} + 32.184 + 0.001658\sin(M) + 0.000014\sin(2M) \ \ [\text{seconds}]$$

where

$$M = 6.24008 + 0.01720197(\text{JD} - 2451545) \ \ [\text{radians}]$$

The quantities in the above equations are

- **Coordinated Universal Time (UTC)** The time standard most commonly used on the Earth, and the time which is used to tag the arrival of events at the observatory by the GPS clocks.

- **Leap Seconds (LS)** Leap seconds are one second corrections which are occasionally applied to UTC to account for the slowing of the Earth's rotation. This correction ensures that the average time of noon and midnight over a year is the same time from year to year. These corrections are applied on the 1st of January or the 1st of July of any required year, where their requirement is determined by the International Earth Rotation and Reference Systems Service[3] .
- **32.184** An offset in seconds needed to maintain consistency with past timing conventions.
- **The Earth's Orbit's Mean Anomaly (M)** The ratio of the time since the last periapsis (point of closest approach) of the Earth's orbit, to the duration of the orbital period, times 2π.
- **Julian Date (JD)** UTC expressed in Julian Date; Number of elapsed days since noon in Greenwich, London, January 1, 4713 BC.

4.11.2 Time of Flight Correction

After the conversion to TDB a time of flight correction must be applied to convert the time recorded on the Earth, to the time at the SSB. This is done in two steps; correcting the arrival time of photons at the Earth's Center to the SSB, and then correcting arrival times at the observatory on the Earth's surface to the Earth's centre.

[3] http://www.iers.org/

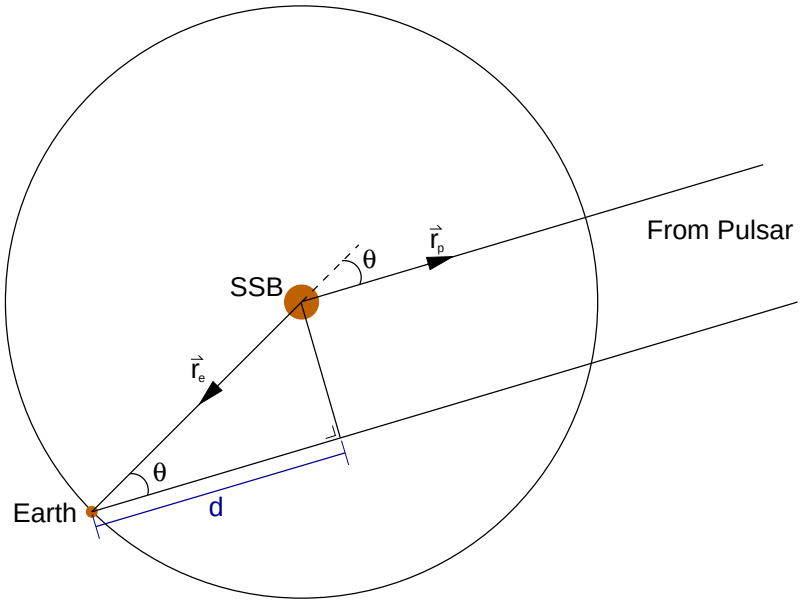

Figure 4–18: Vector diagram for computing the time of flight correction from the Earth's centre to the SSB.

Converting the time from the Earth's center to SSB first requires calculation of the path length difference of the two photons, d, which is

$$d = |\vec{r_e}|cos(\theta) \quad , \quad \cos(\theta) = \frac{\vec{r_e} \cdot \vec{r_p}}{|\vec{r_e}||\vec{r_p}|}$$

where $\vec{r_e}$ is the Earth's positional vector and $\vec{r_p}$ pulsar's positional vector with respect to the SSB and θ is the angle between them (see Figure 4–18). Dividing the path length difference by the speed of light yields the timing correction, thus

$$\Delta t_{EC-SSB} = \frac{d}{c} = \frac{\vec{r_e} \cdot \frac{\vec{r_p}}{|\vec{r_p}|}}{c} \quad , \quad \frac{\vec{r_p}}{|\vec{r_p}|} = (\cos(\alpha)\cos(\delta), \sin(\alpha)\cos(\delta), \sin(\delta))$$

where c is the speed of light and α and δ are the right-ascension and declination of the source respectively. The Earth's position vector $\vec{r_e}$ is obtained from the DE200

Planetary and Lunar Ephemeris published by the Jet Propulsion Laboratory [101, 102], which catalogues the positions of the planets, moons, and major asteroids in the Solar system.

The observatory to Earth's center correction is analogous to the previous correction. The path length difference, d, in this case is given by

$$d = R\sin(A)$$

where R is the radius of the Earth at the point where the observation is made, and A is the angle of elevation of the source at the time of observation. The resulting time of flight correction is

$$\Delta t_{Ob-EC} = \frac{d}{c} = \frac{R\sin(A)}{c}$$

One other possible correction, the Shapiro delay, caused by the curvature of space-time by the gravitational field of the Sun is not calculated. The maximal Shapiro delay occurs when the positions of the Earth, the Sun and observed source coincide in a straight line. Such a configuration is only possible during daylight observations, which are never performed by ground-based gamma-ray instruments. At night, the Shapiro delay is never larger than $7\,\mu$s, which is below the accuracy achieved by the other corrections.

Combining all the corrections above completes the barycentering processes, thus, the time of arrival of a photon at the SSB expressed in TDB, t_b, is given by

$$\begin{aligned} t_b = UTC &+ LS + 32.184 \\ &+ 0.001658\sin(M) + 0.000014\sin(2M) \\ &+ \Delta t_{EC-SSB} + \Delta t_{Ob-EC} \end{aligned}$$

The above corrections are readily performed by free software packages, such as *TEMPO*[4] . In this analysis, a custom-developed software package called *VBARY* was used.

4.12 Phase Folding

Pulsar timing solutions represent a measurement of the rotational frequency of a pulsar along with its first derivative, and sometimes second derivative, at some epoch. Timing solutions allow for the calculation of the pulsar's phase, ϕ, for any time over which the timing solution is considered valid, where the validity is determined by the accuracy of the timing solution and stability of the pulsar's rotational motion. This calculation, called phase folding, tags the measured time of arrival of the photon with the phase of the pulsar's rotation at the time when the photon was emitted. Phase folding is done in the following way. Assuming that the rate of deceleration of the pulsar is constant ($\ddot{\omega} = 0$), the angular frequency at anytime, t, is given by

$$\omega(t) = \omega_0 + \dot{\omega}t$$

[4] http://www.atnf.csiro.au/people/pulsar/tempo/

The angular frequency is defined as

$$\begin{aligned} \omega(t) &= \frac{d}{dt} angle(t) \\ \Rightarrow angle(T) &= \int_{t_0}^{T} \omega(t) dt \\ &= \int_{t_0}^{T} \omega_0 dt + \int_{t_o}^{T} \dot{\omega} t dt \\ &= \omega_0 (T - t_0) + \frac{1}{2} \dot{\omega} (T - t_0)^2 \end{aligned}$$

The phase of the rotation at time T, with respect to some epoch t_0, (both in TDB) is defined as

$$\phi(T) = angle(T - t_0) \, mod \, 2\pi$$

$$\begin{aligned} \Rightarrow \phi(T) &= (\omega_0 (T - t_0) + \frac{1}{2} \dot{\omega} (T - t_0)^2) \, mod \, 2\pi \\ &= (2\pi f_0 (T - t_0) + \frac{1}{2} 2\pi \dot{f} (T - t_0)^2) \, mod \, 2\pi \\ &= (f_0 (T - t_0) + \frac{1}{2} \dot{f} (T - t_0)^2) \, mod \, 1 \end{aligned}$$

where f_0 is the pulsar's frequency and $\dot{f}$ is its first derivative. Monthly timing solutions for the Crab Pulsar, which provide a measurement of f_0 and $\dot{f}$ on the 15th day of each month, are provided by the Jodrell Bank Observatory[5] [73] and were used to phase-fold all of the gamma-ray data used in this work.

[5] ftp://ftp.jb.man.ac.uk/pub/psr/crab/crab2.txt

4.13 Periodic analysis

Once the phase values are calculated they can be examined for a deviation from uniformity. A deviation from uniformity is expected in the presence of pulsar emission, since the nature of a pulsar is that its level of detected emission increases during particular phases.

4.13.1 Binned Analysis

A common approach to searching for periodicity is to bin the phase values in a histogram, which when dealing with pulsars is called a *lightcurve* or *phasogram*. A flat lightcurve indicates that no pulsed emission is present. χ^2 tests against a flat prior can be used to test for uniformity and determine the probability that emission from the pulsar is present in the data. A significant drawback here is that the χ^2 test value is dependent on the number of bins. The appearance of a weak signal in the data is strongly dependent on the number of bins and the exact bin positions. A weak signal, if spread across several bins, can appear consistent with statistical fluctuations. Similarly, grouping background events together with the signal, by choosing a wide binning will also suppress the appearance of the excess. Thus, when dealing with weak signals, binned analysis can easily underestimate the presence of a periodic signal. Repeating the test with several binnings is also undesirable, since the significance of any excess will be reduced with every test against the null prior.

4.13.2 Unbinned Analysis

With prior knowledge of the emission phases, signal and background phase regions can be chosen. The number of events which fall within the signal phase ranges, N_{on}, can be compared against the number which fall within the background phase

ranges, N_{off}, and the significance of any excess can be calculated using Equation 4.7. In this instance, α is the ratio of the size of the signal phase region to the size of the background regions. This is the natural test if the phases of emission are known. However, it is clear that this test is not suitable without prior knowledge of the phase of emission and further, cannot test the significance of an excess which may appear in an unexpected phase region.

4.13.3 H-Test

The *H-Test* [36] was designed specifically to test for weak periodic signals where the light-curve shape is unknown. The *H-Test* builds upon the Z^2_m-*Test* [24], providing a deterministic and optimal way to choose m. The Z^2_m-*Test* tests for periodicity by summing the power of the first m harmonics of a Fourier decomposition of the phase data. Thus

$$Z^2_m = \frac{2}{n}\sum_{k=1}^{m}\left[\left(\sum_{j=1}^{n}\cos(2\pi k\phi_j)\right)^2 + \left(\sum_{j=1}^{n}\sin(2\pi k\phi_j)\right)^2\right] \tag{4.11}$$

where there are n measurement of the pulsar phase ϕ_j. The term in the large square brackets is the power in the k-th Fourier component of the decomposition. It has been shown [48], that the minimal error when representing a distribution by a truncated Fourier decomposition can be determined from the distribution sample itself (in this case the measured phases). The *H-Test* thus evaluates the Z^2_m value at the mode where this error is minimal, which reduces to the formula

$$H = \max_{1<m<\infty}(Z^2_m - 4m + 4) \tag{4.12}$$

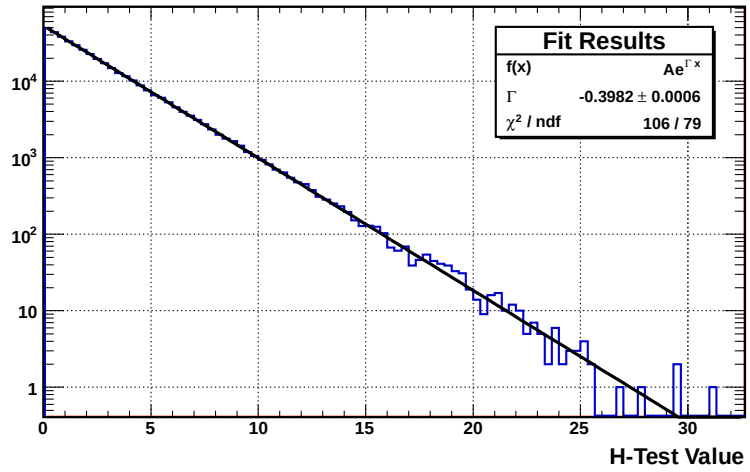

Figure 4–19: Results of a Monte-Carlo simulation, where 400,000 Monte-Carlo data sets, each comprising 300,000 random phase values, were analysed with the *H-Test*. The distribution of *H-Test* values is plotted and fit with the expected functional form shown in Equation 4.14. The results confirm the validity of this equation.

The authors suggest that for all practical purposes, one need not search beyond 20 modes, and thus the *H-Test* is defined as

$$H = \max_{1<m<20}(Z_m^2 - 4m + 4) \tag{4.13}$$

Through Monte-Carlo simulation it was determined that the probability of finding a *H-Test* value H, above some value h is

$$P(H > h) = exp(-0.398h) \tag{4.14}$$

The validity of this equation was tested with 400,000 Monte-Carlo data sets, each comprising 300,000 random phase values, where 300,000 is of the order of the number of real pulsar phase measurements recorded in this work. The result of this test is plotted in Figure 4–19, showing that the equation is valid.

4.14 Conclusion

This chapter has presented the stages involved in the analysis of VERITAS data; from summation of the raw trace values to the calculation of differential energy spectra. It also detailed the particular steps necessary to search for pulsed emission and presented tests to quantify the significance of any pulsed signal present in a data sample. The following chapter will describe a particular observational campaign of the Crab Pulsar and the results of a pulsed emission search.

CHAPTER 5
Data and Analysis Results

5.1 Introduction

The VERITAS data presented in this chapter were accumulated between September 2007 and February 2011. The Crab Nebula is routinely observed in the fall and winter months with the data being used for a range of purposes. Since the nebula is a strong, steady TeV gamma-ray source, data on the nebula are commonly used for Monte Carlo validation, cut optimisation and technical studies. The data presented here represent the highest quality subset of the complete sample. This selection was based on the following criteria:

- Four telescopes must participate. Data were excluded where one or more telescope were not operational due to technical problems or routine maintenance.
- Weather conditions at the site must be A or B grade. The weather assessment is based on data from three far infra-red cameras which measure the atmospheric temperature. Passing clouds lead to variability in the sky temperature. A and B grades are given when the RMS spread of the temperature about the mean run temperature is less than 0.1° or 0.3°, respectively.
- The zenith angle of the observations is less than 25°. This ensures that the observations are made with the lowest possible trigger threshold.
- No anomalies are present in trigger rates or event distributions.

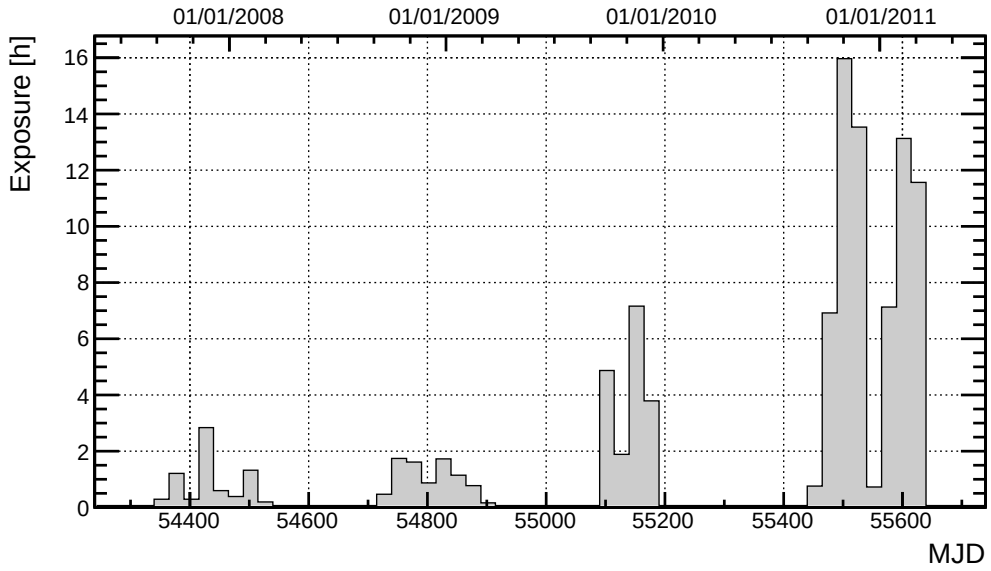

Figure 5–1: The VERITAS exposure duration on the Crab region plotted against observation date. Hints of a pulsed signal in the 2009-2010 data prompted deep observations in the 2010-2011 season.

This selection resulted in a data sample with 103 hours of exposure. Figure 5–1 plots the distribution of this exposure against the date of observation. The analysis presented in this chapter is based on the data accumulated in these 103 hours which, after cuts, resulted in 282092 candidate events from the direction of the Crab Pulsar. Section 5.2 describes the process of determining the analysis cuts used in this work.

Also presented in this chapter is an analysis of *Fermi*-LAT data. The Crab Pulsar phasograms presented were produced from the publicly available *Fermi*-LAT data. High quality photon events (diffuse class) from a 2° radius around the location of the Crab measured between 2008/05/12 and 2010/05/12 with energies above 300 MeV were used to produce the presented phasograms and the sky map plotted in Figure 5–2. This data sample comprises 9282 gamma-ray events. The phase-averaged

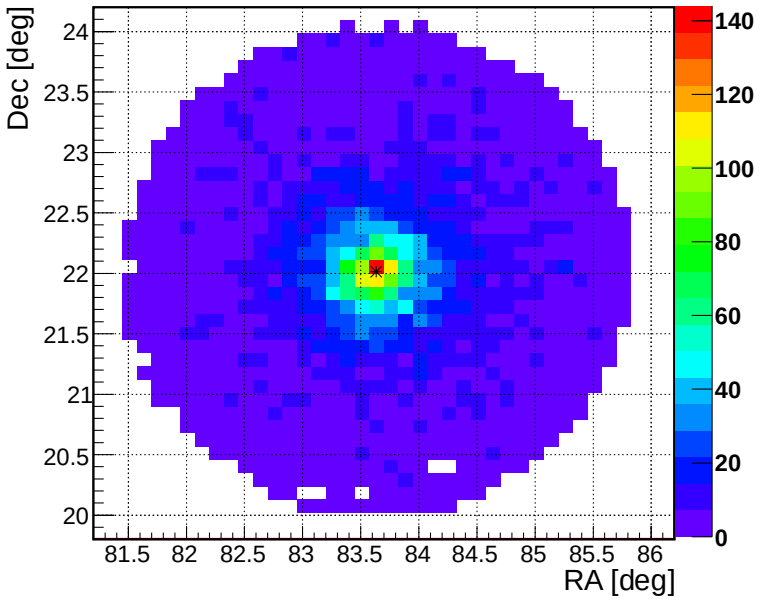

Figure 5–2: Arrival direction of the 9282 gamma-ray events from the *Fermi*-LAT used in this analysis. These events were selected from the high quality photon events (diffuse class) from a 2°-radius region around the location of the Crab measured between 2008/05/12 and 2010/05/12 with energies above 300 MeV. The marker, ✳, indicates the location of the Crab Pulsar.

pulsar spectrum presented was obtained from the authors of the *Fermi*-LAT Crab publication [3].

5.2 Cut Selection

The cuts used in the analysis of both the Crab Nebula and Pulsar are shown in Table 5–1. These cuts were determined by optimising on a pulsed signal which was seen in the VERITAS phasogram after 16 hours of Crab exposure in the 2009-2010 observing season. Originally, a cut optimisation strategy was adopted which mixed simulated gamma-ray data with real VERITAS Crab data. The simulated events were thrown with a power-law energy spectrum with an index of -3.8 and a strength

of 3% of the Crab Nebula above 100 GeV. A signal such as this was assumed for the Crab Pulsar based on the, at the time, newly released *Fermi*-LAT data. These data, combined with an excess above the cut-off energy detailed in an unpublished PhD Thesis from the MAGIC Collaboration, provided evidence for a power-law-type spectrum between 25 and 100 GeV [93]. Using simulated gamma rays as signal and real Crab data as background allowed for an optimisation which favoured the assumed Crab Pulsar spectral shape over the two principal backgrounds; cosmic rays and the strong, steady nebular signal. Inconsistencies between the strength of the pulsed excess found in the analysis presented in this work and the excess found in an independent analysis performed by another VERITAS collaboration member led to a reexamination of the cuts and finally to an optimisation on Crab Pulsar data itself. Training the cuts on the 16-hour data sample boosted the overall sensitivity of the analysis to the Crab Pulsar signal.

The principle difference between the "standard" VERITAS cuts and the cuts used in the analysis presented here is the *size* cut, which is usually never lower than 400 *d.c.* and often as high as 1000 *d.c.*. By choosing smaller and dimmer showers, the event reconstruction performance is degraded, leading to larger errors in the reconstructed core position and arrival direction. The increased error in reconstructed core distance leads to errors in calculating the *mean scaled* parameters and the energy, since the core distance is used to index the LUTs. Thus, when using a lower *size* cut, one must also use looser MSW, MSL and θ^2 cuts, compared to the standard cuts. This degradation in the reconstruction and cut efficiency is tolerated, however, given the increased acceptance a low energies (see Figure 4–17).

Parameter	Cut Value
Size	$>$ 150 *d.c.*
Loss	$<$ 0.2
NTubes	$\geq$ 4
MSW	$<$ 1.12
MSL	$<$ 1.72
θ^2	$<$ 0.045°^2}
Emission Height	$>$ 6.6 *km*
Telescope Combinations	any 2,3,4 (except T1-T4 prior to T1 relocation) any 2,3,4 (after T1 move)

Table 5–1: Cuts used in the analysis of all the VERITAS data presented in this work. These cuts were trained on 16 hours of Crab Pulsar data obtained in the 2009-2010 observing season. In all data accumulated prior to T1's relocation in September 2009, the T1-T4 event combination was rejected in the analysis, due to the large component of muon events which inhabited the data from the two near-by telescopes.

5.3 Crab Phasogram

The arrival times of the VERITAS candidate gamma-ray events from the direction of the Crab were barycentered and phase-folded in a manner described in Sections 4.11 and 4.12 of the previous chapter. The resulting pulse profile is plotted in Figure 5–3. This figure also contains a pulse profile obtained from an analysis of the public *Fermi*-LAT data. The presence of a pulsed signal in the VERITAS data is clear from this figure. A *H-Test* on the VERITAS data returns a value of 45.4. The occurrence of this value by chance has a probability of 1.28×10^{-8} as determined from Equation 4.14. The equivalent statistical significance of this probability is 5.69 standard deviations. Excluding the 16-hour training sample reduced the *H-Test* significance to 3.92 standard deviations. Apparent in the VERITAS phasogram are peaks at both the main and inter-pulse, P1 and P2 respectively. Both P1 and P2

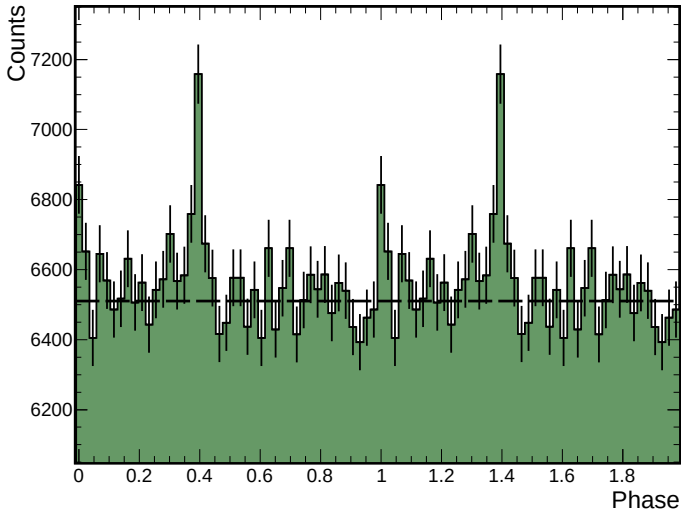

(a) Crab Pulsar Phasogram over two phases from VERITAS data.

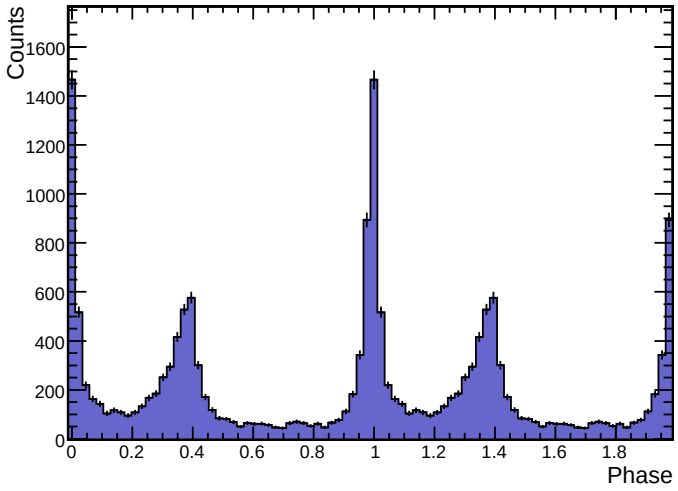

(b) Crab Pulsar phasogram over two phases from *Fermi*-LAT data.

Figure 5–3: The VERITAS phasogram contains all of the VERITAS events which passed cuts (282092 events) from the 103-hour data sample discussed in Section 5.1. The *Fermi* phasogram contains the high quality photon events from a 2°-radius region around the location of the Crab between 12/05/2008 and 12/05/2010 with energies above 300 MeV. This corresponds to 9282 events. Both phasogram are shown over two phases with 86 bins (43 bins per phase).

appear to be narrower in the VERITAS data than in the *Fermi* data. In the VERITAS data, P2 seems to be larger than P1, which would continue the trend noted by MAGIC, who have reported that P1 and P2 have similar amplitudes at 25 GeV.

5.3.1 Phasogram Analysis

The phase distribution of the VERITAS events were analysed using an unbinned maximum likelihood test. The tested model consisted of a flat offset and two symmetric Gaussians with unconstrained means, widths and amplitudes. The constant offset models the uniform phase profile expected from the contamination of events from the Crab Nebula and from the remaining background cosmic-ray events. The floating Gaussians model the possible existence of two peaks in the data, which may be present due to events from the pulsar.

The *Fermi* phase values were filled into a 200-bin histogram which was fit with asymmetric Gaussian functions restricted over the peak phase regions; -0.03 to 0.015 and 0.32 to 0.43. Note that the returned fit values were stable when the number of bins was increased or decreased. The best fit curves are plotted over the binned phase values of both the *Fermi* and VERITAS data in Figure 5–4. The derived values from the fit are shown in Table 5–2.

From the unbinned fit to the VERITAS phase data, the best positions of the two peaks occur at the known position of the Crab main and inter pulse, at phases 0.0 and 0.39. The fitted amplitude of P1 is less than P2, with the ratio of the height of P1 to P2 being 0.76±0.33. This is the reverse of what is seen in the *Fermi* data, where P1 is twice as large as P2, but is not totally unexpected. To quantify the difference between the pulse widths measured by *Fermi* and VERITAS, the widths

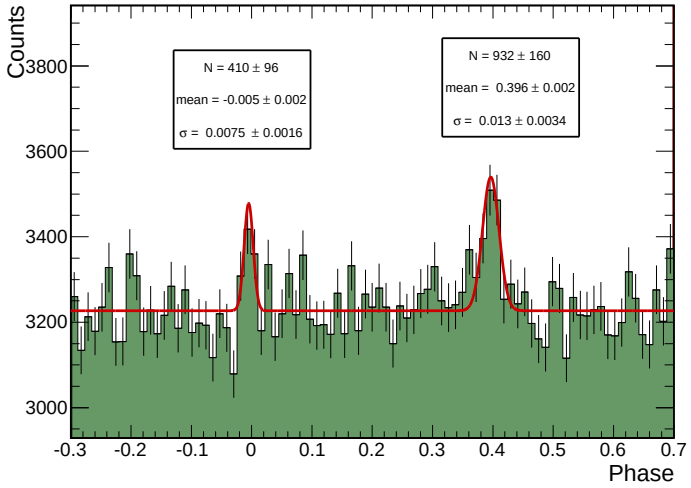

(a) VERITAS pulse profile with the best fit line determined from an unbinned maximum likelihood analysis.

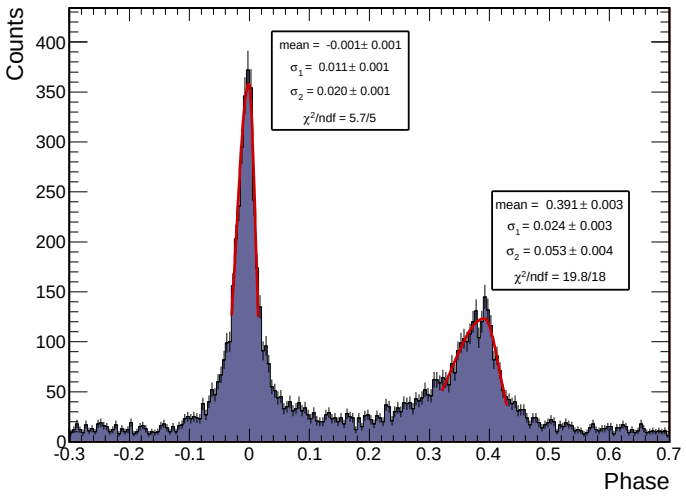

(b) *Fermi* pulse profile with asymmetric Gaussians fitted to the peak regions.

Figure 5–4: The VERITAS data were fit with an unbinned maximum likelihood test with two symmetric Gaussians. The *Fermi* data were binned and fit with asymmetric Gaussians restricted over the peak regions.

Data	Peak	Amplitude	Mean	σ_1	σ_2
VERITAS	P1	410±96	-0.005±0.002	0.0075±0.0016	-
VERITAS	P2	932±160	0.396±0.002	0.0130±0.0034	-
Fermi-LAT	P1	372±19	-0.001±0.001	0.0110±0.001	0.020±0.001
Fermi-LAT	P2	145±12	0.391±0.003	0.0240±0.003	0.053±0.004

Table 5–2: Values returned from the fits to the pulsar phase data. The VERITAS data were fit with an unbinned maximum likelihood test with two symmetric Gaussians. The *Fermi* data were binned and fit with asymmetric Gaussians restricted over the peak regions (the peak amplitudes in the VERITAS fit refer to the Gaussian normalisation values (area)). The *Fermi*-LAT peak amplitudes refer to the height of the maximum bin in the 200-bin histogram. See Figures 5–4.

(σ) from the fits to the VERITAS data were compared to the averages of the widths returned from the asymmetric Gaussian fits to the *Fermi* data. Using this method,

$$\begin{aligned} \frac{2\sigma^V}{\sigma_1^F+\sigma_2^F} &= 0.48 \pm 0.056 \quad \text{for P1} \\ \frac{2\sigma^V}{\sigma_1^F+\sigma_2^F} &= 0.34 \pm 0.049 \quad \text{for P2} \end{aligned} \tag{5.1}$$

where the superscripts F and V label the parameters from the *Fermi* and VERITAS fits respectively. The occurrence of pulses 2 to 3 times narrower above 100 GeV is not expected and represents a new finding from this analysis.

5.3.2 Significance Tests

The phase interval 0.32 and 0.43 is a site of gamma-ray emission from the Crab Pulsar seen by the EGRET telescope above 100 MeV [40]. MAGIC also reported a hint of emission above 60 GeV from this region [18]. This region, and an associated background region between 0.45 and 0.95, have historically become a search region for gamma-ray emission from the Crab. Here, we label this the "A" search region. Given the measured narrow width of the profile peaks above 100 GeV, phase intervals were chosen for subsequent analysis based on the fitted means and widths described

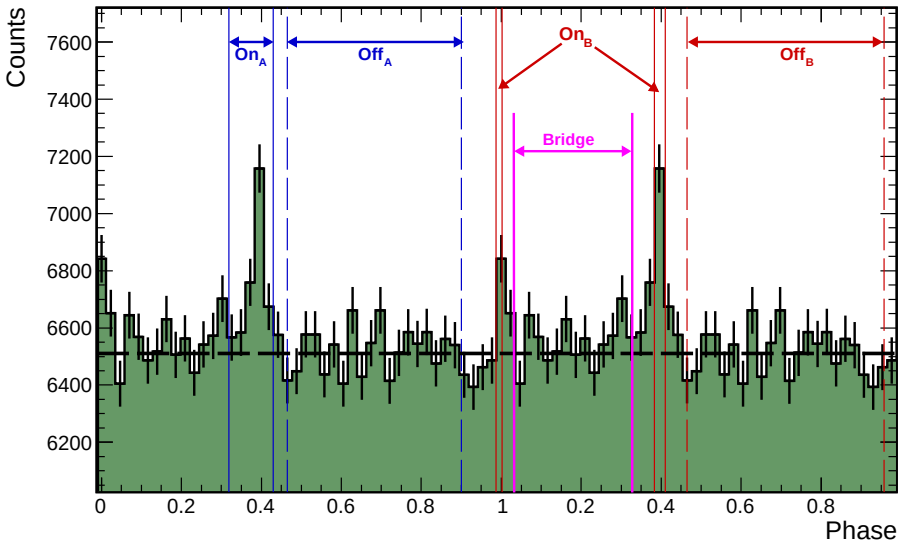

Figure 5–5: VERITAS phasogram over two phases with two different signal and background region labelled. The "On" and "Off" regions labelled "A", were previously defined by EGRET and are the regions within which a hint of emission from the pulsar was found above 60 *GeV* by MAGIC. The "B" regions are based on the unbinned fit to the VERITAS light curve. The "On" regions represent the one sigma widths around the fitted peak positions, and the "Off" region start at distance of 5 sigma from the fitted peak positions. The "bridge region", between the two peaks ranges from 0.032 to 0.32.

earlier. Defined here is a phase interval around the main pulse, from -0.0126 to 0.0024, and around the inter-pulse, from 0.382 to 0.42. These regions represent the one-sigma widths around the fitted peak positions. The associated background phase interval starts and ends at a distance of 5 sigma widths from the fitted peak positions and ranges from 0.465 to 0.957 . Here, we label this the "B" search region. The phase interval from 0.032 to 0.32 was chosen to investigate the "bridge" region, between the two peaks. The boundaries of this region were chosen to start and end at a distance of 5 sigma widths from the fitted peak positions. The "B" background

region is used to estimate the number of background counts in this region. These phase intervals are shown in Figure 5–5.

Using these phase intervals, the number of excess events and the statistical significance of the excess can be computed using the Li and Ma equation (Equation 4.7). These measured excesses and significances are shown in Table 5–3, while the growth of the signal excess and its significance against the number of detected events is plotted in Figure 5–6. The excesses in the main and inter-pulse regions are clearly significant. Emission from the "bridge" region is not significant, occurring at the 1.5σ level.

5.4 Crab Nebula Spectrum

The spectrum of the Crab Nebula was determined from 70 hours of data accumulated after the relocation of Telescope 1 in September 2009. The strong nebula signal consists of 85829 excess events with a statistical significance corresponding to 141 standard deviations. The energy spectrum was calculated in the manner described in Section 4.9 and is plotted in Figure 5–7.

The Crab Nebula TeV gamma-ray spectrum was fit with a power-law function for the form

$$\frac{dF}{dE} = A\left(\frac{E}{E_0}\right)^{\Gamma} \tag{5.2}$$

and with a log-parabolic function of the form

$$\frac{dF}{dE} = A\left(\frac{E}{E_0}\right)^{[\Gamma+\kappa\log_{10}(E/E_0)]} \tag{5.3}$$

suggested by [18]. The fitted curves and fit residuals are shown in Figure 5–7 with the values returned by the fits shown in Table 5–4. Over almost two orders of magnitude

Using Complete Data Set

Region	Peak	On Counts	Off Counts	α	Excess	Significance
A	P1	-	-	-	-	-
A	P2	31980	112381	0.275	1075.22	5.38σ
A	P1+P2	31980	112381	0.275	1075.22	5.38σ
B	P1	4476	137876	0.0304	278.43	4.18σ
B	P2	8374	137876	0.0555	721.20	7.89σ
B	P1+P2	12850	137876	0.0859	999.63	8.68σ
Bridge	-	83345	137876	0.60	560.73	1.53σ

Using Complete Data Set Less 16 Hour Training Sample

Region	Peak	On Counts	Off Counts	α	Excess	Significance
A	P1	-	-	-	-	-
A	P2	26387	93078	0.275	790.5	4.34σ
A	P1+P2	26387	93078	0.275	790.5	4.34σ
B	P1	3688	114232	0.0304	278.43	3.47σ
B	P2	6899	114232	0.0555	210.26	6.72σ
B	P1+P2	10587	114232	0.0859	558.56	7.34σ
Bridge	-	69099	114232	0.60	511.19	1.54σ

Table 5–3: Table of the number of selected events collected within the A and B signal and background regions defined in the text and shown in Figure 5–5. α is the ratio of the size of the signal region to the size of the background region. Equation 4.7 was used to calculate the significance values.

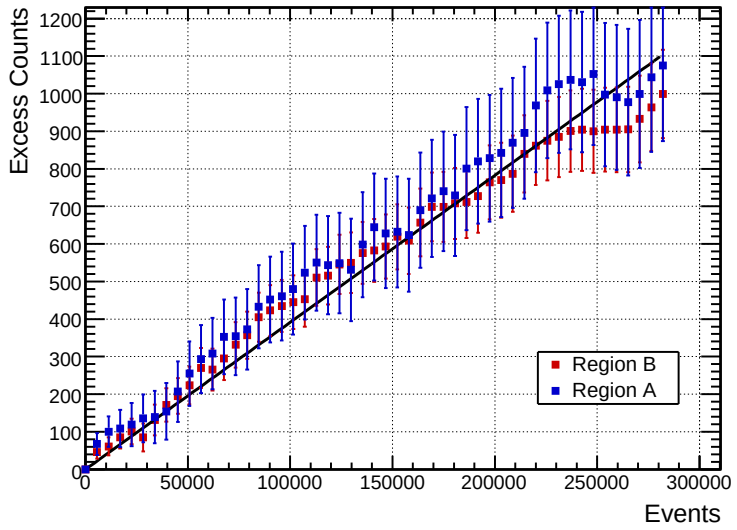

(a) Excess Counts Against Cumulative Counts

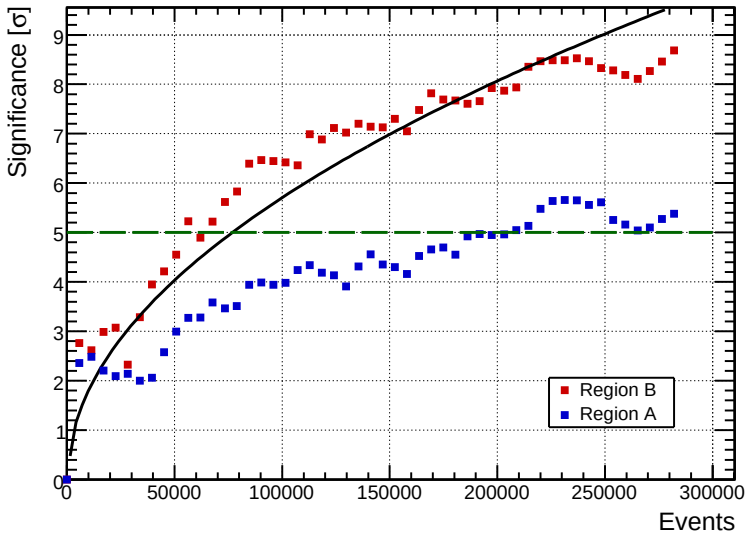

(b) Excess Significance Against Cumulative Counts

Figure 5–6: Plots of the growth of the total signal excess (P1 and P2) and its significance against the number of detected events. The excess grows linearly while the significance grows as the square root, as expected. The A and B signal and background regions are defined in the text and shown in Figure 5–5.

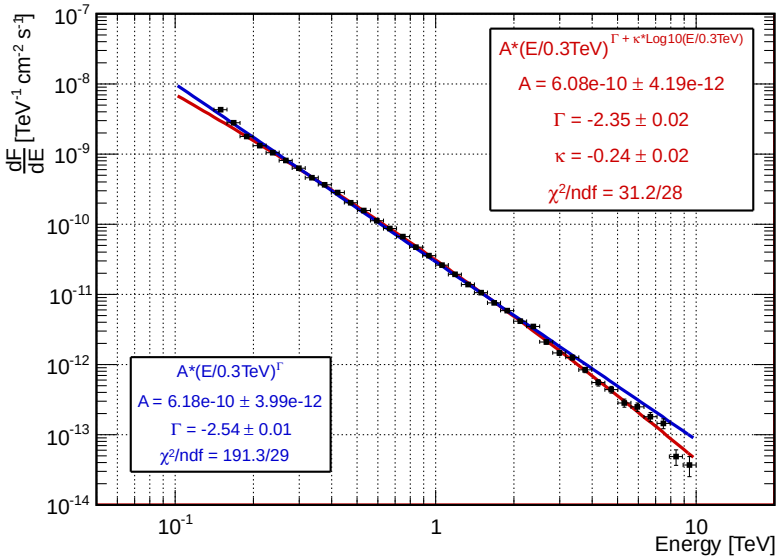

(a) Crab Nebula energy spectrum.

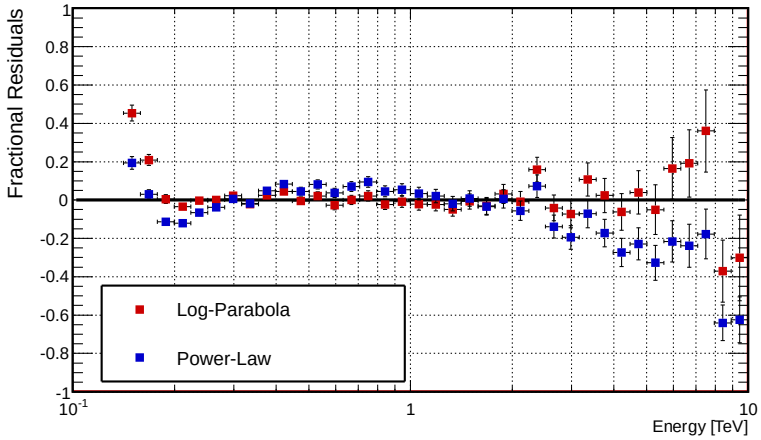

(b) Fit residuals.

Figure 5–7: Plot of the Crab Nebula differential energy spectrum with functional fits. Data were fit over the range 200 GeV to 7 TeV. The curved power law fit is favoured with a χ^2 value of 31.2 for 28 d.o.f. compared to the straight power law fit with a χ^2 value of 191 for 29 d.o.f. The functional form of the power-law and log-parabola are given in Equations 5.2 and 5.3.

Name	Range $[TeV]$	A @300GeV $[TeV^{-1}cm^{-2}s^{-1}]$	Γ	κ	$\chi^2/_{n.d.f}$
Power-Law	0.2 - 7	6.18±0.04×10^{-10}	-2.54±0.01	-	191/29
Log-Parabola	0.2 - 7	6.08±0.04×10^{-10}	-2.35±0.02	-0.24±0.02	31/28
MAGIC Published	0.06 - 7	6.00±0.2 ×10^{-10}	-2.31±0.06	-0.26±0.07	8/7

Table 5–4: Table of the returned values from the fits to the VERITAS Crab Nebula spectrum plotted in Figure 5–7 alongside the published MAGIC results from [18]. The functional form of the power-law and log-parabola are given in Equations 5.2 and 5.3.

in energy, the log-parabolic fit function better represents the data. As is clear from the fit values shown in Table 5–4, the measured spectrum agrees very well with the measurements made by MAGIC.

5.4.1 Nebula Spectrum Systematics

Energy Threshold and Effective Area

While the measured Crab Nebula spectrum agrees well with historical measurements, it is clear from the residuals plot in Figure 5–7 that the two lowest energy bins are systematically higher than the fit model by 20-45%. A departure from the fitted model is also seen above 6 TeV. However at these energies, the statistical error is much larger, and thus the measured flux is still consistent with the fit. The issue affecting the low-energy spectral points is due to an error in assigning the energy of the events. In this energy region the effective area rises steeply with energy (recall Figure 4–17), so small changes in the assignment of the energy to an event can change the effective area for the event by large amounts. In the case here, the effective area has been underestimated by ∼20-45%.

The onset of such effects close to the threshold energy of the detector is not unexpected. Typically an analysis-level energy threshold is chosen which ensures

that events with energies above this threshold are not affected by these systematics. The threshold is typically determined from simulated data and is defined as the peak in the energy distribution of the events which pass analysis cuts; sometimes called the *peak response energy*. This is the energy where the convolution of the falling source energy spectrum and the rising effective area reaches a peak. Below this peak, systematic errors in the calculation of the effective area can affect the spectrum. The response curves for three different source energy spectra are plotted in Figure 5–8.

In this analysis, the peak response energy for a source with a spectral index of -2.4, as determined from Figure 5–8, is 166 GeV. The third lowest energy bin in the Crab Nebula spectrum is the lowest energy bin which is above this threshold and as such can be considered to be unaffected by the sharp rise of the effective area. Indeed, the flux calculated in this energy bin is completely consistent with the fitted curve and with the previous flux measurements made in this energy range by MAGIC. This bin's low edge has an energy of 177 GeV and marks the effective analysis-level energy threshold for this analysis.

Energy Scale

Uncertainty on the absolute energy scale introduces a systematic error on the measured energy spectrum. Here, uncertainties on the Cherenkov light yield, the atmospheric transmission, the mirror reflectivity and PMT quantum efficiencies play a significant role (see Table 5–5). The aggregate uncertainly on the VERITAS energy scale is $\sim$20%.

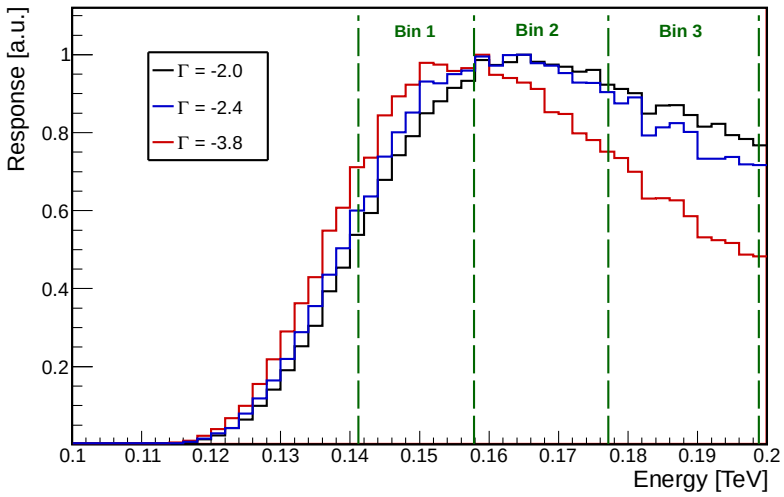

Figure 5–8: Plot of the trigger and selection response of the VERITAS telescopes to sources with power law spectra. These distributions represent the convolution of the falling source energy spectrum and the rising effective area. The peak of the distributions, called the peak response energy, is chosen as the energy threshold for analysis. The position of the three lowest spectral bins are shown. The third lowest energy bin is the lowest bin above the peak response energy.

Component	Uncertainty Level (%)
PMT Absolute Gain	5.0
PMT Pulse Shape	3.0
PMT Quantum Efficiency	5.0
First Dynode Collection Efficiency	2.0
Light cone Reflectivity	3.0
Reflector Shadowing	2.0
Mirror Reflectivity	10.0
Cherenkov Light Production	10.0
Cherenkov Light Transmission	10.0
Quadrature Sum	19.4

Table 5–5: Table of the principal sources of uncertainly affecting the calculation of the absolute energy scale. Stated uncertainly values represent the current best estimates. In most cases uncertainty estimates are based on the level of agreement between independent measurements of the same quantity.

In the case of a power-law spectrum with a spectral index Γ, a shift in the energy scale by a factor f will increase/decrease the flux by a factor, S, such that

$$S = f^{\Gamma+1} \tag{5.4}$$

Thus with an uncertainly of $\pm 20\%$ on the energy scale, the flux of the measured Crab Nebula spectrum has a systematic error of +39%-24%. Figure 5–9 shows the measured spectrum along with the computed systematic error.

Flux Point

To motivate aspects of the analysis detailed in Section 5.5, a single Crab Nebula flux point was calculated over the range 140 GeV to 880 GeV. This point is marked with the green triangle in Figure 5–9. This point has a central energy of 354 GeV and flux of $4.97 \pm 0.03 \times 10^{-10}\, cm^{-2} s^{-1} TeV^{-1}$. This data point includes events below the analysis-level energy threshold and thus is affected by the threshold systematics discussed earlier. This flux value is 21% higher than the flux at the same energy, determined from the spectral fit. While inclusion of events below the threshold energy is unfavourable, it appears that, in this analysis, the error on the flux introduced is smaller than the systematic error introduced by the energy scale uncertainty.

5.5 Crab Pulsar Spectrum

Similar to the Crab Nebula spectrum, the Crab Pulsar spectrum was determined from the > 70 hours of data which were accumulated after the relocation of Telescope 1. This exposure resulted in 856 excess events, with a statistical significance of 7.4 standard deviations using the events which fell within the "B" source and background

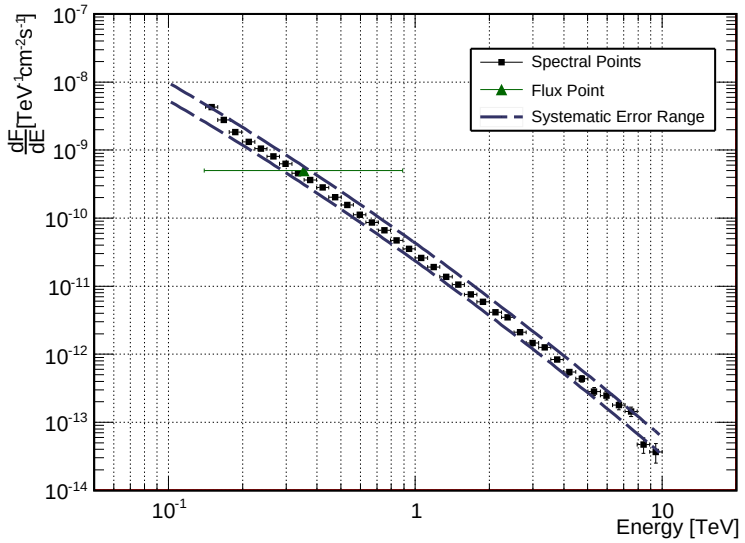

(a) Crab Nebula energy spectrum with systematic uncertainties.

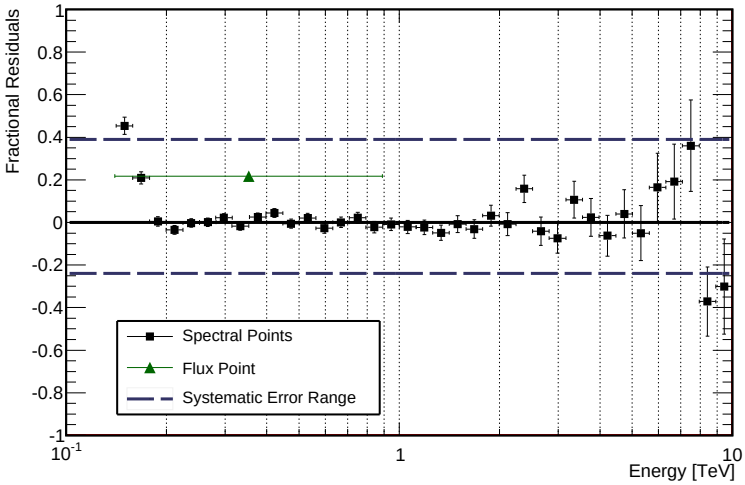

(b) Log-Parabola fit residuals with systematic uncertainties.

Figure 5–9: Plot of the Crab Nebula differential energy spectrum. Systematic errors on the flux are +39% - 24% based on 20% uncertainty on the absolute energy scale. A single flux point calculated over the range 140 GeV to 880 GeV is included. This data point includes events below the peak response energy and is affected by the threshold systematics discussed in the text, yielding a flux value 21% higher than expected.

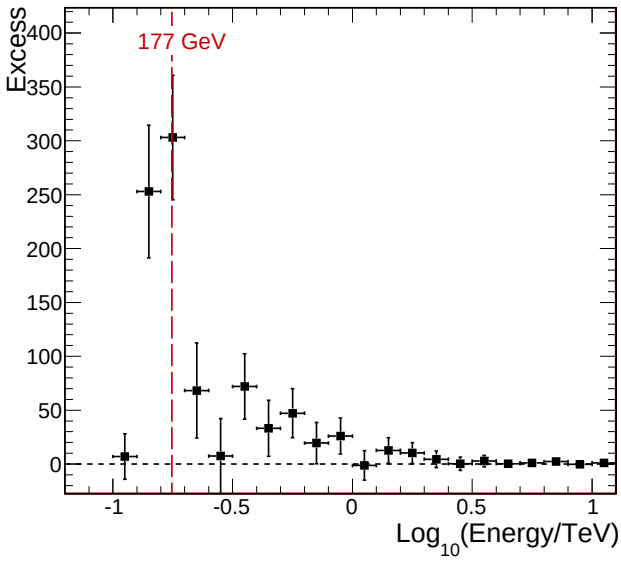

(a) Energy of Crab Pulsar excess events.

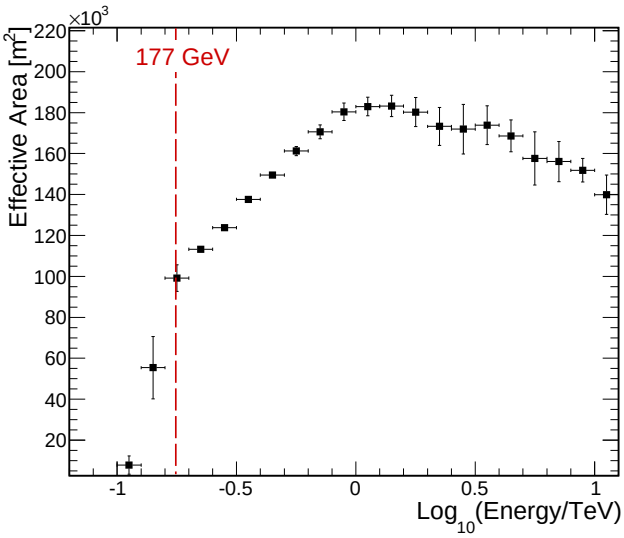

(b) Effective area for Crab Pulsar analysis.

Figure 5–10: The measured energy distribution of excess events from the Crab Pulsar analysis and a plot of the effective area versus energy. The red line at 177 *GeV* marks the analysis-level energy threshold. The measured energies of a large fraction of the excess events fall below this threshold. The effective area falls steeply below this energy.

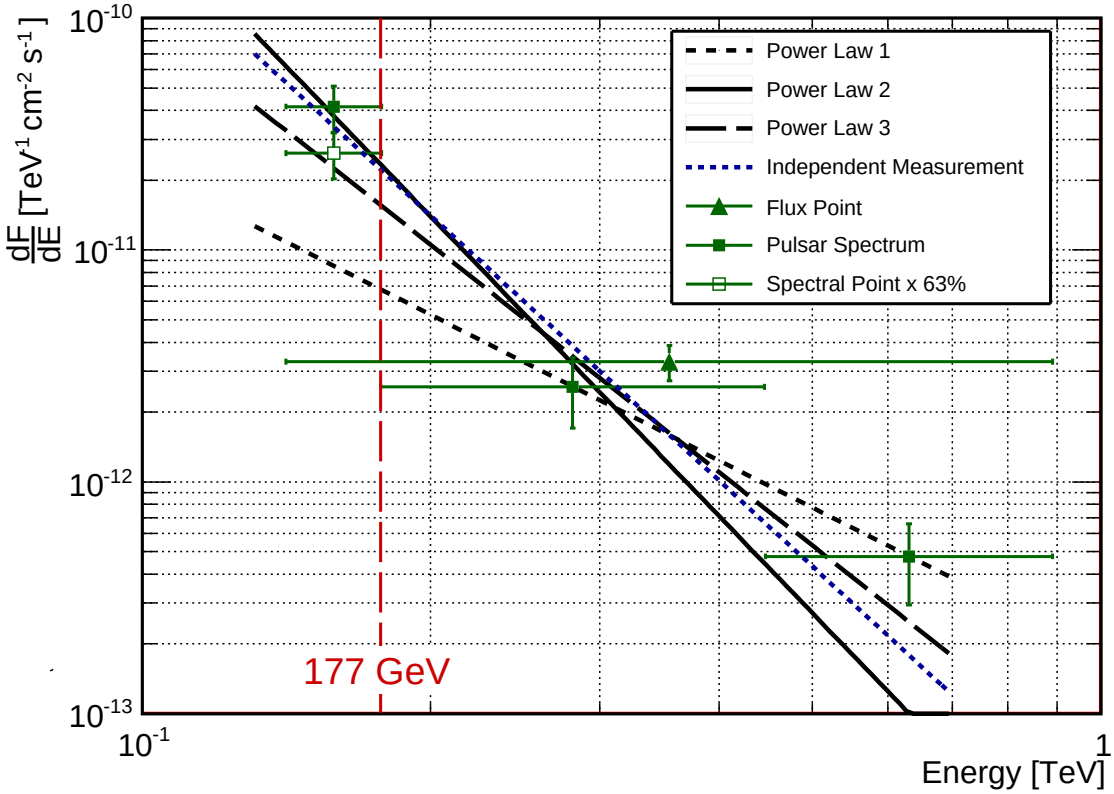

Figure 5–11: VERITAS measurement of the phase-averaged Crab Pulsar energy spectrum. The solid green squares show the raw measured spectrum. The lowest energy spectral point is below the analysis-level energy threshold (177 GeV) so the flux here is likely overestimated. The open green square marks the flux value of the lowest energy point scaled to 63% of its value (reduced by 37%). The green triangle represents a single flux point determined over the energy range from 140 GeV to 880 GeV. From the experience gained with the Crab Nebula, the flux value for this spectral point is likely to be overestimated by ∼20%. The y-axis errors show the statistical error while the x-axis error bars mark the width of the energy bins. The power-law fit to the two points above the analysis-level energy threshold is labelled power-law 1. Power-law 2 fits the three points of the raw measured spectrum (solid green squares). Power-law 3 fits the scaled low energy flux point (open green square) and the two higher energy flux points. The blue dashed curve was determined from an independent analysis of the same data set by another VERITAS collaboration member. The returned values from these fits are shown in Table 5–6.

phase regions discussed in Section 5.3.2. The measured energy distribution of these excess events and a plot of the effective area against energy is shown in Figure 5–10.

It is clear from Figure 5–10 that the measured energy of a large fraction of the excess events falls below 177 GeV; the analysis-level energy threshold. From this figure, it is also clear that the effective area falls sharply below this energy. Given both of these factors, calculating a pulsar spectrum is not straight-forward. To proceed, the following procedures were adopted:

1. Two spectral points were determined from the excess events above 177 GeV. Both spectral points have a statistical significance above three standard deviations.
2. A third spectral point was determined from the excess events falling in the range 140 GeV to 177 GeV. From the experience gained from the Crab Nebula spectrum, the flux attributed to this point is likely to be overestimated by ∼20-45%.
3. The flux of the low energy spectral point was reduced by 37% in an attempt to correct for the likely overestimation.
4. A single flux point was determined from all of the excess events from 140 GeV to 880 GeV. This procedure was previously applied to the Crab Nebula spectral data and resulted in overestimation of the flux by 21%.

The above procedure yields three possible spectra and one all-encompassing spectral point over the range 140 GeV to 880 GeV. These are plotted in Figure 5–11 along with the power-law fits and a power-law curve determined from an independent

Name	Range $[GeV]$	A @200GeV $[TeV^{-1}cm^{-2}s^{-1}]$	Γ	$\chi^2/_{n.d.f}$
Power Law 1	177 - 880	5.25±2.65 $\times 10^{-12}$	-2.08±0.63	Over-constrained
Power Law 2	140 - 880	13.9±2.56 $\times 10^{-12}$	-4.29±0.79	4.9/1
Power Law 3	140 - 880	10.5±2.02 $\times 10^{-12}$	-3.26±0.61	2.9/1
Power Law (indep.)	140 - 400	14.0±2.01 $\times 10^{-12}$	-3.8±0.5	-

Table 5–6: Table of the values returned from the fits to the measured phase-averaged Crab Pulsar energy spectrum plotted in Figure 5–11. The bottom row in the table shows fit values determined from an independent analysis of the same data set by another VERITAS collaboration member.

analysis of the same data set by another VERITAS collaboration member. The returned values from these fits are shown in Table 5–6.

From the three power-law fits determined from this work, the average flux normalisation of the Crab Pulsar at 200 GeV is 9.8±4.2 $\times 10^{-12}\, cm^{-2}s^{-1}TeV^{-1}$. By comparison, the flux of the Crab Nebula at 200 GeV is 1.5±0.02 $\times 10^{-9}\, cm^{-2}s^{-1}TeV^{-1}$ putting the measured flux from the pulsar at less than one percent of the nebular flux.

5.5.1 P1/P2 Spectral Differences

The observation of narrow emission peaks in the VERITAS pulsar profile, and a lack of observed emission in the "bridge" region between the peaks, means that the reported VERITAS spectrum is a good approximation of the phase-averaged spectrum. Due to the small statistical significance of the VERITAS spectral measurement (7.4σ) it is impossible to measure the phase-resolved spectra of the emission. Differences between the main and inter-pulse spectra can, however, be probed.

Discussed earlier was the VERITAS measurement showing that the excess of events in the inter-pulse is about twice as large as the excess in the main-pulse. This

observation and the observation by MAGIC that the number of events in P1 and P2 are equal above 25 GeV [19] allows an estimate of the differences between the spectral shapes of P1 and P2. Assuming the main and inter-pulse can be modelled by power-laws, one can write:

$$\begin{array}{ll} \frac{dF}{dE} = A_1 \left(\frac{E}{E_0}\right)^{\Gamma_1} & \text{for P1} \\ \frac{dF}{dE} = A_2 \left(\frac{E}{E_0}\right)^{\Gamma_2} & \text{for P2} \end{array} \tag{5.5}$$

Using the MAGIC measurement at 25 GeV one can determine that

$$\begin{aligned} \frac{A_1}{\Gamma_1+1}\left(\frac{25\,GeV}{25\,GeV}\right)^{\Gamma_1+1} &= \frac{A_2}{\Gamma_2+1}\left(\frac{25\,GeV}{25\,GeV}\right)^{\Gamma_2+1} \\ \Rightarrow \frac{A_1}{\Gamma_1+1} &= \frac{A_2}{\Gamma_2+1} \end{aligned}$$

Integrating Equation 5.5 from 140 GeV (the energy of the lower edge of the lowest energy VERITAS spectral bin) to infinity and using the VERITAS estimates of the number of events (listed in Table 5–2) one can write

$$\frac{\frac{A_1}{\Gamma_1+1}\left(\frac{140\,GeV}{25\,GeV}\right)^{\Gamma_1+1}}{\frac{A_2}{\Gamma_2+1}\left(\frac{140\,GeV}{25\,GeV}\right)^{\Gamma_2+1}} = \frac{410 \pm 96}{932 \pm 160}$$

This equation reduces to

$$\Gamma_1 - \Gamma_2 = -0.47 \pm 0.168$$

showing that the spectrum of P1 is softer that the spectrum of P2 by 0.47±0.168.

5.5.2 Height of Magnetospheric Emission Site

As discussed in Chapter 2, a relation can be drawn between maximum energy of observed gamma-ray radiation and the distance between the site of the emission and the surface of the neutron star. Since gamma-ray photons undergo pair-creation when they encounter strong magnetic fields, the site of emission of gamma-ray photons

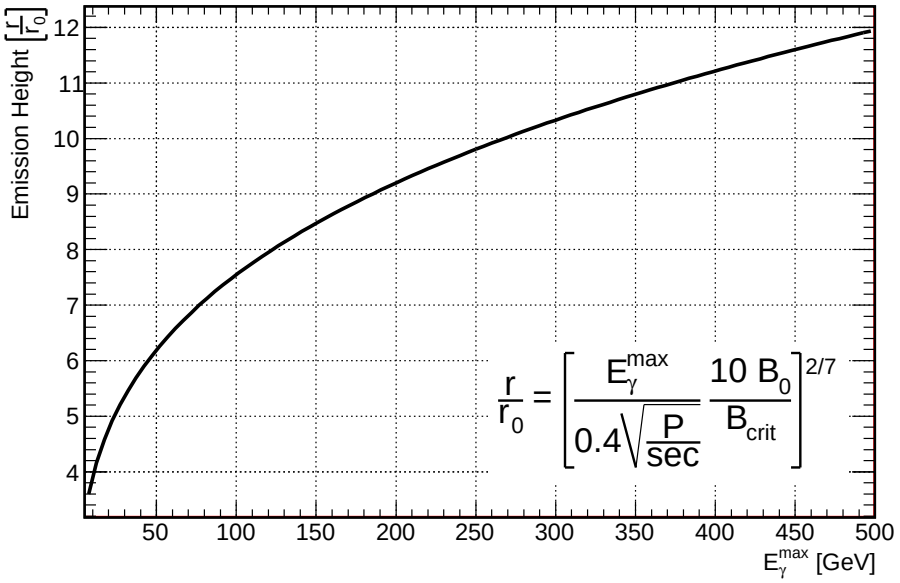

Figure 5–12: Plot of the minimum distance between the gamma-ray emission site and the stellar surface and the energy of the observed photons for the Crab Pulsar. Due to the absorption of gamma-ray photons by pair-creation in strong magnetic fields, observation of VHE gamma-rays allows a bound to be set on the distance between the stellar surface and the site of gamma-ray emission. Rearranging Equation 2.6 and using the measured period, P, and surface magnetic field strength, B_0, of the Crab pulsar (listed in Table 2–2) one can compute the above curve. Using the analysis energy threshold of 177 GeV and the energy of the single spanning flux point of 354 GeV the minimum distance of the emission region above the stellar surface must be 8.8 and 10.8 stellar radii respectively.

must exist beyond a certain distance from the star, if the photons are to escape and be observed. This relation, which is plotted in Figure 5–12, was formulated by [22] and is stated in Equation 2.6. Proceeding conservatively, and setting the maximum observed energy to 177 GeV, a minimum distance of 8.8 stellar radii can be set on the site of emission. Using the central energy of the single flux point spanning the entire gamma-ray excess, 354 GeV, one obtains a limit of 10.8 stellar radii. Both calculations were performed using the measured period 0.033 s and surface magnetic field strength 3.78×10^{12} G of the Crab Pulsar from the ATNF online pulsar catalogue (http://www.atnf.csiro.au/research/pulsar/psrcat) [77]. These limits are the most constraining limits so-far set on the distance between the site of emission and the stellar surface.

5.6 Combined *Fermi* and VERITAS pulsar Spectrum

In Figure 5–13 the measured VERITAS pulsar spectrum is plotted alongside the phase-averaged *Fermi*-LAT spectral points reported in [3]. This combined spectral energy distribution was fit with three functional forms; a power-law function times an exponential cut-off, a broken power-law function and a log-parabolic function. The formula for each of these functions and the returned fit values and fit statistics are reported in Table 5–7.

All of the pulsars so-far measured by *Fermi* display a cut-off in their energy spectrum around a few GeV with the shape of the spectrum beyond the cut-off energy being consistent with an exponential. As discussed in Chapter 2, this observed exponential cut-off is expected if curvature radiation occurring at the radiation-reaction limit is the principal gamma-ray emission mechanism. The VERITAS measurements

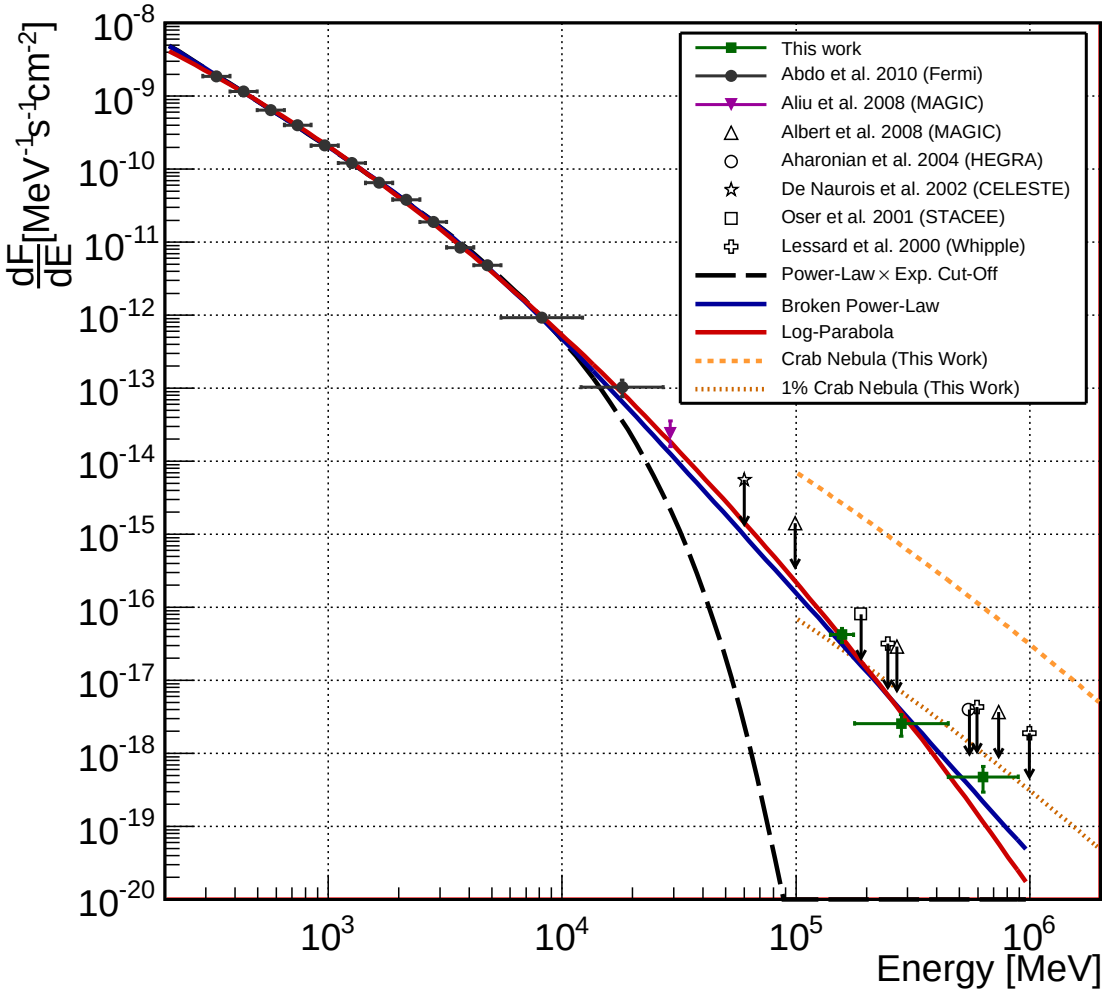

Figure 5–13: Measured spectrum of the Crab Pulsar with *Fermi*-LAT and VERITAS data. A single flux point from MAGIC is included [19], alongside historical upper limits from MAGIC, HEGRA, CELESTE, STACEE and Whipple [18, 8, 37, 88, 70]. The VERITAS data points are those plotted in Figure 5–11. The *Fermi*-LAT data are described in [3]. Overlaid are the best fit curves for three functional forms. Fits were made to the *Fermi*-LAT data and the raw measured VERITAS spectrum. The exponential cut-off is highly disfavoured by the VERITAS data while broken power-law and log-parabolic shapes can provide reasonable fits. The returned values from these fits are shown in Table 5–7.

Power-Law×Exp Cut-Off		Log-Parabola		Broken Power-Law	
$A\,E^{\Gamma}e^{E/E_c}$		$A\left(\frac{E}{E_0}\right)^{[\Gamma+\kappa\log_{10}(E/E_0)]}$		$A\left(\frac{E}{E_b}\right)^{\Gamma_1}/\left[1+\left(\frac{E}{E_b}\right)^{\Gamma_1-\Gamma_2}\right]$	
A	$1.82\pm0.38\times10^{-4}$	A	$2.05\pm0.02\times10^{-10}$	A	$1.25\pm0.49\times10^{-11}$
Γ	-1.96±0.03	Γ	-2.18±0.01	Γ_1	-1.97±0.04
E_c	5.80±0.75	E_0	1 (fixed)	E_b	4.26±0.66
		κ	0.40±0.01	Γ_2	-3.57±0.06
	- - - - -		- - - - -		- - - - -
$\chi^2/_{n.d.f}$	54.5/13	$\chi^2/_{n.d.f}$	18.4/13	$\chi^2/_{n.d.f}$	18.6/12
Prob.	4.8×10^{-7}	Prob.	0.142	Prob.	0.09
Sig.	5.03σ	Sig.	1.46σ	Sig.	1.65σ

Table 5–7: Table of the values returned from the fits to the combined VERITAS and *Fermi*-LAT Crab Pulsar energy spectrum plotted in Figure 5–13. The energy values above have the unit GeV while the normalisation values (A) have units $MeV^{-1}s^{-1}cm^{-2}$. The best fit power-law times an exponential cut-off curve is very similar to the one measured with the *Fermi* data alone where Γ is -1.97±0.02 and E_c is 5.8±0.5 GeV [4]. The inclusion of the VERITAS data, however, excludes this curve at the 5σ level. The broken power-law and log-parabolic curves provide reasonable fits to the combined data set.

reported here, contradict this picture. While there is no theoretical argument in favour of the log-parabolic or broken power-law functions, both can reasonably fit the observed spectrum over four orders of magnitude in energy.

5.6.1 Exclusion of Exponential Cut-Off

As shown in Figure 5–13 and stated in Table 5–7, the VERITAS data exclude an exponential cut-off. From the fit of the combined spectral data, the exponential curve is excluded at a level greater than five standard deviations. The shape of the fitted curve is entirely determined by the *Fermi*-LAT data and predicts a tiny flux in the VERITAS energy range. The three raw VERITAS flux points are 10, 18 and 44 orders of magnitude above the flux predicted by the exponential cut-off (see Figure 5–14). Thus, the significance with which VERITAS detects pulsed emission is essentially the significance of the rejection of the exponential cut-off, since the expected flux is effectively zero. Given this observation, use of the statistically significant event excess below the analysis energy threshold is warranted when ruling out the exponential cut-off, even though the data are affected by a large systematic errors.

To show this, a power-law times an exponential cut-off was fit to the *Fermi* points and the VERITAS single flux point. This flux point, from the experience with the Crab Nebula spectrum, is likely to be over estimated by $\sim$21%. In the fit, the flux point was scaled to 0.1% of its value (see Figure 5–14), which is a very conservative underestimate of the detected flux and far larger than the systematic error on the flux. Once again, the shape of the fitted curve is entirely determined by the *Fermi* points. The $\chi^2/d.o.f$ of the fit is 51.6/11, again ruling out the fit at

a level greater than five standard deviations. This shows that the systematic errors which affect the spectrum do not affect the rejection power with which the VERITAS pulsar measurement can rule out the exponential cut-off.

5.7 Results Summary

Discussed here is the first detection of gamma-ray emission from a pulsar above 100 GeV. Based on over 100 hours of observation, the Crab Pulsar has been detected at both the main- and inter-pulse phases. While the phase of the detected emission is the same in both the high-energy and very-high-energy regime, the peaks in the very-high-energy pulse profile are 2-3 times narrower. The occurrence of this pulse narrowing was not previously expected and constitutes a new finding of this work.

Previously published results from the *Fermi* satellite and the MAGIC telescope favoured a cut-off in the emission from the Crab Pulsar occurring between 5 and 20 GeV. The detection of emission from the Crab Pulsar presented here is not inconsistent with these measurements, however the occurrence of cut-off in the emission is ruled out. A break in the spectrum with a power-law continuing above the break energy (broken power-law) or a curved power-law spectrum (log-parabolic) are consistent with the *Fermi* and MAGIC data and the data presented here, though these shapes are not phenomenologically motivated.

The detection of pulsed emission from the Crab Pulsar can be used to set a lower limit on the distance between the site of gamma-ray emission and the star's surface within the magnetosphere. Using the detected flux at 354 GeV, a limit of 10.8 stellar radii can be set on height of the gamma-ray emission region. This is the most constraining limit so far set.

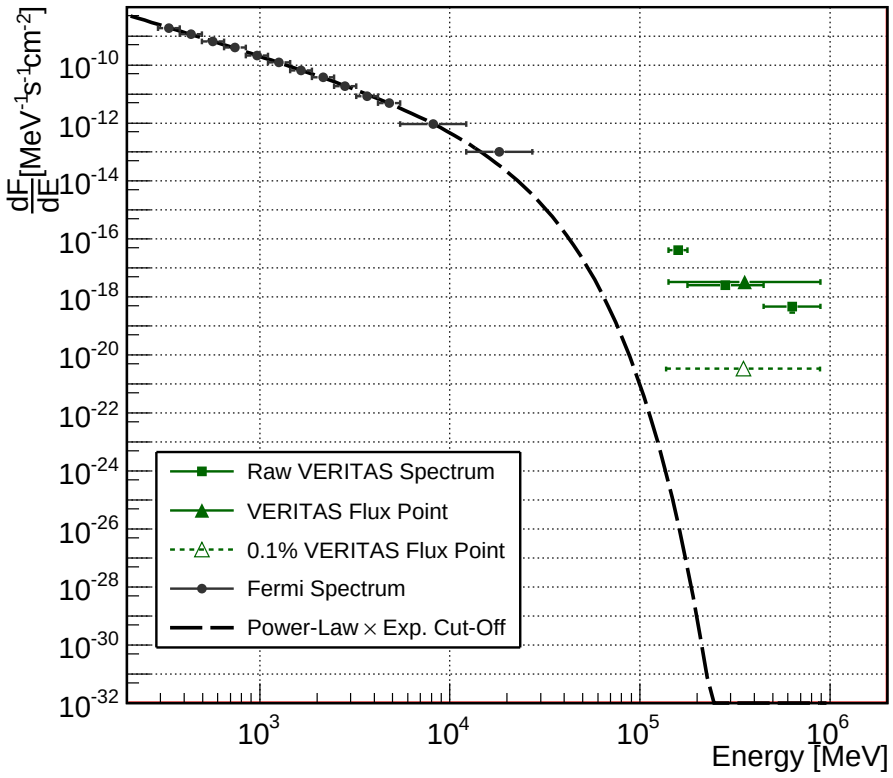

Figure 5–14: Plot of the power-law times an exponential cut-off curve fit to the VERITAS and *Fermi* data. The fit was done to the *Fermi* data and the VERITAS flux point scaled to 0.1% its value. The $\chi^2/d.o.f$ of the fit is 51.6/11, ruling out the fit at 5.12 standard deviations. This shows that the systematic errors which affect the spectrum do not affect the rejection power with which the VERITAS pulsar measurement can rule out the exponential cut-off.

CHAPTER 6
Interpretation and Concluding Remarks

6.1 The VERITAS Detection; What We Learn

The detection of emission from a pulsar above 100 GeV adds significant new information to the pulsar emission puzzle. This information can be used to directly address the two principal open questions in the field, which were introduced in the first chapter; namely:

- Where, within the local environment around the pulsar, does the gamma-ray emission originate?
- What are the radiation mechanisms responsible for the observed gamma-ray emission?

6.1.1 Emission Site

In the Crab Pulsar, the detection of pulsed radiation by VERITAS sets a limit on the minimum height of the emission region to greater than ten stellar radii above the star's surface. This strongly disfavours models which place the site of emission at the surface of the star, such as the Polar Cap model. Observations by *Fermi* and others have previously disfavoured the polar cap as the site of emission and the measurements described here add further evidence against Polar Cap models. Strictly speaking, the VERITAS detection can only be used to argue for or against the site of emission of photons with energies above 100 GeV. However, given the amount of phase-coherence which is seen across the entire electromagnetic spectrum

in the pulse profile of the Crab (recall Figure 2–17), it is more favourable to place the site of all the incoherent emission (optical to gamma-ray) away from the surface.

As well as restricting the location of the gamma-ray emission site, the VERITAS measurement may constrain the geometry of the emission region. The Crab pulse profile measured from the *Fermi* data has peaks which are between two and three times wider than the peaks seen by VERITAS. This feature may occur as a consequence of the geometry of the emission region within the magnetosphere. Depending on how the photon emission energy varies with altitude inside the acceleration region, the narrow peaks seen by VERITAS may indicate that the acceleration region tapers towards, or away from, the neutron star. Detailed modelling is necessary to explain the profile measured by VERITAS and this observation may be used to probe the geometry of the emission site.

6.1.2 Emission Mechanisms

Curvature Radiation

The broad picture of gamma-ray emission from pulsars, which has formed since the launch of *Fermi*, has many unifying aspects. The emission cut-off at a few GeV seen in all 46 pulsars described in the first *Fermi* pulsar catalogue is arguably the most obvious. The spectral shape of the emission from all of these pulsars above the cut-off energy is well described by an exponential and thus this spectral feature would appear to be driven by an underlying physical mechanism common to all gamma-ray pulsars. Since such a feature is easily explained by curvature emission occurring at the radiation-reaction limit, the picture of gamma-ray emission, in the *Fermi* era, has solidified around curvature emission as the principal gamma-ray radiation process.

The detection of the Crab Pulsar above 100 GeV, however, stands out starkly against this picture.

In Chapter 2 the break energy of curvature photons emitted at the radiation-reaction limit was calculated in terms of the basic pulsar parameters (spin period, magnetic field strength etc). Using Equation 2.4 and the Crab Pulsar parameter values (see Table 2–2) one can deduce the break energy of curvature radiation emitted from the outer magnetosphere of the Crab Pulsar to be

$$E_{\gamma}^{break} = 151\, GeV \varepsilon_{\parallel}^{3/4} \xi^{1/2} \tag{6.1}$$

where $\varepsilon_{\parallel}$ is an efficiency factor of the accelerating electric field and ξ is the radius of curvature of the magnetic field in units of the light cylinder radius (see Appendix C) . For the VERITAS detection of emission above 140 GeV to be explained by curvature radiation from the outer magnetosphere, it would require that the accelerating field be almost 100% efficient and that the local radius of curvature be larger than the light cylinder radius. Finding these conditions within a pulsar magnetosphere is highly improbable and thus, curvature emission from the outer magnetosphere can be ruled out as the source of the VERITAS emission. Using the same arguments, the Crab Pulsar measurements made by MAGIC and *Fermi* are barely consistent with Equation 6.1 using typical values for the acceleration efficiency and the radius of curvature. Both of these observations cast into great doubt the role of curvature radiation as the primary gamma-ray emission mechanism above $\sim$1 GeV.

Other Emission Scenarios

Since curvature radiation cannot explain the VERITAS observations, the most likely mechanism for emission within the magnetosphere is inverse-Compton scattering. In the Klein-Nishina regime, the cross-section for scattering is highly suppressed meaning that electrons are inefficiently cooled by the IC-mechanism. However, in the Klein-Nishina regime a large fraction of the electron energy is absorbed by the scattered photon, and thus, depending on the target photon energy, can lead to the VHE flux seen by VERITAS [55].

The evolution of the pulse profile may indicate that synchrotron-self-Compton emission is occurring within the Crab Pulsar [75]. As mentioned in Chapter 2, a feature of SSC emission is the correlation between the power emitted in the synchrotron and inverse-Compton domains. Recall that the relative intensity of P1 and P2 differ, at different wavelengths, with P1 being dominant from radio to soft x-ray energies. In hard x-rays P2 becomes dominant, with P1 becoming dominant again from 100 MeV to 25 GeV. The VERITAS measurement shows that P2 is again dominant above 100 GeV. If SSC is occurring in the Crab Pulsar the harder synchrotron emission of P2 in x-rays would lead to harder emission in the IC gamma-ray domain in P2 and the softer synchrotron emission of P1 would lead to softer emission at gamma-ray energies in P1. This is the trend we see. A photon-by-photon correlation analysis between soft x-rays and MeV gamma-rays (*Fermi*) could be used to test this SSC hypothesis [75].

In general, further study is necessary to fit the picture of gamma-ray emission from pulsars around the VERITAS measurements.

6.2 Future Prospects

Discussed in this work is the first discovery of emission from a pulsar above 100 GeV. While this discovery alone has strong implications, building further on this discovery has the potential to significantly deepen our understanding of pulsars. Chief among the paths forward is the accumulation of more data. Presented in this work is the phase-averaged gamma-ray spectrum of the Crab Pulsar over almost 4 orders of magnitude in energy (Figure 5–13). With more VERITAS data it will become possible to make phase-resolved energy spectra. These can then be matched with the phase-resolved *Fermi* spectra, which continue to gain more statistical power as *Fermi* orbits. Detailed phase-resolved spectra provide unparallelled probes of the gamma-ray emission processes.

Important, also, are data from the MAGIC telescope, which can uniquely probe the region between 25 and 100 GeV. A more detailed mapping of the energy spectrum in this region will enable a better understanding of the spectral components. Probing whether a broken power-law or a log-parabolic shape better fit the data over the whole energy range, or whether the VERITAS data mark the onset of a new spectral component will help in understanding the relationship between the emission above and below $\sim$1 GeV.

In this work, the highest energy Crab Pulsar spectral point occurs at 630 GeV. More data will enable the mapping of the Crab Pulsar spectrum out to higher energies. Such measurements will allow greater constraints to be placed on the minimum altitude of the emission site and will place further bounds on the plausible emission scenarios. Further, if the emission is seen to extend and this feature is found in other

pulsars, then pulsars will be known to contribute to the sub-TeV diffuse emission of the galaxy. This will have important implications for dark matter searches, where unassociated gamma-ray excesses can be interpreted as the remnants of dark matter annihilation.

Extending observations to other pulsars is the primary long-term path opened by this discovery. As the *Fermi* pulsar catalogue expands, and in the light of the VERITAS discovery, the need for observations of these objects above the *Fermi* energy range grows in importance. With deep exposures, and assuming the GeV break seen by *Fermi* is followed by a power-law, the predicted fluxes from the Geminga and Vela pulsars can be detected by the current generation of IACT telescopes. However, beyond the handful of very energetic pulsars, the work of following up on the discoveries of *Fermi* above tens of GeV, will fall to the proposed Cherenkov Telescope Array (CTA) [31].

APPENDIX A
Hillas Parameters

Suppose the i^{th} PMT is given coordinates x_i, y_i (in degrees) and registers a signal s_i. The origin of the coordinate system is in the centre of the array of PMTs. An ellipse is fitted to the image and the Hillas parameters are calculated relative to the centre. For a graphical description of the parameters see Figure 4–5.

The fitting of the ellipse employs the following simple moments:

$$\begin{aligned}
\langle x \rangle &= \frac{\Sigma s_i x_i}{\Sigma s_i}, \\
\langle y \rangle &= \frac{\Sigma s_i y_i}{\Sigma s_i}, \\
\langle x^2 \rangle &= \frac{\Sigma s_i {x_i}^2}{\Sigma s_i}, \\
\langle y^2 \rangle &= \frac{\Sigma s_i {y_i}^2}{\Sigma s_i}, \\
\langle xy \rangle &= \frac{\Sigma s_i x_i y_i}{\Sigma s_i}, \\
\langle x^3 \rangle &= \frac{\Sigma s_i {x_i}^3}{\Sigma s_i}, \\
\langle y^3 \rangle &= \frac{\Sigma s_i {y_i}^3}{\Sigma s_i}, \\
\langle x^2 y \rangle &= \frac{\Sigma s_i {x_i}^2 y_i}{\Sigma s_i}, \\
\langle xy^2 \rangle &= \frac{\Sigma s_i x_i {y_i}^2}{\Sigma s_i},
\end{aligned}$$

and

$$\begin{aligned}
\sigma_{x^2} &= \langle x^2 \rangle - \langle x \rangle^2, \\
\sigma_{y^2} &= \langle y^2 \rangle - \langle y \rangle^2, \\
\sigma_{xy} &= \langle xy \rangle - \langle x \rangle \langle y \rangle, \\
\sigma_{x^3} &= \langle x^3 \rangle - 3\langle x \rangle \langle x^2 \rangle + 2\langle x \rangle^3, \\
\sigma_{y^3} &= \langle y^3 \rangle - 3\langle y \rangle^2 \langle y \rangle + 2\langle y \rangle^3, \\
\sigma_{x^2y} &= \langle x^2 y \rangle - 2\langle xy \rangle \langle x \rangle + 2\langle x \rangle^2 \langle y \rangle - \langle x^2 \rangle \langle y \rangle, \\
\sigma_{xy^2} &= \langle xy^2 \rangle - 2\langle xy \rangle \langle y \rangle + 2\langle x \rangle \langle y \rangle^2 - \langle x \rangle \langle y^2 \rangle.
\end{aligned}$$

Given the following definitions:

$$\begin{aligned}
k &= \sigma_{y^2} - \sigma_{x^2}, \\
l &= \sqrt{k^2 + 4\sigma_{xy}^2}, \\
m &= \langle y^2 \rangle - \langle x^2 \rangle, \\
n &= \sqrt{m^2 + 4\langle xy \rangle^2}, \\
u &= 1 + \frac{k}{l}, \\
v &= 2 - u,
\end{aligned}$$

the Hillas parameters are calculated from:

$$\begin{aligned}
\langle Size\rangle &= \sum s_i, \\
\langle Length\rangle^2 &= \frac{\sigma_{x^2} + \sigma_{y^2} + l}{2}, \\
\langle Width\rangle^2 &= \frac{\sigma_{x^2} + \sigma_{y^2} - l}{2}, \\
\langle Miss\rangle^2 &= \frac{u\langle x\rangle^2 + v\langle y\rangle^2}{2} - \frac{2\langle xy\rangle\sigma_{xy}}{l}, \\
\langle Distance\rangle^2 &= \langle x\rangle^2 + \langle y\rangle^2, \\
\langle Alpha\rangle &= \sin^{-1}\left(\frac{\langle Miss\rangle}{\langle Distance\rangle}\right), \\
\langle Azwidth\rangle^2 &= \frac{\langle x^2\rangle + \langle y^2\rangle - n}{2}.
\end{aligned}$$

The calculation of the parameter *Asymmetry* requires the angle, ψ, between the x-axis and the major axis of the ellipse. It is convenient to define p:

$$\begin{aligned}
\psi &= \tan^{-1}\left(\frac{(k+l)\langle y\rangle + 2\sigma_{xy}\langle x\rangle}{2\sigma_{xy}\langle y\rangle - (k-l)\langle x\rangle}\right), \\
p &= \sigma_{x^3}\cos^3\psi + 3\sigma_{x^2y}\sin\psi\cos^2\psi + 3\sigma_{xy^2}\cos\psi\sin^2\psi \\
&+ \sigma_{y^3}\sin^3\psi, \\
\langle Asymmetry\rangle^3 &= \frac{p}{\langle Length\rangle}.
\end{aligned}$$

APPENDIX B
The VERITAS Collaboration

United States of America

Adler Planetarium and Astronomy Museum

Argonne National Lab

Barnard College, Columbia University

Harvard-Smithsonian Center for Astrophysics

Iowa State University

Purdue University

University of California, Los Angeles

University of California, Santa Cruz

University of Chicago

University of Delaware

University of Iowa

University of Minnesota

University of Utah

Washington University, St. Louis

Ireland

Cork Institute of Technology

Galway-Mayo Institute of Technology

National University of Ireland, Galway

University College Dublin

United Kingdom

University of Leeds

Canada

McGill University

APPENDIX C
Derviation of the formula of the break energy of curvature photons in the outer magnetosphere of the Crab Pulsar

From equation 18.33 in [72], the break angular frequency of curvature emitted photons is

$$\omega_c = 2\pi\nu_c = \frac{3c\gamma^3}{2\rho}$$

where γ is the Lorentz factor of the electrons and ρ is the instantaneous radius of curvature. Thus the break energy is

$$E_\gamma^{break} = h\nu_c = \frac{3hc\gamma^3}{4\pi\rho} \tag{C.1}$$

At the radiation-reaction limit, electrons reach a maximum Lorentz factor of

$$\gamma_{max} \simeq \left(\frac{3\rho^2 E_\parallel}{2e}\right)^{1/4} \tag{C.2}$$

as shown by [23], were $E_\parallel$ is the electric field parallel to the magnetic field. Substituting γ_{max} in this equation for γ in Equation C.1 yields

$$E_\gamma^{break} = \rho^{1/2}\left(\frac{3hc}{4\pi}\right)\left(\frac{3E_\parallel}{2e}\right)^{3/4} \tag{C.3}$$

Now let us cast ρ as ξR_{LC}, where R_{LC} is the radius of the light cylinder defined as

$$R_{LC} = \frac{c}{|\vec{\omega}|} = \frac{c}{2\pi\nu} = \frac{cP}{2\pi} \tag{C.4}$$

where $\vec{\omega}$ is the star's rotational vector, ν is is the star's rotational frequency and P is its rotational period. Let us also cast $E_{\|}$ to be some fraction for the magnetic field, such that

$$E_{\|} = \varepsilon_{\|} B \tag{C.5}$$

where E and B have the same units in the cgs system. Using these substitutions Equation C.3 becomes

$$E_{\gamma}^{break} = \left(\frac{3hc}{4\pi}\right)\left(\frac{c}{2\pi}\right)^{1/2}\left(\frac{3}{2e}\right)^{3/4}\xi^{1/2}P^{1/2}\varepsilon_{\|}^{3/4}B^{3/4} \tag{C.6}$$

Now B can be represented as

$$B = B_{NS}\left(\frac{R_{NS}}{R}\right)^{3} \tag{C.7}$$

which is the functional form of the strength of the B field from a dipole at a distance R where R_{NS} and B_{NS} are the values of the neutron star radius and magnetic field strength respectively. Since we are considering emission in the outer magnetosphere we can replace R by R_{LC}, thus

$$B = B_{NS}\left(\frac{2\pi R_{NS}}{c}\right)^{3}\left(\frac{1}{P}\right)^{3} \tag{C.8}$$

Substituting this into Equation C.6 we get

$$E_{\gamma}^{break} = \left(\frac{3hc}{4\pi}\right)\left(\frac{c}{2\pi}\right)^{1/2}\left(\frac{3}{2e}\right)^{3/4}\left(\frac{2\pi}{c}\right)^{9/4}R_{NS}^{9/4}B_{NS}^{3/4}P^{-7/4}\varepsilon_{\|}^{3/4}\xi^{1/2} \tag{C.9}$$

Rearranging, this becomes

$$E_{\gamma}^{break} = h \left(\frac{3}{2}\right)^{7/4} \left(\frac{2\pi}{ec}\right)^{3/4} R_{NS}^{9/4} B_{NS}^{3/4} P^{-7/4} \varepsilon_{\parallel}^{3/4} \xi^{1/2} \tag{C.10}$$

Using the following values

$$\begin{aligned} h &= 6.626 \times 10^{-27}\ ergs\, s \\ e &= 4.803 \times 10^{-10}\ Fr \\ c &= 2.997 \times 10^{10}\ cm/s \\ R_{NS} &= 1 \times 10^{6}\ cm \\ B_{NS} &= 3.78 \times 10^{12}\ Gauss \\ P &= 3.3 \times 10^{-2}\ s \end{aligned}$$

where Fr is the *franklin* or *statcoulomb* such tha $1\,C = 2997924580\,Fr$, we arrive at

$$E_{\gamma}^{break} = 0.242\,ergs\,\varepsilon_{\parallel}^{3/4} \xi^{1/2} = 151.4\,GeV \varepsilon_{\parallel}^{3/4} \xi^{1/2} \tag{C.11}$$

References

[1] A. A. Abdo, M. Ackermann, M. Ajello, A. Allafort, W. B. Atwood, L. Baldini, J. Ballet, G. Barbiellini, M. G. Baring, D. Bastieri, B. M. Baughman, K. Bechtol, R. Bellazzini, B. Berenji, R. D. Blandford, E. D. Bloom, E. Bonamente, A. W. Borgland, A. Bouvier, J. Bregeon, A. Brez, M. Brigida, P. Bruel, T. H. Burnett, S. Buson, G. A. Caliandro, R. A. Cameron, P. A. Caraveo, S. Carrigan, J. M. Casandjian, C. Cecchi, Ö. Çelik, A. Chekhtman, C. C. Cheung, J. Chiang, S. Ciprini, R. Claus, J. Cohen-Tanugi, J. Conrad, C. D. Dermer, A. de Luca, F. de Palma, M. Dormody, E. d. C. e. Silva, P. S. Drell, R. Dubois, D. Dumora, C. Farnier, C. Favuzzi, S. J. Fegan, W. B. Focke, P. Fortin, M. Frailis, Y. Fukazawa, S. Funk, P. Fusco, F. Gargano, D. Gasparrini, N. Gehrels, S. Germani, G. Giavitto, B. Giebels, N. Giglietto, F. Giordano, T. Glanzman, G. Godfrey, I. A. Grenier, M.-H. Grondin, J. E. Grove, L. Guillemot, S. Guiriec, D. Hadasch, A. K. Harding, E. Hays, G. Hobbs, D. Horan, R. E. Hughes, M. S. Jackson, G. Jóhannesson, A. S. Johnson, T. J. Johnson, W. N. Johnson, T. Kamae, H. Katagiri, J. Kataoka, N. Kawai, M. Kerr, J. Knödlseder, M. Kuss, J. Lande, L. Latronico, S.-H. Lee, M. Lemoine-Goumard, M. Llena Garde, F. Longo, F. Loparco, B. Lott, M. N. Lovellette, P. Lubrano, A. Makeev, R. N. Manchester, M. Marelli, M. N. Mazziotta, W. McConville, J. E. McEnery, S. McGlynn, C. Meurer, P. F.

Michelson, W. Mitthumsiri, T. Mizuno, A. A. Moiseev, C. Monte, M. E. Monzani, A. Morselli, I. V. Moskalenko, S. Murgia, T. Nakamori, P. L. Nolan, J. P. Norris, A. Noutsos, E. Nuss, T. Ohsugi, N. Omodei, E. Orlando, J. F. Ormes, M. Ozaki, D. Paneque, J. H. Panetta, D. Parent, V. Pelassa, M. Pepe, M. Pesce-Rollins, M. Pierbattista, F. Piron, T. A. Porter, S. Rainò, R. Rando, P. S. Ray, M. Razzano, A. Reimer, O. Reimer, T. Reposeur, S. Ritz, L. S. Rochester, A. Y. Rodriguez, R. W. Romani, M. Roth, F. Ryde, H. F.-W. Sadrozinski, A. Sander, P. M. Saz Parkinson, C. Sgrò, E. J. Siskind, D. A. Smith, P. D. Smith, G. Spandre, P. Spinelli, J.-L. Starck, M. S. Strickman, D. J. Suson, H. Takahashi, T. Takahashi, T. Tanaka, J. B. Thayer, J. G. Thayer, D. J. Thompson, L. Tibaldo, D. F. Torres, G. Tosti, A. Tramacere, T. L. Usher, A. Van Etten, V. Vasileiou, C. Venter, N. Vilchez, V. Vitale, A. P. Waite, P. Wang, K. Watters, P. Weltevrede, B. L. Winer, K. S. Wood, T. Ylinen, and M. Ziegler. The Vela Pulsar: Results from the First Year of Fermi LAT Observations. ApJ, 713:154–165, April 2010.

[2] A. A. Abdo, M. Ackermann, M. Ajello, A. Allafort, L. Baldini, J. Ballet, G. Barbiellini, D. Bastieri, K. Bechtol, R. Bellazzini, B. Berenji, R. D. Blandford, E. D. Bloom, E. Bonamente, A. W. Borgland, A. Bouvier, T. J. Brandt, J. Bregeon, A. Brez, M. Brigida, P. Bruel, R. Buehler, S. Buson, G. A. Caliandro, R. A. Cameron, A. Cannon, P. A. Caraveo, J. M. Casandjian, Ö. Çelik, E. Charles, A. Chekhtman, C. C. Cheung, J. Chiang, S. Ciprini, R. Claus, J. Cohen-Tanugi, L. Costamante, S. Cutini, F. D'Ammando, C. D. Dermer, A. de Angelis, A. de Luca, F. de Palma, S. W. Digel, E. do Couto e Silva, P. S.

Drell, A. Drlica-Wagner, R. Dubois, D. Dumora, C. Favuzzi, S. J. Fegan, E. C. Ferrara, W. B. Focke, P. Fortin, M. Frailis, Y. Fukazawa, S. Funk, P. Fusco, F. Gargano, D. Gasparrini, N. Gehrels, S. Germani, N. Giglietto, F. Giordano, M. Giroletti, T. Glanzman, G. Godfrey, I. A. Grenier, M.-H. Grondin, J. E. Grove, S. Guiriec, D. Hadasch, Y. Hanabata, A. K. Harding, K. Hayashi, M. Hayashida, E. Hays, D. Horan, R. Itoh, G. Jóhannesson, A. S. Johnson, T. J. Johnson, D. Khangulyan, T. Kamae, H. Katagiri, J. Kataoka, M. Kerr, J. Knödlseder, M. Kuss, J. Lande, L. Latronico, S.-H. Lee, M. Lemoine-Goumard, F. Longo, F. Loparco, P. Lubrano, G. M. Madejski, A. Makeev, M. Marelli, M. N. Mazziotta, J. E. McEnery, P. F. Michelson, W. Mitthumsiri, T. Mizuno, A. A. Moiseev, C. Monte, M. E. Monzani, A. Morselli, I. V. Moskalenko, S. Murgia, T. Nakamori, M. Naumann-Godo, P. L. Nolan, J. P. Norris, E. Nuss, T. Ohsugi, A. Okumura, N. Omodei, J. F. Ormes, M. Ozaki, D. Paneque, D. Parent, V. Pelassa, M. Pepe, M. Pesce-Rollins, M. Pierbattista, F. Piron, T. A. Porter, S. Rainò, R. Rando, P. S. Ray, M. Razzano, A. Reimer, O. Reimer, T. Reposeur, S. Ritz, R. W. Romani, H. F.-W. Sadrozinski, D. Sanchez, P. M. S. Parkinson, J. D. Scargle, T. L. Schalk, C. Sgrò, E. J. Siskind, P. D. Smith, G. Spandre, P. Spinelli, M. S. Strickman, D. J. Suson, H. Takahashi, T. Takahashi, T. Tanaka, J. B. Thayer, D. J. Thompson, L. Tibaldo, D. F. Torres, G. Tosti, A. Tramacere, E. Troja, Y. Uchiyama, J. Vandenbroucke, V. Vasileiou, G. Vianello, V. Vitale, P. Wang, K. S. Wood, Z. Yang, and M. Ziegler. Gamma-Ray Flares from the Crab Nebula. *Science*, 331:739–, February 2011.

[3] A. A. Abdo, M. Ackermann, M. Ajello, W. B. Atwood, M. Axelsson, L. Baldini, J. Ballet, G. Barbiellini, M. G. Baring, D. Bastieri, K. Bechtol, R. Bellazzini, B. Berenji, R. D. Blandford, E. D. Bloom, E. Bonamente, A. W. Borgland, J. Bregeon, A. Brez, M. Brigida, P. Bruel, T. H. Burnett, G. A. Caliandro, R. A. Cameron, F. Camilo, P. A. Caraveo, J. M. Casandjian, C. Cecchi, Ö. Çelik, A. Chekhtman, C. C. Cheung, J. Chiang, S. Ciprini, R. Claus, I. Cognard, J. Cohen-Tanugi, L. R. Cominsky, J. Conrad, C. D. Dermer, A. de Angelis, A. de Luca, F. de Palma, S. W. Digel, E. d. C. e. Silva, P. S. Drell, R. Dubois, D. Dumora, C. Espinoza, C. Farnier, C. Favuzzi, S. J. Fegan, E. C. Ferrara, W. B. Focke, M. Frailis, P. C. C. Freire, Y. Fukazawa, S. Funk, P. Fusco, F. Gargano, D. Gasparrini, N. Gehrels, S. Germani, G. Giavitto, B. Giebels, N. Giglietto, F. Giordano, T. Glanzman, G. Godfrey, I. A. Grenier, M.-H. Grondin, J. E. Grove, L. Guillemot, S. Guiriec, Y. Hanabata, A. K. Harding, M. Hayashida, E. Hays, R. E. Hughes, G. Jóhannesson, A. S. Johnson, R. P. Johnson, T. J. Johnson, W. N. Johnson, S. Johnston, T. Kamae, H. Katagiri, J. Kataoka, N. Kawai, M. Kerr, J. Knödlseder, M. L. Kocian, M. Kramer, F. Kuehn, M. Kuss, J. Lande, L. Latronico, S.-H. Lee, M. Lemoine-Goumard, F. Longo, F. Loparco, B. Lott, M. N. Lovellette, P. Lubrano, A. G. Lyne, A. Makeev, M. Marelli, M. N. Mazziotta, J. E. McEnery, C. Meurer, P. F. Michelson, W. Mitthumsiri, T. Mizuno, A. A. Moiseev, C. Monte, M. E. Monzani, E. Moretti, A. Morselli, I. V. Moskalenko, S. Murgia, T. Nakamori, P. L. Nolan, J. P. Norris, A. Noutsos, E. Nuss, T. Ohsugi, N. Omodei, E. Orlando, J. F. Ormes, M. Ozaki, D. Paneque, J. H. Panetta, D. Parent, V. Pelassa,

M. Pepe, M. Pesce-Rollins, M. Pierbattista, F. Piron, T. A. Porter, S. Rainò, R. Rando, P. S. Ray, M. Razzano, A. Reimer, O. Reimer, T. Reposeur, S. Ritz, L. S. Rochester, A. Y. Rodriguez, R. W. Romani, M. Roth, F. Ryde, H. F.-W. Sadrozinski, D. Sanchez, A. Sander, P. M. Saz Parkinson, J. D. Scargle, C. Sgrò, E. J. Siskind, D. A. Smith, P. D. Smith, G. Spandre, P. Spinelli, B. W. Stappers, M. S. Strickman, D. J. Suson, H. Tajima, H. Takahashi, T. Tanaka, J. B. Thayer, J. G. Thayer, G. Theureau, D. J. Thompson, S. E. Thorsett, L. Tibaldo, D. F. Torres, G. Tosti, A. Tramacere, Y. Uchiyama, T. L. Usher, A. Van Etten, V. Vasileiou, N. Vilchez, V. Vitale, A. P. Waite, E. Wallace, P. Wang, K. Watters, P. Weltevrede, B. L. Winer, K. S. Wood, T. Ylinen, and M. Ziegler. Fermi Large Area Telescope Observations of the Crab Pulsar And Nebula. ApJ, 708:1254–1267, January 2010.

[4] A. A. Abdo, M. Ackermann, M. Ajello, W. B. Atwood, M. Axelsson, L. Baldini, J. Ballet, G. Barbiellini, M. G. Baring, D. Bastieri, and et al. The First Fermi Large Area Telescope Catalog of Gamma-ray Pulsars. ApJS, 187:460–494, April 2010.

[5] A. A. Abdo, M. Ackermann, M. Ajello, L. Baldini, J. Ballet, G. Barbiellini, D. Bastieri, B. M. Baughman, K. Bechtol, R. Bellazzini, B. Berenji, G. F. Bignami, R. D. Blandford, E. D. Bloom, E. Bonamente, A. W. Borgland, J. Bregeon, A. Brez, M. Brigida, P. Bruel, T. H. Burnett, G. A. Caliandro, R. A. Cameron, P. A. Caraveo, J. M. Casandjian, C. Cecchi, Ö. Çelik, E. Charles, A. Chekhtman, C. C. Cheung, J. Chiang, S. Ciprini, R. Claus, J. Cohen-Tanugi, J. Conrad, C. D. Dermer, F. de Palma, M. Dormody, E. d. C. e. Silva,

P. S. Drell, R. Dubois, D. Dumora, Y. Edmonds, C. Farnier, C. Favuzzi, S. J. Fegan, W. B. Focke, P. Fortin, M. Frailis, Y. Fukazawa, S. Funk, P. Fusco, F. Gargano, D. Gasparrini, N. Gehrels, S. Germani, G. Giavitto, N. Giglietto, F. Giordano, T. Glanzman, G. Godfrey, I. A. Grenier, M.-H. Grondin, J. E. Grove, L. Guillemot, S. Guiriec, D. Hadasch, A. K. Harding, E. Hays, R. E. Hughes, G. Jóhannesson, A. S. Johnson, T. J. Johnson, W. N. Johnson, T. Kamae, H. Katagiri, J. Kataoka, N. Kawai, M. Kerr, J. Knödlseder, M. Kuss, J. Lande, L. Latronico, M. Lemoine-Goumard, F. Longo, F. Loparco, B. Lott, M. N. Lovellette, P. Lubrano, A. Makeev, M. Marelli, M. N. Mazziotta, J. E. McEnery, C. Meurer, P. F. Michelson, W. Mitthumsiri, T. Mizuno, A. A. Moiseev, C. Monte, M. E. Monzani, A. Morselli, I. V. Moskalenko, S. Murgia, P. L. Nolan, J. P. Norris, E. Nuss, T. Ohsugi, N. Omodei, E. Orlando, J. F. Ormes, M. Ozaki, D. Paneque, J. H. Panetta, D. Parent, V. Pelassa, M. Pepe, M. Pesce-Rollins, F. Piron, T. A. Porter, S. Rainò, R. Rando, P. S. Ray, M. Razzano, A. Reimer, O. Reimer, T. Reposeur, L. S. Rochester, A. Y. Rodriguez, R. W. Romani, M. Roth, F. Ryde, H. F.-W. Sadrozinski, A. Sander, P. M. Saz Parkinson, J. D. Scargle, C. Sgrò, E. J. Siskind, D. A. Smith, P. D. Smith, G. Spandre, P. Spinelli, M. S. Strickman, D. J. Suson, H. Takahashi, T. Takahashi, T. Tanaka, J. B. Thayer, J. G. Thayer, D. J. Thompson, L. Tibaldo, D. F. Torres, G. Tosti, A. Tramacere, T. L. Usher, A. Van Etten, V. Vasileiou, C. Venter, N. Vilchez, V. Vitale, A. P. Waite, P. Wang, K. Watters, B. L. Winer, K. S. Wood, T. Ylinen, and M. Ziegler. Fermi-LAT Observations of the Geminga Pulsar. ApJ, 720:272–283, September 2010.

[6] V. A. Acciari, E. Aliu, T. Arlen, T. Aune, M. Bautista, M. Beilicke, W. Benbow, D. Boltuch, S. M. Bradbury, J. H. Buckley, V. Bugaev, Y. Butt, K. Byrum, A. Cannon, A. Cesarini, Y. C. Chow, L. Ciupik, P. Cogan, W. Cui, R. Dickherber, T. Ergin, S. J. Fegan, J. P. Finley, P. Fortin, L. Fortson, A. Furniss, D. Gall, G. H. Gillanders, E. V. Gotthelf, J. Grube, R. Guenette, G. Gyuk, D. Hanna, J. Holder, D. Horan, C. M. Hui, T. B. Humensky, P. Kaaret, N. Karlsson, M. Kertzman, D. Kieda, A. Konopelko, H. Krawczynski, F. Krennrich, M. J. Lang, S. LeBohec, G. Maier, A. McCann, M. McCutcheon, J. Millis, P. Moriarty, R. Mukherjee, R. A. Ong, A. N. Otte, D. Pandel, J. S. Perkins, M. Pohl, J. Quinn, K. Ragan, L. C. Reyes, P. T. Reynolds, E. Roache, H. J. Rose, M. Schroedter, G. H. Sembroski, A. W. Smith, D. Steele, S. P. Swordy, M. Theiling, J. A. Toner, V. V. Vassiliev, S. Vincent, R. G. Wagner, S. P. Wakely, J. E. Ward, T. C. Weekes, A. Weinstein, T. Weisgarber, D. A. Williams, S. Wissel, M. Wood, and B. Zitzer. Detection of Extended VHE Gamma Ray Emission from G106.3+2.7 with Veritas. ApJ, 703:L6–L9, September 2009.

[7] V. A. Acciari, T. Arlen, T. Aune, M. Beilicke, W. Benbow, M. Böttcher, D. Boltuch, S. M. Bradbury, J. H. Buckley, V. Bugaev, and et al. Spectral Energy Distribution of Markarian 501: Quiescent State Versus Extreme Outburst. ApJ, 729:2–+, March 2011.

[8] F. Aharonian, A. Akhperjanian, M. Beilicke, K. Bernlöhr, H.-G. Börst, H. Bojahr, O. Bolz, T. Coarasa, J. L. Contreras, J. Cortina, S. Denninghoff, M. V. Fonseca, M. Girma, N. Götting, G. Heinzelmann, G. Hermann, A. Heusler,

W. Hofmann, D. Horns, I. Jung, R. Kankanyan, M. Kestel, A. Kohnle, A. Konopelko, D. Kranich, H. Lampeitl, M. Lopez, E. Lorenz, F. Lucarelli, O. Mang, D. Mazin, H. Meyer, R. Mirzoyan, A. Moralejo, E. Oña-Wilhelmi, M. Panter, A. Plyasheshnikov, G. Pühlhofer, R. de los Reyes, W. Rhode, J. Ripken, G. Rowell, V. Sahakian, M. Samorski, M. Schilling, M. Siems, D. Sobzynska, W. Stamm, M. Tluczykont, V. Vitale, H. J. Völk, C. A. Wiedner, and W. Wittek. The Crab Nebula and Pulsar between 500 GeV and 80 TeV: Observations with the HEGRA Stereoscopic Air Cerenkov Telescopes. ApJ, 614:897–913, October 2004.

[9] F. Aharonian, A. G. Akhperjanian, G. Anton, U. Barres de Almeida, A. R. Bazer-Bachi, Y. Becherini, B. Behera, K. Bernlöhr, A. Bochow, C. Boisson, J. Bolmont, V. Borrel, J. Brucker, F. Brun, P. Brun, R. Bühler, T. Bulik, I. Büsching, T. Boutelier, P. M. Chadwick, A. Charbonnier, R. C. G. Chaves, A. Cheesebrough, L.-M. Chounet, A. C. Clapson, G. Coignet, M. Dalton, M. K. Daniel, I. D. Davids, B. Degrange, C. Deil, H. J. Dickinson, A. Djannati-Ataï, W. Domainko, L. O'C. Drury, F. Dubois, G. Dubus, J. Dyks, M. Dyrda, K. Egberts, D. Emmanoulopoulos, P. Espigat, C. Farnier, F. Feinstein, A. Fiasson, A. Förster, G. Fontaine, M. Füßling, S. Gabici, Y. A. Gallant, L. Gérard, D. Gerbig, B. Giebels, J. F. Glicenstein, B. Glück, P. Goret, D. Göring, D. Hauser, M. Hauser, S. Heinz, G. Heinzelmann, G. Henri, G. Hermann, J. A. Hinton, A. Hoffmann, W. Hofmann, M. Holleran, S. Hoppe, D. Horns, A. Jacholkowska, O. C. de Jager, C. Jahn, I. Jung, K. Katarzyński, U. Katz, S. Kaufmann, M. Kerschhaggl, D. Khangulyan, B. Khélifi, D. Keogh, D. Klochkov,

W. Kluźniak, T. Kneiske, N. Komin, K. Kosack, R. Kossakowski, G. Lamanna, J.-P. Lenain, T. Lohse, V. Marandon, O. Martineau-Huynh, A. Marcowith, J. Masbou, D. Maurin, T. J. L. McComb, M. C. Medina, R. Moderski, E. Moulin, M. Naumann-Godo, M. de Naurois, D. Nedbal, D. Nekrassov, B. Nicholas, J. Niemiec, S. J. Nolan, S. Ohm, J.-F. Olive, E. de Oña Wilhelmi, K. J. Orford, M. Ostrowski, M. Panter, M. Paz Arribas, G. Pedaletti, G. Pelletier, P.-O. Petrucci, S. Pita, G. Pühlhofer, M. Punch, A. Quirrenbach, B. C. Raubenheimer, M. Raue, S. M. Rayner, M. Renaud, F. Rieger, J. Ripken, L. Rob, S. Rosier-Lees, G. Rowell, B. Rudak, C. B. Rulten, J. Ruppel, V. Sahakian, A. Santangelo, R. Schlickeiser, F. M. Schöck, U. Schwanke, S. Schwarzburg, S. Schwemmer, A. Shalchi, M. Sikora, J. L. Skilton, H. Sol, D. Spangler, Ł. Stawarz, R. Steenkamp, C. Stegmann, F. Stinzing, G. Superina, A. Szostek, P. H. Tam, J.-P. Tavernet, R. Terrier, O. Tibolla, M. Tluczykont, C. van Eldik, G. Vasileiadis, C. Venter, L. Venter, J. P. Vialle, P. Vincent, M. Vivier, H. J. Völk, F. Volpe, S. J. Wagner, M. Ward, A. A. Zdziarski, and A. Zech. Very high energy γ-ray observations of the binary PSR B1259-63/SS2883 around the 2007 Periastron. A&A, 507:389–396, November 2009.

[10] F. Aharonian, A. G. Akhperjanian, A. R. Bazer-Bachi, B. Behera, M. Beilicke, W. Benbow, D. Berge, K. Bernlöhr, C. Boisson, O. Bolz, V. Borrel, T. Boutelier, I. Braun, E. Brion, A. M. Brown, R. Bühler, I. Büsching, T. Bulik, S. Carrigan, P. M. Chadwick, A. C. Clapson, L.-M. Chounet, G. Coignet, R. Cornils, L. Costamante, B. Degrange, H. J. Dickinson, A. Djannati-Ataï, W. Domainko,

L. O. Drury, G. Dubus, J. Dyks, K. Egberts, D. Emmanoulopoulos, P. Espigat, C. Farnier, F. Feinstein, A. Fiasson, A. Förster, G. Fontaine, S. Funk, S. Funk, M. Füßling, Y. A. Gallant, B. Giebels, J. F. Glicenstein, B. Glück, P. Goret, C. Hadjichristidis, D. Hauser, M. Hauser, G. Heinzelmann, G. Henri, G. Hermann, J. A. Hinton, A. Hoffmann, W. Hofmann, M. Holleran, S. Hoppe, D. Horns, A. Jacholkowska, O. C. de Jager, E. Kendziorra, M. Kerschhaggl, B. Khélifi, N. Komin, K. Kosack, G. Lamanna, I. J. Latham, R. Le Gallou, A. Lemière, M. Lemoine-Goumard, J.-P. Lenain, T. Lohse, J. M. Martin, O. Martineau-Huynh, A. Marcowith, C. Masterson, G. Maurin, T. J. L. McComb, R. Moderski, E. Moulin, M. de Naurois, D. Nedbal, S. J. Nolan, J.-P. Olive, K. J. Orford, J. L. Osborne, M. Ostrowski, M. Panter, G. Pedaletti, G. Pelletier, P.-O. Petrucci, S. Pita, G. Pühlhofer, M. Punch, S. Ranchon, B. C. Raubenheimer, M. Raue, S. M. Rayner, M. Renaud, J. Ripken, L. Rob, L. Rolland, S. Rosier-Lees, G. Rowell, B. Rudak, J. Ruppel, V. Sahakian, A. Santangelo, L. Saugé, S. Schlenker, R. Schlickeiser, R. Schröder, U. Schwanke, S. Schwarzburg, S. Schwemmer, A. Shalchi, H. Sol, D. Spangler, Ł. Stawarz, R. Steenkamp, C. Stegmann, G. Superina, P. H. Tam, J.-P. Tavernet, R. Terrier, C. van Eldik, G. Vasileiadis, C. Venter, J. P. Vialle, P. Vincent, M. Vivier, H. J. Völk, F. Volpe, S. J. Wagner, M. Ward, and A. A. Zdziarski. An Exceptional Very High Energy Gamma-Ray Flare of PKS 2155-304. ApJ, 664:L71–L74, August 2007.

[11] F. Aharonian, A. G. Akhperjanian, A. R. Bazer-Bachi, M. Beilicke, W. Benbow, D. Berge, K. Bernlöhr, C. Boisson, O. Bolz, V. Borrel, I. Braun, F. Breitling, A. M. Brown, R. Bühler, I. Büsching, S. Carrigan, P. M. Chadwick, L.-M. Chounet, R. Cornils, L. Costamante, B. Degrange, H. J. Dickinson, A. Djannati-Ataï, L. O'C. Drury, G. Dubus, K. Egberts, D. Emmanoulopoulos, P. Espigat, F. Feinstein, E. Ferrero, A. Fiasson, G. Fontaine, S. Funk, S. Funk, Y. A. Gallant, B. Giebels, J. F. Glicenstein, P. Goret, C. Hadjichristidis, D. Hauser, M. Hauser, G. Heinzelmann, G. Henri, G. Hermann, J. A. Hinton, W. Hofmann, M. Holleran, D. Horns, A. Jacholkowska, O. C. de Jager, B. Khélifi, N. Komin, A. Konopelko, K. Kosack, I. J. Latham, R. Le Gallou, A. Lemière, M. Lemoine-Goumard, T. Lohse, J. M. Martin, O. Martineau-Huynh, A. Marcowith, C. Masterson, T. J. L. McComb, M. de Naurois, D. Nedbal, S. J. Nolan, A. Noutsos, K. J. Orford, J. L. Osborne, M. Ouchrif, M. Panter, G. Pelletier, S. Pita, G. Pühlhofer, M. Punch, B. C. Raubenheimer, M. Raue, S. M. Rayner, A. Reimer, O. Reimer, J. Ripken, L. Rob, L. Rolland, G. Rowell, V. Sahakian, L. Saugé, S. Schlenker, R. Schlickeiser, U. Schwanke, H. Sol, D. Spangler, F. Spanier, R. Steenkamp, C. Stegmann, G. Superina, J.-P. Tavernet, R. Terrier, C. G. Théoret, M. Tluczykont, C. van Eldik, G. Vasileiadis, C. Venter, P. Vincent, H. J. Völk, S. J. Wagner, and M. Ward. Observations of the Crab nebula with HESS. A&A, 457:899–915, October 2006.

[12] F. Aharonian, A. G. Akhperjanian, A. R. Bazer-Bachi, M. Beilicke, W. Benbow, D. Berge, K. Bernlöhr, C. Boisson, O. Bolz, V. Borrel, I. Braun, E. Brion,

A. M. Brown, R. Bühler, I. Büsching, S. Carrigan, P. M. Chadwick, L.-M. Chounet, G. Coignet, R. Cornils, L. Costamante, B. Degrange, H. J. Dickinson, A. Djannati-Ataï, L. O'C. Drury, G. Dubus, K. Egberts, D. Emmanoulopoulos, P. Espigat, F. Feinstein, E. Ferrero, A. Fiasson, G. Fontaine, S. Funk, S. Funk, M. Füßling, Y. A. Gallant, B. Giebels, J. F. Glicenstein, B. Glück, P. Goret, C. Hadjichristidis, D. Hauser, M. Hauser, G. Heinzelmann, G. Henri, G. Hermann, J. A. Hinton, A. Hoffmann, W. Hofmann, M. Holleran, S. Hoppe, D. Horns, A. Jacholkowska, O. C. de Jager, E. Kendziorra, M. Kerschhaggl, B. Khélifi, N. Komin, A. Konopelko, K. Kosack, G. Lamanna, I. J. Latham, R. Le Gallou, A. Lemière, M. Lemoine-Goumard, T. Lohse, J. M. Martin, O. Martineau-Huynh, A. Marcowith, C. Masterson, G. Maurin, T. J. L. McComb, E. Moulin, M. de Naurois, D. Nedbal, S. J. Nolan, A. Noutsos, J.-P. Olive, K. J. Orford, J. L. Osborne, M. Panter, G. Pelletier, S. Pita, G. Pühlhofer, M. Punch, S. Ranchon, B. C. Raubenheimer, M. Raue, S. M. Rayner, A. Reimer, O. Reimer, J. Ripken, L. Rob, L. Rolland, S. Rosier-Lees, G. Rowell, V. Sahakian, A. Santangelo, L. Saugé, S. Schlenker, R. Schlickeiser, R. Schröder, U. Schwanke, S. Schwarzburg, S. Schwemmer, A. Shalchi, H. Sol, D. Spangler, F. Spanier, R. Steenkamp, C. Stegmann, G. Superina, P. H. Tam, J.-P. Tavernet, R. Terrier, M. Tluczykont, C. van Eldik, G. Vasileiadis, C. Venter, J. P. Vialle, P. Vincent, H. J. Völk, S. J. Wagner, and M. Ward. Primary particle acceleration above 100 TeV in the shell-type supernova remnant ¡ASTROBJ¿RX J1713.7-3946¡/ASTROBJ¿ with deep HESS observations. A&A, 464:235–243, March 2007.

[13] F. Aharonian, A. G. Akhperjanian, A. R. Bazer-Bachi, M. Beilicke, W. Benbow, D. Berge, K. Bernlöhr, C. Boisson, O. Bolz, V. Borrel, I. Braun, A. M. Brown, R. Bühler, I. Büsching, S. Carrigan, P. M. Chadwick, L.-M. Chounet, R. Cornils, L. Costamante, B. Degrange, H. J. Dickinson, A. Djannati-Ataï, L. O'C. Drury, G. Dubus, K. Egberts, D. Emmanoulopoulos, P. Espigat, F. Feinstein, E. Ferrero, A. Fiasson, G. Fontaine, S. Funk, S. Funk, M. Füßling, Y. A. Gallant, B. Giebels, J. F. Glicenstein, P. Goret, C. Hadjichristidis, D. Hauser, M. Hauser, G. Heinzelmann, G. Henri, G. Hermann, J. A. Hinton, A. Hoffmann, W. Hofmann, M. Holleran, D. Horns, A. Jacholkowska, O. C. de Jager, E. Kendziorra, B. Khélifi, N. Komin, A. Konopelko, K. Kosack, I. J. Latham, R. Le Gallou, A. Lemière, M. Lemoine-Goumard, T. Lohse, J. M. Martin, O. Martineau-Huynh, A. Marcowith, C. Masterson, G. Maurin, T. J. L. McComb, E. Moulin, M. de Naurois, D. Nedbal, S. J. Nolan, A. Noutsos, K. J. Orford, J. L. Osborne, M. Ouchrif, M. Panter, G. Pelletier, S. Pita, G. Pühlhofer, M. Punch, B. C. Raubenheimer, M. Raue, S. M. Rayner, A. Reimer, O. Reimer, J. Ripken, L. Rob, L. Rolland, G. Rowell, V. Sahakian, A. Santangelo, L. Saugé, S. Schlenker, R. Schlickeiser, R. Schröder, U. Schwanke, S. Schwarzburg, A. Shalchi, H. Sol, D. Spangler, F. Spanier, R. Steenkamp, C. Stegmann, G. Superina, J.-P. Tavernet, R. Terrier, M. Tluczykont, C. van Eldik, G. Vasileiadis, C. Venter, P. Vincent, H. J. Völk, S. J. Wagner, and M. Ward. 3.9 day orbital modulation in the TeV γ-ray flux and spectrum from the X-ray binary LS 5039. A&A, 460:743–749, December 2006.

[14] F. A. Aharonian. *Very high energy cosmic gamma radiation : a crucial window on the extreme Universe*. World Scientific Publishing Co., 2004.

[15] F. A. Aharonian, A. G. Akhperjanian, J. A. Barrio, K. Bernlöhr, H. Bojahr, I. Calle, J. L. Contreras, J. Cortina, A. Daum, T. Deckers, S. Denninghoff, V. Fonseca, J. C. Gonzalez, G. Heinzelmann, M. Hemberger, G. Hermann, M. Heß, A. Heusler, W. Hofmann, H. Hohl, D. Horns, A. Ibarra, R. Kankanyan, J. Kettler, C. Köhler, A. Konopelko, H. Kornmeyer, M. Kestel, D. Kranich, H. Krawczynski, H. Lampeitl, A. Lindner, E. Lorenz, N. Magnussen, H. Meyer, R. Mirzoyan, A. Moralejo, L. Padilla, M. Panter, D. Petry, R. Plaga, A. Plyasheshnikov, J. Prahl, G. Pühlhofer, G. Rauterberg, C. Renault, W. Rhode, A. Röhring, V. Sahakian, M. Samorski, D. Schmele, F. Schröder, W. Stamm, H. J. Völk, B. Wiebel-Sooth, C. Wiedner, M. Willmer, and W. Wittek. The time averaged TeV energy spectrum of MKN 501 of the extraordinary 1997 outburst as measured with the stereoscopic Cherenkov telescope system of HEGRA. A&A, 349:11–28, September 1999.

[16] F. A. Aharonian, A. G. Akhperjanian, J. A. Barrio, K. Bernlöhr, H. Bojahr, J. L. Contreras, J. Cortina, A. Daum, T. Deckers, V. Fonseca, J. C. Gonzalez, G. Heinzelmann, M. Hemberger, G. Hermann, M. Heß, A. Heusler, W. Hofmann, H. Hohl, D. Horns, A. Ibarra, R. Kankanyan, O. Kirstein, C. Köhler, A. Konopelko, H. Kornmeyer, D. Kranich, H. Krawczynski, H. Lampeitl, A. Lindner, E. Lorenz, N. Magnussen, H. Meyer, R. Mirzoyan, A. Moralejo, L. Padilla, M. Panter, D. Petry, R. Plaga, A. Plyasheshnikov, J. Prahl, G. Pühlhofer, G. Rauterberg, C. Renault, W. Rhode, V. Sahakian,

M. Samorski, D. Schmele, F. Schröder, W. Stamm, H. J. Völk, B. Wiebel-Sooth, C. Wiedner, M. Willmer, and H. Wirth. The temporal characteristics of the TeV gamma-radiation from MKN 501 in 1997. I. Data from the stereoscopic imaging atmospheric Cherenkov telescope system of HEGRA. A&A, 342:69–86, February 1999.

[17] F. A. Aharonian and S. V. Bogovalov. Exploring physics of rotation powered pulsars with sub-10 GeV imaging atmospheric Cherenkov telescopes. *New Astronomy*, 8:85–103, February 2003.

[18] J. Albert, E. Aliu, H. Anderhub, P. Antoranz, A. Armada, C. Baixeras, J. A. Barrio, H. Bartko, D. Bastieri, J. K. Becker, W. Bednarek, K. Berger, C. Bigongiari, A. Biland, R. K. Bock, P. Bordas, V. Bosch-Ramon, T. Bretz, I. Britvitch, M. Camara, E. Carmona, A. Chilingarian, J. A. Coarasa, S. Commichau, J. L. Contreras, J. Cortina, M. T. Costado, V. Curtef, V. Danielyan, F. Dazzi, A. De Angelis, C. Delgado, R. de los Reyes, B. De Lotto, E. Domingo-Santamaría, D. Dorner, M. Doro, M. Errando, M. Fagiolini, D. Ferenc, E. Fernández, R. Firpo, J. Flix, M. V. Fonseca, L. Font, M. Fuchs, N. Galante, R. García-López, M. Garczarczyk, M. Gaug, M. Giller, F. Goebel, D. Hakobyan, M. Hayashida, T. Hengstebeck, A. Herrero, D. Höhne, J. Hose, C. C. Hsu, P. Jacon, T. Jogler, R. Kosyra, D. Kranich, R. Kritzer, A. Laille, E. Lindfors, S. Lombardi, F. Longo, J. López, M. López, E. Lorenz, P. Majumdar, G. Maneva, K. Mannheim, O. Mansutti, M. Mariotti, M. Martínez, D. Mazin, C. Merck, M. Meucci, M. Meyer, J. M. Miranda, R. Mirzoyan, S. Mizobuchi, A. Moralejo, D. Nieto, K. Nilsson, J. Ninkovic, E. Oña-Wilhelmi,

N. Otte, I. Oya, D. Paneque, M. Panniello, R. Paoletti, J. M. Paredes, M. Pasanen, D. Pascoli, F. Pauss, R. Pegna, M. Persic, L. Peruzzo, A. Piccioli, M. Poller, E. Prandini, N. Puchades, A. Raymers, W. Rhode, M. Ribó, J. Rico, M. Rissi, A. Robert, S. Rügamer, A. Saggion, A. Sánchez, P. Sartori, V. Scalzotto, V. Scapin, R. Schmitt, T. Schweizer, M. Shayduk, K. Shinozaki, S. N. Shore, N. Sidro, A. Sillanpää, D. Sobczynska, A. Stamerra, L. S. Stark, L. Takalo, P. Temnikov, D. Tescaro, M. Teshima, N. Tonello, D. F. Torres, N. Turini, H. Vankov, V. Vitale, R. M. Wagner, T. Wibig, W. Wittek, F. Zandanel, R. Zanin, and J. Zapatero. VHE γ-Ray Observation of the Crab Nebula and its Pulsar with the MAGIC Telescope. ApJ, 674:1037–1055, February 2008.

[19] E. Aliu, H. Anderhub, L. A. Antonelli, P. Antoranz, M. Backes, C. Baixeras, J. A. Barrio, H. Bartko, D. Bastieri, J. K. Becker, W. Bednarek, K. Berger, E. Bernardini, C. Bigongiari, A. Biland, R. K. Bock, G. Bonnoli, P. Bordas, V. Bosch-Ramon, T. Bretz, I. Britvitch, M. Camara, E. Carmona, A. Chilingarian, S. Commichau, J. L. Contreras, J. Cortina, M. T. Costado, S. Covino, V. Curtef, F. Dazzi, A. De Angelis, E. De Cea del Pozo, R. de los Reyes, B. De Lotto, M. De Maria, F. De Sabata, C. Delgado Mendez, A. Dominguez, D. Dorner, M. Doro, D. Elsässer, M. Errando, M. Fagiolini, D. Ferenc, E. Fernandez, R. Firpo, M. V. Fonseca, L. Font, N. Galante, R. J. Garcia Lopez, M. Garczarczyk, M. Gaug, F. Goebel, D. Hadasch, M. Hayashida, A. Herrero, D. Höhne, J. Hose, C. C. Hsu, S. Huber, T. Jogler, D. Kranich, A. La Barbera, A. Laille, E. Leonardo, E. Lindfors, S. Lombardi, F. Longo,

M. Lopez, E. Lorenz, P. Majumdar, G. Maneva, N. Mankuzhiyil, K. Mannheim, L. Maraschi, M. Mariotti, M. Martinez, D. Mazin, M. Meucci, M. Meyer, J. M. Miranda, R. Mirzoyan, M. Moles, A. Moralejo, D. Nieto, K. Nilsson, J. Ninkovic, N. Otte, I. Oya, R. Paoletti, J. M. Paredes, M. Pasanen, D. Pascoli, F. Pauss, R. G. Pegna, M. A. Perez-Torres, M. Persic, L. Peruzzo, A. Piccioli, F. Prada, E. Prandini, N. Puchades, A. Raymers, W. Rhode, M. Ribó, J. Rico, M. Rissi, A. Robert, S. Rügamer, A. Saggion, T. Y. Saito, M. Salvati, M. Sanchez-Conde, P. Sartori, K. Satalecka, V. Scalzotto, V. Scapin, T. Schweizer, M. Shayduk, K. Shinozaki, S. N. Shore, N. Sidro, A. Sierpowska-Bartosik, A. Sillanpää, D. Sobczynska, F. Spanier, A. Stamerra, L. S. Stark, L. Takalo, F. Tavecchio, P. Temnikov, D. Tescaro, M. Teshima, M. Tluczykont, D. F. Torres, N. Turini, H. Vankov, A. Venturini, V. Vitale, R. M. Wagner, W. Wittek, V. Zabalza, F. Zandanel, R. Zanin, J. Zapatero, O. C. de Jager, E. de Ona Wilhelmi, and MAGIC Collaboration. Observation of Pulsed γ-Rays Above 25 GeV from the Crab Pulsar with MAGIC. *Science*, 322:1221–, November 2008.

[20] J. Arons. Pair creation above pulsar polar caps - Geometrical structure and energetics of slot gaps. ApJ, 266:215–241, March 1983.

[21] C. Baixeras, D. Bastieri, C. Bigongiari, O. Blanch, G. Blanchot, R. Bock, T. Bretz, A. Chilingarian, J. A. Coarasa, E. Colombo, J. C. Contreras, D. Corti, J. Cortina, C. Domingo, E. Domingo, D. Ferenc, E. Fernández, J. Flix, V. Fonseca, L. Font, N. Galante, M. Gaug, M. Garczarczyk, J. Gebauer, M. Giller, F. Goebel, T. Hengstebeck, P. Jacone, O. C. de Jager, O. Kalekin, M. Kestel,

T. Kneiske, A. Laille, M. López, J. López, E. Lorenz, K. Mannheim, M. Mariotti, M. Martínez, K. Mase, M. Merck, M. Meucci, L. Miralles, R. Mirzoyan, A. Moralejo, E. O. Wilhelmi, R. Orduña, D. Paneque, R. Paoletti, D. Pascoli, N. Pavel, R. Pegna, L. Peruzzo, A. Piccioli, A. Roberts, R. Reyes, A. Saggion, A. Sánchez, P. Sartori, V. Scalzotto, T. Schweizer, A. Sillanpaa, D. Sobczynska, A. Stamerra, A. Stepanian, R. Stiehler, L. Takalo, M. Teshima, N. Tonello, A. Torres, N. Turini, V. Vitale, S. Volkov, R. M. Wagner, T. Wibig, and W. Wittek. Commissioning and first tests of the MAGIC telescope. *Nuclear Instruments and Methods in Physics Research A*, 518:188–192, February 2004.

[22] M. G. Baring. High-energy emission from pulsars: the polar cap scenario. *Advances in Space Research*, 33:552–560, 2004.

[23] M. G. Baring. Perspectives on Gamma-Ray Pulsar Emission. *ArXiv e-prints*, December 2010.

[24] R. J Beran. Asymptotic Theory of a Class of Tests for Uniformity of a Circular Distribution. *Ann. Math. Statist.*, 40:1196–1206, 1969.

[25] A. Berk, G. P. Anderson, P. K. Acharya, L. S. Bernstein, L. Muratov, J. Lee, M. Fox, S. M. Adler-Golden, J. H. Chetwynd, M. L. Hoke, R. B. Lockwood, J. A. Gardner, T. W. Cooley, C. C. Borel, and P. E. Lewis. MODTRAN 5: a reformulated atmospheric band model with auxiliary species and practical multiple scattering options: update. In S. S. Shen & P. E. Lewis, editor, *Society of Photo-Optical Instrumentation Engineers (SPIE) Conference Series*, volume 5806 of *Society of Photo-Optical Instrumentation Engineers (SPIE) Conference Series*, pages 662–667, June 2005.

[26] K. Bernlohr. Impact of atmospheric parameters on the atmospheric Cherenkov technique*. *Astroparticle Physics*, 12:255–268, January 2000.

[27] S. M. Bradbury and H. J. Rose. Pattern recognition trigger electronics for an imaging atmospheric Cherenkov telescope. *Nuclear Instruments and Methods in Physics Research A*, 481:521–528, April 2002.

[28] M. C. Chantell, D. Bhattacharya, C. E. Covault, M. Dragovan, R. Fernholz, D. T. Gregorich, D. S. Hanna, G. H. Marion, R. A. Ong, S. Oser, T. O. Tumer, and D. A. Williams. Prototype test results of the solar tower atmospheric Cherenkov effect experiment (STACEE). *Nuclear Instruments and Methods in Physics Research A*, 408:468–485, May 1998.

[29] K. S. Cheng, C. Ho, and M. Ruderman. Energetic radiation from rapidly spinning pulsars. I - Outer magnetosphere gaps. II - VELA and Crab. ApJ, 300:500–539, January 1986.

[30] K. S. Cheng, C. Ho, and M. Ruderman. Energetic Radiation from Rapidly Spinning Pulsars. II. VELA and Crab. ApJ, 300:522–+, January 1986.

[31] T. CTA Consortium. Design Concepts for the Cherenkov Telescope Array. *ArXiv e-prints*, August 2010.

[32] M. K. Daniel. Application of radisonde data to VERITAS simulations. In *International Cosmic Ray Conference*, volume 3 of *International Cosmic Ray Conference*, pages 1329–1332, 2008.

[33] M. K. Daniel. The VERITAS standard data analysis. In *International Cosmic Ray Conference*, volume 3 of *International Cosmic Ray Conference*, pages 1325–1328, 2008.

[34] J. K. Daugherty and A. K. Harding. Electromagnetic cascades in pulsars. ApJ, 252:337–347, January 1982.

[35] J. M. Davies and Cotton E. S. Design of the quartermaster solar furnace. *Solar Energy*, 1:2-3:16–22, 1957.

[36] O. C. de Jager, B. C. Raubenheimer, and J. W. H. Swanepoel. A powerful test for weak periodic signals with unknown light curve shape in sparse data. A&A, 221:180–190, August 1989.

[37] M. de Naurois, J. Holder, R. Bazer-Bachi, H. Bergeret, P. Bruel, A. Cordier, G. Debiais, J.-P. Dezalay, D. Dumora, E. Durand, P. Eschstruth, P. Espigat, B. Fabre, P. Fleury, N. Hérault, M. Hrabovsky, S. Incerti, R. Le Gallou, F. Münz, A. Musquère, J.-F. Olive, E. Paré, J. Québert, R. C. Rannot, T. Reposeur, L. Rob, P. Roy, T. Sako, P. Schovanek, D. A. Smith, P. Snabre, and A. Volte. Measurement of the Crab Flux above 60 GeV with the CELESTE Cerenkov Telescope. ApJ, 566:343–357, February 2002.

[38] J. Dyks and B. Rudak. Two-Pole Caustic Model for High-Energy Light Curves of Pulsars. ApJ, 598:1201–1206, December 2003.

[39] C. E. Fichtel, R. C. Hartman, D. A. Kniffen, D. J. Thompson, H. Ogelman, M. E. Ozel, T. Tumer, and G. F. Bignami. High-energy gamma-ray results from the second small astronomy satellite. ApJ, 198:163–182, May 1975.

[40] J. M. Fierro, P. F. Michelson, P. L. Nolan, and D. J. Thompson. Phase-resolved Studies of the High-Energy Gamma-Ray Emission from the Crab, Geminga, and VELA Pulsars. ApJ, 494:734–+, February 1998.

[41] P. Goldreich and W. H. Julian. Pulsar Electrodynamics. ApJ, 157:869–+, August 1969.

[42] J. A. Goodman and Hawc Collaboration. Physics with HAWC. In D. B. Kieda & P. Gondolo, editor, *2009 Snowbird Particle Astrophysics and Cosmology Workshop (SNOWPAC 2009)*, volume 426 of *Astronomical Society of the Pacific Conference Series*, pages 19–+, July 2010.

[43] J. Hall, V. V. Vassiliev, D. B. Kieda, J. Moses, T. Nagai, and J. Smith. Veritas CFDs. In *International Cosmic Ray Conference*, volume 5 of *International Cosmic Ray Conference*, pages 2851–+, July 2003.

[44] D. Hanna. Calibration Techniques for VERITAS. In *International Cosmic Ray Conference*, volume 3 of *International Cosmic Ray Conference*, pages 1417–1420, 2008.

[45] D. Hanna, A. McCann, M. McCutcheon, and L. Nikkinen. An LED-based flasher system for VERITAS. *Nuclear Instruments and Methods in Physics Research A*, 612:278–287, January 2010.

[46] A. Harding and A. Muslimov. Pulsar Slot Gaps and Unidentified Egret Sources. Ap&SS, 297:63–70, June 2005.

[47] A. K. Harding, J. V. Stern, J. Dyks, and M. Frackowiak. High-Altitude Emission from Pulsar Slot Gaps: The Crab Pulsar. ApJ, 680:1378–1393, June 2008.

[48] J. D Hart. On the Choice of a Truncation Point in Fourier Series Density Estimation. *J. Stat. Comp.*, 21:95 – 116, 1985.

[49] D. Heck, J. Knapp, J. N. Capdevielle, G. Schatz, and T. Thouw. *CORSIKA: a Monte Carlo code to simulate extensive air showers.* February 1998.

[50] A. Hewish. Background to Discovery: Some Recollections. In C. Bassa, Z. Wang, A. Cumming, & V. M. Kaspi, editor, *40 Years of Pulsars: Millisecond Pulsars, Magnetars and More*, volume 983 of *American Institute of Physics Conference Series*, pages 3–7, February 2008.

[51] A. Hewish, S. J. Bell, J. D. Pilkington, P. F. Scott, and R. A. Collins. Observation of a Rapidly Pulsating Radio Source. Nature, 217:709–+, 1968.

[52] A. M. Hillas. Cerenkov light images of EAS produced by primary gamma. In F. C. Jones, editor, *International Cosmic Ray Conference*, volume 3 of *International Cosmic Ray Conference*, pages 445–448, August 1985.

[53] A. M. Hillas, C. W. Akerlof, S. D. Biller, J. H. Buckley, D. A. Carter-Lewis, M. Catanese, M. F. Cawley, D. J. Fegan, J. P. Finley, J. A. Gaidos, F. Krennrich, R. C. Lamb, M. J. Lang, G. Mohanty, M. Punch, P. T. Reynolds, A. J. Rodgers, H. J. Rose, A. C. Rovero, M. S. Schubnell, G. H. Sembroski, G. Vacanti, T. C. Weekes, M. West, and J. Zweerink. The Spectrum of TeV Gamma Rays from the Crab Nebula. ApJ, 503:744–+, August 1998.

[54] J. A. Hinton. The status of the HESS project. *New Astronomy Review*, 48:331–337, April 2004.

[55] K. Hirotani. Gamma-Ray Emissions from Pulsars: Spectra of the TEV Fluxes from Outer Gap Accelerators. ApJ, 549:495–508, March 2001.

[56] K. Hirotani. Outer-Gap versus Slot-Gap Models for Pulsar High-Energy Emissions: The Case of the Crab Pulsar. ApJ, 688:L25–L28, November 2008.

[57] C. M. Hoffman, C. Sinnis, P. Fleury, and M. Punch. Gamma-ray astronomy at high energies. *Reviews of Modern Physics*, 71:897–936, July 1999.

[58] W. Hofmann, I. Jung, A. Konopelko, H. Krawczynski, H. Lampeitl, and G. Pühlhofer. Comparison of techniques to reconstruct VHE gamma-ray showers from multiple stereoscopic Cherenkov images. *Astroparticle Physics*, 12:135–143, November 1999.

[59] J. Holder, R. W. Atkins, H. M. Badran, G. Blaylock, S. M. Bradbury, J. H. Buckley, K. L. Byrum, D. A. Carter-Lewis, O. Celik, Y. C. K. Chow, P. Cogan, W. Cui, M. K. Daniel, I. de La Calle Perez, C. Dowdall, P. Dowkontt, C. Duke, A. D. Falcone, S. J. Fegan, J. P. Finley, P. Fortin, L. F. Fortson, K. Gibbs, G. Gillanders, O. J. Glidewell, J. Grube, K. J. Gutierrez, G. Gyuk, J. Hall, D. Hanna, E. Hays, D. Horan, S. B. Hughes, T. B. Humensky, A. Imran, I. Jung, P. Kaaret, G. E. Kenny, D. Kieda, J. Kildea, J. Knapp, H. Krawczynski, F. Krennrich, M. J. Lang, S. Lebohec, E. Linton, E. K. Little, G. Maier, H. Manseri, A. Milovanovic, P. Moriarty, R. Mukherjee, P. A. Ogden, R. A. Ong, D. Petry, J. S. Perkins, F. Pizlo, M. Pohl, J. Quinn, K. Ragan, P. T. Reynolds, E. T. Roache, H. J. Rose, M. Schroedter, G. H. Sembroski, G. Sleege, D. Steele, S. P. Swordy, A. Syson, J. A. Toner, L. Valcarcel, V. V. Vassiliev, S. P. Wakely, T. C. Weekes, R. J. White, D. A. Williams, and R. Wagner. The first VERITAS telescope. *Astroparticle Physics*, 25:391–401, July 2006.

[60] D. Horns and F. A. Aharonian. The Crab Nebula: Linking MeV Synchrotron and 50 TeV Inverse Compton Photons. In V. Schoenfelder, G. Lichti, & C. Winkler, editor, *5th INTEGRAL Workshop on the INTEGRAL Universe*, volume 552 of *ESA Special Publication*, pages 439–+, October 2004.

[61] E. A. Jackson. A new pulsar atmospheric model. I - Aligned magnetic and rotational axes. ApJ, 206:831–841, June 1976.

[62] J.V. Jelley. *Progress in Elementary Particles and Cosmic Ray Physics*, volume 9, page 41. North Holland, 1967.

[63] J. Kildea, R. W. Atkins, H. M. Badran, G. Blaylock, I. H. Bond, S. M. Bradbury, J. H. Buckley, D. A. Carter-Lewis, O. Celik, Y. C. K. Chow, W. Cui, P. Cogan, M. K. Daniel, I. de La Calle Perez, C. Dowdall, C. Duke, A. D. Falcone, D. J. Fegan, S. J. Fegan, J. P. Finley, L. F. Fortson, D. Gall, G. H. Gillanders, J. Grube, K. J. Gutierrez, J. Hall, T. A. Hall, J. Holder, D. Horan, S. B. Hughes, M. Jordan, I. Jung, G. E. Kenny, M. Kertzman, J. Knapp, A. Konopelko, K. Kosack, H. Krawczynski, F. Krennrich, M. J. Lang, S. Lebohec, J. Lloyd-Evans, J. Millis, P. Moriarty, T. Nagai, P. A. Ogden, R. A. Ong, J. S. Perkins, D. Petry, F. Pizlo, M. Pohl, J. Quinn, M. Quinn, P. F. Rebillot, H. J. Rose, M. Schroedter, G. H. Sembroski, A. W. Smith, A. Syson, J. A. Toner, L. Valcarcel, V. V. Vassiliev, S. P. Wakely, T. C. Weekes, and R. J. White. The Whipple Observatory 10 m gamma-ray telescope, 1997 2006. *Astroparticle Physics*, 28:182–195, October 2007.

[64] M. Kramer. Observations of Pulsed Emission from Pulsars. In C. Bassa, Z. Wang, A. Cumming, & V. M. Kaspi, editor, *40 Years of Pulsars: Millisecond Pulsars, Magnetars and More*, volume 983 of *American Institute of Physics Conference Series*, pages 11–19, February 2008.

[65] H. Krawczynski, D. A. Carter-Lewis, C. Duke, J. Holder, G. Maier, S. Le Bohec, and G. Sembroski. Gamma hadron separation methods for the VERITAS

array of four imaging atmospheric Cherenkov telescopes. *Astroparticle Physics*, 25:380–390, July 2006.

[66] F. Krennrich, I. H. Bond, P. J. Boyle, S. M. Bradbury, J. H. Buckley, D. Carter-Lewis, O. Celik, W. Cui, M. Daniel, M. D'Vali, I. de La Calle Perez, C. Duke, A. Falcone, D. J. Fegan, S. J. Fegan, J. P. Finley, L. F. Fortson, J. Gaidos, S. Gammell, K. Gibbs, G. H. Gillanders, J. Grube, J. Hall, T. A. Hall, D. Hanna, A. M. Hillas, J. Holder, D. Horan, A. Jarvis, M. Jordan, G. E. Kenny, M. Kertzman, D. Kieda, J. Kildea, J. Knapp, K. Kosack, H. Krawczynski, M. J. Lang, S. Lebohec, E. Linton, J. Lloyd-Evans, A. Milovanovic, P. Moriarty, D. Müller, T. Nagai, S. Nolan, R. A. Ong, R. Pallassini, D. Petry, B. Power-Mooney, J. Quinn, M. Quinn, K. Ragan, P. Rebillot, P. T. Reynolds, H. J. Rose, M. Schroedter, G. Sembroski, S. P. Swordy, A. Syson, V. V. Vassiliev, G. Walker, S. P. Wakely, T. C. Weekes, and J. Zweerink. VERITAS: the Very Energetic Radiation Imaging Telescope Array System. *New Astronomy Review*, 48:345–349, April 2004.

[67] H. Kubo, A. Asahara, G. V. Bicknell, R. W. Clay, Y. Doi, P. G. Edwards, R. Enomoto, S. Gunji, S. Hara, T. Hara, T. Hattori, S. Hayashi, C. Itoh, S. Kabuki, F. Kajino, H. Katagiri, A. Kawachi, T. Kifune, L. T. Ksenofontov, T. Kurihara, R. Kurosaka, J. Kushida, Y. Matsubara, Y. Miyashita, Y. Mizumoto, M. Mori, H. Moro, H. Muraishi, Y. Muraki, T. Naito, T. Nakase, D. Nishida, K. Nishijima, M. Ohishi, K. Okumura, J. R. Patterson, R. J. Protheroe, N. Sakamoto, K. Sakurazawa, D. L. Swaby, T. Tanimori, H. Tanimura, G. Thornton, F. Tokanai, K. Tsuchiya, T. Uchida, S. Watanabe,

T. Yamaoka, S. Yanagita, T. Yoshida, and T. Yoshikoshi. Status of the CANGAROO-III project. *New Astronomy Review*, 48:323–329, April 2004.

[68] L. Kuiper, W. Hermsen, G. Cusumano, R. Diehl, V. Schönfelder, A. Strong, K. Bennett, and M. L. McConnell. The Crab pulsar in the 0.75-30 MeV range as seen by CGRO COMPTEL. A coherent high-energy picture from soft X-rays up to high-energy gamma-rays. A&A, 378:918–935, November 2001.

[69] S. Lebohec, C. Duke, and P. Jordan. Minimal stereoscopic analysis for imaging atmospheric Cherenkov telescope arrays. *Astroparticle Physics*, 24:26–31, September 2005.

[70] R. W. Lessard, I. H. Bond, S. M. Bradbury, J. H. Buckley, A. M. Burdett, D. A. Carter-Lewis, M. Catanese, M. F. Cawley, M. D'Vali, D. J. Fegan, J. P. Finley, J. A. Gaidos, G. H. Gillanders, T. Hall, A. M. Hillas, F. Krennrich, M. J. Lang, C. Masterson, P. Moriarty, J. Quinn, H. J. Rose, F. W. Samuelson, G. H. Sembroski, R. Srinivasan, V. V. Vassiliev, and T. C. Weekes. Search for Pulsed TEV Gamma-Ray Emission from the Crab Pulsar. ApJ, 531:942–948, March 2000.

[71] T.-P. Li and Y.-Q. Ma. Analysis methods for results in gamma-ray astronomy. ApJ, 272:317–324, September 1983.

[72] M. S. Longair. *High energy astrophysics. Vol.2: Stars, the galaxy and the interstellar medium*. Cambridge University Press, 1994.

[73] A. G. Lyne, R. S. Pritchard, and F. Graham-Smith. Twenty-Three Years of Crab Pulsar Rotational History. MNRAS, 265:1003–+, December 1993.

[74] Y. Lyubarsky. Pulsar emission mechanisms. In C. Bassa, Z. Wang, A. Cumming, & V. M. Kaspi, editor, *40 Years of Pulsars: Millisecond Pulsars, Magnetars and More*, volume 983 of *American Institute of Physics Conference Series*, pages 29–37, February 2008.

[75] M. Lyutikov, N. Otte, and A. McCann. The very-high energy emission from pulsars: a case for inverse Compton scattering. *ArXiv e-prints*, August 2011.

[76] G. Maier. Monte Carlo studies of the VERITAS array of Cherenkov telescopes. In *International Cosmic Ray Conference*, volume 3 of *International Cosmic Ray Conference*, pages 1413–1416, 2008.

[77] R. N. Manchester, G. B. Hobbs, A. Teoh, and M. Hobbs. The Australia Telescope National Facility Pulsar Catalogue. AJ, 129:1993–2006, April 2005.

[78] M. Mariotti. No significant enhancement in the VHE gamma-ray flux of the Crab Nebula measured by MAGIC in September 2010. *The Astronomer's Telegram*, 2967:1–+, October 2010.

[79] A. McCann, D. Hanna, J. Kildea, and M. McCutcheon. A new mirror alignment system for the VERITAS telescopes. *Astroparticle Physics*, 32:325–329, January 2010.

[80] F. C. Michel. Vacuum gaps in pulsar magnetospheres. ApJ, 227:579–589, January 1979.

[81] F. C. Michel. Theory of pulsar magnetospheres. *Reviews of Modern Physics*, 54:1–66, January 1982.

[82] T. Mineo, C. Ferrigno, L. Foschini, A. Segreto, G. Cusumano, G. Malaguti, G. Di Cocco, and C. Labanti. INTEGRAL observations of the Crab pulsar.

A&A, 450:617–623, May 2006.

[83] P. Morrison. On gamma-ray astronomy. *Il Nuovo Cimento*, 7:858–865, 1958.

[84] R. Narayan and M. Vivekanand. Geometry of pulsar beams - Relative orientations of rotation axis, magnetic axis, and line of sight. A&A, 113:L3–L6, September 1982.

[85] G. National Data Center. U.S. standard atmosphere (1976). Planet. Space Sci., 40:553–554, April 1992.

[86] R. A. Ong. Search for an Enhanced TeV Gamma-Ray Flux from the Crab Nebula with VERITAS. *The Astronomer's Telegram*, 2968:1–+, October 2010.

[87] T. Oosterbroek, I. Cognard, A. Golden, P. Verhoeve, D. D. E. Martin, C. Erd, R. Schulz, J. A. Stüwe, A. Stankov, and T. Ho. Simultaneous absolute timing of the Crab pulsar at radio and optical wavelengths. A&A, 488:271–277, September 2008.

[88] S. Oser, D. Bhattacharya, L. M. Boone, M. C. Chantell, Z. Conner, C. E. Covault, M. Dragovan, P. Fortin, D. T. Gregorich, D. S. Hanna, R. Mukherjee, R. A. Ong, K. Ragan, R. A. Scalzo, D. R. Schuette, C. G. Théoret, T. O. Tümer, D. A. Williams, and J. A. Zweerink. High-Energy Gamma-Ray Observations of the Crab Nebula and Pulsar with the Solar Tower Atmospheric Cerenkov Effect Experiment. ApJ, 547:949–958, February 2001.

[89] Pierre AUGER Collaboration, I. Allekotte, A. F. Barbosa, P. Bauleo, C. Bonifazi, B. Civit, C. O. Escobar, B. García, G. Guedes, M. Gómez Berisso, J. L. Harton, M. Healy, M. Kaducak, P. Mantsch, P. O. Mazur, C. Newman-Holmes, I. Pepe, I. Rodriguez-Cabo, H. Salazar, N. Smetniansky-de Grande,

and D. Warner. The surface detector system of the Pierre Auger Observatory. *Nuclear Instruments and Methods in Physics Research A*, 586:409–420, March 2008.

[90] J. R. Prescott. A statistical model for photomultiplier single-electron statistics. *Nuclear Instruments and Methods*, 39:173–+, January 1966.

[91] F. Rademakers, M. Goto, P. Canal, and R. Brun. ROOT Status and Future Developments. *ArXiv Computer Science e-prints*, June 2003.

[92] P. F. Rebillot, J. H. Buckley, P. Dowkontt, and K. Kosack. The VERITAS Flash ADC Electronics System. In *International Cosmic Ray Conference*, volume 5 of *International Cosmic Ray Conference*, pages 2827–+, July 2003.

[93] M. Rissi. *Detection of Pulsed Very High Energy Gamma-Rays from the Crab Pulsar with the MAGIC telescope using an Analog Sum Trigger*. PhD thesis, ETH Zurich, 2009.

[94] E. Roache, R. Irvin, J. S. Perkins, and et al. Mirror Facets for the VERITAS Telescopes. In *International Cosmic Ray Conference*, volume 3 of *International Cosmic Ray Conference*, pages 1397–1400, 2008.

[95] M. A. Ruderman and P. G. Sutherland. Theory of pulsars - Polar caps, sparks, and coherent microwave radiation. ApJ, 196:51–72, February 1975.

[96] L. Scarsi, K. Bennett, G. F. Bignami, G. Boella, R. Buccheri, W. Hermsen, L. Koch, H. A. Mayer-Hasselwander, J. A. Paul, and E. Pfeffermann. The COS-B experiment and mission. In *ESA SP-124: Recent Advances in Gamma-Ray Astronomy*, pages 3–11, July 1977.

[97] M. Shayduk, T. Hengstebeck, O. Kalekin, N. A. Pavel, and T. Schweizer. A New Image Cleaning Method for the MAGIC Telescope. In *International Cosmic Ray Conference*, volume 5 of *International Cosmic Ray Conference*, pages 223–+, 2005.

[98] D. A. Smith, R. Bazer-Bachi, H. Bergeret, P. Bruel, A. Cordier, G. Debiais, M. de Naurois, J.-P. Dezalay, D. Dumora, P. Eschstruth, P. Espigat, B. Fabre, P. Fleury, B. Giebels, N. Hérault, J. Holder, M. Hrabovsky, R. Legallou, I. Malet, B. Merkel, F. Münz, A. Musquére, J.-F. Olive, E. Paré, J. Québert, T. Reposeur, L. Rob, T. Sako, P. Schovanek, and A. Volte. First Detection of Gamma Rays from the Crab Nebula with the CELESTE "Solar Farm" Cherenkov Detector. *Nuclear Physics B Proceedings Supplements*, 80:163–172, March 2000.

[99] A. Spitkovsky. Pulsar Magnetosphere: The Incredible Machine. In C. Bassa, Z. Wang, A. Cumming, & V. M. Kaspi, editor, *40 Years of Pulsars: Millisecond Pulsars, Magnetars and More*, volume 983 of *American Institute of Physics Conference Series*, pages 20–28, February 2008.

[100] D. H. Staelin and E. C. Reifenstein. Pulsating radio sources near the Crab Nebula. *Science*, 162:1481–1483, 1968.

[101] E. M. Standish. Orientation of the JPL Ephemerides, DE 200/LE 200, to the dynamical equinox of J 2000. A&A, 114:297–302, October 1982.

[102] E. M. Standish. JPL PLANETARY AND LUNAR EPHEMERIDES, ftp://ssd.jpl.nasa.gov/pub/eph/export/, 2005.

[103] S. J. Sturner and C. D. Dermer. On the spectra and pulse profiles of gamma-ray pulsars. ApJ, 420:L79–L82, January 1994.

[104] P. A. Sturrock. A Model of Pulsars. ApJ, 164:529–+, March 1971.

[105] J. Takata and H.-K. Chang. Pulse Profiles, Spectra, and Polarization Characteristics of Nonthermal Emissions from the Crab-like Pulsars. ApJ, 670:677–692, November 2007.

[106] M. Tavani, A. Bulgarelli, V. Vittorini, A. Pellizzoni, E. Striani, P. Caraveo, M. C. Weisskopf, A. Tennant, G. Pucella, A. Trois, E. Costa, Y. Evangelista, C. Pittori, F. Verrecchia, E. Del Monte, R. Campana, M. Pilia, A. De Luca, I. Donnarumma, D. Horns, C. Ferrigno, C. O. Heinke, M. Trifoglio, F. Gianotti, S. Vercellone, A. Argan, G. Barbiellini, P. W. Cattaneo, A. W. Chen, T. Contessi, F. D'Ammando, G. DeParis, G. Di Cocco, G. Di Persio, M. Feroci, A. Ferrari, M. Galli, A. Giuliani, M. Giusti, C. Labanti, I. Lapshov, F. Lazzarotto, P. Lipari, F. Longo, F. Fuschino, M. Marisaldi, S. Mereghetti, E. Morelli, E. Moretti, A. Morselli, L. Pacciani, F. Perotti, G. Piano, P. Picozza, M. Prest, M. Rapisarda, A. Rappoldi, A. Rubini, S. Sabatini, P. Soffitta, E. Vallazza, A. Zambra, D. Zanello, F. Lucarelli, P. Santolamazza, P. Giommi, L. Salotti, and G. F. Bignami. Discovery of Powerful Gamma-Ray Flares from the Crab Nebula. *Science*, 331:736–, February 2011.

[107] F. M. Tettelbach and R. Holdaway, editors. *The Astronomical Almanac for the year 2006*, pages B7–B8. The Stationary Office, Norwich, UK, 1994.

[108] J. A. Toner, V. A. Acciari, A. Cesarini, and et al. Bias Alignment of the VERITAS Telescopes. In *International Cosmic Ray Conference*, volume 3 of

International Cosmic Ray Conference, pages 1401–1404, 2008.

[109] Wu-yang Tsai and Thomas Erber. Photon pair creation in intense magnetic fields. *Phys. Rev. D*, 10(2):492–499, Jul 1974.

[110] VERITAS Collaboration, E. Aliu, T. Arlen, T. Aune, M. Beilicke, W. Benbow, A. Bouvier, S. M. Bradbury, J. H. Buckley, V. Bugaev, K. Byrum, A. Cannon, A. Cesarini, J. L. Christiansen, L. Ciupik, E. Collins-Hughes, M. P. Connolly, W. Cui, R. Dickherber, C. Duke, M. Errando, A. Falcone, J. P. Finley, G. Finnegan, L. Fortson, A. Furniss, N. Galante, D. Gall, K. Gibbs, G. H. Gillanders, S. Godambe, S. Griffin, J. Grube, R. Guenette, G. Gyuk, D. Hanna, J. Holder, H. Huan, G. Hughes, C. M. Hui, T. B. Humensky, A. Imran, P. Kaaret, N. Karlsson, M. Kertzman, D. Kieda, H. Krawczynski, F. Krennrich, M. J. Lang, M. Lyutikov, A. S. Madhavan, G. Maier, P. Majumdar, S. McArthur, A. McCann, M. McCutcheon, P. Moriarty, R. Mukherjee, P. Nuñez, R. A. Ong, M. Orr, A. N. Otte, N. Park, J. S. Perkins, F. Pizlo, M. Pohl, H. Prokoph, J. Quinn, K. Ragan, L. C. Reyes, P. T. Reynolds, E. Roache, H. J. Rose, J. Ruppel, D. B. Saxon, M. Schroedter, G. H. Sembroski, G. D. Şentürk, A. W. Smith, D. Staszak, G. Tešić, M. Theiling, S. Thibadeau, K. Tsurusaki, J. Tyler, A. Varlotta, V. V. Vassiliev, S. Vincent, M. Vivier, S. P. Wakely, J. E. Ward, T. C. Weekes, A. Weinstein, T. Weisgarber, D. A. Williams, and B. Zitzer. Detection of Pulsed Gamma Rays Above 100 GeV from the Crab Pulsar. *Science*, 334:69–, October 2011.

[111] K. P. Watters, R. W. Romani, P. Weltevrede, and S. Johnston. An Atlas for Interpreting γ-Ray Pulsar Light Curves. ApJ, 695:1289–1301, April 2009.

[112] T. C. Weekes. *Very high energy gamma-ray astronomy*. Trevor C. Weekes. IoP Series in astronomy and astrophysics, ISBN 0750306580. Bristol, UK: The Institute of Physics Publishing, 2003, 2003.

[113] T. C. Weekes. The Atmospheric Cherenkov Imaging Technique for Very High Energy Gamma-ray Astronomy. *ArXiv Astrophysics e-prints*, August 2005.

[114] T. C. Weekes, M. F. Cawley, D. J. Fegan, K. G. Gibbs, A. M. Hillas, P. W. Kowk, R. C. Lamb, D. A. Lewis, D. Macomb, N. A. Porter, P. T. Reynolds, and G. Vacanti. Observation of TeV gamma rays from the Crab nebula using the atmospheric Cerenkov imaging technique. ApJ, 342:379–395, July 1989.

[115] A. Weinstein. The VERITAS Trigger System. In *International Cosmic Ray Conference*, volume 3 of *International Cosmic Ray Conference*, pages 1539–1542, 2008.

[116] P. Weltevrede, A. A. Abdo, M. Ackermann, M. Ajello, M. Axelsson, L. Baldini, J. Ballet, G. Barbiellini, D. Bastieri, B. M. Baughman, K. Bechtol, R. Bellazzini, B. Berenji, E. D. Bloom, E. Bonamente, A. W. Borgland, J. Bregeon, A. Brez, M. Brigida, P. Bruel, T. H. Burnett, S. Buson, G. A. Caliandro, R. A. Cameron, F. Camilo, P. A. Caraveo, J. M. Casandjian, C. Cecchi, Ö. Çelik, E. Charles, A. Chekhtman, C. C. Cheung, J. Chiang, S. Ciprini, R. Claus, I. Cognard, J. Cohen-Tanugi, L. R. Cominsky, J. Conrad, S. Cutini, C. D. Dermer, G. Desvignes, A. de Angelis, A. de Luca, F. de Palma, S. W. Digel, M. Dormody, E. d. C. e. Silva, P. S. Drell, R. Dubois, D. Dumora, C. Farnier, C. Favuzzi, S. J. Fegan, W. B. Focke, P. Fortin, M. Frailis, P. C. C. Freire, P. Fusco, F. Gargano, D. Gasparrini, N. Gehrels, S. Germani, G. Giavitto,

B. Giebels, N. Giglietto, F. Giordano, T. Glanzman, G. Godfrey, I. A. Grenier, M.-H. Grondin, J. E. Grove, L. Guillemot, S. Guiriec, Y. Hanabata, A. K. Harding, E. Hays, G. Hobbs, R. E. Hughes, M. S. Jackson, G. Jóhannesson, A. S. Johnson, T. J. Johnson, W. N. Johnson, S. Johnston, T. Kamae, H. Katagiri, J. Kataoka, N. Kawai, M. Keith, M. Kerr, J. Knödlseder, M. L. Kocian, M. Kramer, M. Kuss, J. Lande, L. Latronico, M. Lemoine-Goumard, F. Longo, F. Loparco, B. Lott, M. N. Lovellette, P. Lubrano, A. G. Lyne, A. Makeev, R. N. Manchester, M. N. Mazziotta, J. E. McEnery, S. McGlynn, C. Meurer, P. F. Michelson, W. Mitthumsiri, T. Mizuno, A. A. Moiseev, C. Monte, M. E. Monzani, A. Morselli, I. V. Moskalenko, S. Murgia, P. L. Nolan, J. P. Norris, E. Nuss, T. Ohsugi, N. Omodei, E. Orlando, J. F. Ormes, D. Paneque, J. H. Panetta, D. Parent, V. Pelassa, M. Pepe, M. Pesce-Rollins, F. Piron, T. A. Porter, S. Rainò, R. Rando, S. M. Ransom, M. Razzano, N. Rea, A. Reimer, O. Reimer, T. Reposeur, L. S. Rochester, A. Y. Rodriguez, R. W. Romani, M. Roth, F. Ryde, H. F.-W. Sadrozinski, D. Sanchez, A. Sander, P. M. Saz Parkinson, C. Sgrò, E. J. Siskind, D. A. Smith, P. D. Smith, G. Spandre, P. Spinelli, B. W. Stappers, M. S. Strickman, D. J. Suson, H. Tajima, H. Takahashi, T. Tanaka, J. B. Thayer, J. G. Thayer, G. Theureau, D. J. Thompson, S. E. Thorsett, L. Tibaldo, D. F. Torres, G. Tosti, A. Tramacere, Y. Uchiyama, T. L. Usher, A. Van Etten, V. Vasileiou, C. Venter, N. Vilchez, V. Vitale, A. P. Waite, P. Wang, N. Wang, K. Watters, B. L. Winer, K. S. Wood, T. Ylinen, and M. Ziegler. Gamma-ray and Radio Properties of Six Pulsars Detected by the Fermi Large Area Telescope. ApJ, 708:1426–1441, January 2010.

[117] W.-M. Yao, C. Amsler, D. Asner, R.M. Barnett, J. Beringer, P.R. Burchat, C.D. Carone, C. Caso, O. Dahl, G. D'Ambrosio, A. DeGouvea, M. Doser, S. Eidelman, J.L. Feng, T. Gherghetta, M. Goodman, C. Grab, D.E. Groom, A. Gurtu, K. Hagiwara, K.G. Hayes, J.J. Hernández-Rey, K. Hikasa, H. Jawahery, C. Kolda, Kwon Y., M.L. Mangano, A.V. Manohar, A. Masoni, R. Miquel, K. Mönig, H. Murayama, K. Nakamura, S. Navas, K.A. Olive, L. Pape, C. Patrignani, A. Piepke, G. Punzi, G. Raffelt, J.G. Smith, M. Tanabashi, J. Terning, N.A. Törnqvist, T.G. Trippe, P. Vogel, T. Watari, C.G. Wohl, R.L. Workman, P.A. Zyla, B. Armstrong, G. Harper, V.S. Lugovsky, P. Schaffner, M. Artuso, K.S. Babu, H.R. Band, E. Barberio, M. Battaglia, H. Bichsel, O. Biebel, P. Bloch, E. Blucher, R.N. Cahn, D. Casper, A. Cattai, A. Ceccucci, D. Chakraborty, R.S. Chivukula, G. Cowan, T. Damour, T. DeGrand, K. Desler, M.A. Dobbs, M. Drees, A. Edwards, D.A. Edwards, V.D. Elvira, J. Erler, V.V. Ezhela, W. Fetscher, B.D. Fields, B. Foster, D. Froidevaux, T.K. Gaisser, L. Garren, H.-J. Gerber, G. Gerbier, L. Gibbons, F.J. Gilman, G.F. Giudice, A.V. Gritsan, M. Grünewald, H.E. Haber, C. Hagmann, I. Hinchliffe, A. Höcker, P. Igo-Kemenes, J.D. Jackson, K.F. Johnson, D. Karlen, B. Kayser, D. Kirkby, S.R. Klein, K. Kleinknecht, I.G. Knowles, R.V. Kowalewski, P. Kreitz, B. Krusche, Yu.V. Kuyanov, O. Lahav, P. Langacker, A. Liddle, Z. Ligeti, T.M. Liss, L. Littenberg, L. Liu, K.S. Lugovsky, S.B. Lugovsky, T. Mannel, D.M. Manley, W.J. Marciano, A.D. Martin, D. Milstead, M. Narain, P. Nason, Y. Nir, J.A. Peacock, S.A. Prell, A. Quadt, S. Raby, B.N. Ratcliff, E.A. Razuvaev, B. Renk, P. Richardson, S. Roesler, G. Rolandi, M.T.

Ronan, L.J. Rosenberg, C.T. Sachrajda, S. Sarkar, M. Schmitt, O. Schneider, D. Scott, T. Sjöstrand, G.F. Smoot, P. Sokolsky, S. Spanier, H. Spieler, A. Stahl, T. Stanev, R.E. Streitmatter, T. Sumiyoshi, N.P. Tkachenko, G.H. Trilling, G. Valencia, K. van Bibber, M.G. Vincter, D.R. Ward, B.R. Webber, J.D. Wells, M. Whalley, L. Wolfenstein, J. Womersley, C.L. Woody, A. Yamamoto, O.V. Zenin, J. Zhang, and R.-Y. Zhu. Review of Particle Physics. *Journal of Physics G*, 33:1+, 2006.